Univerza
v Ljubljani
Fakulteta za
gradbeništvo in
geodezijo

DOKTORSKI ŠTUDIJSKI
PROGRAM III. STOPNJE
GRAJENO OKOLJE

Kandidatka:

PATRICIA COTIČ

SINTEZA VEČSENZORSKIH NEPORUŠNIH PREISKAV GRADBENIH KONSTRUKCIJSKIH ELEMENTOV Z UPORABO METOD GRUČENJA

Doktorska disertacija štev.: 9/GO

THE SYNTHESIS OF MULTISENSOR NON-DESTRUCTIVE TESTING OF CIVIL ENGINEERING STRUCTURAL ELEMENTS WITH THE USE OF CLUSTERING METHODS

Doctoral thesis No.: 9/GO

Soglasje k temi doktorske disertacije je dala Komisija za doktorski študij Univerze v Ljubljani
na 28. redni seji, 16. maja 2012.
Za mentorja je bil imenovan izr. prof. dr. Zvonko Jagličić,
za somentorja izr. prof. dr. Vlatko Bosiljkov.
Odobreno je bilo pisanje disertacije v angleškem jeziku.

Ljubljana, 6. maj 2014

Blank page

Univerza
v Ljubljani

Fakulteta za
gradbeništvo in
geodezijo

Komisijo za oceno ustreznosti teme doktorske disertacije v sestavi:

- izr. prof. dr. Zvonko Jagličić,
- izr. prof. dr. Vlatko Bosiljkov,
- prof. dr. Goran Turk,
- doc. dr. Mitja Lakner,
- prof. dr. Janez Dolinšek, UL FMF

je imenoval Senat Fakultete za gradbeništvo in geodezijo na 29. redni seji, 28. marca 2012.

Poročevalce za oceno doktorske disertacije v sestavi:

- prof. dr. Janez Dolinšek, UL FMF,
- dr. rer. nat. Ernst Niederleithinger, BAM Federal Institute for Materials Research and Testing, Berlin,
- doc. dr. Mitja Lakner,
- prof. dr. Goran Turk

je imenoval Senat Fakultete za gradbeništvo in geodezijo na 8. redni seji, 26. februarja 2014.

Komisijo za zagovor doktorske disertacije v sestavi:

- prof. dr. Matjaž Mikoš, dekan UL FGG, predsednik,
- izr. prof. dr. Zvonko Jagličić,
- izr. prof. dr. Vlatko Bosiljkov,
- prof. dr. Janez Dolinšek, UL FMF,
- dr. rer. nat. Ernst Niederleithinger, BAM Federal Institute for Materials Research and Testing, Berlin,
- doc. dr. Mitja Lakner,
- prof. dr. Goran Turk

je imenoval Senat Fakultete za gradbeništvo in geodezijo na 4. dopisni seji, ki je potekala od 24. do 28. aprila 2014.

Blank page

Univerza
v Ljubljani

Fakulteta za
gradbeništvo in
geodezijo

IZJAVA O AVTORSTVU

Podpisana **Patricia COTIČ** izjavljam, da sem avtorica doktorske disertacije z naslovom **Sinteza večsenzorskih neporušnih preiskav gradbenih konstrukcijskih elementov z uporabo metod gručenja**.

Izjavljam, da je elektronska različica v vsem enaka tiskani različici.

Izjavljam, da dovoljujem objavo elektronske različice v digitalnih repozitorijih.

Ljubljana, 6. maj 2014 .....
(podpis)

Blank page

ERRATA

Page with error	Line with error	Incorrect	Correct

Blank page

BIBLIOGRAPHIC-DOCUMENTALISTIC INFORMATION AND ABSTRACT

UDC: **551.509.313:624.012.82:624.012.4:(043.3)**

Author: **Patricia Cotič, B.Sc.**

Supervisor: **Assoc. prof. Zvonko Jagličić, Ph.D.**

Co-advisor: **Assoc. prof. Vlatko Bosiljkov, Ph.D.**

Title: **The synthesis of multisensor non-destructive testing of civil engineering structural elements with the use of clustering methods**

Document type: **doctoral dissertation**

Notes: **100 p., 6 tab., 37 fig., 72 eq., 4 ann., 161 ref.**

Keywords: **non-destructive testing, civil engineering, ground penetrating radar, infrared thermography, ultrasonic, complex resistivity, concrete, masonry, data fusion, image fusion, clustering methods**

Abstract:

In the thesis, clustering-based image fusion of multi-sensor non-destructive (NDT) data is studied. Several hard and fuzzy clustering algorithms are analysed and implemented both at the pixel and feature level fusion. Image fusion of ground penetrating radar (GPR) and infrared thermography (IRT) data is applied on concrete specimens with inbuilt artificial defects, as well as on masonry specimens where defects such as plaster delamination and structural cracking were generated through a shear test. We show that on concrete, the GK clustering algorithm exhibits the best performance since it is not limited to the detection of spherical clusters as are the FCM and PFCM algorithms. We also prove that clustering-based fusion outperforms supervised fusion, especially in situations with very limited knowledge about the material properties and depths of the defects. Complementary use of GPR and IRT on multi-leaf masonry walls enabled the detection of the walls' morphology, texture, as well as plaster delamination and structural cracking. For improved detection of the latter two, we propose using data fusion at the pixel level for data segmentation. In addition to defect detection, the effect of moisture is analysed on masonry using GPR, ultrasonic and complex resistivity tomographies. Within the thesis, clustering is also successfully applied in a case study where a multi-sensor NDT data set was automatically collected by a self-navigating mobile robot system. Besides, the classification of spectroscopic spatial data from concrete is taken under consideration. In both applications, clustering is used for unsupervised segmentation of data.

Blank page

BIBLIOGRAFSKO-DOKUMENTACIJSKA STRAN IN IZVLEČEK

UDK: **551.509.313:624.012.82:624.012.4:(043.3)**

Avtor: **Patricia Cotič, univ. dipl. inž. grad.**

Mentor: **izr. prof. dr. Zvonko Jagličić**

Somentor: **izr. prof. dr. Vlatko Bosiljkov**

Naslov: **Sinteza večsenzorskih neporušnih preiskav gradbenih konstrukcijskih elementov z uporabo metod gručenja**

Tip dokumenta: **doktorska disertacija**

Obseg in oprema: **100 str., 6 pregl., 37 sl., 72 en., 4 pril., 161 vir.**

Ključne besede: **neporušne preiskave, gradbeništvo, georadar, infrardeča termografija, ultrazvočna metoda, kompleksno-uporovna metoda, beton, zidovje, združevanje podatkov, združevanje slik, metode gručenja**

Izvleček:

V disertaciji predstavimo uporabo postopka za združevanje slik večsenzorskih neporušnih preiskav, ki temelji na metodah gručenja. Za združevanje na nivoju posamezne slikovne točke in z uporabo značilnic analiziramo algoritme trdega in mehkega gručenja. Sintezo georadarskih in termografskih podatkov opravimo na rezultatih preiskav betonskih preizkušancev z vgrajenimi anomalijami ter na rezultatih preiskav zidovja s prisotnimi razpokami in odstopanjem ometa zaradi delovanja strižne obremenitve. Na betonskih preizkušancih najboljše deluje algoritem gručenja GK, ker prepoznava razrede gručenja poljubne oblike in ne le sferične kot algoritma FCM in PFCM. V primerih s še posebno omejenim vedenjem o materialnih lastnostih in globini anomalij združevanje z uporabo metod gručenja deluje bolje kot metode nadzorovanega združevanja podatkov. Na večslojnih kamnitih zidovih lahko z uporabo georadarja in infrardeče termografije zaznamo morfologijo in teksturo zidov ter odstopanje ometa in nastanek razpok. Za izboljšano zaznavanje odstopanja ometa in razpok predlagamo združevanje podatkov na nivoju posamezne slikovne točke za segmentacijo slik. Z georadarsko, ultrazvočno in geoelekrično tomografijo opravimo na zidovju tudi raziskavo vpliva stopnje vlažnosti zidovja na občutljivost neporušnih metod. Metode gručenja uporabimo tudi za združevanje neporušnih podatkov navigacijskega večsenzorskega robotnega sistema. Poleg tega izvedemo tudi klasifikacijo spektroskopskih podatkov betonskih preizkušancev. V obeh primerih metode gručenja uporabimo za segmentacijo podatkov.

Blank page

ACKNOWLEDGEMENT

I would like to express my deepest appreciation to my supervisor, Dr. Zvonko Jagličić, and my co-advisor, Dr. Vlatko Bosiljkov, for guidance during my research. Without you, this dissertation would not have materialized. I would particularly like to express my warmest gratitude to Zvonko, who allowed me to spend hours on my Physics study. Without your optimism, encouragement and support both studies would hardly have been completed.

I am deeply grateful to my supervisor at BAM, Dr. Ernst Niederleithinger, who guided me into the world of NDT and cluster analysis and gave me insightful comments and suggestions on my research. Only with your leading charm and the splendid working atmosphere from all the colleagues at BAM, Div. 8.2, the work done was made possible. I would particularly like to thank Dr. Christiane Trela, Dr. Ute Effner and Dr. Sabine Kruschwitz for the extensive support with the work done on the masonry specimen "Asterix". Special thanks also to Gerd Wilsch for the LIBS data, as well as to Dr. Markus Stoppel for the BetoScan data. The valuable ideas on data fusion from Dr. Parisa Shokouhi are acknowledged. Marco Lange, Sean Smith and Jens Wöstmann were the guys willing to help me at any time. You taught me many tricks in the lab and contributed to almost all the work I did at BAM. You and especially Christian Köpp and Sebastian Goldschmidt, were my best German teachers. I would also like to express my special thanks to Julia Wolf, Maria Grohmann and Sabine Müller for the friendship and the time we spent in Berlin.

I would also like to thank my colleagues at UL FGG. Particularly, Dr. Violeta Bokan-Bosiljkov for her valuable instructions and generous support, as well as Dr. Dejan Kolarič for his contribution on the numerical simulation on heat propagation. Special thanks also to Franci Čepon, Damjan Špeglič and Primož Murn for extensive measurement support. A big thank goes to the colleagues at IMFM, who contributed to my work in a number of ways. Part of the experimental work could not have been done without the cooperation with people from other institutes. I thank Dr. Aleksander Zidanšek (Jožef Stefan International Postgraduate School) and his group for the use of their radar system, as well as Vid Peterman (Modri Planet, d.o.o.) for performing DIC.

I sincerely thank Dr. David Antolinc, Petra Štukovnik and Meta Kržan from UL FGG, with whom discussions illuminated my work significantly. You've become my dear friends that also contribute to my life experiences.

Finally, I would like to express my warmest gratitude to my parents, who were greatly tolerant and supportive during these three and half years. *Hvala vama!* I owe my deepest thank to my dear sister Karolina, who gave me insightful comments and suggestions on my English writing. Jože, without you, the thesis in this form would not become true. Your love and encouragement has inspired my work enormously. The thesis is dedicated to *You*.

Blank page

"I think nature's imagination
is so much greater than man's,
she's never going to let us relax"

– Richard Feynman

Blank page

TABLE OF CONTENTS

Bibliographic-documentalistic information and abstract . . . III

Bibliografsko-dokumentacijska stran in izvleček . . . V

Acknowledgement . . . VII

1 Introduction **1**

1.1 Scientific background and motivation . . . 1

1.2 Aims and scope . . . 4

2 Basic principles of selected NDT methods **7**

2.1 Overview of NDT methods used in civil engineering . . . 7

2.2 Ground penetrating radar . . . 8

2.2.1 Electromagnetic properties of building materials and the energy storage-loss mechanisms . . . 9

2.2.2 Wave nature of electromagnetic fields . . . 10

2.2.3 Reflection and refraction of electromagnetic waves . . . 12

2.2.4 Horizontal and vertical resolution . . . 13

2.3 Complex resistivity . . . 13

2.3.1 Electrical polarization . . . 14

2.3.2 Apparent and true resistivities . . . 15

2.3.3 Electrode configurations . . . 16

2.4 Infrared thermography . . . 17

2.4.1 Interaction of incident radiation with matter . . . 19

2.4.2 Thermal emission . . . 19

2.4.3 Conduction heat transfer . . . 21

2.4.4 Quantitative data analysis in pulsed thermography . . . 22

2.4.4.1 Thermal contrast . . . 23

2.4.4.2 Pulsed phase thermography . . . 24

2.5 Ultrasonic . . . 27

2.5.1 Acoustic wave theory . . . 27

2.5.2 Reflection and refraction of acoustic waves . . . 29

2.5.3 Acoustic attenuation and dispersion . . . 29

2.5.4 Piezoelectric transducers . . . 30

3 NDT Data Fusion with Clustering **31**

3.1 Introduction to data fusion . . . 31
3.2 A data fusion framework . . . 31
3.3 Cluster analysis . . . 34
3.3.1 Distance and similarity . . . 34
3.3.2 Objective function-based clustering – a general note . . . 34
3.3.3 Objective function-based clustering algorithms . . . 36
3.3.3.1 Hard clustering . . . 36
3.3.3.2 Fuzzy clustering . . . 37
3.3.4 Validity measures . . . 41
3.3.5 Objective function-based clustering algorithm scheme . . . 42

4 Non-destructive testing of laboratory concrete specimens with inbuilt defects and inclusions 45
4.1 Experimental . . . 45
4.1.1 Specimen description . . . 45
4.1.2 Methods . . . 46
4.2 Results . . . 48
4.2.1 Characterization of defects and inclusions using infrared thermography . . 48
4.2.1.1 Thermal contrast . . . 48
4.2.1.2 Pulsed phase thermography . . . 52
4.2.1.3 Numerical simulation . . . 55
4.2.2 Sensitivity evaluation of ground penetrating radar and infrared thermography 58

5 Conclusion and Outlook 61

Summary 65

6 Razširjeni povzetek v slovenskem jeziku (Extended abstract in Slovene) 67
6.1 Uvod . . . 67
6.2 Osnove izbranih neporušnih metod . . . 69
6.3 Združevanje podatkov z gručenjem . . . 72
6.4 Neporušne preiskave laboratorijskih betonskih preizkušancev z vgrajenimi anomalijami . . . 74
6.4.1 Eksperimentalne metode in materiali . . . 74
6.4.2 Rezultati . . . 74
6.5 Neporušne preiskave laboratorijskih ometanih večslojnih kamnitih zidov . . . 76

6.5.1 Eksperimentalne metode in materiali 76
6.5.2 Rezultati 77
6.6 Neporušne preiskave laboratorijskega opečnatega zidu pod vplivom različne vlažnosti 78
6.6.1 Eksperimentalne metode in materiali 78
6.6.2 Rezultati 78
6.7 Neporušne preiskave z večsenzorskim robotnim sistemom BetoScan 79
6.7.1 Eksperimentalne metode in materiali 80
6.7.2 Rezultati 80
6.8 Uporaba metod gručenja za avtomatsko klasifikacijo spektroskopskih podatkov na betonskih preizkušancih 81
6.8.1 Eksperimentalne metode in materiali 81
6.8.2 Rezultati 81
6.9 Zaključki in obeti 82

References **85**

List of Publications **95**

Blank page

LIST OF TABLES

Table 2.1: The typical range of relative dielectric permittivity ε_r, electric conductivity σ, wave velocity v and attenuation coefficient α of most common building materials measured at 100 MHz (Daniels, 2004: 74, 90). The values for the materials marked with an asterisk (*) are taken from Wendrich (2009: 21). . 12

Table 2.2: Thermal properties (mass density ρ_m, thermal conductivity k, specific heat c_p, thermal diffusivity α) of most common building materials (Brink, 2005: 119). 22

Table 2.3: The typical range of longitudinal sound wave velocity v_l of some building materials (Wendrich, 2009: 11). 29

Table 4.1: Material and concrete cover of inbuilt defects in specimens S0–S3. 46

Table 4.2: The frequency of the maximal phase contrast f_{ch} for defects in specimen S0. 53

Table 4.3: The simulation results of C_{max}, t_{Cmax} and f_{ch} for defects at depths of 1.5, 3.5, 6 and 7.5 cm (see Fig. 4.17). 57

Blank page

LIST OF FIGURES

Figure 1.1: Failure mechanisms on concrete structures: (a) a schematic presentation (Banville, 2008: 2), (b) spalling of concrete due to a chloride attack of embedded reinforcement (Banville, 2008: 2), (c) rebar corrosion with visible cracking of concrete. 2

Figure 2.1: Schematic illustration of the GPR signal reflection from boundaries with different dielectric properties, and the different visualization modes – an A-scan, B-scan and C-scan (Kohl, 2005: 819). 9

Figure 2.2: Common electrode arrangements in resistivity surveys and their configuration factors K. In the figure, a refers to the dipole separation length, n is the dipole separation factor, C1 and C2 are the current injection electrodes, and P1 and P2 measure the potential. 16

Figure 2.3: The arrangement of electrodes for a 2D resistivity survey of a brickwork specimen and the sequence of measurements used to build up a pseudo-section with the Wenner array (modified after Loke, 2011: 26). 17

Figure 2.4: The principle of optical IRT techniques in reflection mode – pulsed thermography (PT), square pulse thermography (SPT), lock-in thermography (LT) and step heating thermography (SHT). Particularly, the different used waveforms for heat generation are presented. 18

Figure 2.5: The spectral distribution of EM radiation from a blackbody at different temperatures as described by Planck's law. The arrows mark the wavelength where the blackbody at a particular temperature radiates the most. From the inset (y-axis is logarithmic), it can be seen that a blackbody at room temperature (300 K) radiates much less than bodies of some 1000 K even in the IR region. 20

Figure 2.6: The definition of the thermal contrast $C(t)$ as the difference in surface temperatures above the defect T_{def} and sound area T_{sound}. Here, C_{max} refers to the maximal thermal contrast and t_{Cmax} is its corresponding time. 24

Figure 2.7: The Fourier transform of a pulse with amplitude A_p and duration t_p. 24

Figure 2.8: (a) The principle of pulsed phase thermography (PPT) and (b) presentation of the phase contrast curve with the frequency of the maximal phase contrast f_{ch}. 26

Figure 3.1: Data fusion schemes at pixel-level fusion, feature-level fusion and symbol-level fusion. 32

Figure 3.2: Schematic diagram of the architecture of a generalized system for NDT data fusion (modified after Gros *et al.*, 1995: 2). 33

Figure 3.3: The distance norms used in fuzzy clustering algorithms (Babuška, 2009: 70). 35

Figure 3.4: Representation of partitioning a data set of two variables into three clusters. The assignment of observations (data points) to a specific cluster (here, red, green or blue) is associated by the colour. For a specific observation $\mathbf{x_j}$, the distances to the three cluster centres $\mathbf{v_1}$, $\mathbf{v_2}$, $\mathbf{v_3}$ are marked as well. 36

Figure 3.5: The principle of hard and fuzzy clustering. 37

Figure 3.6: Flowchart of a generalized clustering algorithm. 43

Figure 4.1: Sketches of laboratory concrete test specimens with inbuilt defects. 46

Figure 4.2: The IR camera FLIR A320 used for the thermographic measurements. . . . 47

Figure 4.3: The radar system used for the GPR measurements. 47

Figure 4.4: Thermograms of specimen S0 at different cooling down times. Each image has a different colour scaling. 48

Figure 4.5: The time dependent thermal contrast $C(t)$ for defects in specimen S0 after 30 min of heating. 48

Figure 4.6: The time dependent thermal contrast $C(t)$ for defects in specimens S1 and S2 after 30 min of heating: (a) for a water and an air defect at a depth of 3 cm, and (b) for a polystyrene defect at a depth of 4.6 cm with present reinforcement of two densities (5 and 10 cm). 49

Figure 4.7: (a) A contrast image and (b) a timegram of specimen S0 after 30 min of heating. 50

Figure 4.8: (a) A contrast image and (b) a timegram of specimen S1 after 30 min of heating. 50

Figure 4.9: (a) A contrast image and (b) a timegram of specimen S2 after 30 min of heating. 50

Figure 4.10: (a) A contrast image and (b) a timegram of specimen S3 after 30 min of heating. 50

Figure 4.11: Dependence of (a) the maximal thermal contrast C_{max} and (b) its corresponding time t_{Cmax} on the depth of defects for different heating times (15, 30 and 45 min). The dotted lines are guides to the eye. 51

Figure 4.12: The fitting result for C_{max} and t_{Cmax} using the model proposed by Balageas *et al.* (2.36). Experimental results for defects in specimen S0 obtained at a heating time of 30 min were used. 52

Figure 4.13: The frequency dependent phase contrast $\Delta\phi$ for (a) the defect at a depth of 1.5 cm and (b) the defect at a depth of 3 cm in specimen S0 after 45 min of heating and 150 min of cooling. 53

Figure 4.14: The fitting result for f_{ch} using the model proposed by Arndt *et al.* (2.44). Experimental results for defects in specimen S0, obtained after 45 min of heating and 150 min of cooling, were used. 54

Figure 4.15: IR images obtained for specimen S3: (a) the thermogram obtained directly after heating, (b) the contrast image and (c) the phase contrast image at a frequency of $3.7 \cdot 10^{-3}$ Hz. 54

Figure 4.16: The phase contrast images at (a) a frequency of $6.2 \cdot 10^{-4}$ Hz for specimen S1 and (b) at a frequency of $3.0 \cdot 10^{-4}$ Hz for specimen S2. In Fig. 4.16a, the upper defect refers to air (b), the lower to water (d). In Fig. 4.16b, the right part of the image refers to the part of the specimen with dense reinforcement. The red squares mark the defects position, labelled according to Table 4.1. . 55

Figure 4.17: A 2D numerical model simulating two cross-sections of a concrete specimen with inbuilt polystyrene defects (white colour). The points on the surface where temperature was monitored are marked with red dots. 56

Figure 4.18: (a) The time dependent thermal contrast $C(t)$ and (b) the frequency dependent phase contrast $\Delta\phi$ for defects at depths of 1.5, 3.5, 6 and 7.5 cm after 30 min of simulated heating and 120 min of simulated cooling. The inset in Fig. 4.18a presents the time evolution of thermal contrast for the whole cooling period of 120 min. 57

Figure 4.19: (a) The fitting results for C_{max} and t_{Cmax} using the model proposed by Balageas *et al.* (2.36) and (b) the fitting results for f_{ch} using the model proposed by Arndt *et al.* (2.44). 58

Figure 4.20: A schematic presentation of true positive (TP), true negative (TN), false positive (FP) and false negative (FN) calls for the detection of a defect. . . 59

Figure 4.21: The results of sensitivity evaluation in terms of c_sens (in %) for GPR (full marks) and IRT (empty marks) with respect to the material and depth of the defects in specimens S0–S2. The dotted lines are guides to the eye. . . . 60

Figure 4.22: The imaging results of specimen S3 with marked polystyrene plates according to Table 4.1: (a) a GPR depth slice at a depth of 1.5 cm and (b) an IR phase contrast image at a frequency of $3.7 \cdot 10^{-4}$ Hz. 60

Blank page

KAZALO PREGLEDNIC

Preglednica 2.1: Okvirne vrednosti relativne dielektrične konstante ε_r, električne prevodnosti σ, hitrosti valovanja v in atenuacijskega koeficienta α za najpogostejše gradbene materiale pri frekvenci valovanja 100 MHz (Daniels, 2004: 74, 90). Vrednosti za materiale označene z zvezdico (*) so vzete po Wendrich (2009: 21). 12

Preglednica 2.2: Termične lastnosti (gostota ρ_m, toplotna prevodnost k, specifična toplota c_p, termična difuzivnost α) najpogostejših gradbenih materialov (Brink, 2005: 119). 22

Preglednica 2.3: Okvirne vrednosti hitrosti longitudinalnih zvočnih valov v_l v nekaterih gradbenih materialih (Wendrich, 2009: 11). 29

Preglednica 4.1: Material in krovni sloj betona vgrajenih anomalij v preizkušancih S0–S3. 46

Preglednica 4.2: Frekvenca pri maksimalnem faznem kontrastu f_{ch} za anomalije v preizkušancu S0. 53

Preglednica 4.3: Rezultat simulacije za C_{max}, t_{Cmax} in f_{ch} za anomalije na globinah 1,5, 3,5, 6 in 7,5 cm (glej sliko 4.17). 57

Blank page

KAZALO SLIK

Slika 1.1: Mehanizmi propadanja betonskih konstrukcij: (a) shematičen prikaz (Banville, 2008: 2), (b) odstopanje betona zaradi korozije armature kot posledica vdora kloridnih ionov (Banville, 2008: 2), (c) korozija armaturne palice z vidnim razpokanjem betona. 2

Slika 2.1: Shematični prikaz odboja georadarskega signala na mejah materialov z različnimi dielektričnimi konstantami. Prikazani so še načini grafičnega prikazovanja rezultatov – grafični prikaz refleksijske sledi (A-scan), radargram georadarskega profila (B-scan) in grafični prikaz prereza (C-scan) (Kohl, 2005: 819). 9

Slika 2.2: Tipične geometrijske razporeditve elektrod in ustrezni konfiguracijski faktorji K pri geoelektričnih meritvah. Na sliki parameter a označuje razdaljo med dipoloma, n je faktor razdalje med diploma, C1 in C2 sta tokovni elektrodi, P1 in P2 pa merita napetost. 16

Slika 2.3: Razporeditev elektrod pri geometrijski razporeditvi Wenner za 2D geoelektrično meritev opečnatega preizkušanca ter sosledje meritev, ki ustvari psevdo prerez (prirejeno po Loke, 2011: 26). 17

Slika 2.4: Princip delovanja tehnik optične IRT v odbojnem načinu merjenja – pulzne termografije (PT), termografije s kvadratnim pulzom (SPT), termografije z odzivom na periodično motnjo (LT) in termografije s stopničastim pulzom (SHT). Za vsako tehniko je prikazan način ogrevanja. 18

Slika 2.5: Spektralna porazdelitev sevanja črnega telesa pri različnih temperaturah telesa kakor ga opisuje Planckov zakon. Navpične puščice označujejo valovno dolžino, pri kateri telo z izbrano temperaturo seva največ energije. Iz vložene slike (skala na ordinatni osi je logaritemska) je razvidno, da telesa s sobno temperaturo (300 K) tudi v IR območju sevajo precej manj kot telesa s temperaturo nekaj tisoč Kelvinov. 20

Slika 2.6: Določitev temperaturnega kontrasta $C(t)$ iz razlike med površinsko temperaturo nad anomalijo T_{def} in površinsko temperaturo nad homogenim področjem T_{sound}. Pri tem C_{max} označuje maksimalni temperaturni kontrast, t_{Cmax} pa čas nastopa le-tega. 24

Slika 2.7: Fourierjeva transformacija pulza z amplitudo A_p in dolžine t_p. 24

Slika 2.8: (a) Princip delovanja pulzno-fazne termografije (PPT) in (b) prikaz krivulje faznega kontrasta in frekvence, pri kateri nastopi maksimalni fazni kontrast f_{ch}. 26

Slika 3.1: Združevanje podatkov na nivoju slikovne točke, z uporabo značilnic in na simbolnem nivoju. 32

Slika 3.2: Shematični prikaz arhitekture splošnega sistema za združevanje podatkov (prirejeno po Gros *et al.*, 1995: 2). 33

Slika 3.3: Norme uporabljene v algoritmih za mehko združevanje (Babuška, 2009: 70). . 35

Slika 3.4: Prikaz gručenja množice podatkov dveh spremenljivk v tri razrede. Razporeditev posameznega podatka v ustrezen razred je na sliki ponazorjena z barvo razreda (rdeči, zeleni ali modri). Za podatek $\mathbf{x_j}$ so prikazane razdalje do središč razredov $\mathbf{v_1}$, $\mathbf{v_2}$, $\mathbf{v_3}$. 36

Slika 3.5: Princip delovanja trdega in mehkega gručenja. 37

Slika 3.6: Diagram poteka splošnega algoritma za gručenje podatkov. 43

Slika 4.1: Skice laboratorijskih betonskih preizkušancev z vgrajenimi anomalijami. . . . 46

Slika 4.2: Termokamera FLIR A320, ki smo jo uporabili pri raziskavah. 47

Slika 4.3: Georadarski sistem MALÅ Geoscience, ki smo ga uporabili pri raziskavah. . . 47

Slika 4.4: Termogrami za preizkušanec S0 pri različnih časih ohlajanja. Vsaka slika ima svojo temperaturno skalo. 48

Slika 4.5: Potek časovno odvisnega temperaturnega kontrasta $C(t)$ za različno globoke anomalije v preizkušancu S0 po 30 min segrevanju. 48

Slika 4.6: Potek časovno odvisnega temperaturnega kontrasta $C(t)$ za anomalije v preizkušancih S1 in S2 po 30 min segrevanju: (a) za vodno in zračno anomalijo na globini 3 cm ter (b) za anomalijo iz stiropora na globini 4,6 cm in ob prisotni armaturi rastra 5 oz. 10 cm. 49

Slika 4.7: (a) Kontrastna slika in (b) časovna slika za preizkušanec S0 po 30 min segrevanju. 50

Slika 4.8: (a) Kontrastna slika in (b) časovna slika za preizkušanec S1 po 30 min segrevanju. 50

Slika 4.9: (a) Kontrastna slika in (b) časovna slika za preizkušanec S2 po 30 min segrevanju. 50

Slika 4.10: (a) Kontrastna slika in (b) časovna slika za preizkušanec S3 po 30 min segrevanju. 50

Slika 4.11: Odvisnost (a) maksimalnega temperaturnega kontrasta C_{max} in (b) časa njegovega nastopa t_{Cmax} od globine anomalije za različne čase gretja (15, 30 in 45 min). Črta le povezuje merske točke za lažje spremljanje rezultatov. 51

Slika 4.12: Rezultat prilagajanja eksperimentalnih podatkov za C_{max} in t_{Cmax} z modelom po enačbi (2.36). Vključeni so rezultati za anomalije v preizkušancu S0 za čas gretja 30 min. 52

Slika 4.13: Potek frekvenčno odvisnega faznega kontrasta $\Delta\phi$ za (a) anomalijo na globini 1,5 cm in (b) za anomalijo na globini 3 cm v preizkušancu S0 po 45 min segrevanju in merjenju ohlajanja za 150 min. 53

Slika 4.14: Rezultat prilagajanja eksperimentalnih podatkov za f_{ch} z modelom po enačbi (2.44). Vključeni so rezultati za anomalije v preizkušancu S0, dobljeni po 45 min segrevanju in merjenju ohlajanja za 150 min. 54

Slika 4.15: IR slike za preizkušanec S3: (a) termogram ob začetku snemanja, (b) kontrastna slika in (c) fazno-kontrastna slika pri frekvenci $3,7 \cdot 10^{-3}$ Hz. 54

Slika 4.16: Fazno-kontrastna slika pri (a) frekvenci $6,2 \cdot 10^{-4}$ Hz za preizkušanec S1 in pri (b) frekvenci $3,0 \cdot 10^{-4}$ Hz za preizkušanec S2. Na sliki 4.16a je zračna anomalija zgoraj (b), vodna anomalija pa spodaj (d). Na sliki 4.16b je gostejša armatura na desni strani. Rdeči kvadrati označujejo območje anomalij (za oznake anomalij glej preglednico 4.1). 55

Slika 4.17: 2D numerični model, ki ponazarja dva prereza betonskega preizkušanca z vgrajenimi anomalijami iz stiropora (belo območje). Točke na sprednji strani modela, kjer smo spremljali temperaturo, so označene z rdečimi pikami. 56

Slika 4.18: (a) Potek časovno odvisnega temperaturnega kontrasta $C(t)$ in (b) potek frekvenčno odvisnega faznega kontrasta $\Delta\phi$ za anomalije na globinah 1,5, 3,5, 6 and 7,5 cm po 30 min simuliranem segrevanju in 120 min simuliranem ohlajanju. Vložena slika na sliki 4.18a prikazuje potek temperaturnega kontrasta za čas celotnega ohlajanja (120 min). 57

Slika 4.19: (a) Rezultat prilagajanja podatkov za C_{max} in t_{Cmax} z modelom po enačbi (2.36) in (b) rezultat prilagajanja podatkov za f_{ch} z modelom po enačbi (2.44). . . . 58

Slika 4.20: Shematični prikaz kazalcev za vrednotenje zaznavanja anomalij: pravilno pozitivni (TP), pravilno negativni (TN), napačno pozitivni (FP) in napačno negativni (FN). 59

Slika 4.21: Rezultat občutljivostne analize za georadar (polni znaki) in IRT (prazni znaki) v odvisnosti od materiala in globine anomalij v preizkušancih S0–S2. Rezultati so podani v % parametra c_sens. Pikčasti črti povezujeta merske točke za lažje spremljanje rezultatov. 60

Slika 4.22: Grafični prikaz rezultatov za preizkušanec S3 z označenimi ploščami iz stiropora (preglednica 4.1): (a) georadarski grafični prikaz prereza na globini 1,5 cm in (b) IR fazno-kontrastna slika pri frekvenci $3,7 \cdot 10^{-4}$ Hz. 60

Blank page

LIST OF APPENDICES

APPENDIX A: Article 1 – Image fusion for improved detection of near-surface defects in NDT-CE using unsupervised clustering methods

APPENDIX B: Article 2 – Validation of non-destructive characterization of the structure and seismic damage propagation of plaster and texture in multi-leaf stone masonry walls of cultural-artistic value

APPENDIX C: Article 3 – Effect of moisture on the reliability of void detection in brickwork masonry using radar, ultrasonic and complex resistivity tomography

APPENDIX D: Article 4 – Unsupervised clustering of laser-induced breakdown spectroscopy data from concrete

Blank page

ABBREVIATIONS

AC	Alternating current
AE	Acoustic emission
AFC	Adaptive fuzzy clustering algorithm
CE	Civil engineering
CFRP	Carbon fibre reinforced plastic
CR	Complex resistivity
DC	Direct current
DIC	Digital image correlation
D-S	Dempster-Shafer
EM	Electromagnetic
EMW	Electromagnetic waves
FCM	Fuzzy c-means algorithm
FFT	Fast Fourier transform
FPCM	Fuzzy-possibilistic c-means algorithm
FT	Fourier transform
GK	Gustafson-Kessel algorithm
GKAρ	Gustafson-Kessel algorithm with adaptive cluster volumes
GPR	Ground penetrating radar
IE	Impact-echo
IRT	Infrared thermography
IT	Inductive thermography
LIBS	Laser-induced breakdown spectroscopy
LMMSE	Linear minimum mean square error
LT	Lock-in thermography
NCFCM	Noise handling fuzzy c-means algorithm
NDE	Non-destructive evaluation
NDT	Non-destructive testing
NDT-CE	Non-destructive testing in civil engineering
PCM	Possibilistic c-means algorithm
PFCM	Possibilistic-fuzzy c-means algorithm
PPT	Pulsed phase thermography
PT	Pulsed thermography
PZT	Lead zirconate titanate

S	Separation index
SAFT	Synthetic aperture focusing technique
SC	Partition index
SHT	Step heating thermography
SPT	Square pulse thermography
TWT	Two-way travel time
UT	Ultrasound thermography
XB	Xie and Beni's index

1 INTRODUCTION

1.1 Scientific background and motivation

Among the numerous methods developed for the inspection of materials and structures, non-destructive testing (NDT) techniques provide the advantage of preserving the inspected object undamaged [1]. Their application to civil engineering (CE) structures originally emerged in the 1940s for the assessment of homogeneity and compressive strength of concrete using techniques such as rebound hammer, a windsor probe test, a pull-out test and ultrasonic pulse velocity method, which are today standardized methods [2, 3]. Due to the fast development of both new building materials and construction techniques, the development of potential non-destructive methods for controlling the quality of a building process is nowadays still an important research field (*e.g.* for the detection of aggregate segregation, excessive amount of entrapped air voids and honeycombs[1] due to inappropriate material properties and/or construction techniques).

Relatively recently attention has focused on the loss of durability of existing building structures, caused by both material degradation and impacts of *e.g.* seismic action in relation to inappropriate construction. To ensure accurate repair and retrofitting of such structures rather than demolition and construction of new ones, the evaluation of their current state together with damage assessment with minimal possible interference, is urgently required. To overcome the limits of visual inspection and testing samples extracted from the structure by drilling, many NDT methods have been proposed. Acoustic, dielectric, electric and thermal methods have arisen mainly from geophysics, as well as from NDT in aerospace for the inspection of composite structures. Currently, only a few standards for particular application of NDT-CE methods are available [1, 3, 5]. Hence, to bring NDT into practice, an extensive validation process of the methods performance with respect to the various possible defect assessment applications is required [6].

Damage of concrete structures (mostly referred to bridges, parking garages and tunnels) reflects in cracking, spalling and delamination [7] (see Fig. 1.1). In most cases it is a result of deterioration mechanisms such as frost action, a sulphate attack, an alkali-silica reaction as well as reinforcement corrosion [4, 7]. Except from frost action, all processes are induced by the ingress of de-icing salts into the pore system of the cement matrix in combination with insufficient concrete quality and poor workmanship, which results in excessive amount of entrapped air voids and honeycombs as well as insufficient concrete cover above the reinforcement [8]. Damage assessment of masonry structures, among which a large proportion represents cultural heritage assets, is apart from the effect of de-icing salts related to the presence of high moisture content with even trapped water and internal voids. Moreover, particularly stone masonry buildings in European Mediterranean countries are highly vulnerable to seismic action, resulting in leaf detachment and cracks [9].

[1] Segregation refers to separation of the components of fresh concrete, resulting in a non-uniform arrangement of aggregates, whereas honeycombs occur in case the space between aggregates is not filled [4].

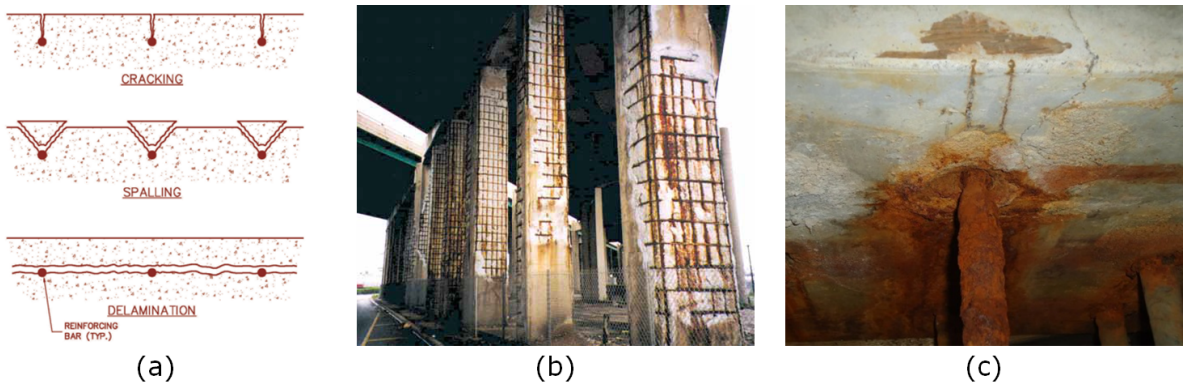

Figure 1.1: Failure mechanisms on concrete structures: (a) a schematic presentation (Banville, 2008: 2), (b) spalling of concrete due to a chloride attack of embedded reinforcement (Banville, 2008: 2), (c) rebar corrosion with visible cracking of concrete.
Slika 1.1: *Mehanizmi propadanja betonskih konstrukcij: (a) shematičen prikaz (Banville, 2008: 2), (b) odstopanje betona zaradi korozije armature kot posledica vdora kloridnih ionov (Banville, 2008: 2), (c) korozija armaturne palice z vidnim razpokanjem betona.*

To visualize the internal structure and to detect most of the above mentioned damages affecting CE structures, methods such as ground penetrating radar (GPR), ultrasonic, impact-echo (IE) and infrared thermography (IRT) are most commonly used [10, 11, 12]. Contrary to the inspection of metal and composite structures, where most research is focused on the detection of cracks, the application of the above mentioned methods in CE has to account for both the heterogeneous material structure and a variety of possible defects and inclusions. With respect to this, NDT-CE methods are characterized by different penetration depths, as well as different sensitivity to the physical properties of the material. However, this requires extensive validation processes of the methods performance with respect to the type of defects and material inspected [6]. In the recent two decades, an outstanding progress has been made in the characterisation of NDT-CE methods with respect to specific testing problems, for which a literature overview is given below.

GPR proves to be a highly effective method for the detection of reinforcement and metal inclusions, but at the same time dense reinforcement greatly decreases the penetration capability of electromagnetic waves (EMW) and thus decreases the efficiency in detection of defects below reinforcement [13, 14]. In case the thickness of a structural element is known, the determination of the moisture and salt concentration in the material is possible since moisture greatly affects the velocity of EMW. Apart from velocity, the moisture and salt concentration largely affect the attenuation of the radar signal [13, 15, 16], whereas pore size distribution and distribution of aggregates in the material affect the penetration capabilities to a smaller extent [14]. The effect of unfilled and grouted joints as well as the presence of larger voids in different layered brick masonry was investigated in [17]. Here, the researchers concluded that unfilled joints can be observed in the radargrams as small hyperbolas, as well as the modifications resulting after the joints were grouted. Moreover, it was found that the detection of the multi-layered structure is based on the measurements of the travel time, amplitude and phase of the reflected radar signal.

Ultrasonic has been employed for the thickness estimation of concrete structural elements [18], as well as for the detection of reinforcement and tendon ducts [18, 19, 20] and for the detection

of surface cracks [20, 21]. The physical basis for most of the experimental ultrasonic results obtained from the investigation of grouting faults in tendon ducts was explained by Krause *et al.* [22] and Im *et al.* [23] and further confirmed by Krause *et al.* using modelling techniques [24]. For the investigation of grouting faults in tendon ducts and thickness estimation of structural elements, IE was proposed as an alternative method to ultrasonic [23, 25, 26, 27]. However, for the inspection of thin structures, IE was found to perform poor since most of the input energy is transformed into shear and surface waves producing interference due to reflections at edges [6].

Apart from the investigation of concrete structures, IE was applied for evaluating the integrity of bonding in stone masonry structures and was in addition recommended for the detection of larger voids and for the monitoring of the quality of grouting repairs [28]. However, in general, GPR, the sonic pulse velocity method and IRT were proposed for assessing the bonding condition, monitoring the quality of grouting repairs, detecting the multi-layered structure and leaf detachment, as well as the presence of larger voids and higher moisture content in masonry structures [9, 29, 30, 31, 32, 33]. It should be noticed that for the inspection of historic masonry buildings, particularly the non-contact IRT has gained interest. Here, pulsed thermography was applied for the characterization of the surface and interfaces, more exactly for the detection of delamination, the masonry texture, filled vs. unfilled mortar joints [9, 31, 34, 35], as well as for the investigation of plastered mosaics [36, 37, 38]. Apart from pulsed thermography, lock-in thermography was applied on masonry for moisture measurements [39], as well as for the structural visualization at different depths [40]. Basic research on quantitative analysis of experimental and numerical pulsed thermography data was performed on concrete specimens with inbuilt defects [41, 42, 43, 44, 45].

For the monitoring of micro-cracking activity at different levels of loading of concrete structures, acoustic emission (AE) was proposed [46, 47]. For the on-site investigation of historic structures on the other hand, IRT and ultrasonic were used for assessing the depth of surface cracks [48], as well as their orientation [49]. However, up till now, no methods have been proposed for the detection of internal cracks in masonry. A surface crack activation could only be observed from the displacement field when applying digital image correlation (DIC) to masonry walls subjected to shear loading [50, 51].

The given review indicates the capabilities and limitations of the currently used NDT techniques. Apart from the fact that each method can only measure certain physical properties and penetrate to a certain depth range, the methods' performance is also greatly affected by the heterogeneous nature of building materials and structures. Therefore, the utilization of more than one method or one method in different modes, *i.e.* multi-sensor testing [52, 53], would generally be required to fully characterize the objects under inspection and to increase the accuracy of the evaluation. The first example of a multi-sensor inspection of concrete structures appears in the works by Krause *et al.* [18, 54] and Pöpel and Flohrer [55], where thickness measurements of structural elements and the detection of reinforcement are performed using GPR, ultrasonic and IE, as well as GPR and covermeter, respectively. Dérobert *et al.* [56] stress the benefits of combined use of GPR, IE, covermeter and radiography for the inspection of a post-tensioned beam before its

autopsy by means of hydro-demolition, whereas Naumann and Haardt [57] study the potential of combined use of GPR, acoustic, electrical and magnetic flux methods for the inspection of highway structures. Further studies on multi-sensor inspection of concrete structures cover research on the detection, localization and characterization of surface-breaking cracks using electrical resistivity and ultrasonic [58], as well as the detection and visualization of inclusions using GPR, ultrasonic and IE [27]. On masonry, a combination of GPR, electrical and acoustic methods have been employed for the detection of moisture, inclusions, as well as defects such as leaf detachment and voids [9, 59, 60, 61].

Although the aforementioned studies have shown the benefit of multi-sensor testing to overcome the limitations of individual techniques, data processing and interpretation of the results were performed for each NDT technique individually. In practice, where large inspection areas and/or data sets should be evaluated, this is both costly and time consuming and is additionally subjected to human error interpretation and does not provide a straightforward evaluation of the structural condition. To overcome these constraints, current and future research shed light on automated and computer controlled data analysis with systematic integration of information from multiple sources – data fusion [62]. Data fusion has long been used for military applications [52]. However, in the field of non-destructive evaluation (NDE), it was first introduced in 1994 in the conference papers by Georgel and Lavayssière [63] and Gros *et al.* [64]. Since then, research on data fusion has emerged rapidly for NDE applications in aerospace and nuclear industry. Different fusion algorithms have been proposed based on optimization methods, multi-resolution approaches [65, 66, 67], heuristic methods [68], probabilistic methods such as Bayesian inference and Dempster-Shafer (D-S) evidence [69, 65, 70, 71, 72, 73, 74], as well as fuzzy logic [71, 75].[2]

Taking into account that NDT results are commonly presented in 2D or 3D image formats rather than as numerical data, special interest has been devoted to the development of fully automated image processing and computer visualization [62]. However, only few of the above presented references report on the application of image fusion, based on eddy current and IRT images from composite and steel structures [69, 65, 73, 67]. In NDT-CE applications, image fusion was performed on GPR data acquired at different frequencies and polarizations, and on GPR and ultrasonic data on prestressed concrete bridge beams and test specimens for the detection of grouting faults in tendon ducts, as well as for the detection of reinforcement placed at larger depths [14, 76, 77]. However, here, the applied fusion techniques were restricted to simple arithmetical methods such as minimal or maximal amplitude and averaging.

1.2 Aims and scope

The main goal of this thesis was to develop an image fusion methodology based on clustering techniques, which would enable more efficient and reliable evaluation of multi-sensor NDT data in CE applications. For image fusion, clustering methods have already been applied in medical imaging for pattern recognition, *e.g.* for the detection of cancerous cells from magnetic resonance images [78] and mammograms [79], as well as for subsurface zonation by cooperative inversion of

[2]For a comprehensive state-of-the-art on data fusion in NDE, refer *e.g.* to [53] and [62].

multi-method geophysical data [80, 81]. Their main advantage is that they can work fully unsupervised. This is of particular interest in implementing NDT in practice in terms of automated application by trained engineers and technicians rather than scientists.

In the thesis, the aim was fulfilled by the implementation of hard – the k-means algorithm [82] – as well as different fuzzy clustering algorithms. For fuzzy clustering, the conventional probabilistic fuzzy c-means (FCM) by Bezdek [83], as well as its noise handling variant (NCFCM) [84] and the distance adaptive Gustafson-Kessel (GK) algorithm [85], were used. In addition, two fuzzy possibilistic clustering algorithms were analysed: the possibilistic c-means (PCM) with repulsion [86] and the possibilistic-fuzzy c-means (PFCM) [87].

Apart from developing and testing the image fusion technique for multi-sensor NDT, the thesis aimed at studying the NDT-CE methods performance with respect to different defects present in the structure as well as the material's condition. Sensitivity analyses were performed on GPR and IRT measurements on laboratory concrete specimens with inbuilt defects and stone masonry walls subjected to plaster delamination and crack propagation. Moreover, the effect of moisture on the reliability of void detection in brickwork masonry was studied using GPR, ultrasonic and complex resistivity (CR) tomography.

Four laboratory concrete specimens served for basic studies on the detection of near-surface defects in CE such as voids, localized water and delamination, as well as for the detection of inclusions such as pipes and reinforcement. GPR and IRT were chosen since they were regarded as complementary methods in the near-surface region (up till a depth of 10 cm). Both methods were also chosen for non-destructive assessment of laboratory plastered multi-leaf stone masonry walls. Here, the measurements aimed at evaluating the masonry texture and morphology, as well as plaster detachment and structural cracking due to simulated seismic activity through stepwise in-plane cyclic shear test. A complementary use of GPR and IRT was particularly considered in order to enable a relatively fast inspection with minimal impact on the damaged structure during the shear test. In practice, the material characterization with defect detection by means of NDT plays a crucial role for masonry with artistic or cultural heritage value. Here, the evaluation of the structural condition with minimal interference is of particular importance.

As already mentioned, moisture is considered as an important parameter that may influence the state and degradation of masonry. Therefore, the performance of NDT-CE methods with respect to the moisture of the material was studied on a laboratory brickwork specimen. For this task, GPR, ultrasonic and CR tomographies were investigated. Since the tomographic technique delivers a 3D visualization of the structure, the detection of a larger void was particularly considered with respect to the humidity level of masonry.

During the course of this work, the developed clustering algorithms were implemented into two data fusion frameworks for practical application: the framework for a multi-sensor robot system – the BetoScan robot system, and for a fully automated classification of spectroscopic spatial data from concrete for cement identification.

The thesis is organized as follows. The following chapter introduces the NDT-CE methods. Particularly, the physical concepts of GPR, IRT, ultrasonic and CR are presented. Chapter 3 briefly describes the aspects of image fusion, focusing on cluster analysis. Hard and several fuzzy clustering methods are presented and followed by the algorithm derivation. Chapter 4 presents the results obtained from the sensitivity evaluation of GPR and IRT on laboratory concrete specimens, focusing on the characterization of defects and inclusions using IRT. Further fusion of this data set is covered in the article given in Appx. A. This article also gives the results from the BetoScan robot system. The main outcomes from the application of GPR and IRT on stone masonry walls are presented in the article given in Appx. B. Experimental measurement results from the investigation of brickwork masonry are covered in the article in Appx. C. Clustering of laser-induced breakdown spectroscopy (LIBS) data from a concrete specimen is presented in Appx. D. The thesis is summarized by the main findings of the presented research and outlooks in chapter 5. The main part of the thesis is followed by an extended abstract of the thesis in Slovene, given in chapter 6.

2 BASIC PRINCIPLES OF SELECTED NDT METHODS

2.1 Overview of NDT methods used in civil engineering

NDT-CE methods can be broadly classified into two categories – *acoustic* and *electromagnetic* methods. Both are based on the wave propagation with energy transfer that can be mathematically described by the second order partial differential wave equation. While for acoustic methods, the propagation of mechanical acoustic waves through a medium is of importance, electromagnetic methods are based on the propagation and radiation of electromagnetic waves. Therefore, different physical properties of the material are measured – with acoustic methods the information about the materials elastic properties is obtained, whereas electromagnetic methods are sensitive to the material electromagnetic properties.

All acoustic methods have in common the basic principle, which is recording acoustic waves propagating in the material after the generation of a mechanical disturbance. For recording, a piezoelectric transducer is most commonly used. However, according to [11], factors such as the used frequency range and the type of the acoustic wave generator (elastic impact hammer and spheres, as well as piezoelectric transducers) further distinguish the acoustic methods used in CE:

- *Micro-seismic methods* that operate in the frequency range $f = 100\,\text{Hz} - 1\,\text{kHz}$ [11] and are mostly applied to the investigation of masonry arch bridges where deep penetration is essential.
- *Sonic pulse velocity method* where an elastic hammer generates acoustic waves in the frequency range $f = 500\,\text{Hz} - 10\,\text{kHz}$ [11]. Due to the method's poor resolution, but deep penetration (results from the low frequency range), the method is particularly recommended for qualitative condition evaluation of masonry structures and for control of the quality of grouting repairs [88].
- *Impact-echo (IE)*, which emerged from pile testing using frequencies lower than 1 kHz and is nowadays also used for thickness estimation of concrete slabs using frequencies up to 80 kHz [89]. The method is based on the measurement of resonant frequencies, resulting mainly from the reflections from the external boundary [12].
- *Ultrasonic*, which uses piezoelectric transducers for acoustic wave generation in the frequency range above 20 kHz [11].
- *Acoustic emission (AE)*, which is based on the recording of acoustic waves generated within the material undergoing stress. This principle is contrary to the recording of actively generated waves with transducers or a mechanical impact that is common in other acoustic methods [46, 90].

The classification of various electromagnetic methods is, however, much broader than it is for acoustic methods. Here, the techniques are not only classified by the part of the electromagnetic spectrum they employ, but they also differ greatly in their sensitivity to different material properties and thus the used instrumentation. With respect to the measurement of dielectric, magnetic and electric properties, the following classification is most common [11]:

- *Ground penetrating radar (GPR)*, which is based on antenna emissions of radio frequency signals and their penetration through a medium, as well as on the recording of reflected signals from irregularities with different dielectric properties in the material.
- *Eddy current* or commercially also known as the *covermeter method*, which uses the principle of electric induction to determine the thickness of the concrete cover above the reinforcement [11].
- *Electrical resistivity methods* (also *geoelectrics*) such as the conventional *resistivity method* and *complex resistivity (CR)*[1] that are based on the measurement of potential difference between two electrodes as the result of an electric current injection [91].
- *Electromagnetic potential methods* which measure the electric potentials resulting from an applied electromagnetic field. In CE, the most common is the *half-cell potential method*, which is based on the measurement of the electrochemical potentials of the embedded reinforcement relative to a reference electrode, known as a half-cell placed at the concrete surface [11, 92].

Apart from the above methods, *infrared thermography (IRT)* is based on the recording of IR radiation from the previously heated surface of a specimen and is thus sensitive to the material thermal properties, whereas *radiography* measures the absorption of very high frequency electromagnetic radiation (X-rays and gamma rays) or the absorption of a neutron flux, with respect to the density of the material [11].

The following sections present the basic physics related to four NDT methods taken into account in the main part of the thesis – GPR, CR, IRT and ultrasonic. The techniques' fundamental theoretical concepts will be introduced, as well as their challenges and limitations.

2.2 Ground penetrating radar

The first use of pulsed EMW to detect the structure of buried objects dates back to 1926 [93]. However, it was not before the 1980s when the first commercially available GPR system appeared [94], and since then the technique has emerged in a variety of other applications [95].

GPR is based on the generation and propagation of EM pulses in the radio-frequency range within the material, and the detection of either reflected or transmitted EM signals using an antenna [94]. For CE applications, the typical frequency of EM pulses is between 300 MHz and 2.5 GHz [76]. Upon the signal propagation into a dielectrically lossy material, the wave exhibits scattering and attenuation, as well as refraction and reflection from dielectric discontinuities enabling the detection of defects, which is the primary aim of NDT inspections. The estimated defect depths depends both on the waves' velocity as well as on the travel time needed from transmission to reflection and recording of the signal, *i.e.* the two-way travel time (TWT) [94]. A point measurement of the reflected EM energy from internal discontinuities builds up a GPR trace – a time dependant variation of the signals energy (with amplitude and polarity). However,

[1] CR may in general refer to both the induced polarization method as well as to spectral induced polarization. Spectral induced polarization refers to the induced polarization method performed at several frequencies.

during a radar measurement, several measurement points are collected along the scanning line – a GPR profile. The visualization of the GPR trace refers to an A-scan, whereas the visualization of the GPR profile refers to a B-scan, also termed radargram [76]. The GPR principle of the signal reflection from boundaries with different dielectric properties, as well as different visualization modes (an A-scan, B-scan and time slice or C-scan), are presented in Fig. 2.1. It is worth noticing that the GPR trace does not only include reflections from discontinuities, but is also affected by the direct air wave which appears first in the A-scan, as well as by the direct ground wave and the critically refracted lateral wave [96].

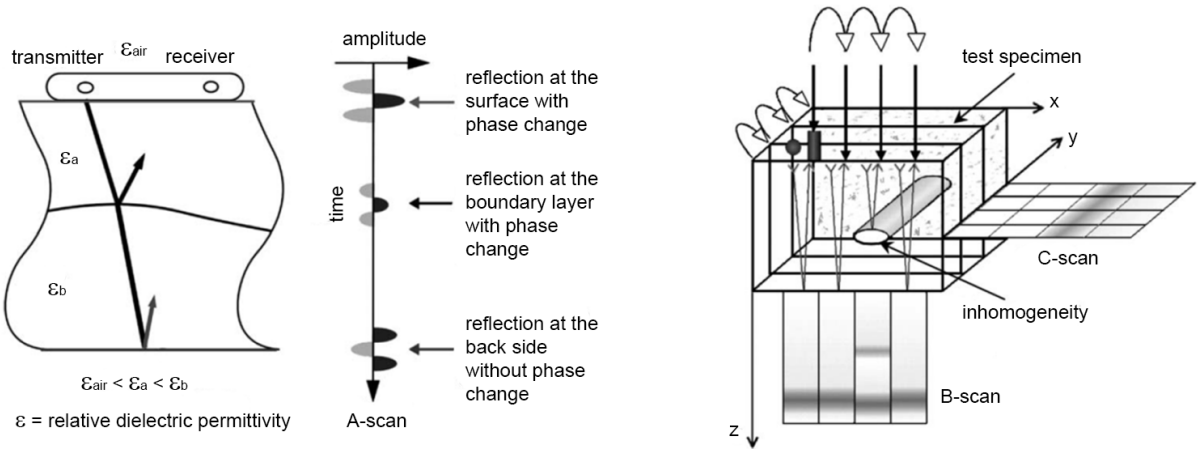

Figure 2.1: Schematic illustration of the GPR signal reflection from boundaries with different dielectric properties, and the different visualization modes – an A-scan, B-scan and C-scan (Kohl, 2005: 819).
Slika 2.1: *Shematični prikaz odboja georadarskega signala na mejah materialov z različnimi dielektričnimi konstantami. Prikazani so še načini grafičnega prikazovanja rezultatov – grafični prikaz refleksijske sledi (A-scan), radargram georadarskega profila (B-scan) in grafični prikaz prereza (C-scan) (Kohl, 2005: 819).*

2.2.1 Electromagnetic properties of building materials and the energy storage-loss mechanisms

Quantities that determine the materials' response to an EM field are dielectric permittivity (ε), magnetic permeability (μ) and electric conductivity (σ), where all quantities determine the stored and released energy. ε is related to the constrained charge displacement in the electric field – the polarization process – and thus to the stored electric field energy, μ is related to the distortion of intrinsic atomic and molecular magnetic moments in the magnetic field – magnetisation – and thus to the stored magnetic field energy, and σ is related to the free charge movement in the electric field, which results in electric field energy released as heat. The statements can be mathematically described by the constitutive equations [96]

$$\mathbf{D} = \varepsilon\mathbf{E}, \tag{2.1a}$$

$$\mathbf{B} = \mu\mathbf{H}, \tag{2.1b}$$

$$\mathbf{J} = \sigma\mathbf{E}, \tag{2.1c}$$

where $\mathbf{D}$ is the dielectric displacement field vector, $\mathbf{E}$ is the electric field strength vector, $\mathbf{B}$ is the magnetic flux density vector, $\mathbf{H}$ is the magnetic field strength vector and $\mathbf{J}$ is the electric current density vector.

In the general case of an inhomogeneous, anisotropic and nonlinear medium, ε, μ and σ are tensors, dependent on the position, direction and on the strength of the EM field. However, in the context of GPR applications, a homogeneous, isotropic and linear material can be assumed, resulting in scalar quantities [96]. Nonetheless, in real lossy (dispersive) materials, **D**, **B** and **J** may not be directly related to the energy field strength components according to Eq. (2.1a)–(2.1c), but exhibit a particular time-history dependence on the temporarily preceding field (radiated field due to moving charges) with respect to the frequency dependent polarization or magnetization phenomena. Hence, the material properties are frequency-dependent complex quantities, such that

$$\varepsilon(\omega) = \varepsilon' - i\,\varepsilon'', \tag{2.2a}$$

$$\mu(\omega) = \mu' - i\,\mu'', \tag{2.2b}$$

$$\sigma(\omega) = \sigma' - i\,\sigma'', \tag{2.2c}$$

where the imaginary dielectric permittivity ε'' and magnetic permeability μ'' relate to the relaxation energy losses in the polarization and magnetization processes, respectively. Similarly, the imaginary electric conductivity σ'' quantifies the energy stored during polarization of free charges. In the context of GPR applications, only ε and σ are of importance as most building materials are generally nonmagnetic [96].

In general, polarization processes in materials can be of various types: electronic (circular orbits of electrons become elliptical), atomic (distortion of atoms), dipolar (the rotation of dipole molecules into alignment with the electric field) and Max-Wagner (accumulation of free ionic charges at boundaries at frequencies below 10 MHz) [96, 97]. All polarization processes are frequency dependent, where the imaginary dielectric constant relates to the energy released in the relaxation process [94]. However, for the GPR frequency range, the most important polarization process is the dipolar due to free and bound water molecules in the material. Here, the maximal released energy occurs around 10–20 GHz, which limits the high-frequency range of GPR [94]. Similarly, energy losses due to electric conductivity of ionic charge transport in water are most pronounced at the frequency range of 10–300 MHz, which defines the low-frequency limit of GPR [94]. However, the high-frequency limit is apart from the polarization processes determined by scattering losses, which become apparent at wavelengths approaching the size of particles [97]. In addition to material attenuation losses due to σ' and ε'', as well as target scattering losses, the GPR gain decreases along the path also as a result of energy spreading loss [94, 95].

2.2.2 Wave nature of electromagnetic fields

The foundations of GPR are governed by the Maxwell equations coupling the electric and magnetic fields, as well as by the constitutive laws describing the materials' response to an EM field [96]. By coupling both of them, the wave equation for the electric and magnetic field is

obtained, which for the electric field vector $\mathbf{E}$ yields [96]

$$\nabla \times \nabla \times \mathbf{E} + \mu\sigma\frac{\partial \mathbf{E}}{\partial t} + \mu\varepsilon\frac{\partial^2 \mathbf{E}}{\partial^2 t} = 0. \tag{2.3}$$

For a conducting dielectric, the resulting electric field can be described as a function of distance, z, and time, t, by [95]

$$\mathbf{E}(z,t) = \mathbf{E_0}\, e^{-\alpha z} e^{i(\omega t - \beta z)}, \tag{2.4}$$

where the first exponential term relates to attenuation and the second to propagation of EMW. Parameter α is the material attenuation coefficient, β the phase constant, ω the angular frequency, $\omega = 2\pi f$, and f is the frequency of EMW. By relating α and β to a complex propagation factor for a dispersive medium, k, such that $ik = \alpha + i\beta = i\omega\sqrt{\mu\,(\varepsilon' - i\varepsilon'')}$,[2] the attenuation coefficient α and wave velocity v can be expressed as [95, 96]

$$\alpha = \frac{\sigma}{2}\sqrt{\frac{\mu}{\varepsilon}} = \omega\left[\frac{\mu\varepsilon'}{2}\left(\sqrt{1+\tan^2\delta} - 1\right)\right]^{1/2}, \tag{2.5a}$$

$$v = \frac{1}{\sqrt{\mu\varepsilon}} = c\left[\frac{\mu_r\varepsilon_r'}{2}\left(\sqrt{1+\tan^2\delta} + 1\right)\right]^{-1/2}, \tag{2.5b}$$

where c is the velocity of EMW in free space, ε_r is the relative dielectric permittivity of the medium, related to ε and the free-space dielectric permittivity, ε_0, by $\varepsilon_r = \varepsilon/\varepsilon_0$, μ_r is the relative magnetic permeability of the medium, related to μ and the free-space magnetic permeability, μ_0, by $\mu_r = \mu/\mu_0$, and $\tan\delta$ is the loss tangent quantifying the ratio between the total energy loss and the total energy storage due to both dipolar and conductivity effects as [96]

$$\tan\delta = \frac{\sigma' + \omega\varepsilon''}{\omega\varepsilon' - \sigma''}. \tag{2.6}$$

According to Eq. (2.5a), higher frequencies result in greatly attenuated EM propagation. Thus, lower frequencies have to be used with GPR to penetrate deeper. For low-loss conditions, the following can be assumed

$$\tan\delta \approx \frac{\sigma'}{\omega\varepsilon'} \leq 1, \tag{2.7}$$

which yields the low-loss conditions for the frequency independent attenuation coefficient and the wave velocity[3]

$$\alpha = \frac{\sigma}{2}\sqrt{\frac{\mu}{\varepsilon}}, \tag{2.8a}$$

$$v = \frac{c}{\sqrt{\varepsilon_r}}. \tag{2.8b}$$

[2]Note that according to Daniels [95] and other literature on GPR, the term complex propagation factor k is mostly used for the relation $ik = \alpha + i\beta$, although strikly speaking k is the complex wavenumber and is related to the complex propagation factor $\bar{\gamma}$ by $\bar{\gamma} = -ik$.

[3]Eq. (2.8b) is obtained by assuming $\mu_r = 1$, which holds for most building materials.

From Eq. (2.8a) it can be seen that the electric conductivity affects the EMW attenuation the most.

Using Eq. (2.8b), the wavelength of the EMW in low-lossy materials can be estimated according to

$$\lambda = \frac{v}{f} = \frac{c}{f\sqrt{\varepsilon_r}}. \tag{2.9}$$

Table 2.1 summarizes the typical range of relative dielectric permittivity ε_r, electric conductivity σ, wave velocity v and attenuation coefficient α of various building materials measured at 100 MHz.

Table 2.1: The typical range of relative dielectric permittivity ε_r, electric conductivity σ, wave velocity v and attenuation coefficient α of most common building materials measured at 100 MHz (Daniels, 2004: 74, 90). The values for the materials marked with an asterisk (*) are taken from Wendrich (2009: 21).
Preglednica 2.1: *Okvirne vrednosti relativne dielektrične konstante ε_r, električne prevodnosti σ, hitrosti valovanja v in atenuacijskega koeficienta α za najpogostejše gradbene materiale pri frekvenci valovanja 100 MHz (Daniels, 2004: 74, 90). Vrednosti za materiale označene z zvezdico (*) so vzete po Wendrich (2009: 21).*

Material	$\boldsymbol{\varepsilon_r}$	$\boldsymbol{\sigma}$ **(S/m)**	$\boldsymbol{v}$ **(m/ns)**	$\boldsymbol{\alpha}$ **(dB/m)**
Air	1	0	0.300	0
Freshwater	81	10^{-6}–10^{-2}	0.033	0.01
Sea water	81	100	0.01	100
Concrete dry	4–10	10^{-3}–10^{-2}	0.11	2–12
Concrete wet	10–20	10^{-2}–10^{-1}	0.08	10–25
Brick dry*	4–8	$< 10^{-3}$	0.12	< 2
Brick wet*	8–12	10^{-2}	0.09	9–11
Limestone dry	7	10^{-8}–10^{-6}	0.11	0.5–10
Limestone wet	8	10^{-2}–10^{-1}	0.11	1–20
Sandstone dry	2–5	10^{-6}–10^{-5}	0.15	2–10
Sandstone wet	5–10	10^{-4}–10^{-2}	0.11	4–20

2.2.3 Reflection and refraction of electromagnetic waves

When the GPR signal encounters a subsurface discontinuity, both reflection and refraction of EMW occur with respect to both geometric characteristics of the target and its dielectric properties as well as the dielectric properties of the medium. The change in amplitude of the reflected signal from a planar boundary is governed by the reflection coefficient r

$$r = \frac{Z_2 - Z_1}{Z_2 + Z_1}, \tag{2.10}$$

where Z_1 and Z_2 are the electromagnetic impedances of medium 1 and 2 and $Z = \mathbf{E}/\mathbf{H}$. In a nonmagnetic and low-lossy medium and a single frequency of radiation, the above expression may be simplified to [95]

$$r = \frac{\sqrt{\varepsilon_{r2}} - \sqrt{\varepsilon_{r1}}}{\sqrt{\varepsilon_{r2}} + \sqrt{\varepsilon_{r1}}}, \tag{2.11}$$

where ε_{r1} and ε_{r2} are the relative dielectric permittivities of medium 1 and 2.

Considering that the reflection coefficient has a positive value when $\varepsilon_{r2} > \varepsilon_{r1}$ and otherwise a negative one, amplitude changes can be detected with respect to the dielectric contrasts at boundaries.

2.2.4 Horizontal and vertical resolution

The resolution of an antenna is defined by the ability to resolve two closely spaced features [94]. For GPR, two resolution components are important: vertical (range or depth) – Δ_V – and horizontal (plan) – Δ_H – resolution. The vertical resolution relates to the temporal resolution to differentiate two adjacent signals in time, whereas the horizontal resolution is the ability to differentiate two targets placed at the same depth [95]. Both are dependent on the antenna characteristics (system bandwidth B) and material properties by [96]

$$\Delta_V \geq \frac{v}{4B} = \frac{\lambda_c}{4}, \tag{2.12a}$$

$$\Delta_H \geq \sqrt{\frac{vd}{2B}} = \sqrt{\frac{\lambda_c d}{2}}, \tag{2.12b}$$

where $B = f_c$ for impulse GPR [96] and f_c is the centre frequency of the antenna signal, λ_c is related to f_c according to Eq. (2.9) and d is the distance to the target.

It should be noted that the expression for the horizontal resolution (2.12b) results from the Fresnel zone concept, *i.e.* the interference of reflected signals from targets placed at a distance d with the radiated EM field occurs in an ellipsoidal volume of radius Δ_H (the Fresnel zone) [96]. The interference effects hence directly limit the ability to resolve two closely spaced targets at the same depth.

However, in addition to the vertical resolution, the shallowest targets to be detected are determined by the GPR near-field region, which extends up till the depth of $1.5\lambda_c$ [95]. However, the strongest antenna induction/coupling effects appear in the reactive near-field region. Thus, for the minimal detectable distance to targets, a recommendation of $d_{min} = \lambda_c/2\pi$ has been given as the boundary between the reactive and radiating near-field region for an electrically small antenna [96]. For most GPR applications in CE, the use of a small bow-tie dipole or butterfly antennae is the most common. However, the antenna characteristics and the GPR system will not be reviewed herein. An excellent description is given in [95] and [96].

2.3 Complex resistivity

In 1912 the Schlumberger brothers performed the first electrical resistivity survey to estimate the subsurface conductivity over a region of interest [98]. A four-electrode array was used, where the outer two electrodes served for current injection and the inner two measured the resulting electrical potential difference. Nowadays, several electrode array configurations can be used and combined in a multi-electrode acquisition survey producing 2D and 3D data sets. With this *resistivity imaging* or *geoelectric tomography*, the resistivity distribution of a medium can be

obtained using tomographic inversion routines.

The two electrically based resistivity methods – the resistivity and the CR method – determine the resistivity of a material from the measured potential difference between two electrodes after current injection according to Ohm's law. However, their main difference is that CR uses alternating currents (AC) of high frequencies and is more sensitive than the normal resistivity method, which uses either direct currents (DC) or AC of low frequencies (up to 20 Hz) [91]. Therefore, CR is able to detect materials of very low conductivity that can hardly be detected using the conventional resistivity method [99].

2.3.1 Electrical polarization

The term CR directly reflects that when AC is used, the materials' frequency dependent complex resistivity (also electrical impedance) is of significance, where the real component ρ' refers to the electrical resistivity and the imaginary component ρ'' to the reactivity and polarization phenomenon, such that[4]

$$\rho(\omega) = \rho' - i\,\rho'' = |\rho|\, e^{i\delta} = \frac{1}{\sigma(\omega)}, \tag{2.13}$$

where $|\rho|$ is the resistivity magnitude – the in-phase amplitude ratio between the measured voltage waveform and the transmitted current waveform, and δ is the phase angle – the time shift of both waveforms. It yields:

$$|\rho| = \sqrt{\rho'^2 + \rho''^2}, \tag{2.14a}$$

$$\delta = \arg(\rho(\omega)). \tag{2.14b}$$

The complex conductivity and resistivity result from the polarization phenomenon of porous building materials when subjected to an electric current, which is called induced polarization. According to Marshall and Madden, the two main sources of low-frequency induced polarization are electrolytic and electrode polarizations [100, 101]. For building materials, the electrolytic polarization is the most important due to ions in the pore space water [101]. However, correct understanding of induced polarization is much more complex and is not within the scope of this thesis.

To combine the above introduced induction polarization with the preceding section on GPR, it should be noted that in a general case, polarization phenomena occur due to both separation of constrained charges – dielectric polarization (see section 2.2.1), as well as induced polarization. The two processes are coupled through the Maxwell generalization of Ampère's law

$$\nabla \times \mathbf{H} = \mathbf{J} + \frac{\partial \mathbf{D}}{\partial t}, \tag{2.15}$$

where the term $\partial\mathbf{D}/\partial t$ also refers to the displacement current density vector. Using the consti-

[4]Note that as for GPR applications, electrical conductivity and resistivity are assumed to be scalar values, independent of the position, direction and on the strength of the electric field.

tutive equations for **D** (2.1a) and **J** (2.1c), a relation between the total current density vector and a time-varying electric field, $\mathbf{E} = \mathbf{E_0}\, e^{i\omega t}$, may be written as [101]

$$\mathbf{J_{tot}} = [1/\rho(\omega) + i\omega\,\varepsilon(\omega)]\,\mathbf{E}. \tag{2.16}$$

However, for frequencies used in CR measurements (lower than 10^5 Hz), the displacement current contribution is usually ignored [101]. Thus, the above equation generalizes to Ohm's law, expressed by the constitutive equation for **J** (2.1c). Relating **E** to the electric potential Φ, by the Poisson's equation, $\mathbf{E} = -\nabla\Phi$, Ohm's law writes as

$$\mathbf{J} = -\sigma\,\nabla\Phi. \tag{2.17}$$

2.3.2 Apparent and true resistivities

The aim of a resistivity survey is to obtain the resistivity of a medium from measured potential distribution after current injection. For a point current source located at position (x_s, y_s, z_s), the relationship between the electric current density and the injected current I, yields [99, 102]

$$\nabla \cdot \mathbf{J} = \frac{I}{\mathrm{d}V} \cdot \delta(x - x_s)\,\delta(y - y_s)\,\delta(z - z_s), \tag{2.18}$$

where $\mathrm{d}V$ is the elemental volume surrounding the current source and δ is the Dirac delta function. Using Eq. (2.17), the above equation can be rewritten to

$$-\nabla \cdot [\sigma(x, y, z)\,\nabla\Phi(x, y, z)] = \frac{I}{\mathrm{d}V} \cdot \delta(x - x_s)\,\delta(y - y_s)\,\delta(z - z_s), \tag{2.19}$$

which is the governing equation for assessing the potential distribution in a medium due to a radially emitted current from a point source.

For a fictitious homogeneous half-space, where the equipotential surfaces are hemispheres, the analytical solution for the electric potential at a distance r in the medium from a single point current electrode is given by [99]

$$\Phi = \frac{\rho I}{2\pi r}. \tag{2.20}$$

In actual field surveys, a four-electrode arrangement is preferred, separating current injection (with a positive and negative current electrode C1 and C2) from voltage measurement (with potential electrodes P1 and P2) to minimize the influence of contact resistance. Thus, the potential distribution in the medium is a superposition of potentials produced from both of the current electrodes. From the measured potential difference $U = \Delta\Phi$ between electrodes P1 and P2, an apparent resistivity ρ_a can be calculated from the applied current and for a given electrode arrangement by [99]

$$\rho_a = K\,\frac{U}{I}, \tag{2.21}$$

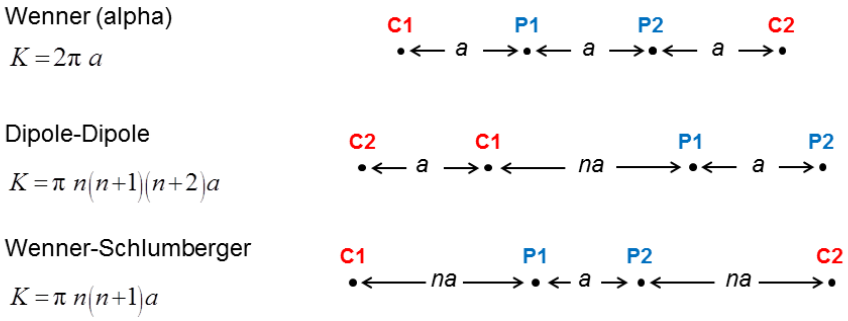

Figure 2.2: Common electrode arrangements in resistivity surveys and their configuration factors K. In the figure, a refers to the dipole separation length, n is the dipole separation factor, C1 and C2 are the current injection electrodes, and P1 and P2 measure the potential.
Slika 2.2: *Tipične geometrijske razporeditve elektrod in ustrezni konfiguracijski faktorji K pri geoelektričnih meritvah. Na sliki parameter a označuje razdaljo med dipoloma, n je faktor razdalje med diploma, C1 in C2 sta tokovni elektrodi, P1 in P2 pa merita napetost.*

where

$$K = 2\pi \left(\frac{1}{r_{C1P1}} - \frac{1}{r_{C2P1}} - \frac{1}{r_{C1P2}} + \frac{1}{r_{C2P2}} \right)^{-1} \tag{2.22}$$

is a configuration factor that depends on the electrode arrangement and r_{ij} is the distance between electrodes i and j. The most commonly used electrode configurations and their corresponding configuration factors are presented in Fig. 2.2.

The term *apparent resistivity* is used to relate to the resistivity of a homogeneous and isotropic half-space that would produce the measured relationship between the potential difference and the current for a given electrode array [99]. In other words, the apparent resistivity relates to the average resistivity of an inhomogeneous material over the total current path length. To obtain the true resistivity distribution of the investigated inhomogeneous medium, an inversion problem has to be solved. Solving this problem mathematically means adapting a resistivity distribution model iteratively until the calculated apparent resistivities match the measured ones within acceptable limits. To perform this, a general least-square optimization method can be used. However, beside the used optimization method, the calculated model parameters depend on the way the model is discretized. For 2D and 3D arbitrary problems, the most versatile methods are the finite-difference and finite-element methods [99].

2.3.3 Electrode configurations

In practice, the most commonly used electrode configurations for 2D imaging survey are the Wenner, dipole-dipole, Wenner-Schlumberger, pole-pole and pole-dipole (Fig. 2.2). They all have advantages and disadvantages and differ in the depth penetration capabilities, the sensitivity to vertical and horizontal changes in the resistivity distribution, the horizontal data coverage and the signal strength. Especially for noisy environments, the Wenner array has shown to be a good choice due to its high signal strength and good vertical resolution [99]. To enable a good horizontal resolution and data coverage, the dipole-dipole array is more suitable. However, this electrode configuration has very low signal strength for large dipole-dipole distances and is

relatively insensitive to vertical changes in the resistivity distribution. The Wenner-Schlumberger array is a suitable choice when both good horizontal and vertical resolution are needed and is therefore a compromise between the Wenner and dipole-dipole arrays. In Fig. 2.3 a sequence of measurements used to build up a pseudo-section (distribution of apparent resistivities in a section) with the Wenner array is shown.

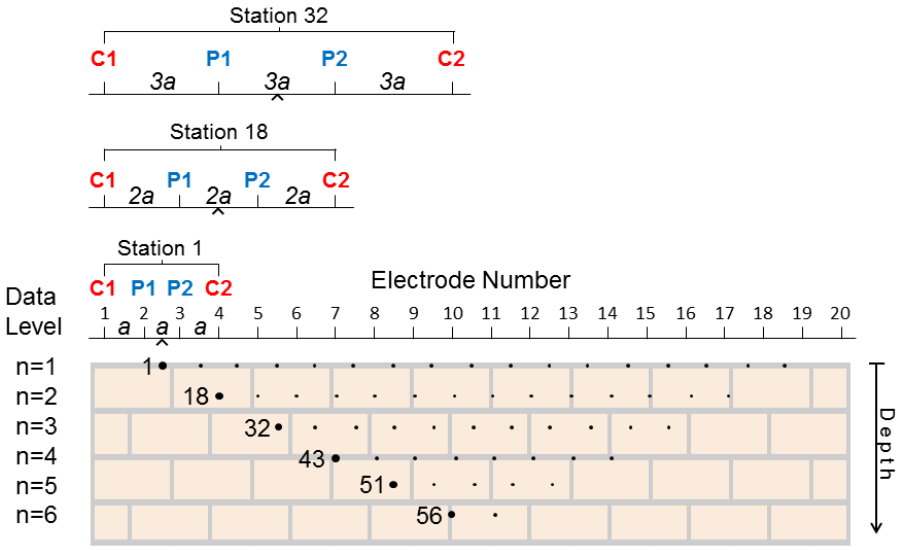

Figure 2.3: The arrangement of electrodes for a 2D resistivity survey of a brickwork specimen and the sequence of measurements used to build up a pseudo-section with the Wenner array (modified after Loke, 2011: 26).
Slika 2.3: *Razporeditev elektrod pri geometrijski razporeditvi Wenner za 2D geoelektrično meritev opečnatega preizkušanca ter sosledje meritev, ki ustvari psevdo prerez (prirejeno po Loke, 2011: 26).*

2.4 Infrared thermography

The first IRT application for NDT dates back to 1935, when Nichols used a radiometer to check the uniformity of heated steel slabs after stell-rolling [103]. However, the first commercially available IR camera for military applications appeared in the 1960s [104] and later found its way also in NDT.

IRT is based on the recording of the emitted IR radiation from a specimen's surface through the assessment of surface temperatures, with the aim to resolve the underlying structure [104]. For NDT, both *passive* and *active* IRT can be performed. However, active IRT in general enables the detection of smaller thermal contrasts in the medium since it employs an external energy source brought to the specimen. Hence, it is the most desired way of applying IRT in NDT. Several testing techniques can be used for active IRT:

- *Pulsed thermography* (PT), which is based on the application of a short pulse (for a few milliseconds) to the specimen and later recording of the surface temperature decay [105, 106].
- *Square pulse thermography* (SPT), which has been proposed as an extension to PT. The difference from PT is that here, longer square pulses (for a few seconds to a few minutes) are employed. However, since the principle of PT and SPT is the same, only the term PT

is often used.

- *Lock-in thermography* (LT), which is based on the generation of thermal waves in the specimen by using modulated heating. The thermal waves amplitudes and phases are measured relative to the launched modulation signal [107].
- *Step heating thermography* (SHT), where the increase in surface temperature is monitored during the application of a relatively long uniform heating [108].
- *Ultrasound thermography* (UT), also known as *vibrothermography* or *thermosonics*, where a modulated ultrasonic (or sonic) pulse is used for internal heat generation. UT is based on the principle that externally induced mechanical vibrations generate thermal waves inside the specimen by direct conversion between mechanical and thermal energy. Heat is released by friction at locations where abnormalities appear, which enables direct defect detection [104, 109].
- *Inductive thermography* (IT), where eddy currents are used for internal heat generation [109].

From the above techniques, PT, SPT, LT and SHT can be classified as optical techniques, where heat is delivered to the specimen by either reflection or transmission of the incident radiation [109]. The principle of all optical IRT techniques in reflection mode is presented in Fig. 2.4. In particular, the different waveforms used for heat generation are presented.

The thesis specifically deals with SPT in reflection mode, being the technique most often used in NDT-CE. However, since SPT employs the experimental and data processing principles of PT, and most literature on NDT-CE uses the term PT, the term PT will be used hereinafter.

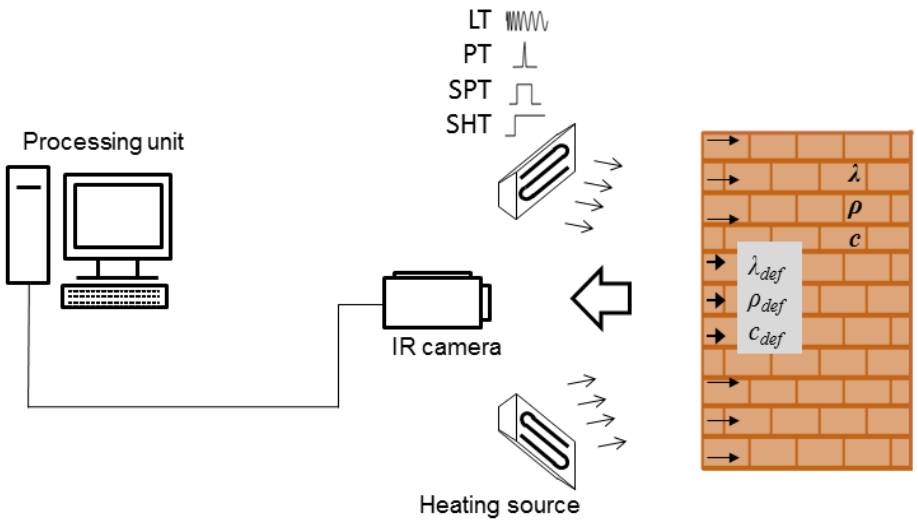

Figure 2.4: The principle of optical IRT techniques in reflection mode – pulsed thermography (PT), square pulse thermography (SPT), lock-in thermography (LT) and step heating thermography (SHT). Particularly, the different used waveforms for heat generation are presented.
Slika 2.4: *Princip delovanja tehnik optične IRT v odbojnem načinu merjenja – pulzne termografije (PT), termografije s kvadratnim pulzom (SPT), termografije z odzivom na periodično motnjo (LT) in termografije s stopničastim pulzom (SHT). Za vsako tehniko so prikazani različni načini ogrevanja.*

2.4.1 Interaction of incident radiation with matter

When an incident radiation strikes the surface of a medium, part of the total incident heat flux density ($\mathbf{j_i}$) is reflected ($\mathbf{j_r}$), part absorbed ($\mathbf{j_a}$) and transmitted ($\mathbf{j_t}$), contrary to a perfect blackbody, where all radiation is absorbed. In thermal equilibrium, the energy conservation law yields the total flux exchange

$$\mathbf{j_i} = \mathbf{j_r} + \mathbf{j_a} + \mathbf{j_t}. \tag{2.23}$$

The individual heat flux fractions may be expressed by the material's radiation characteristics: reflectance r, absorbance a and transmittance t. In general, these quantities depend on the radiation wavelength, orientation of the incident flux and/or reflected flux, as well as on the temperature and quality of the surface [104]. For IRT in practice, values are assumed to be constants for a particular temperature range, *i.e.* total-hemispheric quantities, in accordance with the spectral[5] (independence on the wavelengths) and hemispheric conditions (uniform reflection and transmission over the total hemispheric space), so that Eq. (2.23) rewrites to

$$r + a + t = 1. \tag{2.24}$$

When examining building structures with relatively large thickness, the transmitted energy is considered to be minimal, with $t \approx 0$.

An object that absorbs heat well also radiates well. This is expressed by the Kirchhoff's law of thermal radiation

$$e = a, \tag{2.25}$$

where e is the emissivity, defined as the ratio between the emitted radiation from a surface of an real object and the radiation that would be emitted from an ideally blackbody surface.

2.4.2 Thermal emission

IRT is based on the recording of IR radiation, emitted from a body. For NDT applications, particularly the middle IR range (1.5–20 μm) is of importance [104]. The total thermal emission from a surface of temperature T and with the total-hemispheric emissivity e can be expressed by the radiant intensity $j^*(T)$ (also termed radiant exitance) as [110]

$$j^*(T) = e\,\sigma_{sb} T^4, \tag{2.26}$$

where σ_{sb} is the Stefan-Boltzmann constant. The above equation describes that the thermal emission from an object that will strike the IR camera detector depends on the object's surface temperature and emissivity. Thus, a high emissivity value is desired, which holds for most building materials. For concrete, brick and plaster, emissivity ranges from 0.9 to 0.95 [104]. In

[5] An object whose material radiation characteristics are in general independent on the radiation wavelength is called a *gray body*.

general, emissivity depends on the quality and roughness of the surface, as well as on the spectral and geometrical distribution of the radiation. However, for IRT applications in NDT-CE, the total-hemispheric emissivity is a good approximation.

The physics of thermal emission from bodies can in general be understood by *Planck's law*, which describes the spectral distribution of EM radiation from a blackbody and writes [110]:

$$\frac{\mathrm{d}j_b^*}{\mathrm{d}\lambda}(\lambda, T) = \frac{2\pi hc^2}{\lambda^5} \cdot \frac{1}{\mathrm{e}^{hc/\lambda k_B T} - 1}, \tag{2.27}$$

where $\mathrm{d}j_b^*/\mathrm{d}\lambda\,(\lambda, T)$ is the spectral radiancy and describes the fraction of radiant intensity $j_b^*(\lambda, T)$ in a range of wavelengths from λ to $\lambda + \mathrm{d}\lambda$. In Eq. (2.27), h is the Planck constant, c is the velocity of EM waves in free space, k_B is the Boltzmann constant, T refers to the temperature of the blackbody and subscript b relates to the blackbody. As can be seen from Fig. 2.5, a blackbody at room temperature radiates the most in the IR region of the EM spectrum. This phenomenon is exploited by IRT for NDT applications.

The wavelength where the spectral radiancy in Eq. (2.27) is maximal for a given temperature is given by *Wien displacement law* and writes

$$\lambda_{max} T = 2898\,\mu\mathrm{m\,K}. \tag{2.28}$$

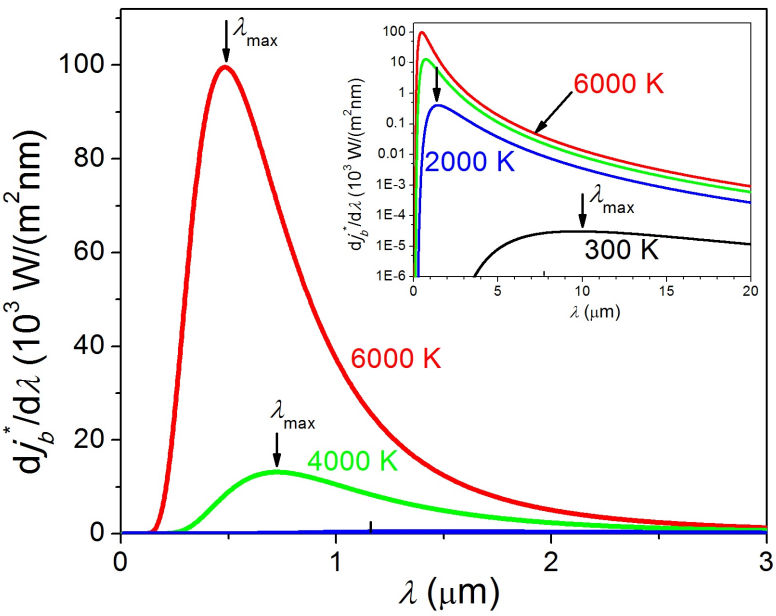

Figure 2.5: The spectral distribution of EM radiation from a blackbody at different temperatures as described by Planck's law. The arrows mark the wavelength where the blackbody at a particular temperature radiates the most. From the inset (y-axis is logarithmic), it can be seen that a blackbody at room temperature (300 K) radiates much less than bodies of some 1000 K even in the IR region.
Slika 2.5: *Spektralna porazdelitev sevanja črnega telesa pri različnih temperaturah telesa kakor ga opisuje Planckov zakon. Navpične puščice označujejo valovno dolžino, pri kateri telo z izbrano temperaturo seva največ energije. Iz vložene slike (skala na ordinatni osi je logaritemska) je razvidno, da telesa s sobno temperaturo (300 K) tudi v IR območju sevajo precej manj kot telesa s temperaturo nekaj tisoč Kelvinov.*

By integrating the spectral radiancy described by Planck's law over all wavelengths, the radiant intensity of a blackbody for a given temperature $j_b^*(T)$ is obtained as given by *Stefan-Boltzmann law*. Eq. (2.26) is a generalization of Stefan-Boltzmann law to describe the radiant intensity from real bodies with respect to the their surface emissivity.

2.4.3 Conduction heat transfer

As can be seen from Eq. (2.26), the detected radiation depends on the object's surface temperature that changes with respect to the heat transfer processes. According to the first law of thermodynamics, which is the law of energy conservation, part of the total absorbed incident energy will be stored in the system, whereas another part will be lost by convection and radiation heat transfer. Radiation losses are given by Eq. (2.26), whereas convection losses are related to the heat transferred from an object's surface by a moving fluid so that the heat flux density j may be expressed by Newton's law of cooling

$$j = \bar{h}\,(T_S - T_F)\,, \tag{2.29}$$

where $\bar{h}$ is the average convective heat transfer coefficient, T_S is the object's surface temperature and T_F is the temperature of the moving fluid.

The energy stored in the system will undergo an unsteady conduction heat transfer due to the variable temperature distribution within the body. Conduction refers to the heat transfer within a solid that is not in thermal equilibrium, *i.e.* it is a result of a temperature gradient. On the microscopic level, the energy is transferred by physical interactions between neighbouring constituents [104]. It is worth noticing that conduction is of paramount importance for the IRT concept used in NDT, since it depends on the material thermal properties. Hence, the presence of a particular abnormality with different thermal properties within the specimen will be directly reflected on the detected surface temperature distribution as an abnormal temperature pattern.

The basic equation for the conduction mechanism is the *Fourier law of thermal conduction*, which is a result of experimental evidence. It describes that the heat flux density $\mathbf{j}$ is proportional to the material's thermal conductivity k and the negative temperature gradient ∇T, according to

$$\mathbf{j} = -k\nabla T. \tag{2.30}$$

In many engineering problems where the surface of the investigated structure is very large compared to its thickness, a unidimensional heat flux approximation can be assumed. For a semi-infinite slab, the unidimensional heat flux in the x-direction writes

$$j_x = -k\frac{\mathrm{d}T}{\mathrm{d}x}. \tag{2.31}$$

Eq. (2.30) or (2.31) only holds for stationary heat conduction. However, for IRT, this approximation cannot be assumed valid. In fact, the unsteady distribution of the surface temperature is also the phenomenon that is exploited for defect characterization in IRT for NDT. Hence, to

obtain the temperature distribution, the *Fourier diffusion equation* should be taken into account, which for a generalized dimension writes as [111]

$$\frac{\partial T}{\partial t} = \alpha \nabla^2 T, \tag{2.32}$$

where $\alpha = k/c_p\rho_m$ is the thermal diffusivity, ρ_m is the mass density, c_p is the specific heat at constant pressure and

$$\nabla^2 = \frac{\partial^2}{\partial x^2} + \frac{\partial^2}{\partial y^2} + \frac{\partial^2}{\partial z^2}$$

is the Laplace operator. Thermal properties of most building materials are given in Table 2.2.

Table 2.2: Thermal properties (mass density ρ_m, thermal conductivity k, specific heat c_p, thermal diffusivity α) of most common building materials (Brink, 2005: 119).
Preglednica 2.2: *Termične lastnosti (gostota ρ_m, toplotna prevodnost k, specifična toplota c_p, termična difuzivnost α) najpogostejših gradbenih materialov (Brink, 2005: 119).*

Material	$\boldsymbol{\rho_m}$ **(kg/m^3)**	$\boldsymbol{k}$ **(W/m K)**	$\boldsymbol{c_p}$ **(J/kg K)**	$\boldsymbol{\alpha}$ **(m^2/s)**
Air at 30 °C	1.149	0.026	1007	$2.28 \cdot 10^{-5}$
Water	1000	0.600	4180	$1.40 \cdot 10^{-7}$
Concrete	2400	2.100	1000	$8.75 \cdot 10^{-7}$
Brick	2000	1.050	900	$5.83 \cdot 10^{-7}$
Polystyrene 30	15	0.030	1500	$1.33 \cdot 10^{-6}$
Lime mortar	1700	0.850	1050	$4.60 \cdot 10^{-7}$
Cement mortar	2000	1.200	1050	$6.67 \cdot 10^{-7}$
Gypsum mortar	1200	0.350	850	$3.43 \cdot 10^{-7}$
Mortar	1900	0.930	800	$6.12 \cdot 10^{-7}$

Assuming rather simple conditions such as a semi-infinite isotropic plate with finite thickness L, neglected thermal losses and an instantaneous heat pulse (with assumed Dirac delta function shape) applied to the plate, the solution for the surface temperature reduces to [112, 113]

$$T(t) = \frac{Q}{c_p\rho_m L}\left[1 + 2\sum_{n=1}^{\infty}(-1)^n \exp\left(-\frac{n^2\pi^2\alpha\, t}{L^2}\right)\right], \tag{2.33}$$

where Q is the amount of heat absorbed per unit area through the sample face.

However, for the inspection of defects in CE, complex geometries have to be taken into account, as well as a finite heat pulse and thermal losses. Hence, the problem is in most cases solved with numerical methods such as finite-difference or finite-element approaches.

2.4.4 Quantitative data analysis in pulsed thermography

In IRT for NDT, data is in most cases collected for a given time period in forms of 2D IR images called *thermograms*, which present the surface temperature distribution. As a result, 3D data sets are obtained, with two spatial dimensions and the time. It should be noted that the recording as well as heating times for the inspection of building materials range for some minutes, contrary

to IRT applied in aerospace, where heat pulse durations range from a few milliseconds to a few seconds [114].

Contrary to GPR, CR and ultrasonic, thermal data do not directly provide the estimation of the defect depth, which, in general, is of utmost importance in NDE. Nonetheless, quantitative data analysis procedures have been proposed and will be briefly described in the sequel.

2.4.4.1 Thermal contrast

After the application of a heat pulse in PT, the generated thermal front penetrates into the specimen by thermal diffusion. The presence of a defect within the structure alters the diffusion rate once the thermal front reaches the defect, which is reflected on the surface temperature distribution. Thus, the time t when a defect appears with highest contrast directly relates to the defect's depth. It has been shown that as a rough estimate, the time t and the thermal contrast C relate to the defect depth z_{def} by [115, 116]

$$t \propto \frac{z_{def}^2}{\alpha}, \tag{2.34a}$$

$$C \propto \frac{1}{z_{def}^3}, \tag{2.34b}$$

where the thermal contrast is given by [104]

$$C(t) = T_{def}(t) - T_{sound}(t), \tag{2.35}$$

where T_{def} relates to the surface temperature above the defect and T_{sound} to the sound area.

Due to the above relations, a qualitative estimation of the defect depths may be performed by presenting a *contrast image*, where each pixel is associated with the value of its maximal thermal contrast $C_{max} = \max C(t)$. Similarly, *timegrams* – images referring to times when C_{max} appear, t_{Cmax} – may be used [117]. This data processing approach is also known as *thermal tomography* [104]. Definition of the thermal contrast according to Eq. (2.35) is for a specimen with defects given in Fig. 2.6. The maximal thermal contrast C_{max} and its corresponding time t_{Cmax} are presented as well.

However, according to Balageas *et al.* [118], a quantitative estimation of defect depths was proposed from the inspection of carbon-epoxy composites. It relates z_{def} to C_{max} and t_{Cmax} by the following expression

$$z_{def} = A\sqrt{t_{Cmax}}\, {C_{max}}^n \ \mathrm{m\,K^{-n}\,s^{-1/2}}, \tag{2.36}$$

where A and n are dimensionless coefficients.

The above equation is an inverse problem as coefficients A and n have to be previously determined from calibration curves obtained on the same material and under the same heating conditions. An additional disadvantage of this approach is that the position of the non-defect area has to

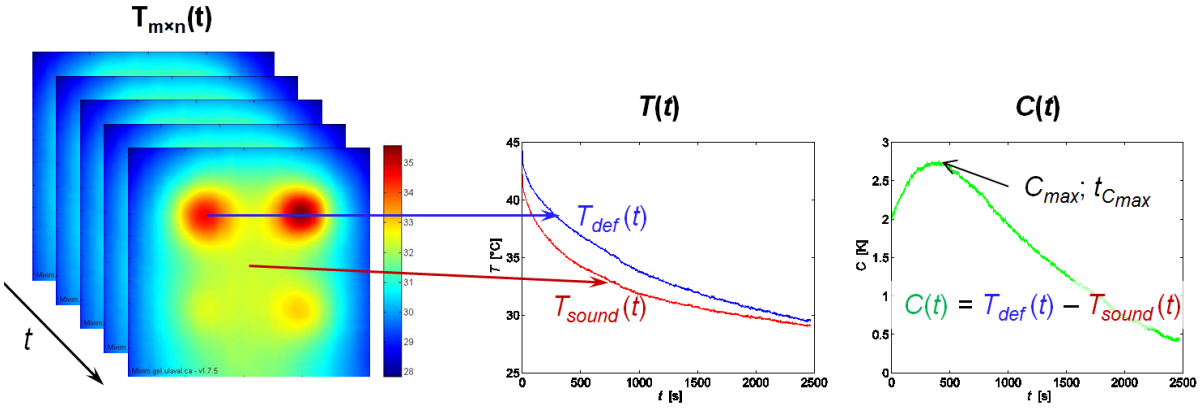

Figure 2.6: The definition of the thermal contrast $C(t)$ as the difference in surface temperatures above the defect T_{def} and sound area T_{sound}. Here, C_{max} refers to the maximal thermal contrast and t_{Cmax} is its corresponding time.
Slika 2.6: *Določitev temperaturnega kontrasta $C(t)$ iz razlike med površinsko temperaturo nad anomalijo T_{def} in površinsko temperaturo nad homogenim področjem T_{sound}. Pri tem C_{max} označuje maksimalni temperaturni kontrast, t_{Cmax} pa čas nastopa le-tega.*

be known *a priori* in order to calculate the thermal contrast [119]. Finally, the thermal contrast between the defective vs. non-defective area has shown to be smaller due to the blurring effect of all frequencies composed in the pulse compared to the more advanced techniques based on phase characteristics [104, 120], as the technique described below.

2.4.4.2 Pulsed phase thermography

Pulsed phase thermography (PPT) [114] is a data analysis technique for PT, but employs the data analysis principle of lock-in thermography (LT), as well as the principle of the thermal wave theory. Contrary to LT, where the specimen is excited with one particular frequency, pulsed heating can be considered as inspection with multiple frequencies simultaneously since mathematically, a pulse of amplitude A_p and finite duration t_p can be decomposed into several sinusoidal waves [121] with the frequency distribution following (see also Fig. 2.7)

$$F(\omega) = A_p t_p \,\mathrm{sinc}(\omega t_p/2) = \frac{A_p t_p \sin(\omega t_p/2)}{\omega t_p/2}. \tag{2.37}$$

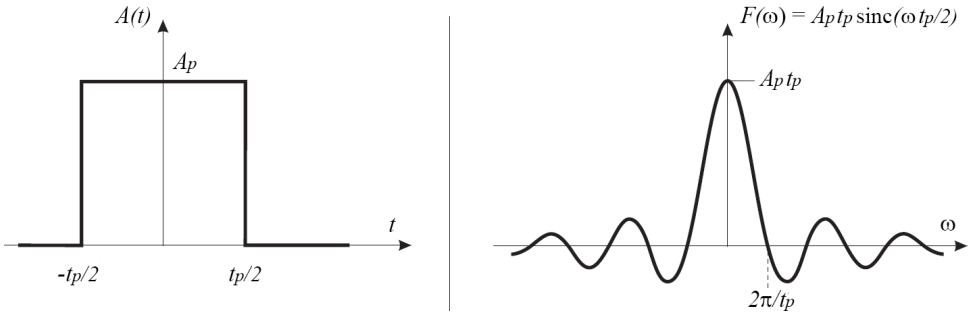

Figure 2.7: The Fourier transform of a pulse with amplitude A_p and duration t_p.
Slika 2.7: *Fourierjeva transformacija pulza z amplitudo A_p in dolžine t_p.*

In PPT the extraction of various frequency content is performed by a discrete 1D Fourier transform (FT) of the time evolution $T(t)$ for each pixel of the data set of N thermograms by the formula[6] [122]

$$F_n = \frac{1}{N}\sum_{k=0}^{N-1} T(k)\mathrm{e}^{-2\pi ikn/N} = \mathrm{Re}F_n + i\,\mathrm{Im}F_n, \tag{2.38}$$

where $t = k\Delta t$ and Δt is the time interval between individually collected thermogrames. The frequency $f_n = \omega_n/2\pi$ is given by $f_n = n/N\Delta t$, where n is the frequency increment. Due to the symmetry of FT[7] and the Nyquist criterion [122], the maximal frequency that can be obtained is $f_{max} = 1/2\Delta t$ [123]. It is worth noticing that due to Euler's formula $e^{i\,\omega t} = \cos(\omega t)+i\,\sin(\omega t)$ and the Fourier series analogy, the real component $\mathrm{Re}F_n$ can be regarded as the cosine contribution, whereas the imaginary component $\mathrm{Im}F_n$ may be regarded as the sine contribution for a given angular frequency ω_n since the following holds[8]

$$T(t) = \sum_{n=0}^{\infty} F_n\,\mathrm{e}^{i\omega_n t} = \sum_{n=0}^{\infty}\left[\mathrm{Re}F_n\,\cos(\omega_n t) - \mathrm{Im}F_n\,\sin(\omega_n t)\right] = \sum_{n=0}^{\infty} A_n\,\cos(\omega_n t - \phi_n), \tag{2.39}$$

where amplitudes A_n and phases ϕ_n are then computed by

$$A_n = |F_n| = \sqrt{\mathrm{Re}F_n{}^2 + \mathrm{Im}F_n{}^2}, \tag{2.40a}$$

$$\phi_n = \arg(F_n). \tag{2.40b}$$

By applying the above procedure for each pixel of the thermogram sequence, ampligram and phasegram sequences are obtained for a range of frequencies as displayed in Fig. 2.8.

The interpretation of the amplitude and phase images is coupled with the thermal wave theory. Strongly attenuated and dispersive thermal waves are generated within the specimen after a heat pulse is applied. For a semi-infinite slab, onto which a sinusoidal heating is applied with angular frequency ω (as in LT), the resulting temperature distribution is given by [124]

$$T(z,t) = T_0\,\mathrm{e}^{-z/\mu}\,\cos\left(\omega t - \phi(z)\right), \tag{2.41}$$

where μ is the thermal diffusion length and ϕ is the phase of thermal waves given by

$$\mu = \sqrt{\frac{2\alpha}{\omega}} = \frac{\lambda}{2\pi}, \tag{2.42a}$$

$$\phi(z) = \frac{2\pi z}{\lambda} = \frac{z}{\mu}. \tag{2.42b}$$

[6]Due to the lengthy computation of discrete FT, Eq. (2.38) is for practical computations replaced by the Fast FT (FFT) algorithm, commonly available in commercial software packages.

[7]The produced real part of $F(f)$ is an even (symmetrical) function, whereas the imaginary part is an odd (antisymmetrical) function. This property is reflected on the amplitude $A(f)$ and phase $\phi(f)$ profiles, which are even and odd with respect to zero frequency [120].

[8]For a proper amplitude $T(t)$, the expression for $T(t)$ has to be multiplied with Δt.

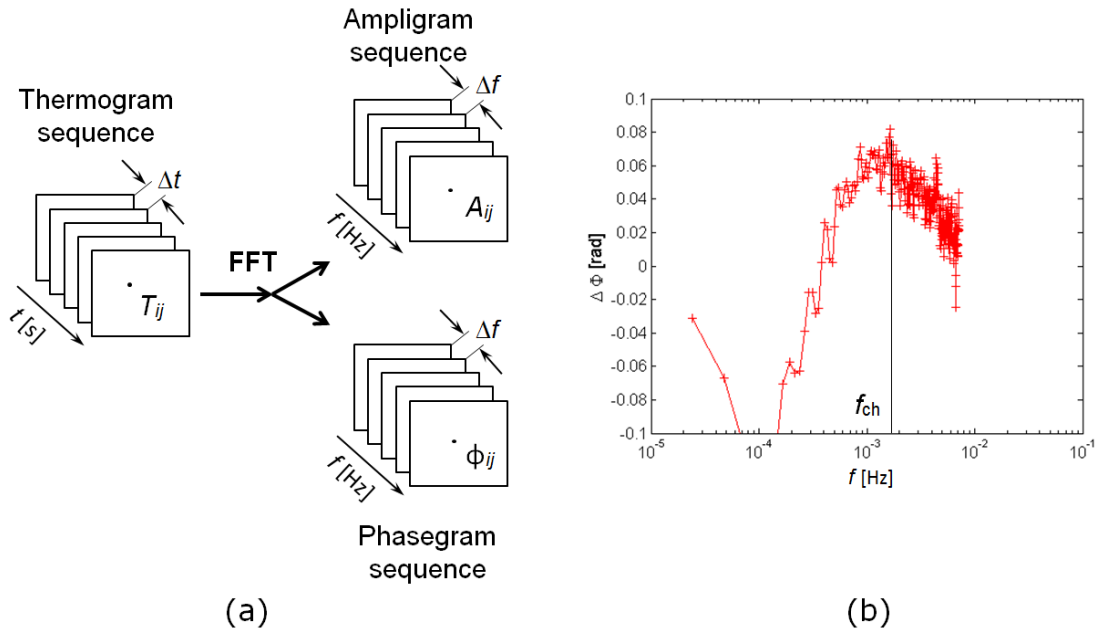

Figure 2.8: (a) The principle of pulsed phase thermography (PPT) and (b) presentation of the phase contrast curve with the frequency of the maximal phase contrast f_{ch}.
Slika 2.8: *(a) Princip delovanja pulzno-fazne termografije (PPT) in (b) prikaz krivulje faznega kontrasta in frekvence, pri kateri nastopi maksimalni fazni kontrast* f_{ch}.

Eq. (2.42a) directly implies that higher modulation frequencies are restricted to the near-surface region. Hence, for PT in CE applications, more energy should be concentrated at lower frequencies, which is provided by a longer heat pulse (see Eq. (2.37) and Fig. 2.7). In addition, by comparing Eq. (2.41) to (2.39) it is evident that both amplitudes as well as phases carry the information about the thermal waves diffusion length. However, it has been shown that amplitude images exhibit a low-pass filter behaviour – resolve the internal structure up to a particular depth, whereas phase images exhibit the band-pass filter behaviour – resolve the structure within a particular depth range [104]. Thus, phase images are less sensitive to non-uniform heating, variable surface emissivity [121] and probe approximately twice deeper than amplitude images [125], for which the maximal observation depth is restricted to approximately μ [126]. However, especially at high frequencies, phase images are sensitive to noise [104], but as low frequencies are of interest in CE, phase images are of particular importance.

For quantitative inversion of PPT data, methods such as neural networks, wavelets, as well as statistical methods have been proposed [104]. Recently, an approach based on the phase contrast calculation has been given by Ibarra-Castanedo [120, 127] (the phase contrast is defined in analogy with the thermal contrast given in (2.35), $\Delta\phi(f) = \phi_{def}(f) - \phi_{sound}(f)$ – see also Fig. 2.8). It states that defects may be detected up to a depth-dependent, so called blind frequency f_b. According to the relation given in (2.42a), the value is smaller for deeper defects. By combining Eq. (2.42a) and (2.42b), Ibarra-Castanedo proposed the following equation for the estimation of defects depth

$$z_{def} = C_1\sqrt{\frac{\alpha}{\pi f_b}} = C_1\mu, \tag{2.43}$$

as well as an alternative approach for badly sampled data [127]. Here, α is the diffusivity of the material (sound area) and C_1 is a correlation coefficient. $C_1 = 1$ directly holds for amplitude images due to the low-pass filter principle, whereas for phase images, the reported values range up to 2 [128]. Nonetheless, both approaches failed in CE [129] and hence, Arndt[9] introduced an alternative equation, based on the frequency of the maximal phase contrast f_{ch} [131, 123] (see Fig. 2.8),

$$z_{def} = k_c \sqrt{\frac{\alpha}{f_{ch}}}, \tag{2.44}$$

with the correlation factor k_c that has to be assessed for various conditions. However, for both amplitude and phase images it has been shown that k_c is almost independent of the heating time and may therefore be roughly set to 1 [130].

2.5 Ultrasonic

The ultrasonic pulse method (shortly ultrasonic) is a well established method in medicine and for the investigation of metals. However, as late as in the 1990s, ultrasonic was first applied in CE for thickness measurements of structural elements [18] and localisation of reinforcement and tendon ducts [54], as well as for the characterization of surface cracks [132] in concrete structures.

The method is based on the generation, propagation and recording of either reflected or transmitted sound waves in the ultrasonic region, *i.e.* at frequencies above 20 kHz. For NDT-CE applications, the typical frequency range is 50–200 kHz [12]. Contrary to other acoustic methods use in NDT-CE (see section 2.1), ultrasonic uses piezoelectric transducers for both sound wave generation and recording. The features which distinguish ultrasonic from GPR are that ultrasonic waves travel about 100,000 times slower than EMW and that they can easily penetrate materials such as metals [133]. On the other hand, the GPR signal is almost totally reflected by a metal.

Ultrasonic can be performed by single point-contact measurements that in general suffer from being slow and require a good coupling provided by a coupling agent [11]. However, for the investigation of concrete structures using the ultrasonic echo technique (records the reflected ultrasonic waves), a multi-sensor ultrasonic echo array system has been used [22, 134]. Here, the system consists of several dry point-contact transducers which alternately act as a pulser or receiver. The collected data is then processed using the SAFT (Synthetic Aperture Focusing Technique) algorithm [135], which gives a 2D or 3D reconstructed image of the aperture covered by the array.

2.5.1 Acoustic wave theory

Contrary to EMW, sound waves are mechanical waves that require a medium to propagate. Here, the sound energy is transferred by the deformation of matter, more exactly the oscillation

[9]The adaptation of PPT proposed by Arndt for qualitative and quantitative data analysis in CE was later termed square pulse thermography (SPT) in the frequency domain [130].

of constituents close to its equilibrium place, which generates pressure changes. For an isotropic, homogeneous, linear, and dispersion-less material, the propagation of sound waves is governed by the acoustic wave equation which for the pressure p writes[10] [133]

$$\frac{\partial^2 p}{\partial t^2} = v^2 \cdot \nabla^2 p, \tag{2.45}$$

and has the general solution in the form of

$$p(z,t) = p_0 \, \mathrm{e}^{i(\omega t - \beta z)}, \tag{2.46}$$

where ω is the angular frequency and β is the phase constant. The dependence between the pressure p and the speed of sound v is given by

$$v^2 = \frac{\partial p}{\partial \rho_m}, \tag{2.47}$$

where ρ_m is the mass density.

The particles in solids can oscillate both in the direction of wave propagation as well as perpendicularly to the direction, which results in longitudinal (or volumetric for 3D solids) and shear deformations, respectively. The quantity that describes the tendency of the material to deform under pressure is the modulus of elasticity. Particularly, the Young's modulus E relates to longitudinal deformations, the shear modulus G to shear deformations and the bulk modulus K to volumetric deformations. With respect to the deformations induced in solids, longitudinal (compression) and transverse (shear) waves exist. In a 3D homogeneous solid, their sound velocities are given by the following equations [136]

$$v_l = \sqrt{\frac{K + {}^4\!/_3 \, G}{\rho_m}} = \sqrt{\frac{E\,(1-\mu)}{\rho_m\,(1+\mu)(1-2\mu)}}, \tag{2.48a}$$

$$v_t = \sqrt{\frac{G}{\rho_m}} = \sqrt{\frac{E}{2\rho_m(1+\mu)}}, \tag{2.48b}$$

where μ is the Poisson's ratio[11] which describes the ratio between the transverse and axial strain and ranges from 0 to 0.5 [137]. Considering this, v_l is always larger than v_t, according to $v_l \geq \sqrt{2}\, v_t$. The right side of the above equations are obtained by applying the following relations [133]:

$$K = \frac{E}{3(1-2\mu)}, \tag{2.49a}$$

$$G = \frac{E}{2(1+\mu)}. \tag{2.49b}$$

From Eq. (2.48a) and (2.48b) it is evident that in materials that cannot exhibit shear deformations

[10] The acoustic wave equation may be equivalently written for both the pressure p and the particle velocity u.

[11] Note that in this section, μ refers to the Poisson's ratio and should not be related to magnetic permeability.

with $G = 0$ (like liquids and gases), only longitudinal waves can be generated. The longitudinal wave velocities for some building materials are given in Table 2.3.

Table 2.3: The typical range of longitudinal sound wave velocity v_l of some building materials (Wendrich, 2009: 11).
Preglednica 2.3: *Okvirne vrednosti hitrosti longitudinalnih zvočnih valov v_l v nekaterih gradbenih materialih (Wendrich, 2009: 11).*

Material	$\boldsymbol{v_l}$ **(m/s)**
Air	344
Concrete	3000–4830
Brickwork masonry	2000–3500
Sandstone	2300–2800
General stone	2000–4800

2.5.2 Reflection and refraction of acoustic waves

Upon the propagation in a material, acoustic waves exhibit reflection and refraction from subsurface discontinuities, similarly to EMW. The fraction of sound energy being reflected and transmitted is governed by the acoustic impedance of the medium. It is an intrinsic material property related to the mass density and speed of sound in the medium by the following relation [136]

$$Z = \rho_m v. \tag{2.50}$$

For the ultrasonic measurement, differences in the acoustic impedance of the medium and discontinuities are of importance since this enables defect detection. For an ultrasonic wave incident on a planar boundary, the reflection coefficient r and the transmission coefficient t are given by [136]

$$r = \frac{Z_2 - Z_1}{Z_2 + Z_1}, \tag{2.51a}$$

$$t = \frac{2Z_2}{Z_2 + Z_1}, \tag{2.51b}$$

where Z_1 and Z_2 are the acoustic impedances of medium 1 and 2.

2.5.3 Acoustic attenuation and dispersion

The acoustic wave theory introduced in section 2.5.1 is based on the assumption of an isotropic, homogeneous, linear, loss-less and dispersion-less material. As for the EM properties of building materials (see section 2.2.1), the first three conditions are for simplification in most cases assumed valid, whereas the acoustic attenuation and dispersion have to be taken into account.

The attenuation of acoustic waves can be introduced in Eq. (2.46) in the same analogy as for EMW with the complex propagation factor k, such that $ik = \alpha + i\beta$, where here, α refers to the acoustic attenuation coefficient [133]. The pressure solution is then rewritten in the form given for the electric field in Eq. (2.4). The acoustic attenuation reflects on the sound velocity (2.50) by the introduction of a complex acoustic impedance, similarly as for the electrical impedance (2.13).

In general, the acoustic attenuation has several sources: the heat release due to deformation of the material caused by the travelling wave (also referred to as thermoelastic loss), the phonon viscosity phenomenon, as well as the Rayleigh scattering loss from aggregates, pores and impurities [133]. All terms are frequency-dependent, referring to the acoustic dispersion. Since the phonon viscosity phenomenon becomes important only at very high frequencies, it's contribution is not considered for ultrasonic applications in NDT [133]. For low frequencies used in NDT-CE, the principal component is the Rayleigh scattering from objects with dimensions close to the sound wavelength. Here, the attenuation is strongly frequency-dependent ($\alpha \propto \omega^4$) [133]. It is interesting to notice that in concrete and masonry, the acoustic wavelengths are smaller than EM wavelengths for the used frequency range (the acoustic wavelengths are thus closer to the size of aggregates, pores and impurities). Therefore, for ultrasonic, the Rayleigh scattering is more pronounced than it is for GPR.

Water molecules embedded in the material result in even stronger scattering and can greatly reduce the signal intensity. The effect of water on the scattering intensity was the scope of a study using GPR, CR and ultrasonic on brickwork masonry. The methods performance with respect to the moisture content of the masonry was taken under consideration. The results are presented in the article given in Appx. C.

2.5.4 Piezoelectric transducers

For ultrasonic, piezoelectric transducers are used for both wave generation and receiving. Piezoelectricity refers to the phenomenon that when a piezoelectric material undergoes stress, both strain as well as a potential difference are produced between the opposite faces of the material producing an electrical signal [133]. As such, the conversion of electrical signals into mechanical vibrations is employed in the transmitting mode, and the conversion of mechanical vibrations into electrical signals in the receiving mode. The physics of the piezoelectric effect can be understood in the way that when stress is applied to the material, a molecular dipole moment is induced (due to the asymmetric distribution of positive and negative charges). This generates a net polarization, which results in a potential difference [133].

Prior to the 1950s, piezoelectric crystals made from quartz were used as piezoelectric transducers. Nowadays, most piezoelectric ceramic materials used in NDT are based on the lead zirconate titanate (PZT) family. PZT exhibits good piezoelectric properties, is easy to manufacture in various shapes and sizes, can operate at low voltage and is usable up to 300 °C [138]. However, beside the piezoelectric element, additional components build the piezoelectric transducer in order to provide effective damping and enough mechanical energy.

For the scope of this thesis, ultrasonic tomography was performed on masonry by single point-contact measurements (see Appx. C). Here, a coupling agent is required to provide the required contact. As noted in [139], several agents can be used, such as glycerine, vaseline and even water for horizontal inspections. Based on the results given by Wendrich when using ultrasonic on masonry [139], vaseline was chosen in our experiment since it yielded the strongest signal.

3 NDT DATA FUSION WITH CLUSTERING

3.1 Introduction to data fusion

According to Gros [62], NDT data fusion can be thought as multi-sensor fusion, *i.e.* synergistic use of information from multiple sensors/sources in order to facilitate data interpretation and increase the probability of defect detection. Its application in NDE emerged from many fields, including military applications (target tracking, airborne surveillance), robotics, remote sensing, pattern recognition and medical imaging [140]. Although it has been almost two decades since data fusion was introduced in NDE [63, 64] and an outstanding progress has been made in aerospace and nuclear industry, NDT data fusion remains a challenging task. Due to the ongoing development of new sensors and/or techniques, as well as an increasing number of potential applications of NDT, there is no general data fusion model, which could handle numerous applications. Moreover, due to the increasing requirements on the accuracy of NDT and NDE on one hand, as well as on the cost and time efficient inspections (resulting in incomplete data with limited resolution) on the other hand, the development of efficient fusion models is of major importance. In addition, a data fusion model for NDE-CE should account for the extremely heterogeneous material to be investigated and for an even larger variety of possible applications on-site.

3.2 A data fusion framework

Data fusion can in general be performed on data sets of different dimensions – signals, 2D images or on the whole volume. Moreover, several modes of a single NDT method can be considered (*e.g.* multiple polarizations or frequencies), or several NDT methods. This thesis focuses on image fusion, as well as on data fusion from multiple NDT methods.

Taking into account that different methods respond both complementarily as well as by overlapping performance, a good data fusion model should integrate the detected features, where methods respond complementarily, but also discriminate different features detected by several sources [53]. To fulfil this task, several fusion algorithms have been proposed based on optimization methods, multi-resolution approaches, heuristic methods and probabilistic methods, which can be further classified to Bayesian inference, Dempster-Shafer (D-S) evidence and fuzzy logic. For image fusion, these methods can be introduced into a data fusion framework at three different levels [53]:

- pixel-level fusion,
- feature-level fusion,
- symbol-level fusion.

At pixel level, images are fused at each pixel individually without using pre-processing units. The information from fusion is obtained after image classification using optimization, multi-resolution or heuristic methods, as well as cluster analysis. On the other hand, feature and symbol level fusion are applied on a higher level, using the information obtained in the pre-processing step. Feature-level fusion tends to fuse features extracted by segmentation in the

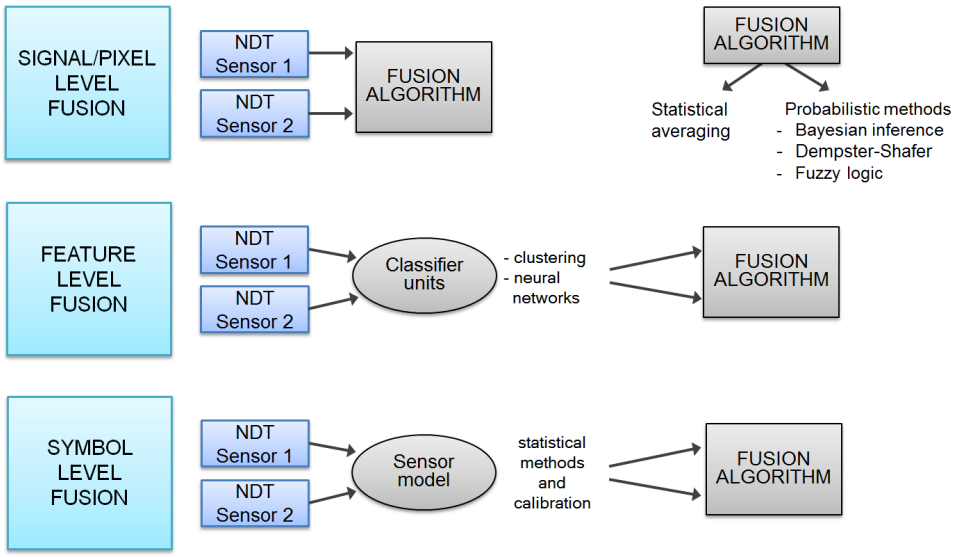

Figure 3.1: Data fusion schemes at pixel-level fusion, feature-level fusion and symbol-level fusion.
Slika 3.1: *Združevanje podatkov na nivoju slikovne točke, z uporabo značilnic in na simbolnem nivoju.*

pre-processing step using *e.g.* clustering or neural networks, whereas symbol level fusion is in most cases based on sensor modelling. At both levels, the pre-processing units are fused using averaging or probabilistic methods. The concept of various data fusion schemes is illustrated in Fig. 3.1.

One of the main restrictions in using optimization methods such as the LMMSE (linear minimum mean square error) approach is proper definition of the input LMMSE filter. Similarly, also the implementation of the alternative Kalman filter remains a complex problem for NDT applications. Multi-resolution approaches using particularly wavelets require an appropriate wavelet filter with definition of the decomposition level to be used. Similarly, the heuristic neural networks require a good training data set, which is in most cases hard to accomplish, especially for NDT-CE. For higher-level fusion schemes (feature- and symbol-level), which employ probabilistic methods, a challenging task remains to correctly assign the conditional and *a priori* probabilities, as well as mass functions, which govern the evaluation. Although many studies have proposed different approaches for its calculation [73, 71, 141, 74], none of the methods can work fully unsupervised. On the contrary, clustering methods require some sensitivity measures to be set, which, however, does not affect the analysis significantly as evident throughout our work, but they do not need prior knowledge on the statistical data distribution. This is especially promising in the field of NDT-CE, where knowledge about sample composition is limited due to the large diversity of specimens.

The thesis focuses on clustering-based unsupervised image fusion. Throughout the work, clustering methods were introduced into various data fusion models both at a low level, as well as at a higher feature level. For the investigation of stone masonry walls and for the multi-sensor data set collected by the BetoScan robot system, clustering techniques were utilized for image segmentation at the pixel level. Here, this concept of image fusion was found more appropriate since the physical data contained in the images from various NDT methods were not linked to the

same spatial position (all methods did not give a depth dependant data visualization). Moreover, since the severity of damage was of interest rather than a complete visualization of the internal structure, an image fusion model based on segmentation was derived for defect detection.

On the other hand, data obtained from several sources for the investigation of the laboratory concrete specimens were linked to a common spatial position. Thus, feature-level fusion was employed, where membership information from fuzzy clustering methods served as pre-processing units. In the case of the concrete specimens, a comparison with supervised symbol-level fusion was additionally performed as presented in the article given in Appx. A. Moreover, a feature-level based fusion model was also proposed for the derivation of smooth depth profiles of sodium content in the cement, where clustering methods were applied for the classification of spatially acquired LIBS spectra.

Before introducing the concept of cluster analysis and presenting different clustering methods, a note to a complete data fusion framework will be given. The architecture of a generalized system for NDT data fusion can be divided into 3 main stages: data registration, data fusion and expert system reasoning [142]. Data registration is a prior step before data fusion and refers to the association of data from multiple sources to physical points on the specimen [53]. Data alignment to a common region as well as adjustment to a common spatial resolution are performed. In addition, signal/image processing steps may be employed at this level, such as signal enhancement, filtering and migration of GPR data, analysis of IR thermal images in the frequency domain, the inversion procedure of complex resistivity data, to name just a few. At the next step, a data fusion algorithm as presented above is applied. The last stage introduces the reasoning of an intelligent system, which refers to situation assessment and failure analysis [142]. The architecture of a generalized system for NDT data fusion is shown in Fig. 3.2.

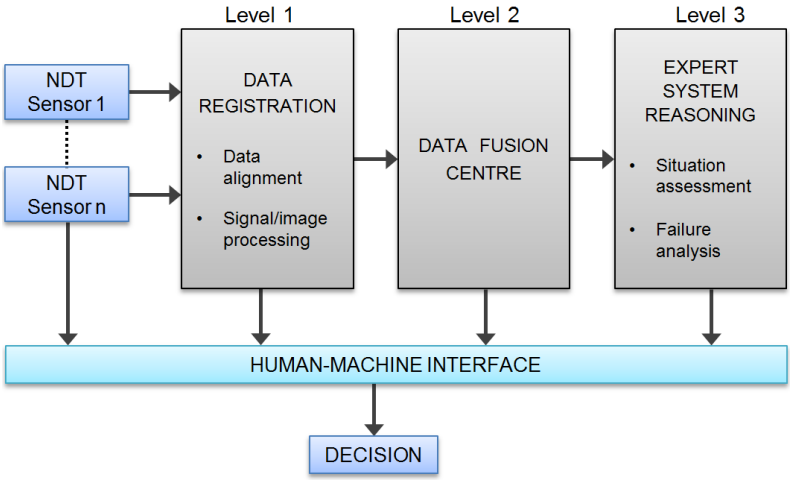

Figure 3.2: Schematic diagram of the architecture of a generalized system for NDT data fusion (modified after Gros *et al.*, 1995: 2).
Slika 3.2: *Shematični prikaz arhitekture splošnega sistema za združevanje podatkov (prirejeno po Gros et al., 1995: 2).*

Among the three stages of the presented model, the last reasoning stage is particularly application dependant and should be applied at the final stage of a data fusion model. Thus, the development

of a data fusion framework within the thesis was restricted to the application of the first two steps – data registration and data fusion. The specific image processing steps of particular NDT methods are presented in chapter 4, as well as throughout the specific applications given in the appendices. The different data fusion algorithms are explained in detail in the appendices as well. However, their common basis, *i.e.* cluster analysis, is introduced in the following sections of this chapter, where different clustering methods are also presented.

3.3 Cluster analysis

Clustering or cluster analysis means grouping a set of data (observations) into subsets (clusters, groups or classes). It can be done hierarchically (subsequent division into clusters and sub-clusters) or partitionally (determination of all clusters at once) according to the following criteria [143]:

- *Homogeneity* of clusters, *i.e.* the members of a cluster should be as similar as possible.
- *Heterogeneity* among clusters, *i.e.* members belonging to different clusters should be as dissimilar as possible.

3.3.1 Distance and similarity

The term similarity, according to which clustering is performed, refers to differences in observational properties (variables). A common measure of similarity between two observations $\mathbf{x_1}$, $\mathbf{x_2}$ is the Euclidean norm/distance d, which can be for M variables written as[1]

$$d^2(\mathbf{x_1}, \mathbf{x_2}) = \sum_{i=1}^{M} (x_{1i} - x_{2i})^2 = \|\mathbf{x_1} - \mathbf{x_2}\|^2 = (\mathbf{x_1} - \mathbf{x_2})^T(\mathbf{x_1} - \mathbf{x_2}). \tag{3.1}$$

The Euclidean distance, introduced in most clustering algorithms, implies a view of the data clusters with a hyper-spherical geometry. To avoid this constraint, a generalization has been proposed by the Mahalanobis distance, which induces hyper-ellipsoidal clusters with [144]

$$d^2(\mathbf{x_1}, \mathbf{x_2}) = \|\mathbf{x_1} - \mathbf{x_2}\|_{\mathbf{A}}^2 = (\mathbf{x_1} - \mathbf{x_2})^T\mathbf{A}(\mathbf{x_1} - \mathbf{x_2}), \tag{3.2}$$

where $\mathbf{A}$ refers to a norm-inducing matrix [145].

The different distance functions employed in fuzzy clustering algorithms are presented in Fig. 3.3. Note that the difference between the diagonal norm and the Mahalonobis norm is that the diagonal norm restricts the axes of the hyper-ellipsoid to the coordinate axes, whereas in the Mahalonobis norm, they are arbitrary.

3.3.2 Objective function-based clustering – a general note

Partitional clustering builds clusters of data sets on the basis of the minimization of a certain objective function (thus the term *objective function-based clustering*) and can therefore be treated

[1] A list of common distance functions can be found in Table 1.1 in [144].

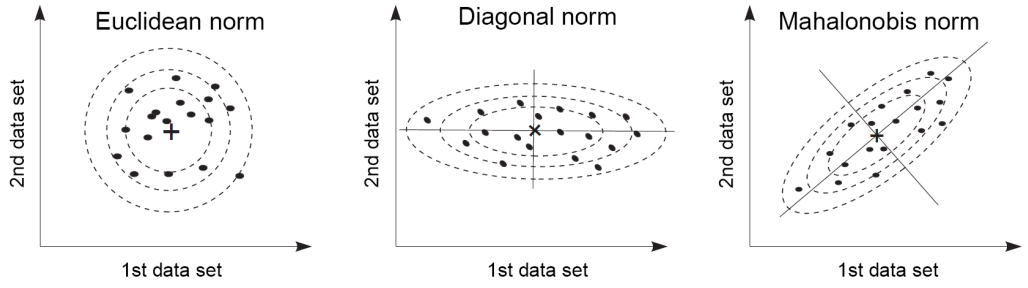

Figure 3.3: The distance norms used in fuzzy clustering algorithms (Babuška, 2009: 70).
Slika 3.3: *Norme uporabljene v algoritmih za mehko združevanje (Babuška, 2009: 70).*

as an optimization technique. For a given data set $\mathbf{X}$ of N observations, where each consist of n measured variables[2]

$$\mathbf{X} = \begin{bmatrix} x_{1,1} & x_{1,2} & \cdots & x_{1,N} \\ x_{2,1} & x_{2,2} & \cdots & x_{2,N} \\ \vdots & \vdots & \ddots & \vdots \\ x_{n,1} & x_{n,2} & \cdots & x_{n,N} \end{bmatrix}, \tag{3.3}$$

partitioning into c number of clusters is performed by iteratively assigning labels u_{ij} to column vectors in $\mathbf{X}$ by partition matrix $\mathbf{U} = [u_{ij}]_{c\times N}$, so that the observations are moved in each step to the cluster, the centre of which is closest to them, until a convergence limit is reached. A generalized objective function (functional) J to be minimized in partitioning the data can be defined as the sum of the distances of N observations from their respective cluster centre $\mathbf{v}$

$$J_m(\mathbf{U}, \mathbf{V}; \mathbf{X}) = \sum_{i=1}^{c} \sum_{j=1}^{N} u_{ij}^m d_{ij}^2, \tag{3.4}$$

where $d_{ij} = \|\mathbf{x_j} - \mathbf{v_i}\|_{\mathbf{A}}$. Note that for the Euclidean distance, $\mathbf{A}$ is identity matrix. A graphical representation of partitioning a data set of two variables into three clusters is given in Fig. 3.4.

With respect to the partition matrix $\mathbf{U}$, the resulting partitions (and also clustering methods presented in section 3.3.3) may be classified as hard (or crisp), fuzzy probabilistic or fuzzy possibilistic [146]. Hard and fuzzy probabilistic partition matrices have to satisfy the conditions that each cluster is nontrivial (does not include all patterns and is nonempty), as well as that the total membership degree of each observation sums to 1. We state this by

$$\sum_{i=1}^{c} u_{ij} = 1, \quad \forall j \in \{1, \ldots, N\}, \tag{3.5a}$$

$$0 < \sum_{j=1}^{N} u_{ij} < N, \quad \forall i \in \{1, \ldots, c\}. \tag{3.5b}$$

[2]For $\mathbf{X}$, the matrix notation may be replaced by a column vector notation for each observation $\mathbf{x_j} = [x_{1j}, x_{2j}, \ldots, x_{nj}]^T, \mathbf{x_j} \in \mathbb{R}^n$ so that the data set may be denoted by $\mathbf{X} = \{\mathbf{x_1}, \mathbf{x_2}, \ldots, \mathbf{x_N}\}$.

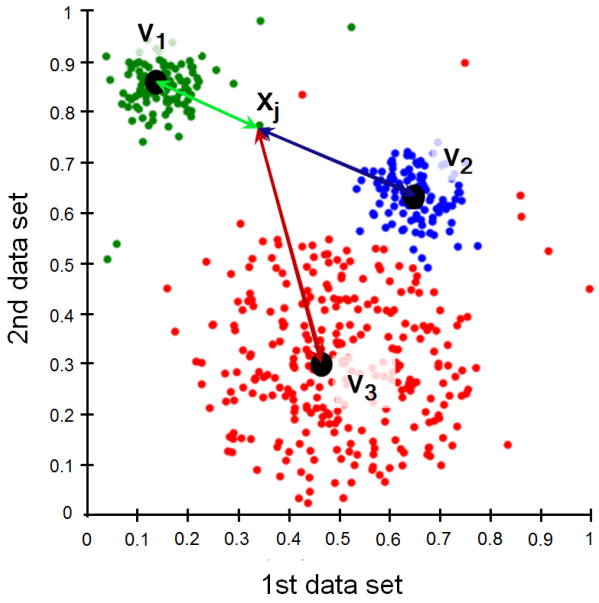

Figure 3.4: Representation of partitioning a data set of two variables into three clusters. The assignment of observations (data points) to a specific cluster (here, red, green or blue) is associated by the colour. For a specific observation $\mathbf{x_j}$, the distances to the three cluster centres $\mathbf{v_1}$, $\mathbf{v_2}$, $\mathbf{v_3}$ are marked as well.
Slika 3.4: *Prikaz gručenja množice podatkov dveh spremenljivk v tri razrede. Razporeditev posameznega podatka v ustrezen razred je na sliki ponazorjena z barvo razreda (rdeči, zeleni ali modri). Za podatek* $\mathbf{x_j}$ *so prikazane razdalje do središč razredov* $\mathbf{v_1}$, $\mathbf{v_2}$, $\mathbf{v_3}$.

The main difference in hard vs. fuzzy partition, is that for hard partition,

$$u_{ij} \in \{0, 1\}, \tag{3.6}$$

whereas for fuzzy, it follows that

$$u_{ij} \in [0, 1], \tag{3.7}$$

i.e., for hard clustering, each observation belongs to a single cluster, whereas for fuzzy clustering, observations may be associated to several clusters with a given membership degree (thus "probabilistic clustering"). Eq. (3.7) holds for both fuzzy probabilistic and possibilistic clustering. However, the main difference between the two is that possibilistic clustering drops the constraint that the memberships of each observation have to make a total of 1 over all clusters as in Eq. (3.5a). The functioning of hard vs. fuzzy clustering is illustrated in Fig. 3.5.

3.3.3 Objective function-based clustering algorithms

3.3.3.1 Hard clustering

A very common hard clustering algorithm is the *k-means* algorithm [82], which uses the Euclidean distance given in (3.1) and satisfies the restrictions for the hard partition matrix given by (3.5a),(3.5b),(3.6), which yields simplified equation (3.4), $J(\mathbf{V}; \mathbf{X}) = \sum_{i=1}^{c} \sum_{j=1}^{N} d_{ij}^2$. For the k-means, the cluster centres correspond to the mean value of their observations, which can be

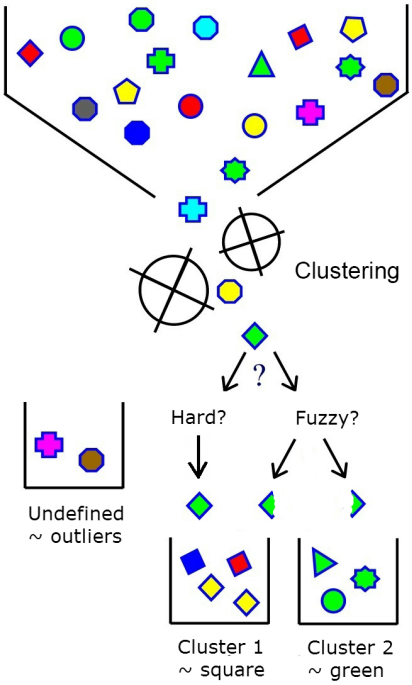

Figure 3.5: The principle of hard and fuzzy clustering.
Slika 3.5: *Princip delovanja trdega in mehkega gručenja.*

for the i-th cluster centre defined as

$$\mathbf{v_i} = \frac{\sum_{k=1}^{N_i} \mathbf{x_k}}{N_i} \tag{3.8}$$

where $\mathbf{x_k}$ is an observation classified to the i-th cluster and N_i is the number of observations in the i-th cluster.

3.3.3.2 Fuzzy clustering

In this chapter, first, the standard *fuzzy c-means* (FCM) algorithm will be introduced, followed by its extensions – the *Gustafson-Kessel* (GK) algorithm, which uses an adaptive distance measure, as well as *noise* and *possibilistic* clustering, which account for outliers.

Fuzzy c-means clustering

The FCM algorithm [83] with the FCM functional and the Euclidean distance defined by (3.1) and (3.4) can be regarded as the conventional fuzzy clustering algorithm since it forms the basis for other fuzzing algorithms. It is a probabilistic clustering algorithm, where u_{ij} describes the membership of observation $\mathbf{x_j}$ to the i-th cluster. The "fuzzing" exponent or "fuzzifier" m introduced in (3.4) is a positive real number and determines the fuzziness of the resulting partition. It is recommended to range from 1.2 to 2 [143]. In our version of the FCM (and its extensions), m was fixed to 2, being the value most recommended by other authors [144, 145].[3]

[3]For the effect of the fuzzifier values on the membership function, refer to Figure 1.9 in [144].

To minimize J_m, which represents a nonlinear optimization problem,[4] it can be shown that u_{ij} and $\mathbf{v_i}$ should be updated in each iteration by

$$u_{ij} = \frac{1}{\sum_{k=1}^{c} (d_{ij}/d_{kj})^{2/(m-1)}}, \tag{3.9a}$$

$$\mathbf{v_i} = \frac{\sum_{j=1}^{N} u_{ij}^m \cdot \mathbf{x_j}}{\sum_{j=1}^{N} u_{ij}^m}. \tag{3.9b}$$

Gustafson-Kessel clustering

Several algorithms which employ an adaptive distance norm to overcome the restriction of hyperspherical clusters of the FCM algorithm, so called "fuzzy c varieties", have been proposed [143]. However, in the thesis, we refer to the GK algorithm [85], a probabilistic extension of the FCM algorithm, which uses the Mahalanobis norm (3.2) and the same functional as the FCM (3.4).[5] Here, each cluster has its own norm-inducing matrix. However, for a feasible solution, $\mathbf{A_i}$ of the i-th cluster should be calculated on the basis of the cluster volume ρ_i and the fuzzy covariance matrix $\mathbf{F_i}$,[6]

$$\mathbf{A_i} = [\rho_i \det(\mathbf{F_i})]^{1/n} \cdot \mathbf{F_i}^{-1}, \tag{3.10a}$$

$$\mathbf{F_i} = \frac{\sum_{j=1}^{N} u_{ij}^m (\mathbf{x_j} - \mathbf{v_i})(\mathbf{x_j} - \mathbf{v_i})^T}{\sum_{j=1}^{N} u_{ij}^m}. \tag{3.10b}$$

Since Gustafson and Kessel proposed the original GK algorithm, some extensions have been proposed, such as the adaptive fuzzy clustering (AFC) algorithm [148] or the GK algorithm with adaptive cluster volumes (GKAρ) [149]. However, since the AFC and GKAρ algorithms were found to produce poor partitions if little is known about the initial determination of the cluster volumes, we used the general GK algorithm with cluster volumes fixed to $\rho_i = 1$ [149]. To improve the numerical performance of the original GK algorithm (to account for the singularity problems

[4]The stacionary points of the FCM functional (3.4) are found with Picard iteration through the first-order conditions by adjoining the constraint (3.5a) to J_m by means of Lagrange multipliers and by setting the gradients of J_m with respect to $\mathbf{U}$, $\mathbf{V}$ and λ to zero [146].

[5]The Gath-Geva algorithm [147] is also a well-known extension of the FCM with adaptive distance measure. Here, the distance norm involves an exponential part and therefore decreases faster than the GK algorithm. However, since it enables the possibility to detect clusters of varying shapes and volumes, it requires good initialization. As the initialization with the FCM algorithm did not produce a proper solution, its performance is not considered in the thesis.

[6]For a feasible solution, matrix $\mathbf{A_i}$ should vary in the optimization process with its determinant fixed (corresponding to the optimization of the cluster shape with a fixed volume ρ_i).

of **F**), we used the algorithm proposed by Babuška *et al.* [150], where two additional parameters (β and γ) are introduced. Parameter β limits the condition number of **F**, and $\gamma \in [0,1]$ is the tuning parameter which constraints the clusters to have a more or less equal shape.

The GK algorithm cannot be used in a fully automatic mode as some preliminary information about the cluster size needs to be given. Kruse *et al.* [146] recommended using the final FCM partition for the initialization of GK partitioning. This was also used in our version of the algorithm.

Noise clustering

The sensitivity of the FCM to outliers can be overcome by using noise clustering [84], where an additional noise cluster is introduced. For the noise centre $\mathbf{v_c}$, the distance of the observation $\mathbf{x_j}$ to $\mathbf{v_c}$ is $d_{cj} = \delta$ for each observation. Therefore, the distances in Eq. (3.4) and (3.9a) should be replaced according to

$$d_{ij} = \|\mathbf{x_j} - \mathbf{v_i}\| \quad \text{for} \quad 1 \leq j \leq N,\, 1 \leq i \leq c-1, \tag{3.11a}$$

$$d_{ij} = \delta \quad \text{for} \quad 1 \leq j \leq N,\, i = c,$$

$$\delta^2 = \lambda \cdot \frac{\sum_{i=1}^{c-1} \sum_{j=1}^{N} d_{ij}^2}{N(c-1)}. \tag{3.11b}$$

For the calculation of δ, parameter λ was estimated by using the standard deviation of the inter-point distances [84]. However, to achieve the best partition, we further multiplied this parameter by factor L, using 1 as the default value (the values taken into account for this parameter will be discussed within the results). Similarly as for the FCM, noise clustering is applicable to the GK or the k-means algorithms.

Possibilistic clustering

Apart from noise clustering described above, fuzzy possibilistic clustering algorithms are able to deal with noisy data. Since they drop the constraint that the memberships of each observation have to sum to 1 over all clusters (see section 3.3.2), memberships should rather be interpreted as the typicality of a data point to a specific cluster [146]. The original possibilistic c-means (PCM) algorithm by Krishnapuram and Keller [151] helps to identify outliers, but at the same time is also sensitive to initialization and very often generates coincident clusters. Therefore, we refer to two modifications of the PCM.

In 1997, Pal *et al.* proposed a mixed c-means approach called the fuzzy-possibilistic c-means (FPCM) algorithm [152]. The model is based on generating both membership and typicality values. Typicalities to a cluster are constrained to sum to 1 over all data points, which however was found to produce unrealistic results for large data sets. To avoid the problems of the FPCM, the same authors proposed a new model, possibilistic-fuzzy c-means (PFCM) [87]. Since NDT data sets are relatively large, only the improved PFCM algorithm will be taken into account,

where the following objective function should be minimized

$$J_{m,\eta}(\mathbf{U},\mathbf{T},\mathbf{V};\mathbf{X},\gamma) = \sum_{i=1}^{c}\sum_{j=1}^{N}\left(a\,u_{ij}^{m} + b\,t_{ij}^{\eta}\right)\cdot d_{ij}^{2} + \sum_{i=1}^{c}\gamma_i\sum_{j=1}^{N}(1-t_{ij})^{\eta}\,, \tag{3.12}$$

where $a > 0$, $b > 0$, $m > 1$ and $\eta > 1$ are user-defined parameters and γ_i should be calculated by [151]

$$\gamma_i = K\cdot\frac{\sum\limits_{j=1}^{N} u_{ij}^{m}\cdot d_{ij}^{2}}{\sum\limits_{j=1}^{N} u_{ij}^{m}}, \quad K > 0. \tag{3.13}$$

To minimize $J_{m,\eta}$, the necessary conditions for memberships u_{ij}, typicalities t_{ij} and cluster centres are

$$u_{ij} = \frac{1}{\sum\limits_{k=1}^{c}\left(d_{ij}/d_{kj}\right)^{2/(m-1)}}, \tag{3.14a}$$

$$t_{ij} = \frac{1}{1+\left(\frac{b}{\gamma_i}\cdot d_{ij}^{2}\right)^{1/(\eta-1)}}, \tag{3.14b}$$

$$\mathbf{v_i} = \frac{\sum\limits_{j=1}^{N}\left(a\,u_{ij}^{m} + b\,t_{ij}^{\eta}\right)\cdot\mathbf{x_j}}{\sum\limits_{j=1}^{N}\left(a\,u_{ij}^{m} + b\,t_{ij}^{\eta}\right)}. \tag{3.14c}$$

In our algorithm we used the final FCM partition for initialization as for the GK. The default parameter values were set to $a = 1$, $b = 1$, $m = 2$ and $\eta = 2$. While optimizing these parameters, m remained fixed to its default value since this was the most suitable choice made by the authors of the FCM.

Besides using the mixed c-means approach, we employed a PCM variant using a repulsion term proposed by Timm *et al.* [86]. The objective function of PCM with repulsion is given by the following equation

$$J_{m}(\mathbf{T},\mathbf{V};\mathbf{X},\gamma,\omega) = \sum_{i=1}^{c}\sum_{j=1}^{N} t_{ij}^{m}\cdot d_{ij}^{2} + \sum_{i=1}^{c}\gamma_i\sum_{j=1}^{N}(1-t_{ij})^{m} + \omega\cdot\sum_{i=1}^{c}\sum_{k=1,k\neq i}^{c}\left(1/d^{2}(\mathbf{v_i},\mathbf{v_k})\right), \tag{3.15}$$

where ω is a user-defined parameter. Here, the necessary conditions are given by

$$t_{ij} = \frac{1}{1 + \left(\frac{1}{\gamma_i} \cdot d_{ij}^2\right)^{1/(m-1)}}, \tag{3.16a}$$

$$\mathbf{v_i} = \frac{\sum_{j=1}^{N} t_{ij} \cdot \mathbf{x_j} - \omega \cdot \sum_{k=1, k\neq i}^{c} \left(\mathbf{v_k}/d^2(\mathbf{v_i}, \mathbf{v_k})\right)}{\sum_{j=1}^{N} t_{ij} - \omega \cdot \sum_{k=1, k\neq i}^{c} \left(1/d^2(\mathbf{v_i}, \mathbf{v_k})\right)}. \tag{3.16b}$$

As for the PFCM, the final FCM partition was used for initialization.

3.3.4 Validity measures

All clustering algorithms described above require the number of clusters c to be determined in advance. The selection of the optimal cluster number, which yields the best partition is a user-defined parameter. However, to perform partitioning without subjective judgement, one can use validity measures to assess the suitability of a partition for a different c, taking into account both compactness and separation between clusters [83]. Compactness should be thought of as a measure of data scattering within a cluster and therefore the optimum c should minimize the compactness, but maximize the separation between clusters [78]. Several quality validity indices have been introduced (see *e.g.* Abonyi and Feil [153]). In our case, we used three of them that account for both compactness and separation of clusters, as well as fuzziness:

1. The **partition index *SC(c)***, describing the ratio of the sum of compactness and separation of the clusters, where normalization is done by the fuzzy cardinality of each cluster N_i [78]:

$$SC(c) = \sum_{i=1}^{c} \frac{\sum_{j=1}^{N} u_{ij}^m \|\mathbf{x_j} - \mathbf{v_i}\|^2}{N_i \sum_{k=1}^{c} \|\mathbf{v_i} - \mathbf{v_k}\|^2}. \tag{3.17}$$

2. The **separation index *S(c)***, which uses the same nominator as SC, but the minimal separation between clusters as the denominator [78]:

$$S(c) = \frac{\sum_{i=1}^{c} \sum_{j=1}^{N} u_{ij}^m \|\mathbf{x_j} - \mathbf{v_i}\|^2}{N \cdot \min_{i,k,i\neq k} \|\mathbf{v_i} - \mathbf{v_k}\|^2}. \tag{3.18}$$

3. **Xie and Beni's index *XB(c)***, which uses the same nominator as the SC and S indices, but the minimal distance of data points to cluster centres as the denominator [154]:

$$XB(c) = \frac{\sum_{i=1}^{c}\sum_{j=1}^{N} u_{ij}^{m}\|\mathbf{x_j} - \mathbf{v_i}\|^2}{N \cdot \min_{i,j}\|\mathbf{x_j} - \mathbf{v_i}\|^2}. \tag{3.19}$$

As fuzzy cardinality normalization of the SC index makes it insensitive to cluster size, the S and XB indices were taken into account when searching for the optimal number of clusters, whereas the SC index was used to estimate the quality of different partitions for a specific number of clusters. A good partition should minimize all three validity indices.

Although the above validity indices have been proposed to automatically define the optimal number of clusters, they are all to some extent affected to monotonicity and can derive conflicting results [144]. In the case of the results of most studied NDT data sets, they did not deliver a proper interpretation of the results. Here, the number of clusters was rather defined according to the suspected severity of the damage and the heterogeneity of the inspected material (refer to the results).

3.3.5 Objective function-based clustering algorithm scheme

A generalized objective function-based clustering algorithm scheme starts with a random grouping of observations into clusters based on the initialized partition matrix (the minimum number of clusters to be chosen is 2 and all have to be non-empty). In the following steps, the observations are moved to the cluster whose centre is closer to them, resulting in a change of the overall association and movement of cluster centres. The iterative computation (update) of the cluster centres and the partition matrix is performed until no further movement occur, *i.e.* when a convergence is reached. Since clustering algorithms converge to a local minima of the functional, the result is dependent on the initial random partition. Thus clustering should be repeated several times.

For the initialization of the partition matrix, a simple approach is a random selection of the cluster centres and the computation of the corresponding partition matrix [145]. This approach was also used in our algorithms. The termination criterion is reached when the norm of the difference between two successive partition matrices $\mathbf{U_{iter+1}}$ and $\mathbf{U_{iter}}$ does not exceed a certain termination tolerance ε. The choice of ε is application oriented and was for our purposes fixed to 10^{-4} [144], whereas the maximum allowed iterations were set to 200. The algorithm scheme for a generalized clustering algorithm (based on the calculation of cluster centres and the partition matrix) is presented in Fig. 3.6.

The version of the FCM and GK algorithms we employed is based on the algorithms proposed by Balasko *et al.* [155], whereas the noise and possibilistic clustering algorithms were written by ourselves. The clustering algorithms as well as the complete data fusion frameworks were implemented in MATLAB R2012a.

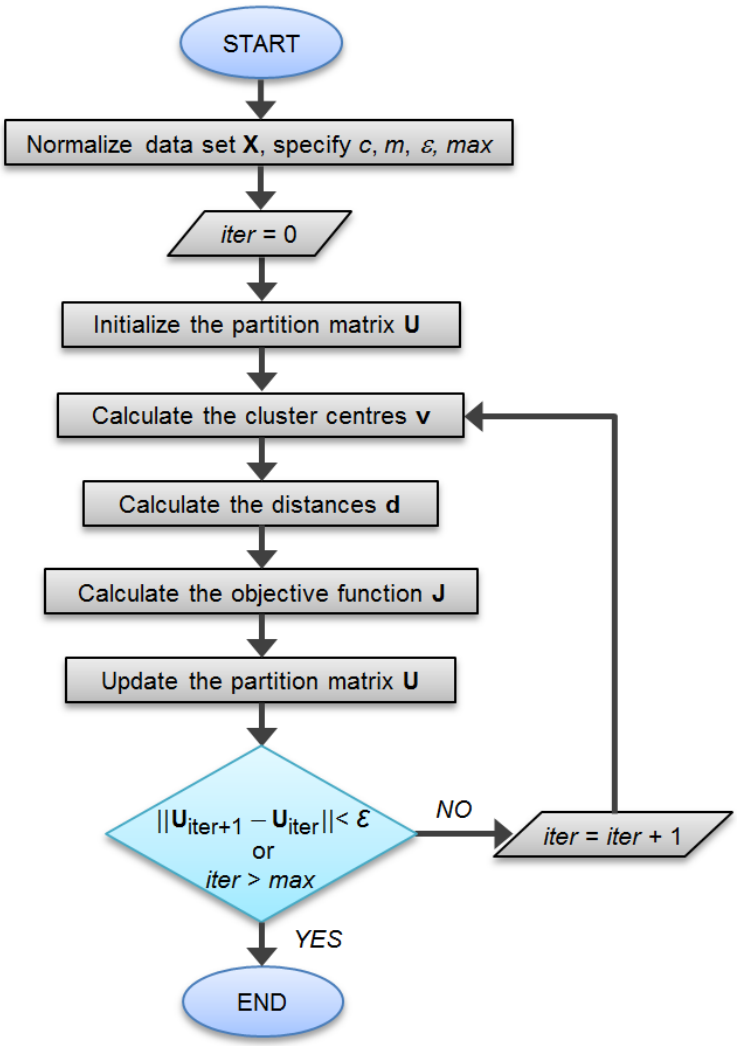

Figure 3.6: Flowchart of a generalized clustering algorithm.
Slika 3.6: *Diagram poteka splošnega algoritma za gručenje podatkov.*

4 NON-DESTRUCTIVE TESTING OF LABORATORY CONCRETE SPECIMENS WITH INBUILT DEFECTS AND INCLUSIONS

In this chapter, a sensitivity evaluation of GPR and IRT is performed based on the results from laboratory concrete specimens. The outcomes of this study served for further symbol level fusion of GPR and IRT data as presented in the article in Appx. A. Although specimen description and methods are given in the corresponding article, they are reviewed herein for better understanding of the presented results. It should be mentioned that for the task of this study, concrete specimens were preferred over masonry since they have a more homogeneous structure, which enables a more controlled study of the effects material properties have on the detection of defects.

As a prerequisite for data fusion of GPR and IRT data along the depth, an analysis of the possibilities of data characterization using IRT was performed. Techniques based on the thermal contrast and PPT as presented in section 2.4.4, were used. Apart from the search for a quantitative depth retrieval, the thermal contrast was used to study the effects of typical defects and inclusions in building structures on the performance of IRT.

4.1 Experimental

4.1.1 Specimen description

For this study, four laboratory concrete specimens were constructed. All have a size of $50 \times 50 \times 15$ cm^3 and were made from the same concrete. Due to their complex internal structure, self-consolidating concrete was used with a maximum aggregate size of 4/8 mm (crushed limestone was used as aggregate). A cement type CEM I 42.5R and a superplastificator Sika Viscocrete 5 NPL were used. As can be seen in Fig. 4.1, all specimens contain inbuilt anomalies varying in material (polystyrene, air and water) and depth below the surface. Defect specifications are given in Table 4.1. The anomalies in specimen S0 served to study the methods' sensitivity with respect to different defects depth. Anomalies in specimens S1, S2 and S3 feature some of the most typical defects and inclusions in building structures, such as localized water and the presence of voids (S1), reinforcement (S2), as well as pipes and delamination (S3). The inbuilt cuboids in specimens S0 and S2 have a size of $8 \times 8 \times 6\,cm^3$, whereas the size of voids in S1 is $8 \times 8\,cm^2$ with varying depth (the voids were from one side open in order to fill them with water). The reinforcement in S2 is of two densities (horizontal distance between bars is 5 and 10 cm, respectively) with a concrete cover of 2.5 cm. The polystyrene plates that simulate delamination in specimen S3 have a thickness of 1 cm (a) and 2 cm (b), and the diameters of the plastic pipes are 1, 1.5 and 2.5 cm (from left to right in Fig. 4.1, S3). All defects in specimen S3 have a concrete cover of 1.5–2 cm.

It is worth mentioning that artificial voids of various shapes and sizes particularly serve to study honeycombs in concrete structures, as well as air voids in masonry structures. Honeycombs are quite common in practice, but are very difficult to create in a laboratory during casting the concrete. Therefore, they are often simulated by polystyrene voids or rubber balls [8].

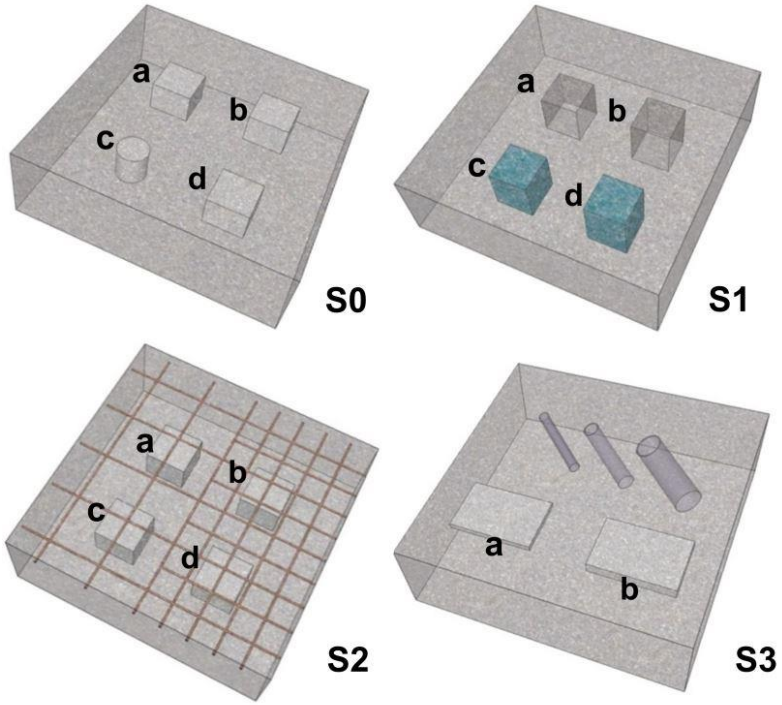

Figure 4.1: Sketches of laboratory concrete test specimens with inbuilt defects.
Slika 4.1: *Skice laboratorijskih betonskih preizkušancev z vgrajenimi anomalijami.*

Table 4.1: Material and concrete cover of inbuilt defects in specimens S0–S3.
Preglednica 4.1: *Material in krovni sloj betona vgrajenih anomalij v preizkušancih S0–S3.*

Defect	Defect material	Concrete cover (cm)
S0 a	polystyrene	3/6
S0 b	polystyrene	1.5/7.5
S0 c,d	polystyrene	4.5
S1 a	air	6
S1 b	air	3
S1 c	water	6
S1 d	water	3
S2 a,b	polystyrene	6.6
S2 c,d	polystyrene	4.6
S3 a,b	polystyrene	1.5–2
S3 pipes	plastic	1.5–2

4.1.2 Methods

For IRT, two IR heaters (1.2 kW each) were used for heating the specimens surface at a distance of 45 cm. Within the optimization of the heating time, the specimens were heated for 5, 15, 30 and 45 min.

Thermographic data was acquired with a FLIR A320 IR camera (Fig. 4.2) (for camera specifications, see [156]). The camera detects IR radiation in a spectral range of 7.5–13 μm with a bolometer-type focal plane array having a resolution of 320×240 pixels and a thermal sensitivity

of 50 mK (at 30 °C). Data can be acquired at a frequency of 30 Hz.

The cooling down behaviour was monitored for 45 min (for the PPT technique, 150 min as a longer observation time is required to obtain a smaller frequency increment in FT – see section 2.4.4). At a frequency of 30 Hz such long observation time would produce a data file of some 10 GB. Thus, the frequency of image registration was reduced to 0.2 Hz, which gave a data file of approximately 1 GB. For controlling the camera and for setting the parameter values of a thermographic measurement, FLIR ResearchIR Max 3.2 was used. Data processing was further performed with Matlab R2012a.

Figure 4.2: The IR camera FLIR A320 used for the thermographic measurements.
Slika 4.2: *Termokamera FLIR A320, ki smo jo uporabili pri raziskavah.*

The GPR data was obtained with the equipment from MALÅ Geoscience, using a 1.6 GHz monostatic shielded antenna (Fig. 4.3). A calibrated survey wheel was used and radargrams were collected in both directions with a line spacing of 5 cm and a point distance of 0.5 cm.

Figure 4.3: The radar system used for the GPR measurements.
Slika 4.3: *Georadarski sistem MALÅ Geoscience, ki smo ga uporabili pri raziskavah.*

The GPR data was collected in forms of a 3D data set. Data processing was performed with the Reflexw commercial software, Ver. 6.0.5 [157]. First, a proper profile coordinate assignment was determined. Next, header gain removal, DC-shift and static correction (correction of the maximal phase and start time movement) were applied. As the detection of very shallow defects was of interest, the true zero position of A-scans was determined carefully. Based on the results from many previous test measurements, the 1st minimum was selected as the true zero position. A detailed description on the selection of the true zero position can be found in [158].

4.2 Results

4.2.1 Characterization of defects and inclusions using infrared thermography

The surface temperature distribution of specimen S0 immediately after heating, as well as after 15, 30 and 45 min of cooling is presented in Fig. 4.4. It can be seen that the time of defect detection is directly related to defects depth. The shallowest defects a and b (at a depth of 1.5 cm and 3 cm) appear immediately after heating, whereas the more deeper defects c and d (at a depth of 4.5 cm) appear after 15 min of cooling.

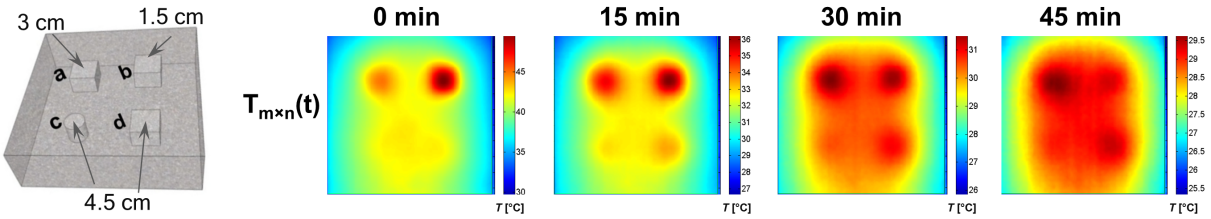

Figure 4.4: Thermograms of specimen S0 at different cooling down times. Each image has a different colour scaling.
Slika 4.4: *Termogrami za preizkušanec S0 pri različnih časih ohlajanja. Vsaka slika ima svojo temperaturno skalo.*

4.2.1.1 Thermal contrast

The time dependent thermal contrast $C(t)$ is for the S0 defects at different depths presented in Fig. 4.5 after 30 min of heating. It can be seen that with increasing defects depth, the thermal contrast decreases, whereas the time of the maximal thermal contrast t_{Cmax} increases. Moreover, from the graph it is evident that defects up till a depth of 6 cm could be detected (the defect at a depth of 7.5 cm has a negative C_{max} and thus was not detected).

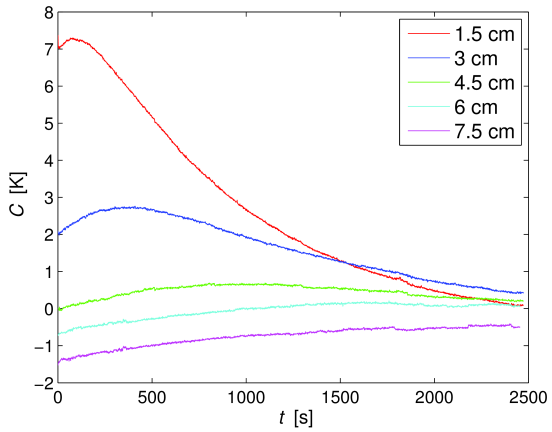

Figure 4.5: The time dependent thermal contrast $C(t)$ for defects in specimen S0 after 30 min of heating.
Slika 4.5: *Potek časovno odvisnega temperaturnega kontrasta $C(t)$ za različno globoke anomalije v preizkušancu S0 po 30 min segrevanju.*

Besides defects, localized water or higher moisture content as well as reinforcement may be present in building structures, which could affect the detection of defects with an IR camera.

Therefore, for specimens S1 and S2 the effect of both localized water and reinforcement of two densities was analysed. In Fig. 4.6a it can be seen that for a water anomaly, the thermal contrast represents only half of the thermal contrast obtained for the air defect. Hence, the detection of water is greatly reduced compared to air, whereas on the other hand, the change in t_{Cmax} between water and air is negligible. The latter is in accordance with Eq. (2.34a), $z \propto \sqrt{\alpha \cdot t_{Cmax}}$, which relates t_{Cmax} for a given defect depth only to the thermal diffusivity of a sound area, here concrete. However, the observed dependence of C_{max} on the thermal properties of defects is contrary to Eq. (2.34b), $z \propto \sqrt[3]{1/C_{max}}$. Nevertheless, a decrease in C_{max} could be explained by higher thermal conductivity of water compared to air, and thus by a smaller difference in thermal conductivity between the defect and sound area (thermal conductivity of air is 0.026 W/m K, of water 0.6 W/m K and of concrete 2.1 W/m K). Similar conclusions can be made for results in Fig. 4.6b. Here, it is evident that reinforcement with a horizontal distance of 10 cm between bars affects the detection of a polystyrene defect at a depth of 4.6 cm only slightly. However, the thermal contrast is reduced by approximately 30 % when a dense reinforcement with a horizontal distance of 5 cm between bars is present. The reduction in thermal contrast when reinforcement is present is in accordance with higher thermal conduction of iron compared to concrete.

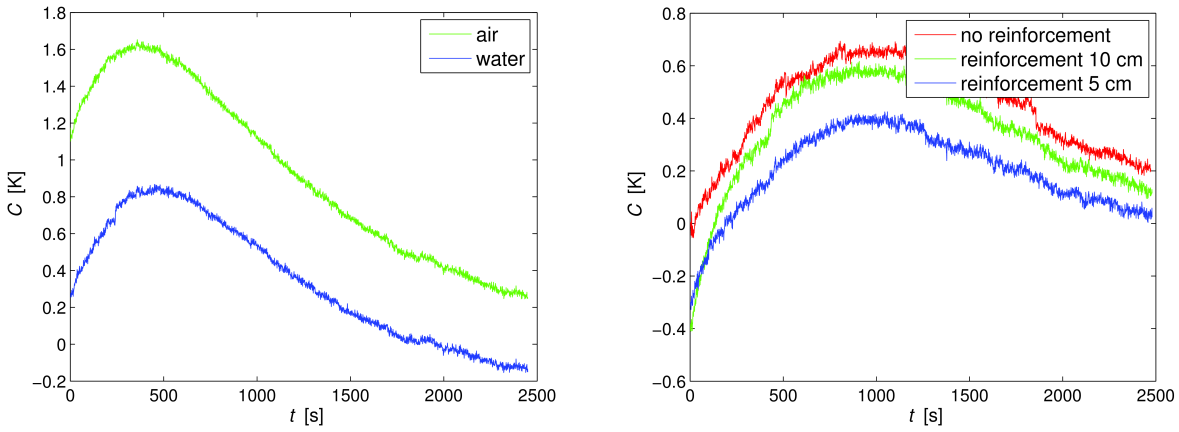

(a) **(b)**

Figure 4.6: The time dependent thermal contrast $C(t)$ for defects in specimens S1 and S2 after 30 min of heating: (a) for a water and an air defect at a depth of 3 cm, and (b) for a polystyrene defect at a depth of 4.6 cm with present reinforcement of two densities (5 and 10 cm).
Slika 4.6: *Potek časovno odvisnega temperaturnega kontrasta $C(t)$ za anomalije v preizkušancih S1 in S2 po 30 min segrevanju: (a) za vodno in zračno anomalijo na globini 3 cm ter (b) za anomalijo iz stiropora na globini 4,6 cm in ob prisotni armaturi rastra 5 oz. 10 cm.*

The above results indicate that the thermal contrast may be greatly affected by the type of anomaly, whereas t_{Cmax} is mostly affected by the depth of defects. Thus, the interpretation of both C_{max} and t_{Cmax} could qualitatively characterize the defect, *i.e.* determine the material properties of the defects as well as their depths. This can be achieved by contrast images and timegrams introduced in section 2.4.4.1. Here, each pixel of the image is associated with the value of C_{max} and t_{Cmax}, respectively. Contrast images and timegrams of all specimens are shown in Fig. 4.7–4.10. From the timegram in Fig. 4.7b it is clear that the defects in S0 appear at different depths, whereas the defects in the timegrams in Fig. 4.8 and 4.9 relate to the same depth. Here, contrast images reveal different material properties of the defects. In addition,

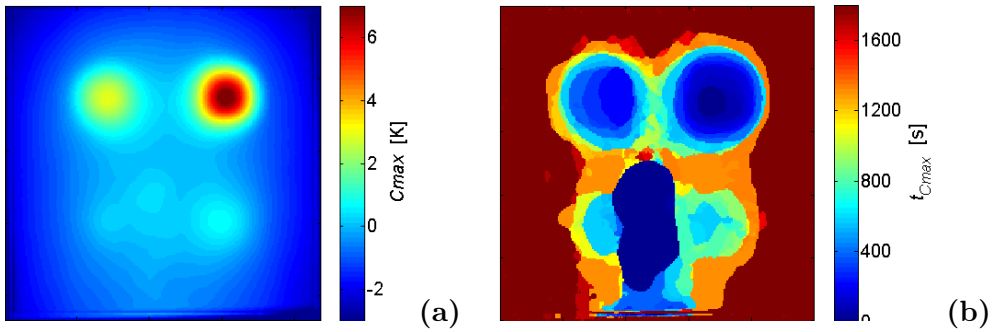

Figure 4.7: (a) A contrast image and (b) a timegram of specimen S0 after 30 min of heating.
Slika 4.7: *(a) Kontrastna slika in (b) časovna slika za preizkušanec S0 po 30 min segrevanju.*

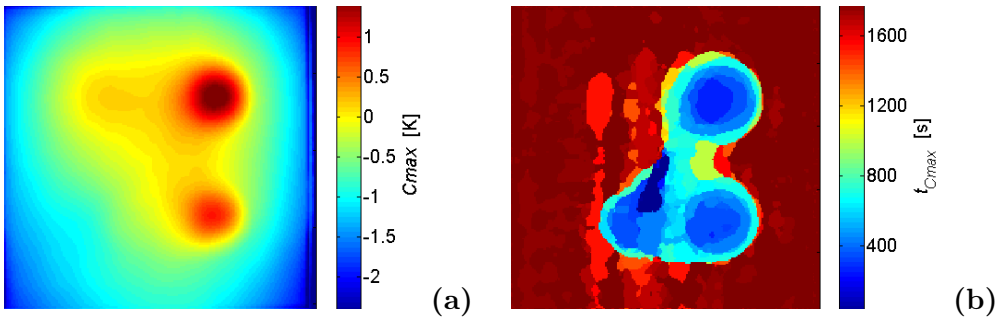

Figure 4.8: (a) A contrast image and (b) a timegram of specimen S1 after 30 min of heating.
Slika 4.8: *(a) Kontrastna slika in (b) časovna slika za preizkušanec S1 po 30 min segrevanju.*

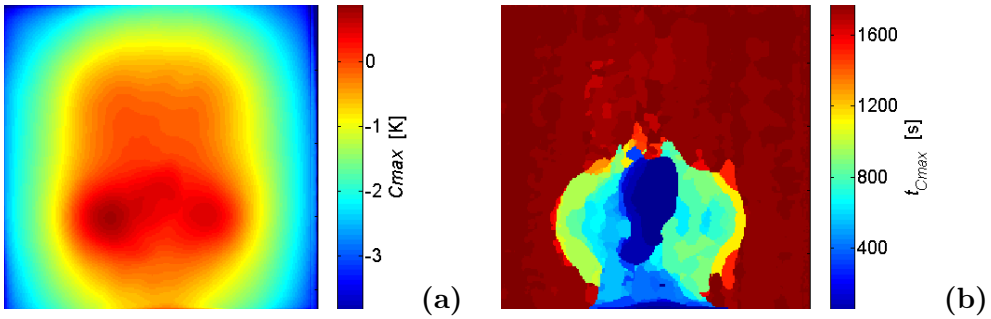

Figure 4.9: (a) A contrast image and (b) a timegram of specimen S2 after 30 min of heating.
Slika 4.9: *(a) Kontrastna slika in (b) časovna slika za preizkušanec S2 po 30 min segrevanju.*

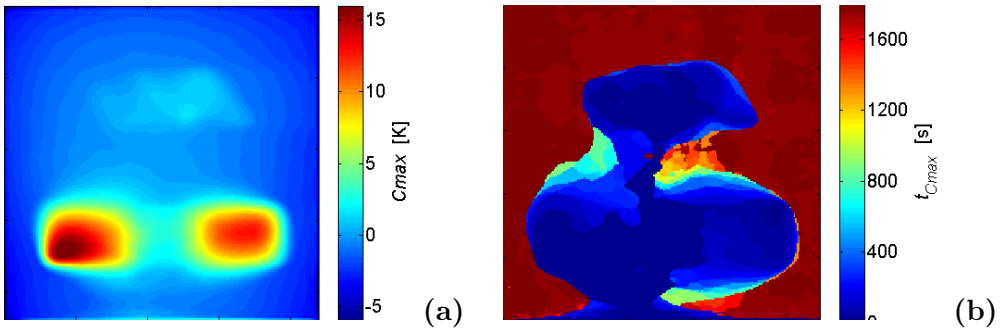

Figure 4.10: (a) A contrast image and (b) a timegram of specimen S3 after 30 min of heating.
Slika 4.10: *(a) Kontrastna slika in (b) časovna slika za preizkušanec S3 po 30 min segrevanju.*

the contrast image in Fig. 4.8a slightly detects even the air defect at a depth of 6 cm (top left defect), which could not be observed in the thermograms. However, the greatest advantage of

this data processing technique is that a qualitative characterization of defects may be performed with only two images, rather than with the whole sequence of thermograms. Therefore, data evaluation is greatly simplified and the time needed for data analysis can be reduced. Both is of high importance for the application of thermography in practice.

Regardless of the specimen and defects inspected, the detection of defects is also dependent on the heating time. The results of C_{max} and t_{Cmax} with respect to defect depths and different heating times are presented in Fig. 4.11. It can be seen that for all defects, the optimal heating time is 30 min, since it yields the highest thermal contrast and the deepest penetration (up till 6 cm). It is interesting to notice that both shorter (15 min) and longer (45 min) heating times gave smaller thermal contrast and penetration (up till 4.5 cm). These results are not in accordance with the results from concrete specimens as reported in [41], where defects at a depth of more than 4 cm were taken into account. Here, higher thermal contrast was obtained by increasing the heating time. An explanation for lower values of C_{max} at 45 min of heating time could be that above the more shallow defects, more heat started to accumulate also in the surrounding. This could reflect in the changed behaviour of the reference profile.

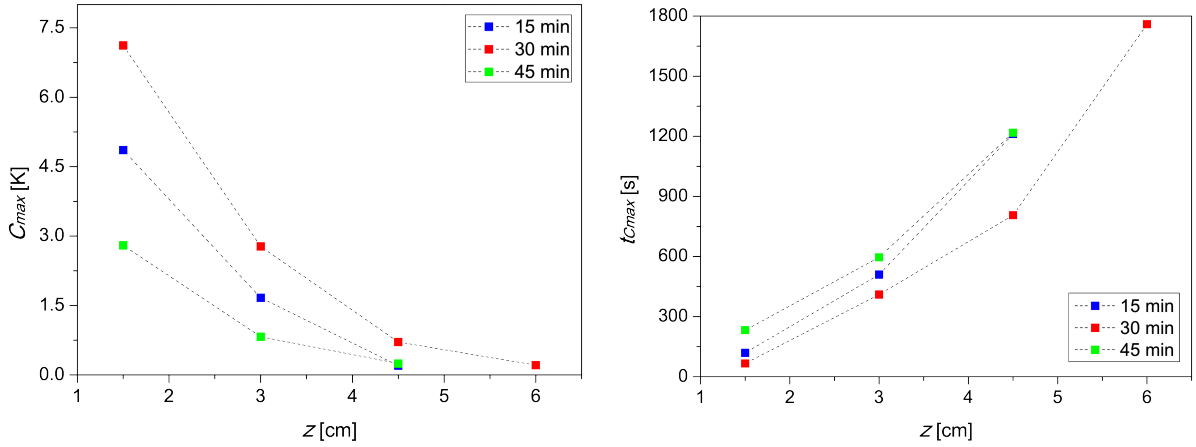

Figure 4.11: Dependence of (a) the maximal thermal contrast C_{max} and (b) its corresponding time t_{Cmax} on the depth of defects for different heating times (15, 30 and 45 min). The dotted lines are guides to the eye.
Slika 4.11: *Odvisnost (a) maksimalnega temperaturnega kontrasta C_{max} in (b) časa njegovega nastopa t_{Cmax} od globine anomalije za različne čase gretja (15, 30 in 45 min). Črta le povezuje merske točke za lažje spremljanje rezultatov.*

As can be seen in Fig. 4.11, C_{max} and t_{Cmax} exhibit a particular dependence on the depth of defects. This was tried to be modelled by Eq. (2.36) proposed by Balageas *et al.* from the testing of carbon-epoxy composites. The fitting results for the optimal heating time of 30 min are presented in Fig. 4.12. It is evident that the model cannot properly describe the dependence of C_{max} and t_{Cmax} on the depth of defects (the coefficient of determination is $R^2 = 0.25$). For this, several explanations are possible. The heating time was much longer compared to the heating times used for the inspection of composite structures. Therefore, the temperature increased inside the specimen already during heating. Moreover, in our experiment, different boundary conditions were present (convective and radiating losses occurred only at three edges of the specimen), which could particularly affect the surface temperature evolution of the areas

above defects. In addition, non-ideal heating, as well as inaccurate estimation of C_{max} and t_{Cmax} at larger depths (see Fig. 4.5), could contribute. It is worth mentioning that also slight tilting of the defects during concreting could occur, which reflects in a small deviation of defect depths from the reference given in Table 4.1. However, the problem of fitting experimental values to this model was also stressed by Maldague [104] for the results obtained on metal and composite structures. As a more accurate parameter than t_{Cmax}, Maldague suggests using $t_{C1/2max}$, when half of C_{max} is obtained. Moreover, the use of the inverse technique based on a numeric model is recommended. However, particularly for CE structures, the latter concept could be hardly brought into practice. In most cases, thermographic measurements are not performed under well-defined conditions. The heating process can hardly be modelled properly and the thermal properties of structures may differ to a large extent. Moreover, regardless of the data analysis technique used, the poor depth penetration of the thermal contrast remains. Therefore, the use of PPT, which was found a powerful technique both in aerospace applications [128] as well as in CE [130], was examined.

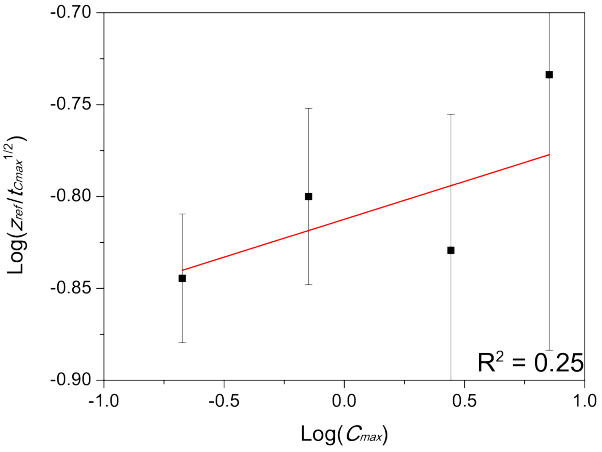

Figure 4.12: The fitting result for C_{max} and t_{Cmax} using the model proposed by Balageas *et al.* (2.36). Experimental results for defects in specimen S0 obtained at a heating time of 30 min were used.
Slika 4.12: *Rezultat prilagajanja eksperimentalnih podatkov za C_{max} in t_{Cmax} z modelom po enačbi* (2.36). *Vključeni so rezultati za anomalije v preizkušancu S0 za čas gretja 30 min.*

4.2.1.2 Pulsed phase thermography

When using PPT, amplitudes and phases are obtained from the thermogram sequence, as explained in section 2.4.4.2. The phase contrast $\Delta\phi$ of the area above defects at a depth of 1.5 cm and 3 cm in specimen S0 is presented in Fig. 4.13. It can be seen that for deeper defects, the maximal phase contrast appears at smaller frequencies f_{ch}, which is in accordance with the definition of the thermal diffusion length μ and the phase of thermal waves as given by Eq. (2.42a) and (2.42b). Similar behaviour was already observed by Castanedo when testing a carbon fibre reinforced plastic (CFRP) specimen [128] and by Arndt when testing concrete specimens [129, 130]. The results of f_{ch} for all defects in specimen S0 are given in Table 4.2. It should be noted that for a better estimation of f_{ch}, zero-padding [122] up till 2^{13} points was used before applying FFT. For zero-padding, the last recorded temperature of each pixel was used. Although relatively many "artificial" points were added to the thermogram sequence, this only slightly affected the outcome of FFT as the surface temperature was almost stabilized after 150 min of monitored

cooling. On the other hand, a much smaller frequency increment of $\Delta f = 2.4 \cdot 10^{-5}$ Hz could be obtained.

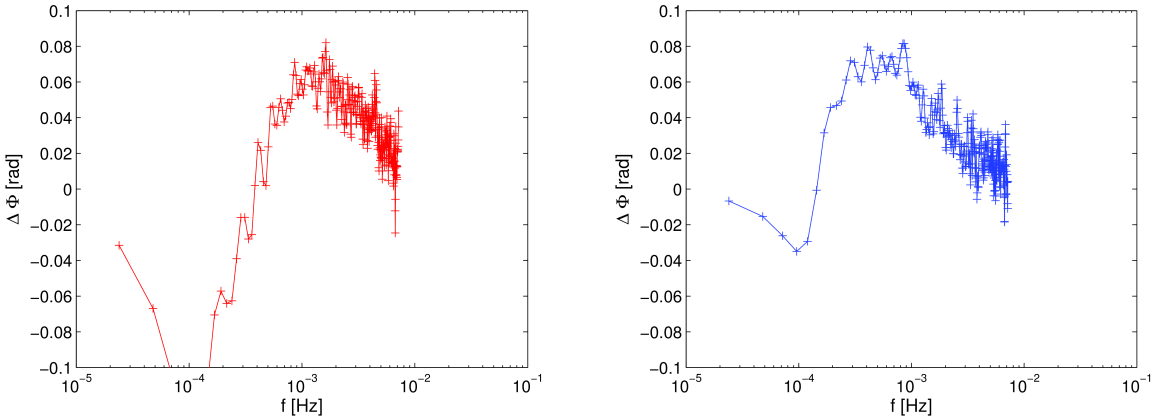

Figure 4.13: The frequency dependent phase contrast $\Delta\phi$ for (a) the defect at a depth of 1.5 cm and (b) the defect at a depth of 3 cm in specimen S0 after 45 min of heating and 150 min of cooling.
Slika 4.13: *Potek frekvenčno odvisnega faznega kontrasta $\Delta\phi$ za (a) anomalijo na globini 1,5 cm in (b) za anomalijo na globini 3 cm v preizkušancu S0 po 45 min segrevanju in merjenju ohlajanja za 150 min.*

Table 4.2: The frequency of the maximal phase contrast f_{ch} for defects in specimen S0.
Preglednica 4.2: *Frekvenca pri maksimalnem faznem kontrastu f_{ch} za anomalije v preizkušancu S0.*

z_{ref} (± 0.5 cm)	f_{ch} (Hz)
1.5	$1.60 \cdot 10^{-3}$
3	$4.3 \cdot 10^{-4}$
4.5	$1.9 \cdot 10^{-4}$
6	$1.4 \cdot 10^{-4}$
7.5	$1.0 \cdot 10^{-4}$

Fig. 4.14 presents the results obtained when fitting experimental data for f_{ch} in Table 4.2 to Eq. (2.44). It can be seen that the data fits the model with high accuracy (the coefficient of determination is $R^2 = 0.99$). Here, the value of the correlation factor k_c from Eq. (2.44) is $k_c = 1.11$. According to Arndt [129], this parameter is only slightly dependent on the heating time and in addition, for a rough estimate of the defect depths, $k_c = 1$ is a good approximation. Moreover, as can be seen in Fig. 4.14, even the deepest defect (at a depth of 7.5 cm) can be observed using PPT. The fact that Eq. (2.44) can properly describe the dependence of f_{ch} on defect depths and that $k_c = 1$ is a good approximation makes it possible to consider phase images at given frequencies as depth slices. This concept was used for the fusion of GPR and IR phase images as described in the article given in Appx. A.

At this point it is also worth mentioning the good performance of phase images or rather phase contrast images, which were used in the data fusion process. Here, each pixel is associated with the value of the maximal phase contrast, similarly as contrast images refer to the values of the maximal thermal contrast. In Fig. 4.15, the thermogram obtained directly after heating (a), the contrast image (b) and the phase contrast image at a frequency of $3.7 \cdot 10^{-3}$ Hz (c) are presented

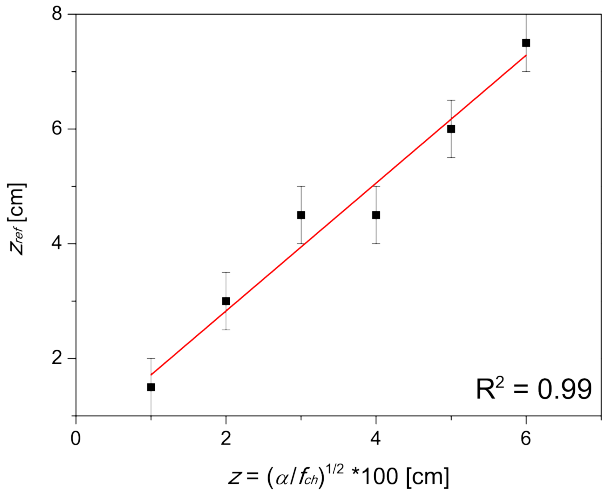

Figure 4.14: The fitting result for f_{ch} using the model proposed by Arndt *et al.* (2.44). Experimental results for defects in specimen S0, obtained after 45 min of heating and 150 min of cooling, were used.
Slika 4.14: *Rezultat prilagajanja eksperimentalnih podatkov za f_{ch} z modelom po enačbi* (2.44). *Vključeni so rezultati za anomalije v preizkušancu S0, dobljeni po 45 min segrevanju in merjenju ohlajanja za 150 min.*

for specimen S3. Here, all defects appear at a depth of 1.5–2 cm. It can be seen that the signal-to-noise ratio of the thermogram is too low to detect the plastic pipes. However, the thermogram reveals that part of specimen surface above the polystyrene plates is warmer, which could be referred to as a slight tilting of plates during concreting. On the other hand, the contrast image has higher signal-to-noise ratio than the thermogram, but exhibits poorer spatial resolution since it does not detect the tilted plates. The phase contrast image exhibits both high signal-to-noise ratio as well as extremely good spatial resolution. Both the plastic pipes and tilted plates can be visualized well.

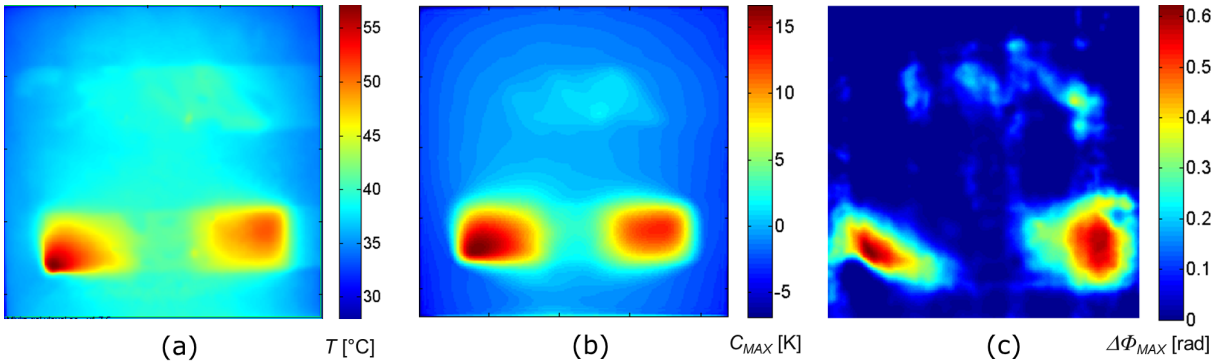

Figure 4.15: IR images obtained for specimen S3: (a) the thermogram obtained directly after heating, (b) the contrast image and (c) the phase contrast image at a frequency of $3.7 \cdot 10^{-3}$ Hz.
Slika 4.15: *IR slike za preizkušanec S3: (a) termogram ob začetku snemanja, (b) kontrastna slika in (c) fazno-kontrastna slika pri frekvenci* $3,7 \cdot 10^{-3}$ *Hz.*

The good performance of phase contrast images can also be seen in Fig. 4.16 for specimen S1 (a) and S2 (b). The images also show that the frequency f_{ch} is independent (or only slightly dependent) on the thermal properties of defects since both air- and water defects can be observed at the same frequency (Fig. 4.16a). This is in accordance with Eq. (2.44) and (2.34a), relating f_{ch} and t_{Cmax} only to the defect depths. Moreover, it is evident that the water defect reduces the

phase contrast compared to air, and the same is true for the detection of the defect below dense reinforcement. Hence, similar as the thermal contrast, the phase contrast shows dependence on the thermal conductivity of defects. This is also in accordance with Eq. (2.42b), relating the phase to thermal conductivity.

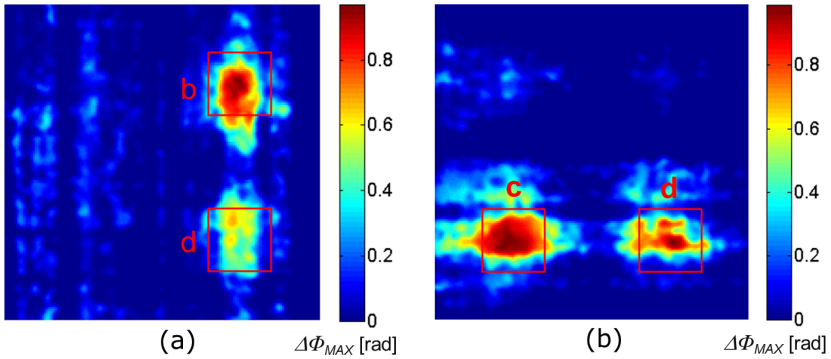

Figure 4.16: The phase contrast images at (a) a frequency of $6.2 \cdot 10^{-4}$ Hz for specimen S1 and (b) at a frequency of $3.0 \cdot 10^{-4}$ Hz for specimen S2. In Fig. 4.16a, the upper defect refers to air (b), the lower to water (d). In Fig. 4.16b, the right part of the image refers to the part of the specimen with dense reinforcement. The red squares mark the defects position, labelled according to Table 4.1.
Slika 4.16: *Fazno-kontrastna slika pri (a) frekvenci* $6,2 \cdot 10^{-4}$ *Hz za preizkušanec S1 in pri (b) frekvenci* $3,0 \cdot 10^{-4}$ *Hz za preizkušanec S2. Na sliki 4.16a je zračna anomalija zgoraj (b), vodna anomalija pa spodaj (d). Na sliki 4.16b je gostejša armatura na desni strani. Rdeči kvadrati označujejo območje anomalij (za oznake anomalij glej preglednico 4.1).*

4.2.1.3 Numerical simulation

The conclusions drawn from the analysis of experimental data using the thermal contrast and PPT were further evaluated using numerical modelling. The work was performed with the help of Dr. Dejan Kolarič (UL FGG) using Mathematica. In particular, a 2D model was analysed (Fig. 4.17), simulating two cross-sections of a concrete specimen measuring $50 \times 50 \times 15\,\mathrm{cm}^3$ with inbuilt polystyrene defects. However, note that the arrangement of defects is not the same as in specimen S0. Here, defects appear at depths 1.5, 3.5, 6 and 7.5 cm.

Modelling specifications

For the simulation, finite differences were used and the second order Crank-Nicolson method with uniform partition in space and time. The space increment (the difference between two consecutive space points) along the x-axis was $\Delta x = 0.9375\,\mathrm{mm}$ and along the y-axis $\Delta y = 1.6892\,\mathrm{mm}$, whereas the time increment was set to $\Delta t = 0.5\,\mathrm{s}$.

Apart from heat conduction governed by Eq. (2.32), radiation (2.26) and convection (2.29) losses were taken into account at all edges. For the average convective heat transfer coefficient $\bar{h} = 10\,\mathrm{W/m^2\,K}$ was used and the surface emissivity was set to 0.91 (for concrete). A heat flux density of $j = 600\,\mathrm{W/m^2}$ on the specimen surface was determined based on experimental results. The temperature of the surrounding was set to 293.15 K. For concrete, a thermal diffusivity of $\alpha = 8.86 \cdot 10^{-7}\,\mathrm{m^2/s}$ ($\rho_m = 2371\,\mathrm{kg/m^3}$, $c_p = 1000\,\mathrm{J/kg\,K}$, $k = 2.1\,\mathrm{W/m\,K}$) was used, whereas for polystyrene $\alpha = 1.0 \cdot 10^{-6}\,\mathrm{m^2/s}$ ($\rho_m = 25\,\mathrm{kg/m^3}$, $c_p = 1400\,\mathrm{J/kg\,K}$, $k = 0.035\,\mathrm{W/m\,K}$) was used. The heating time was set to 30 min, whereas the cooling down was monitored for 120 min.

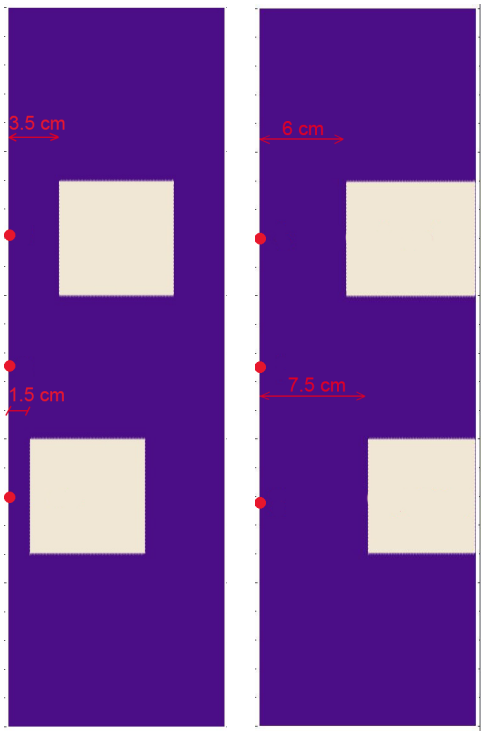

Figure 4.17: A 2D numerical model simulating two cross-sections of a concrete specimen with inbuilt polystyrene defects (white colour). The points on the surface where temperature was monitored are marked with red dots.
Slika 4.17: *2D numerični model, ki ponazarja dva prereza betonskega preizkušanca z vgrajenimi anomalijami iz stiropora (belo območje). Točke na sprednji strani modela, kjer smo spremljali temperaturo, so označene z rdečimi pikami.*

Modelling results

During the simulation, the temperature evolution was monitored at selected points on the surface of the model (marked with red dots in Fig. 4.17). Surface points above defect areas, as well as reference surface points were taken into account. The simulated data were evaluated using the thermal contrast and the PPT technique in the same way as for the evaluation of the results of the experiment (see the preceding sections). The results for C_{max}, t_{Cmax} and f_{ch} are summarized in Table 4.3. It can be seen that all results obtained from simulation match the experimental values very well (compare to Fig. 4.11 and Table 4.2). However, the simulation yields slightly higher values of the thermal contrast and as a result, enables the detection of the deepest defect. This could mostly be related to inaccurate modelling of the material as well as of the heating process. Moreover, the neglect of additional effects present in the experiment could have a contribution. However, since the simulation yields also smaller values of t_{Cmax}, the sound material (concrete), was probably modelled with higher thermal conductivity than the thermal conductivity of the investigated specimens. The fact that an increase in thermal conductivity of the sound material results in a smaller t_{Cmax} is in accordance with Eq. (2.34a), where $z \propto \sqrt{\alpha \cdot t_{Cmax}}$. Since the thermal front propagates faster, it reaches the defect earlier. This dependence of t_{Cmax} on the thermal conductivity of concrete was also noticed by Maierhofer *et al.* [45]. The discrepancy in the thermal conductivity of the modelled concrete compared to the concrete of the measured specimens is also in accordance with the higher values of f_{ch} obtained

Table 4.3: The simulation results of C_{max}, t_{Cmax} and f_{ch} for defects at depths of 1.5, 3.5, 6 and 7.5 cm (see Fig. 4.17).
Preglednica 4.3: *Rezultat simulacije za C_{max}, t_{Cmax} in f_{ch} za anomalije na globinah 1,5, 3,5, 6 in 7,5 cm (glej sliko 4.17).*

z_{ref} (cm)	C_{max} (K)	t_{Cmax} (s)	f_{ch} (Hz)
1.5	9.28	40	$1.74 \cdot 10^{-3}$
3.5	2.21	430	$4.6 \cdot 10^{-4}$
6	0.65	1220	$1.7 \cdot 10^{-4}$
7.5	0.12	1550	$1.5 \cdot 10^{-4}$

during simulation. According to Eq. (2.44), where $z \propto \sqrt{\alpha / f_{ch}}$, higher thermal diffusivity (and thus thermal conductivity) results in a higher f_{ch} for a given depth.

The time dependent thermal contrast $C(t)$ from the simulation is presented in Fig. 4.18a for all defects. Compared to the evolution of the thermal contrast for defects in specimen S0, the simulated thermal contrast exhibits faster decrease in time. This could be again attributed to different thermal conductivity of the modelled concrete or, even more likely, to higher thermal conductivity of modelled polystyrene. However, it is not easy to derive certain conclusions, since for the evolution of the thermal contrast in time, also material density and specific heat (or rather thermal diffusivity) play an important role. The frequency evolution of the simulated phase contrast in Fig. 4.18b resembles the one obtained from the experimental data (Fig. 4.13). The simulated results additionally reveal that contrary to the maximal thermal contrast, the maximal phase contrast decreases only slightly with increasing defect depth. This contributes to deeper penetration of phase images.

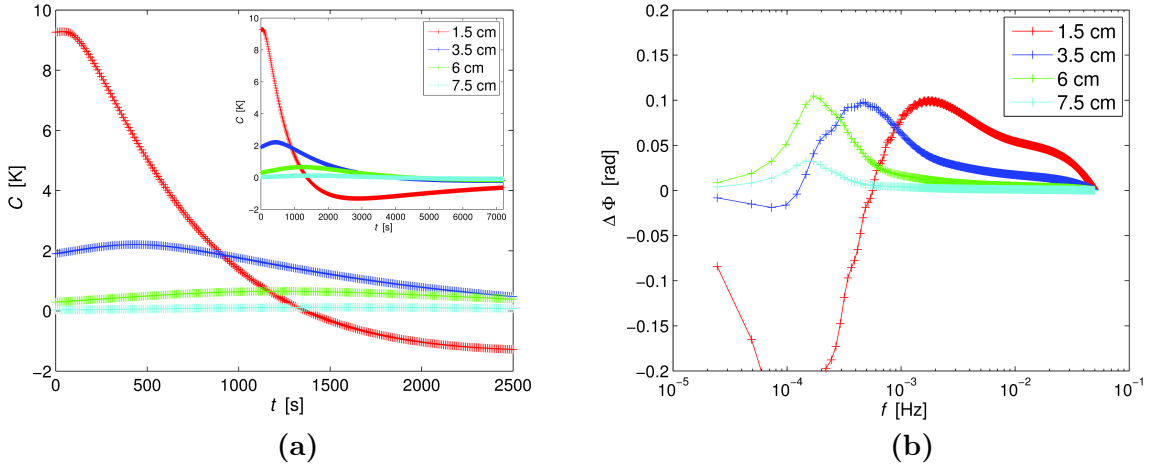

Figure 4.18: (a) The time dependent thermal contrast $C(t)$ and (b) the frequency dependent phase contrast $\Delta\phi$ for defects at depths of 1.5, 3.5, 6 and 7.5 cm after 30 min of simulated heating and 120 min of simulated cooling. The inset in Fig. 4.18a presents the time evolution of thermal contrast for the whole cooling period of 120 min.
Slika 4.18: *(a) Potek časovno odvisnega temperaturnega kontrasta $C(t)$ in (b) potek frekvenčno odvisnega faznega kontrasta $\Delta\phi$ za anomalije na globinah 1,5, 3,5, 6 and 7,5 cm po 30 min simuliranem segrevanju in 120 min simuliranem ohlajanju. Vložena slika na sliki 4.18a prikazuje potek temperaturnega kontrasta za čas celotnega ohlajanja (120 min).*

Finally, the simulated data was fitted to the models given by Eq. (2.36) and (2.44). The results presented in Fig. 4.19 confirm the outcome of the measurements. Therefore, we propose that a longer heating time, compared to the heating times used for the inspection of composite structures, has the largest contribution to the deviation of C_{max} and t_{Cmax} from the model proposed by Balageas *et al.*

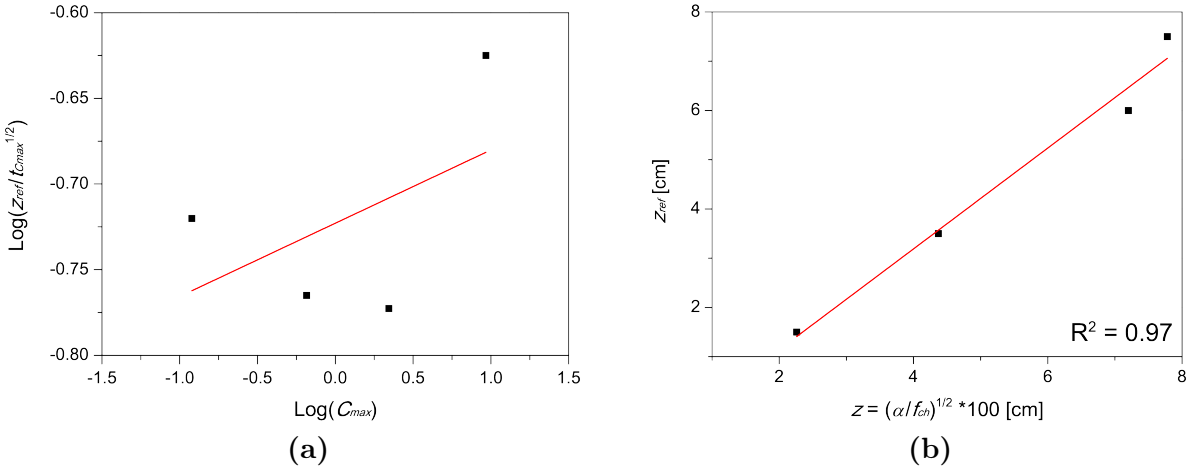

Figure 4.19: (a) The fitting results for C_{max} and t_{Cmax} using the model proposed by Balageas *et al.* (2.36) and (b) the fitting results for f_{ch} using the model proposed by Arndt *et al.* (2.44).
Slika 4.19: *(a) Rezultat prilagajanja podatkov za* C_{max} *in* t_{Cmax} *z modelom po enačbi* (2.36) *in (b) rezultat prilagajanja podatkov za* f_{ch} *z modelom po enačbi* (2.44).

The results from both the experiment and the simulation have proven good performance of PPT in defect depth retrieval. In addition, PPT yielded high signal-to-noise ratio and spatial resolution of phase images. However, it should be stressed that this technique requires relatively long monitoring of the cooling behaviour. As an alternative to the required long monitoring, zero-padding can be applied before FFT. This was also used in our study. Nevertheless, the thermal contrast is a useful tool for the thermal analysis when neither quantitative characterization of defects nor high spatial resolution are required.

4.2.2 Sensitivity evaluation of ground penetrating radar and infrared thermography

For the sensitivity evaluation and later data fusion of IRT and GPR, data sets were further normalized. For GPR data, a global normalization was performed according to the maximal amplitude present in the data set. For IRT data, normalized phase contrasts were taken into account. Data alignment was performed and a common spatial reference of 5 mm was established for both data sets.

The performance of both NDT methods with respect to different defect materials and depths was quantitatively evaluated based on a ground truth reference from the known position of inbuilt defects. For the GPR C-scans and IR phase contrast images, sensitivity and specificity values [159] were calculated from the number of true positive (TP), true negative (TN), false

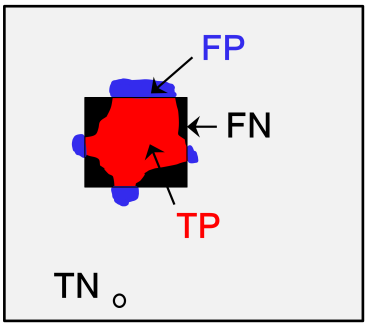

Figure 4.20: A schematic presentation of true positive (TP), true negative (TN), false positive (FP) and false negative (FN) calls for the detection of a defect.
Slika 4.20: *Shematični prikaz kazalcev za vrednotenje zaznavanja anomalij: pravilno pozitivni (TP), pravilno negativni (TN), napačno pozitivni (FP) in napačno negativni (FN).*

positive (FP) and false negative (FN) calls (see Fig. 4.20) by using

$$sens = \frac{TP}{TP + FN}, \tag{4.1a}$$

$$spec = \frac{TN}{TN + FP}, \tag{4.1b}$$

where positive and negative refer to an identified and a rejected defect, respectively. Thus, a true positive call means that a pixel was correctly identified as a defect. A combined sensitivity measure c_sens was further calculated by

$$c\_sens = \frac{a \cdot sens + b \cdot spec}{a + b}, \tag{4.2}$$

where weights a and b refer to the specimen's corresponding defect and non-defect area, respectively. As a prerequisite for the sensitivity calculation, a threshold value was determined for both GPR and IRT data, which defines weather a defect was detected or not (the limit for positive and negative calls). For the threshold value, the mean value of all data values corresponding to the defects area was chosen.

The results from sensitivity calculation are presented in Fig 4.21. The results for polystyrene defects (blue marks) show that the performance of GPR (full marks) is largely decreased at the very near-surface region, where a sensitivity of $c\_sens = 84.5\,\%$ is obtained. However, the sensitivity increases rapidly already at the depth of 3 cm and varies only to a small extent up till the depth of 7.5 cm. The poor performance of GPR very close to the surface is expected due to the antenna coupling/induction effects in the near-surface region. Contrary to GPR, the sensitivity of IRT (empty marks) decreases along the depth. It has to be noted that IRT exhibits such good depth penetration particularly due to the use of phase images. Nevertheless, it is expected that the methods capability would drop remarkably at greater depths.

The results in Fig. 4.21 further show that the performance of IRT is more affected by the material properties of the defects than it is in the case of GPR. This was particularly expressed in the case of a water defect at a depth of 6 cm, where a sensitivity of $c\_sens = 56.7\,\%$ could only be detected for IRT (this value is not presented in Fig. 4.21). On the other hand, GPR

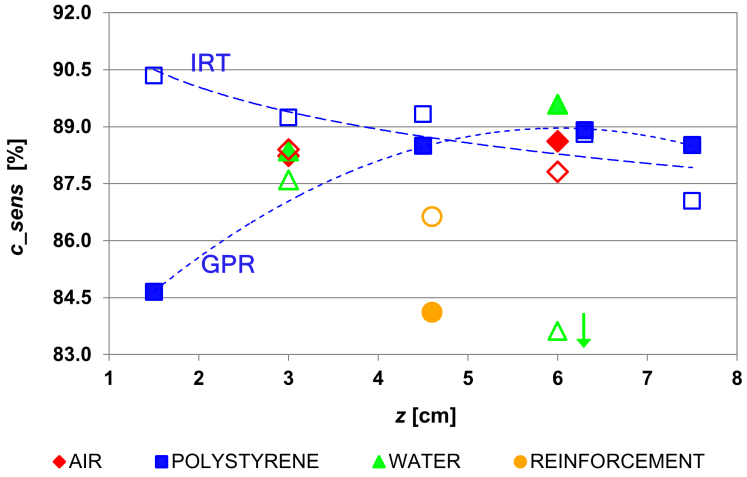

Figure 4.21: The results of sensitivity evaluation in terms of *c_sens* (in %) for GPR (full marks) and IRT (empty marks) with respect to the material and depth of the defects in specimens S0–S2. The dotted lines are guides to the eye.
Slika 4.21: *Rezultat občutljivostne analize za georadar (polni znaki) in IRT (prazni znaki) v odvisnosti od materiala in globine anomalij v preizkušancih S0–S2. Rezultati so podani v % parametra c_sens. Pikčasti črti povezujeta merske točke za lažje spremljanje rezultatov.*

responded to the detection of water defects by increased sensitivity, which is in accordance with the greater difference in the dielectric constant between water and concrete than it is between air and concrete. Moreover, as expected, the detection of defects below dense reinforcement (orange marks) is more reduced in the case of GPR since much of the EM signal is reflected at the reinforcement.

For specimen S3, the GPR depth slice at 1.5 cm and the corresponding IR phase contrast image at a frequency of $3.7 \cdot 10^{-4}$ Hz are shown in Fig 4.22. It can be seen that especially in the region of plastic pipes, GPR exhibits poor contrast. This was further justified by the sensitivity evaluation of the right polystyrene plate (b), which yielded 75.4 % and 90.5 % for GPR and IRT, respectively (the left plate seems to have tilted during concreting and was thus not assessed). By correlating these results with the ones in Fig. 4.21, it can be concluded that the performance of GPR decreases greatly for the detection of near-surface defects.

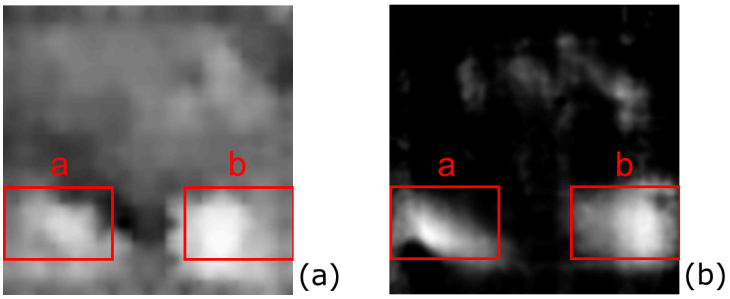

Figure 4.22: The imaging results of specimen S3 with marked polystyrene plates according to Table 4.1: (a) a GPR depth slice at a depth of 1.5 cm and (b) an IR phase contrast image at a frequency of $3.7 \cdot 10^{-4}$ Hz.
Slika 4.22: *Grafični prikaz rezultatov za preizkušanec S3 z označenimi ploščami iz stiropora (preglednica 4.1): (a) georadarski grafični prikaz prereza na globini 1,5 cm in (b) IR fazno-kontrastna slika pri frekvenci* $3,7 \cdot 10^{-4}$ *Hz.*

5 CONCLUSION AND OUTLOOK

The central aim of the thesis was to develop an image fusion methodology based on clustering techniques, which would enable more efficient and reliable evaluation of multi-sensor NDT data in CE applications. The thesis presents the application of clustering techniques for data fusion of multi-sensor NDT of laboratory concrete and masonry specimens, as well as their implementation into two data fusion frameworks for practical application.

Most data fusion applications on metal and composite structures in the aerospace industry deal with methods of validated performance and focus on the detection of well-defined defects such as notches. Hence, the research on data fusion generally confronts the reduction of noise. However, to fully characterize the structure under inspection and increase the accuracy of the evaluation in CE, data fusion has to account for the complementary and overlapping performance of NDT-CE methods. Besides, several not yet standardized applications need to be addressed. The thesis in particular focused on the detection of near-surface defects in concrete and masonry structures using GPR and IRT – an issue that is rarely tackled in NDT-CE. Before data fusion, the methods' performance with respect to various testing problems was validated. In particular, laboratory concrete specimens aimed at studying the effect of different material properties under well-defined conditions.

The sensitivity of GPR and IRT on concrete was evaluated in terms of GPR depth slices and IR phase contrast images, the latter resulting from using the pulsed phase thermography technique, which enables depth characterization of defects. The results show that whilst the sensitivity of GPR increases with increasing depth, for IRT it decreases. However, already at a depth of 3–4.5 cm, GPR reaches the performance which remains constant up till 7.5 cm. This directly reflects that the functioning of GPR is largely affected by the reactive near-field region (for the used antenna, it extends up till a depth of 1 cm [96]), while the close radiating near-field region has a minor effect. IRT has an extremely high probability of defect detection, which decreases only slowly up till 7.5 cm. Its good behaviour in particular resulted from using IR phase contrast images. These exhibited much deeper penetration than thermograms and contrast images and in addition yielded high signal-to-noise ratio as well as extremely good spatial resolution, enabling the detection of thin defects such as pipes. As expected, the detection of defects below dense reinforcement was greatly decreased when GPR was used compared to IRT since much of the EM signal is reflected at the reinforcement. However, it was observed that the contrast in the dielectric constant and thermal conductivity between defects and sound area governs the material characterization of defects. Hence, GPR more accurately detects a water anomaly than an air anomaly, and the opposite is true for IRT.

The well-known position of defects in the concrete specimens enabled a quantitative evaluation of the data fusion results. Here, data fusion was performed on a feature level since a complete visualization of the structure along the depth was of interest rather than only the detection of defects. Fuzzy clustering was employed to derive classifier units in terms of memberships for each pixel, which were later fused using simple weighted averaging. Among the tested fuzzy probabilistic clustering algorithms (FCM, GK, NCFCM), as well as fuzzy possibilistic clustering

algorithms (PFCM, PCM with repulsion), the PCM with repulsion in general produces coincident clusters as the original PCM algorithm, whereas the NCFCM classified signals of very high amplitude (detected defects) as noise. For the hard k-means algorithm it was observed already from the results of the spectroscopic spatial data on concrete that the algorithm is very susceptible to initialization and was therefore not taken into account. In general, the FCM, PFCM and GK algorithms exhibited good functioning, where particularly the performance of PFCM resembled the one of FCM. This suggests that noise could have a minor effect on the resulting partition in the case of inspection of most typical defects in concrete structures, which is contrary to the inspection of structures in the aerospace industry [67, 69, 65]. However, among all algorithms, the GK with the parameter γ set to $\gamma = 0.1$ was found the most powerful since it also provided the best visualization of plastic pipes. As the relevance of only IRT was of importance for the detection of pipes, elongated clusters were produced. This restricted their detection by FCM and PFCM, which are sensitive to spherical clusters.

A comparison of clustering-based feature level fusion with symbol level fusion confirmed the robust performance of clustering in situations with very limited knowledge about the material properties and depth of defects. Clustering in general increased the reliability of the NDT inspection in cases where the methods had an overlapping penetration capability and sensitivity to different physical properties. Moreover, in cases where one method greatly dominated over the other (complementary behaviour), they worsened its performance only to a small extent. On the other hand, supervised fusion using weighted averaging and D-S deteriorated the level of detection if weights were not assigned according to the reliability of the respective NDT method.

A complementary use of GPR and IRT proved also beneficial for the inspection of plastered stone walls. Apart from the detection of the walls' texture and morphology with the multi-leaf structure, seismic related damage of various extents could be detected. The plaster delamination could be particularly well resolved using IRT, as an air gap as small as 2 mm could be resolved, whereas the minimal detectable air gap with GPR measured 8 mm. This indicates that the first limit state of plaster could be resolved with high reliability when using IRT, whereas only the extent of damage referred to the third limit state could be detected by the 1.6 GHz GPR. Hence, IRT can be regarded as a potential method for defining the performance limit state of the plaster on multi-leaf masonry walls in practice. Particularly in the case of masonry walls in cultural heritage structures, the use of a non-contact method such as IRT plays an important role for defining the characteristic limit points of the plaster. Here, the walls have very often valuable frescoes, stuccoes or mosaics.

IRT proved additionally capable of detecting surface and subsurface crack patterns below the 2–3.5 cm thick plaster. However, we show that phase images at higher frequencies should be used in order to resolve small thermal contrasts resulting from cracking compared to the lowest frequency, which is better suited for imaging the underlying texture and the delamination pattern. This implies that the frequency, at which a defect was detected, could not be correlated with the defect's depth according to the equation proposed by Arndt [131] and which performed well on concrete. Two effects could contribute to this – the extremely heterogeneous structure of masonry

as well as the very shallow depth. Therefore, for masonry in practice, where delamination can occur at different depths, a synthesis of GPR and IRT results would be crucial to characterize the defects. We show that by employing the GK clustering algorithm for the segmentation of GPR and IR data, both delamination as well as cracks could be characterized. In this context it should be mentioned that the thesis aimed in deriving a validation of the methods' performance for the detection of internal cracks with respect to their size. Unfortunately, IRT revealed the subsurface crack pattern from only one tested wall, which restricted the validation process. Therefore, this could even not exclude the possibility that the detected "cracks" refer to the contours of a detected delamination.

The effect of moisture on the detection of voids in masonry was tackled through GPR, ultrasonic and CR tomographies. In general, ultrasonic data showed higher sensitivity to moisture and greater scattering than GPR data. This phenomenon could be explained by both a greater effect of ambient vibrations on the ultrasonic data, and a stronger difference in the acoustic properties of masonry materials (brick, mortar) compared to the change in the electromagnetic properties. Albeit all techniques proved capable of detecting the large air void, their efficiency differed significantly. GPR tomography is by far the most reliable technique for assessing voids in both dry and wet masonry. On the other hand, ultrasonic tomography requires longer measuring times, and a reliable tomographic image can be achieved solely by a carefully performed automatic picking of travel times. CR tomography turned out to be a reliable technique even at low humidity levels, although it is limited by lower depth resolution than the other two methods and suffers from poor electrode coupling, which might even largely affect the interpretation of the reconstructed resistivities. As already debated in [101], the interpretation of complex resistivities on masonry is limited to their magnitudes. To explore the performance of the analysed methods with respect to the moisture level in more detail, further research should focus on more humidity conditions, as well as different tomography configurations.

Along with the defined goals of the thesis, clustering was implemented into two NDT-data fusion frameworks for practical application. Their use for NDE of data from the multi-sensor BetoScan robot system provided a characterization of the damage. By applying clustering on data from potential mapping, eddy current and microwave moisture sensors, a reinforced concrete floor affected by corrosion could be segmented into damage zones. Moreover, the potential sources of the corrosion process, such as carbonation and high chloride concentration, could be identified. In addition, the application of clustering for cement identification of spectroscopic (LIBS) spatial data from concrete proved particularly beneficial. As both noise and spatial resolution affect the spectra, the noise handling clustering algorithms NCFCM and PFCM provided the best separation of spectra dominated by cement or aggregate content. The resulting sodium depth profiles gave an almost ideal fit to the reference profile and outperformed the standard classification based on the O/Ca criterion to a large extent. The proposed parameter optimization model enables the algorithms to work fully unsupervised. The greatly improved data evaluation process of the LIBS technique will play an important role in the implementation of the in situ mobile system, which is currently under construction and will bring LIBS into a productive environment.

For an NDT multi-sensor system such as the BetoScan, image fusion with clustering is of particular importance. Its main advantage is that it can work almost fully unsupervised. This is of particular interest in implementing NDT in practice in terms of automated application by trained engineers and technicians rather than scientists. Applied on the low pixel level fusion, it provides a segmented image, which may characterize the defects present in the structure as well as the extent of damage. Delivering only one reliable image, which takes into account the correlation between the various NDT methods, rather than multiple ones to the end-user is of the utmost importance. However, when applying clustering at the higher feature level fusion, the whole internal structure may be visualized. This approach is especially promising for NDT on concrete, where a complete visualization of structures is generally favourable. Particularly in the cases of large and/or hardly accessible inspection areas, a multi-sensor robot or scanning system comprising GPR, ultrasonic, IE and other methods is needed. For a reliable, fast and an efficient inspection, data should be acquired at different polarizations, frequencies and spatial resolutions of the measurement system. It is believed that clustering could handle the data fusion of various testing problems. Nonetheless, further research should also be devoted to the potential symbol level fusion. With respect to this, a more detailed sensor modelling should be performed for various NDT methods. Further research that goes beyond the frontiers of this thesis will be devoted to the sensitivity evaluation of the methods' penetration capabilities.

SUMMARY

Non-destructive testing (NDT) methods, such as ground penetrating radar (GPR), ultrasonic, impact-echo (IE) and infrared thermography (IRT), are due to the non-invasive effect they have on the structure more and more often used as an alternative for visual inspection in combination with destructive tests on samples extracted from the structure. However, with respect to the composition and condition of the inspected structure, all methods exhibit different penetration capability and sensitivity to the material physical properties. Hence, an extensive sensitivity evaluation should be carried out with respect to several not yet standardized applications.

It is evident that regardless of the knowledge about the methods' performance, multi-sensor testing is required for a complete inspection of the structure. This also rises the need for an efficient and reliable data processing technique. Contrary to most data fusion methods, clustering does not require the knowledge about the structural composition and can thus work unsupervised. In the thesis their functioning was tested on the results from the inspection of concrete and masonry structures. Hard and fuzzy clustering algorithms were analysed. As a hard clustering algorithm, the k-means was taken into account, whereas for the fuzzy ones, the conventional fuzzy c-means (FCM) and its variants were used. These are either better suited for handling noisy data (noise handling fuzzy c-means (NCFCM), possibilistic c-means (PCM) with repulsion, possibilistic-fuzzy c-means (PFCM)) or use an adaptive distance norm (Gustafson-Kessel (GK)).

The main research on the possibilites of defect detection in the near-surface region was performed on four laboratory concrete specimens using GPR and IRT. In the analysis, the material properties, type, shape and size of anomalies were taken into account. Particularly, voids, localized water, delamination, plastic pipes and reinforcement were simulated. Special consideration was put on the data evaluation of the results using pulsed thermography. Techniques based on the thermal contrast and pulsed phase thermography (PPT) were employed. The phase contrast images enabled accurate depth characterization of anomalies and deeper probing. In addition, they exhibited high contrast and good spatial resolution. Thus, for the sensitivity evaluation of GPR and IRT, phase contrast images were used together with GPR C-scans. The evaluation revealed that the sensitivity of GPR is lower than the one of IRT up till a depth of 3–4.5 cm. For IRT, the sensitivity decreases only slowly up till 7.5 cm, which particularly resulted from using phase contrast images. For both methods it could be observed that the material characterization of defects is predominantly governed by the contrast in dielectric constant and thermal conductivity between defects and sound area. Hence, GPR more accurately detects a water anomaly than an air anomaly, and the opposite is true for IRT.

For the synthesis of GPR C-scans and IR phase contrast images, feature level fusion was employed, where classifier units were obtained using clustering. Among all tested clustering algorithms, the GK with parameter γ set to $\gamma = 0.1$ was found the most powerful as it exhibited both robust performance and enabled the best detection of plastic pipes. The detection of pipes was possible since the GK algorithm is not limited to the detection of spherical clusters as are the FCM and PFCM algorithms. These two algorithms however revealed similar behaviour,

which indicates that noise has only a modest effect on the detection of most typical defects in concrete structures. The robust performance of clustering-based data fusion in situations with very limited knowledge of the structure was further confirmed using symbol level fusion.

The complementary use of GPR and IRT also enabled a complete structural characterization of plastered multi-leaf stone walls. In this case, GPR and IRT were particularly selected since they enable inspection with minimal interference on the structure. This is of paramount importance in the case of inspection of masonry walls in cultural heritage buildings. Apart from the detection of the walls' morphology and texture, plaster delamination could be detected as a result of simulated seismic activity using a cyclic shear test. A comparison with the results from the 3D digital image correlation technique revealed that a delamination corresponding to the first limit state of the plaster (≈ 2 mm air gap) could be resolved using IRT, whereas only the extent of damage referred to the third limit state (≈ 8 mm air gap) could be detected by GPR. By using IR phase images at higher frequencies, surface and subsurface cracks could be detected, whereas the delamination and texture were detected when using phase images at the lowest frequency. For IRT, the extremely heterogeneous masonry structure prevented a quantitative evaluation of thermal data, which could be performed on concrete. Hence, we proposed a data fusion performed at the pixel level for the segmentation of data. This enabled the detection of both plaster delamination and cracks.

The performance of NDT methods with respect to the moisture of the material was studied on a laboratory brickwork specimen. In particular, the detection of a larger void was considered using GPR, ultrasonic and complex resistivity (CR) tomographies. The measurements revealed that ultrasonic is more sensitive to changes in the moisture content than GPR and in addition, exhibits also greater scattering of data. GPR proved to be the most reliable technique for the detection of voids in both dry and wet masonry. To enable good void detection when using ultrasonic tomography, longer measuring times would be required, as well as an accurate selection of the first travel time. Also when using CR tomography, the void could be detected at both moisture conditions of the masonry. However, the method exhibited poor depth resolution compared to GPR and ultrasonic. In addition, efficient imaging of the resistivity distribution was restricted by poor electrode coupling.

Clustering methods were successfully implemented into two NDT systems – for data fusion of a multi-sensor BetoScan robot system and for classification of spectroscopic spatial data from concrete. Clustering methods were applied on the pixel level for the segmentation of data. For the identification of the cement matrix in concrete specimens using spectroscopic (LIBS) data, the NCFCM and PFCM algorithms exhibited the best performance. For these algorithms, the proposed parameter optimization model enabled a fully automated classification of data. This is of great significance for the implementation of LIBS into a productive environment. In the case of the multi-sensor data sets from the BetoScan system, clustering provided the segmentation of a reinforced concrete floor affected by corrosion into damage zones.

6 RAZŠIRJENI POVZETEK V SLOVENSKEM JEZIKU (EXTENDED ABSTRACT IN SLOVENE)

6.1 Uvod

Pregled ožjega znanstvenega področja in opredelitev znanstvenega problema

V gradbeništvu se prve neporušne metode za preiskave tlačne trdnosti strjenega betona pojavijo okoli leta 1940. Večina izmed teh metod (metoda z udarno-povratnim kladivom, preizkus s sondo Windsor, preizkus izvlečne sile, ultrazvočna metoda) je danes standardiziranih [2, 3]. Šele v zadnjih nekaj letih usmerjamo intenzivno raziskovanje v možnost uporabe neporušnih metod za oceno stanja obstoječih gradbenih konstrukcij, ki bodisi vsebujejo konstrukcijske napake bodisi je na njih prisotno propadanje materiala zaradi zunanjih vplivov na konstrukcijo. Na velikem deležu betonskih konstrukcij (predvsem mostovi, garažne hiše in predori) je propadanje materiala posledica vdora topnih soli v pore cementne matrike [4, 7]. Le-to v kombinaciji z neustrezno materialno sestavo in majhnim krovnim slojem betona vodi do korozije armature, razpokanja in odstopanja krovne plasti betona [7]. Zidane konstrukcije, od katerih je velik delež stavb kulturne dediščine, imajo poleg prisotnih topnih soli pogosto povečano vlažnost in slabšo povezanost zidovja. V mediteranskem območju so zidane konstrukcije še dodatno prizadete zaradi večje potresne aktivnosti [9].

Trenutna ocena stanja obstoječih konstrukcij temelji na vizualni oceni v kombinaciji s porušnimi preiskavami odvzetih vzorcev. Tak pristop ne omogoča zanesljive ocene stanja in obenem predstavlja velik poseg na konstrukcijo. Zato so bile kot alternativa predlagane metoda georadarja, ultrazvočna metoda, metoda udarec-odmev, infrardeča termografija (IRT) idr. [10, 11, 12]. Vse te metode imajo zaradi heterogene strukture gradbenih materialov in množice prisotnih anomalij v konstrukcijskih elementih spremenljivo penetracijsko sposobnost in občutljivost na fizikalne lastnosti materialov. Zato je le malo primerov uporabe teh metod v praksi standardiziranih [1, 3, 5]. To zahteva obsežno analizo občutljivosti metod glede na področja njihove uporabe v praksi [6].

Metoda georadarja se je v raziskavah tako betonskih kot tudi zidanih konstrukcijskih elementov pokazala kot učinkovita metoda za zaznavanje armature in za oceno vlažnosti ter koncentracije soli v materialu [13, 14, 16]. Za oceno debeline betonskih konstrukcijskih elementov, zaznavanje mehke armature in zaščitnih cevi za prednapetje so raziskovalci uspešno uporabili ultrazvočno metodo [18, 19, 20]. Nedavne raziskave poročajo tudi o uporabi ultrazvočne metode in metode udarec-odmev za preučevanje napak ob injektiranju zaščitnih cevi za prednapetje [22, 23, 27]. Sadri [28] uporabi metodo udarec-odmev tudi za ugotavljanje povezanosti kamnitega zidu ter jo predlaga za zaznavanje večjih votlin in za kontrolo uspešnosti injektiranja. Za zaznavanje večslojnosti in povezanosti zidov, odstopanj ometa, prisotnosti večjih votlin ter vlažnosti zidovja večina raziskav poroča o uspešni uporabi georadarja, metode s kladivom in IRT [9, 29, 30, 31, 32, 33]. Predvsem IRT ima zaradi nekontaktne narave veliko prednost pri preiskovanju zidanih objektov kulturne dediščine. Uporabili so jo za vizualizacijo podometne teksture in za zaznavanje odstopanja posameznih plasti [9, 31, 34, 35]. Na objektih kulturne dediščine so IRT in ultrazvočno metodo uporabili še za določitev globine površinskih razpok [48] in njihove orientacije [49]. Za

raziskave razpokanosti betonskih konstrukcijskih elementov zaradi delovanja obtežbe predlagajo metodo akustične emisije [46, 47].

Razvidno je, da je za celostno karakterizacijo preiskovane strukture potrebna uporaba več neporušnih metod, tj. večsenzorska meritev [52, 53]. Številni avtorji so v svojih delih že primerjali rezultate različnih neporušnih metod na betonskih [18, 54, 55, 56, 57, 58, 27] in zidanih [9, 59, 60, 61] konstrukcijskih elementih, vendar so obdelavo podatkov izvedli neodvisno za posamezno metodo. V praksi, kjer je največkrat potrebna obdelava velikega števila podatkov, je tak pristop časovno potraten in drag. Poleg tega je tudi podvržen subjektivni oceni rezultatov. Sintezo podatkov večsenzorskih preiskav, ki bi omogočila avtomatsko obdelavo podatkov, so v gradbeništvu opravili na prednapetih mostnih nosilcih. Združeni so bili različni georadarski podatki (pridobljeni pri različnih frekvencah in v obeh polarizacijskih smereh) kot tudi georadarski in ultrazvočni podatki [14, 76, 77]. Avtorji teh del so za sintezo rezultatov uporabili preproste matematične algoritme. Naprednejši algoritmi, ki omogočajo bolj natančno združevanje podatkov neporušnih preiskav, so bili predlagani za preiskave materialov v letalski in jedrski industriji. Uporabili so algoritme, ki temeljijo na nevronskih mrežah, valovni analizi, Bayesovi analizi in Dempster-Shaferjevi (D-S) teoriji evidenc [69, 65, 73, 67].

Glavni cilji in vsebina doktorske disertacije

Glavni namen disertacije je bil razvoj ustreznega postopka za združevanje slik, ki bi temeljil na metodah gručenja in bi omogočil učinkovito in zanesljivo obdelavo podatkov večsenzorskih neporušnih preiskav gradbenih konstrukcijskih elementov. Metode gručenja so že uporabili pri združevanju slik. Pri medicinskem slikanju so jih uporabili za razpoznavanje vzorcev, kot so tumorne celice [78, 79], v geofiziki pa za določitev geološke slojevitosti [80, 81]. Glavna prednost metod gručenja je, da lahko delujejo avtomatizirano. To omogoča obdelovanje podatkov neporušnih preiskav brez subjektivnega vpliva in izkušenosti raziskovalca, kar je bistvenega pomena za prenos metod v inženirsko prakso.

V disertaciji smo za združevanje slik večsenzorskih neporušnih preiskav uporabili algoritme trdega in mehkega gručenja, in sicer trdo metodo k-srednjih vrednosti [82], osnovno mehko metodo c-srednjih vrednosti [83] ter njene različice. Te bodisi bolje obvladujejo močno zašumljene podatke [84, 86, 87] bodisi uporabljajo prilagojeno normo [85].

Poleg razvoja ustrezne tehnike združevanja slik smo v okviru dela opravili tudi analizo občutljivosti več neporušnih metod. Analizo smo opravili na rezultatih preiskav betonskih in zidanih laboratorijskih preizkušancev. Obravnavali smo tako različne konstrukcijske anomalije kot tudi različne materialne lastnosti preiskovane strukture.

Osnovne raziskave možnosti zaznavanja anomalij v območju blizu površja smo opravili z georadarjem in IRT na štirih laboratorijskih betonskih preizkušancih. Vključili smo različne anomalije: votline, lokalizirano vodo, odstopanje plasti, plastične cevi in armaturo. Preiskave smo opravili z georadarjem in IRT, ker smo ju ocenili kot komplementarni metodi za zaznavanje v območju blizu površja (do globine 10 cm). Obe metodi smo uporabili tudi za neporušne preiskave labo-

ratorijskih večslojnih kamnitih zidov. Preučili smo možnost zaznavanja teksture in morfologije zidov ter odstopanja ometa in nastanka razpok zaradi delovanja strižne obremenitve. Namen preiskave je bil raziskati možnosti uporabe izbranih metod za preiskave zidov v objektih kulturne dediščine. Tu so neporušne preiskave še posebej pomembne, saj zahtevamo čim manjši poseg v konstrukcijo.

Na inštitutu BAM smo na opečnatem zidovju preverili občutljivost neporušnih metod na prisotnost vlage v zidovju. Uporabili smo georadarsko, ultrazvočno in geoelektrično (kompleksno-uporovno) tomografijo. Ker tomografska tehnika omogoča 3D vizualizacijo, smo posebej preučili zaznavanje večje votline glede na pogoje vlažnosti zidovja.

V okviru doktorskega dela smo metode gručenja uvedli v dvoje aplikativnih ogrodij združevanja podatkov na inštitutu BAM: za združevanje podatkov večsenzorskega robotnega sistema BetoScan kot tudi za popolnoma avtomatizirano klasifikacijo spektroskopskih podatkov betonskih preizkušancev.

6.2 Osnove izbranih neporušnih metod

Neporušne metode v gradbeništvu v grobem razvrščamo v dve glavni skupini – zvočne in elektromagnetne. Zvočne metode temeljijo na širjenju mehanskega zvočnega valovanja in so zato občutljive na elastične lastnosti materialov, medtem ko elektromagnetne (EM) metode temeljijo na merjenju EM lastnosti materialov kot posledica širjenja elektromagnetnega valovanja (EMV). Med zvočne metode sodijo mikroseizmične metode, metoda s kladivom, metoda udarec-odmev, ultrazvočna metoda in metoda akustične emisije. Izmed EM metod so najbolj poznane georadar, metoda z vrtinčnimi tokovi, elektro-uporovne metode ter EM potencialne metode. Poleg omenjenih metod v gradbeništvu uporabljamo še IRT in radiografijo. Slednja temelji na merjenju absorpcije visokofrekvenčnega EMV (rentgenskih ali gama žarkov) ali toka nevtronov v odvisnosti od gostote materiala.

Georadar

Georadar temelji na generiranju in širjenju EM pulzov v radiofrekvenčnem območju znotraj preiskovanega materiala ter detekciji bodisi odbitega bodisi prepuščenega valovanja z uporabo antene [94]. Za preiskovanje gradbenih konstrukcijskih elementov je najpogostejša uporaba anten s središčno frekvenco valovanja med 300 MHz in 2,5 GHz [76]. EMV se pri širjenju skozi material sipa, njegova jakost slabi, obenem se tudi odbija in lomi na mejnih ploskvah anomalij z drugačnimi dielektričnimi konstantami, kot je dielektrična konstanta preiskovanega medija. Za georadarske meritve v odbojnem načinu je za zaznavanje anomalij ključna razlika v dielektričnih konstantah, saj je amplituda odbitega valovanja, ki prispe do antene, določena z zvezo [95]

$$r = \frac{\sqrt{\varepsilon_{r2}} - \sqrt{\varepsilon_{r1}}}{\sqrt{\varepsilon_{r2}} + \sqrt{\varepsilon_{r1}}}, \tag{6.1}$$

kjer sta ε_{r1} in ε_{r2} relativni dielektrični konstanti dveh različnih medijev. Njihova razlika se odraža v spremembi amplitude in faze zaznanega odbitega valovanja.

Pri merjenju v odbojnem načinu globino anomalije z določimo na podlagi povprečne hitrosti EMV v snovi v in časa potovanja EMV od oddajne do sprejemne antene t v skladu z enačbo

$$z = \frac{vt}{2} = \frac{ct}{2\sqrt{\varepsilon_r}}, \tag{6.2}$$

kjer je c hitrost EMV v vakuumu in ε_r relativna dielektrična konstanta preiskovanega materiala. Seveda pa smo pri zaznavanju anomalij omejeni z ločljivostjo antene in s penetracijsko sposobnostjo valovanja, na katero najbolj vplivata uporabljena frekvenca valovanja in električna prevodnost snovi.

Pri georadarski meritvi zberemo več točkovnih meritev (refleksijskih sledi) v georadarski profil, kjer prikažemo časovno odvisnost amplitude odbitega valovanja. Princip georadarske meritve z zaznavanjem odbojev EMV od mej materialov z različnimi dielektričnimi konstantami je razviden iz slike 2.1. Prikazani so tudi različni načini grafičnega prikazovanja rezultatov: grafični prikaz refleksijske sledi (A-scan), radargram georadarskega profila (B-scan) in grafični prikaz prereza (C-scan).

Kompleksno-uporovna metoda

Vse elektro-uporovne metode (tudi geoelektrične metode) določajo specifično upornost snovi na podlagi meritve napetosti med dvema elektrodama kot posledica električnega toka v skladu z Ohmovim zakonom. Kompleksno-uporovna metoda za razliko od navadne uporovne metode uporablja izmenični tok visokih frekvenc in je zato bolj občutljiva na meritve specifične upornosti [99].

Pri meritvi specifične upornosti materialov največkrat uporabljamo štiri elektrode na površini preizkušanca, da zmanjšamo vpliv kontaktnih napetosti. Pri tem sta dve tokovni elektrodi, dve pa merita napetost. Če območje preizkušanca opišemo s polprostorom, lahko za znan električni tok I in ob meritvi napetosti U med elektrodama izračunamo navidezno specifično upornost kot [99]

$$\rho_a = K\,\frac{U}{I}, \tag{6.3}$$

kjer je K konfiguracijski faktor in je odvisen od geometrijske razporeditve elektrod. Nekaj najbolj tipičnih geometrijskih razporeditev elektrod je prikazanih na sliki 2.2. Izraz navidezna specifična upornost poudarja, da gre za povprečno specifično upornost merjene snovi za območje med elektrodama. Prave specifične upornosti nehomogene strukture dobimo šele z inverznim računom, kjer po korakih popravljamo razporeditev specifične upornosti numeričnega modela, dokler se izračunane navidezne specifične upornosti dovolj dobro približajo merjenim.

Infrardeča termografija

IRT nam da podatke o površinski temperaturi preizkušanca. Temelji na zaznavanju IR sevanja, ki ga telo pri določeni temperaturi oddaja. Za neporušne preiskave je najpogostejša uporaba aktivne IRT, kjer z zunanjim grelcem v preizkušancu povzročimo nestacionaren toplotni tok. Glede na

način ogrevanja ločimo tri tehnike aktivne IRT [104, 109]: pulzna termografija [1], termografija z odzivom na periodično motnjo in termografija s stopničastim pulzom. V disertaciji smo uporabili pulzno termografijo, ki je v gradbeništvu najbolj pogosta.

Gostoto energijskega toka, ki ga telo s temperaturo T izseva, opiše enačba [104]

$$j^* = e\,\sigma_{sb}T^4, \tag{6.4}$$

kjer je σ_{sb} Stefan-Boltzmannova konstanta in e emisivnost površine preizkušanca. Za večino gradbenih materialov (beton, malto, opeko) je emisivnost med 0,9 in 0,95 [104]. Sevanje teles lahko razlagamo s sevanjem črnega telesa, za katerega velja Planckov zakon. Ta opiše spektralno porazdelitev izsevane energije, ki je za črno telo pri različnih temperaturah prikazana na sliki 2.5. Poleg sevanja je za IRT ključnega pomena tudi poznavanje procesov prenosa toplote v snovi, ki vplivajo na časovni potek površinske temperature. Odstopanje v porazdelitvi površinske temperature od pričakovane nakazuje na pojav anomalije v preizkušancu.

V primerjavi z metodami, kot so npr. georadar, ultrazvočna metoda ali geoelektrične metode, je IRT hitrejša, relativno poceni in ne potrebuje fizičnega stika med preizkušancem in kamero. Slabost metode pa je majhen globinski doseg in zahtevna karakterizacija anomalije, predvsem njene globine. Za oceno globine anomalije sta bila na podlagi rezultatov preiskav materialov v strojništvu predlagana dva glavna pristopa k obdelavi podatkov. Prvi temelji na temperaturnem kontrastu, drugi, pulzno-fazna termografija, na obdelavi podatkov v frekvenčni domeni. Pri tehniki temperaturnega kontrasta je za oceno globine anomalije predlagan izraz, ki temelji na maksimalnem temperaturnem kontrastu in času njegovega nastopa [118], medtem ko je za pulzno-fazno termografijo predlagan izraz, ki uporablja frekvenco pri maksimalnem faznem kontrastu [131, 123].

Ultrazvočna metoda

Ultrazvočna metoda temelji na generiranju, širjenju in zaznavanju bodisi odbitega bodisi prepuščenega zvočnega valovanja v ultrazvočnem območju, tj. pri frekvencah nad 20 kHz. Za preiskave v gradbeništvu najpogosteje uporabljamo frekvence v območju 50–200 kHz [12]. Za razliko od ostalih zvočnih metod, uporabljenih za neporušne preiskave v gradbeništvu, ultrazvočna metoda uporablja piezoelektrični senzor tako za oddajnik kot za sprejemnik valovanja.

Za širjenje zvočnega valovanja je za razliko od EMV potreben medij, saj se valovanje širi z deformiranjem snovi oz. natančneje z nihanjem delcev snovi okoli ravnovesnih leg. V trdni snovi lahko delci nihajo vzdolž smeri širjenja valovanja, kar povzroča longitudinalne deformacije, ali pa prečno na smer valovanja, kar povzroča transverzalne deformacije. Glede na to, katera vrsta deformacij je v snovi povzročena, ločimo longitudinalno (tlačno) in transverzalno (strižno) valovanje. Hitrost longitudinalnega valovanja je večja od hitrosti transverzalnega, obe pa sta odvisni od gostote snovi, elastičnega modula in Poissonovega števila [133].

[1] V pulzno termografijo uvrščamo tudi termografijo s kvadratnim pulzom, kjer preizkušanec segrevamo dlje časa (običajno nekaj minut).

Pri merjenju v odbojnem načinu globino anomalije določimo podobno kot pri georadarju z enačbo $z = vt/2$ (6.2), pri čemer je v hitrost longitudinalnega oz. transverzalnega valovanja. Za zaznavanje anomalij je potrebna dovolj velika razlika v zvočni impedanci, saj je delež odbitega valovanja določen z [136]

$$r = \frac{Z_2 - Z_1}{Z_2 + Z_1}, \tag{6.5}$$

kjer sta Z_1 in Z_2 zvočni impedanci dveh različnih medijev in $Z = \rho_m v$ [136], kjer je ρ_m gostota snovi.

Ultrazvočne preiskave lahko opravimo kot posamezne točkovne meritve. Slabost teh je, da so razmeroma dolgotrajne, rabimo pa tudi sredstvo (npr. glicerin, vazelin ali vodo), ki zagotovi dober stik senzorja s preizkušancem [11]. Za preiskovanje betonskih konstrukcijskih elementov v odbojnem načinu se zato raje uporablja sistem več ultrazvočnih senzorjev [22, 134].

6.3 Združevanje podatkov z gručenjem

Model združevanja podatkov

Združevanje podatkov neporušnih preiskav lahko razumemo kot sintezo večsenzorskih podatkov [62]. Združevanje lahko poteka na nivoju posameznih signalov, 2D slik ali celotnega volumna, združujemo pa lahko tudi rezultate ene same neporušne metode (npr. georadarski podatki, pridobljeni pri različnih frekvencah ali polarizacijah antene) ali rezultate večih metod. V disertaciji obravnavamo združevanje slik več neporušnih metod.

Za združevanje podatkov neporušnih preiskav so raziskovalci predlagali različne algoritme, ki temeljijo na metodah optimizacije, večločljivostni analizi, hevrističnih metodah in statističnih metodah (Bayesova analiza, Dempster-Shaferjeva (D-S) teorija evidenc, mehka logika) [53]. Ne glede na uporabljeni algoritem lahko združevanje slik poteka na treh nivojih: na nivoju posamezne slikovne točke, z uporabo značilnic in na simbolnem nivoju [53]. Pri slednjih dveh uporabimo informacije, ki jih pridobimo v koraku predhodne obdelave podatkov. Značilnice pridobimo s predhodno segmentacijo slik (npr. s pomočjo gručenja ali nevronskih mrež), medtem ko za združevanje podatkov na simbolnem nivoju uporabimo podatke senzorja.

Glavna prednost metod gručenja pred ostalimi zgoraj omenjenimi metodami združevanja podatkov je, da ne potrebujemo v naprej poznane statistične porazdelitve podatkov. To ima bistven pomen pri združevanju podatkov neporušnih preiskav v gradbeništvu, saj je vedenje o sestavi preizkušancev še posebno slabo zaradi množice različnih anomalij v praksi.

Metode gručenja

Gručenje pomeni razvrstitev množice podatkov v podmnožice (razrede, skupine) na način, da so podatki, ki pripadajo istemu razredu čim bolj podobni, podatki različnih razredov pa naj se čim bolj razlikujejo [143]. Pri gručenju z namensko funkcijo je tipična mera, ki pove, kako sta si dva podatka podobna, Evklidska norma. Gručenje množice podatkov pričnemo z naključno

razporeditvijo v naprej določeno število razredov c. Razporeditev nato korakoma popravljamo tako, da je vsak podatek razvrščen v tisti razred, da je njegova razdalja do središča razreda najmanjša. To je značilnost trdega gručenja. Pri mehkem gručenju lahko podatek razporedimo v več razredov hkrati z določeno mero pripadnosti u. Za poljuben podatek j in razred i tako velja, da je mera pripadnosti pri trdem gručenju $u_{ij} \in \{0, 1\}$, pri mehkem pa $u_{ij} \in [0, 1]$. Mehko gručenje naprej delimo na verjetnostno in možnostno gručenje. Pri verjetnostnem zahtevamo, da je vsota vseh verjetnosti nahajanja določenega podatka enaka 1, pri možnostnem pa tega pogoja ni.

Razporeditev N podatkov v število razredov c poteka ob pogoju minimizacije namenske funkcije, ki jo opišemo kot

$$J_m(\mathbf{U}, \mathbf{V}; \mathbf{X}) = \sum_{i=1}^{c} \sum_{j=1}^{N} u_{ij}^m d_{ij}^2, \tag{6.6}$$

kjer je $d_{ij} = \|\mathbf{x_j} - \mathbf{v_i}\|_{\mathbf{A}}$ razdalja podatka $\mathbf{x_j}$ do središča razreda $\mathbf{v_i}$. Matrika $\mathbf{A}$ pri tem definira vrsto norme. Minimizacija namenske funkcije predstavlja nelinearen optimizacijski problem, ki zahteva, da $\mathbf{v_i}$ in u_{ij} v vsakem koraku znova izračunamo.

Enačba (6.6) posebej opisuje verjetnostno gručenje. Najbolj osnovna metoda verjetnostnega gručenja je mehka metoda c-srednjih vrednosti (FCM) [83], ki uporablja Evklidsko normo, kjer je $\mathbf{A}$ enotska matrika. Zaradi tega predpostavlja sferično obliko razredov. Dodatna slabost te metode je še, da je razmeroma občutljiva na podatke, kjer je prisotno veliko šuma. Za opis razredov različnih geometrij (ne le sferične oblike) lahko uporabimo druge algoritme, ki temeljijo na verjetnostnem gručenju, in sicer: Gustafson-Kessel (GK) [85], algoritem prilagodljivega mehkega gručenja (AFC) [148] ter algoritem GK s prilagodljivimi volumni razredov (GKAρ) [149]. Vsi trije uporabljajo normo, kjer je matrika $\mathbf{A}$ odvisna od volumna posameznega razreda in mehke kovariančne matrike.

Za opis močno zašumljenih podatkov lahko uporabimo algoritme verjetnostnega gručenja, ki uvedejo dodaten razred za najbolj zašumljene podatke [84], ter algoritme, ki temeljijo na možnostnem gručenju. Poleg osnovnega mehkega možnostnega gručenja (PCM) [151] sodijo v to skupino algoritmov še FPCM [152], PFCM [87] in PCM s kazenskim členom [86]. Vsi algoritmi poleg matrike verjetnosti nahajanja podatkov $\mathbf{U} = \{u_{ij}\}$ uporabljajo še matriko tipičnosti $\mathbf{T} = \{t_{ij}\}$, za katero velja

$$0 < \sum_{i=1}^{c} t_{ij} \leq 1, \quad \forall j \in \{1, \ldots, N\}. \tag{6.7}$$

Zato moramo pri postopku minimizacije namenske funckije v vsakem koraku preračunati $\mathbf{v_i}$, u_{ij} in t_{ij}.

Omeniti velja, da je pred začetkom gručenja treba določiti število razredov c. Za avtomatsko določitev optimalnega števila razredov lahko uporabimo različne kazalce [153], vendar lahko vsi v določenih primerih privedejo do napačnih rezultatov. Tudi v večini naših primerov uporabe

gručenja niso dali ustreznih rezultatov. Za podatke neporušnih preiskav se je kot boljša izbira števila razredov izkazala stopnja ocenjene poškodovanosti strukture oz. heterogenosti merjenega materiala.

6.4 Neporušne preiskave laboratorijskih betonskih preizkušancev z vgrajenimi anomalijami

6.4.1 Eksperimentalne metode in materiali

Za preiskave smo pripravili štiri betonske preizkušance dimenzij $50 \times 50 \times 15\,\mathrm{cm}^3$. Kot je razvidno iz slike 4.1, imajo preizkušanci vgrajene različne anomalije, ki smo jih opisali v preglednici 4.1. Z anomalijami iz stiropora v preizkušancu S0 smo raziskovali vpliv različne globine enake anomalije na uspešnost zaznavanja z georadarjem in s termokamero. Vključki v preizkušancih S1–S3 pa simulirajo tipične napake in vključke v gradbenih konstrukcijskih elementih, kot so lokalizirana voda in zračne votline (S1), armatura (S2), instalacijske cevi in delaminacija (S3).

Za preiskave z IRT smo uporabili termokamero FLIR A320 (slika 4.2), ki s sistemom bolometrov zaznava IR svetlobo z valovno dolžino med 7,5 in 13 µm, njena maksimalna občutljivost pa je 50 mK (pri 30 °C). Za gretje preizkušancev smo uporabili IR grelca z močjo po 1,2 kW, postavljena 45 cm od površine preizkušanca, da je bilo zagotovljeno približno enakomerno segrevanje. V sklopu optimizacije časa segrevanja smo preizkušance greli 5, 15, 30 in 45 min. Temperaturno ohlajanje smo spremljali 45 min (za potrebe pulzno-fazne termografije 150 min) pri frekvenci zajemanja slik 0,2 Hz.

Georadarske meritve smo opravili z georadarskim sistemom MALÅ Geoscience. Uporabili smo zaščiteno oddajno-sprejemno anteno s središčno frekvenco 1,6 GHz (slika 4.3). Georadarske profile smo zajemali s pomočjo merilnega koleščka v obeh smereh pri medsebojnem razmiku med vzporednimi georadskimi profili 5 cm in pri razmiku med posameznimi točkovnimi meritvami 0,5 cm (razmik med georadarskimi sledmi). Za združevanje georadarskih podatkov z rezultati IRT smo uporabili grafične prikaze prereza. Te smo pridobili s koraki predhodne obdelave, in sicer z odstranitvijo ojačitve signala, premikom signala in popravkom začetnega časa.

6.4.2 Rezultati

Karakterizacija anomalij z infrardečo termografijo

Karakterizacijo anomalij z IRT smo opravili s pomočjo temperaturnega kontrasta in tehnike pulzno-fazne termografije. Iz slike 4.6 je razvidno, da lahko zračno in vodno anomalijo ločimo iz razlike v temperaturnem kontrastu. Za to je v največji meri odgovorna razlika v toplotni prevodnosti med anomalijo in preiskovanim materialom, v našem primeru betonom. Znižanje temperaturnega kontrasta za anomalijo pod armaturno mrežo rastra 5 cm prav tako vpliva na slabše zaznavanje anomalij, medtem ko armaturna mreža rastra 10 cm ne vpliva na potek temperaturnega kontrasta. Rezultati na slikah 4.5 in 4.6 kažejo, da je temperaturni kontrast močno odvisen od vrste anomalije, medtem ko je čas t_{Cmax}, tj. čas nastopa maksimalnega temperaturnega kontrasta (C_{max}), od te skoraj neodvisen in določen le z njeno globino. To omogoča, da z

opazovanjem obeh parametrov, C_{max} in t_{Cmax}, kvalitativno določimo vrsto anomalije in njeno globino. Ugotovitev potrjujejo kontrastne in časovne slike vseh preizkušancev na slikah 4.7–4.10.

Na sliki 4.11 vidimo, da je pri vseh globinah (1,5–7,5 cm) optimalni čas segrevanja 30 min. Tam namreč doseže C_{max} največje vrednosti in obenem najgloblji doseg – do 6 cm. Odvisnost C_{max} in t_{Cmax} od globine anomalije smo poskušali opisati z modelom po enačbi (2.36). Rezultati prilagajanja (slika 4.12) kažejo, da model ne more opisati eksperimentalnih rezultatov (vrednost determinacijskega koeficienta znaša $R^2 = 0,25$). V nasprotju s tem pa lahko model po enačbi (2.44), ki temelji na pulzno-fazni termografiji in frekvenci največjega faznega kontrasta f_{ch}, z veliko natančnostjo opiše eksperimentalne rezultate (vrednost determinacijskega koeficienta znaša $R^2 = 0,99$) – glej sliko 4.14. Ugotovitve eksperimentalnih rezultatov potrjujejo tudi rezultati numerične simulacije (sliki 4.18 in 4.19).

Ugotovitev, da lahko f_{ch} natančno koreliramo z globino anomalije, omogoča, da fazne slike pri določenih frekvencah interpretiramo kot slike na ustrezni globini. Dodatna prednost fazno-kontrastnih slik je, da različne termične lastnosti anomalij vplivajo le na velikost faznega kontrasta, ne pa na f_{ch} (slika 4.16). Fazno-kontrastne slike imajo obenem velik kontrast in zelo dobro prostorsko ločljivost (slika 4.15). Za združevanje z georadarskimi grafičnimi prikazi prereza smo zato uporabili fazno-kontrastne slike.

Analiza občutljivosti georadarja in infrardeče termografije

Občutljivost georadarske metode in IRT na zaznavanje anomalij pri različnih globinah smo kvantitativno ocenili s predlaganim parametrom c_sens, kot ga podaja enačba (4.2). Rezultati zbrani na sliki 4.21 kažejo, da ima georadar nizko vrednost c_sens na globini 1,5 cm ($c\_sens = 84,5\,\%$), kar potrjujejo tudi slike preizkušanca S3 na sliki 4.22. Kljub temu se njegova vrednost že na globini 3 cm naglo poveča. V nasprotju z georadarjem občutljivost IRT z globino pada, obenem pa je metoda tudi bolj občutljiva na spremembe materialnih lastnosti anomalij.

Združevanje podatkov s kvantitativno validacijo

Georadarske in IR slike smo združili z uporabo značilnic po enačbi (8) v prilogi A (v nadaljevanju poglavja 6.4.2 sklicevanje na članek v prilogi A opuščam, saj se vsi nadaljnji rezultati navezujejo nanj). Kot značilnice so služile mere pripadnosti podatkov u_{ij}, ki smo jih predhodno dobili z gručenjem. Rezultate združevanja z gručenjem smo kvantitativno ovrednotili s parametrom c_sens ter primerjali z rezultati simbolnega združevanja podatkov. Za simbolno združevanje smo uporabili uteženo povprečje in D-S teorijo evidenc, za uteži oz. verjetnostne mase pa uporabili rezultate občutljivostne analize.

Kvalitativni rezultati združevanja so prikazani na slikah 2–4. Za preizkušanec S1, kjer sta bili vrednosti c_sens za georadar in IRT zelo podobni, je razvidno, da dobimo s simbolnim združevanjem podobne rezultate kot z združevanjem z uporabo značilnic. Na sliki preizkušanca S2 pa se pokaže, da združevanje z uporabo značilnic bistveno izboljša zaznavanje anomalije pod gostejšo armaturno mrežo, obenem pa zmanjša šum zaradi zaznane armaturne mreže na georadarski sliki. Tudi za preizkušanec S3 (slika 4) dobimo z združevanjem z gručenjem večji kontrast slike kot s

simbolnim združevanjem, saj lahko jasneje zaznamo cevi v preizkušancu.

Kvantitativni rezultati združevanja so zbrani v preglednici 2 (pri združevanju z uporabo značilnic prikazujemo le rezultate, ki smo jih dobili z uporabo metode FCM). Pokaže se, da združevanje georadarskih in IR slik z uporabo značilnic v splošnem poveča zanesljivost neporušne preiskave. Celo v primeru preizkušanca S3, kjer je bila občutljivosti IRT bistveno večja od občutljivosti georadarja, je to združevanje le malenkost poslabšalo občutljivost IRT. Simbolno združevanje z uporabo uteženega povprečja in D-S teorije evidenc da zelo podobne rezultate. V primerih, ko je bila večja utež dodeljena neporušni metodi z boljšo sposobnostjo zaznavanja, sta obe metodi navkljub pričakovanjem le malenkostno povečali občutljivost preiskave. V primerih, ko utež ni bila v skladu z občutljivostjo georadarja in IRT (preizkušanec S2 z armaturo), pa sta metodi bistveno poslabšali sposobnost zaznavanja, kar kaže na veliko odvisnost simbolnega združevanja od izbire uteži.

Primerjava delovanja različnih algoritmov mehkega gručenja je podana na sliki 5 in v preglednici 3. Algoritem PFCM da zelo podobne rezultate kot osnovni mehki algoritem FCM, kar kaže na dejstvo, da šum ne vpliva na zaznavanje obravnavanih anomalij. To je v nasprotju z združevanjem rezultatov neporušnih preiskav materialov v strojništvu, kjer je vpliv šuma izrazit [67]. Za delovanje algoritma GK se izkaže, da je parameter γ najbolje omejiti na $\gamma = 0,1$. Pri tem doseže algoritem GK podobno obnašanje kot FCM, obenem pa tudi bolje kot FCM in PFCM zazna cevi. Algoritem GK izkazuje glede na robustnost metode in sposobnost zaznavanja majhnih sprememb v strukturi najboljše delovanje.

6.5 Neporušne preiskave laboratorijskih ometanih večslojnih kamnitih zidov

6.5.1 Eksperimentalne metode in materiali

Neporušne preiskave smo v okviru evropskega projekta PERPETUATE (www.perpetuate.eu) opravili na štirih laboratorijskih ometanih trislojnih kamnitih zidovih dimenzije $100 \times 150 \times 40\,\mathrm{cm}^3$. Za gradnjo smo uporabili pol obdelan kamen iz apnenca ter apneno malto. Dva zidova sta imela v vsaki drugi vrsti povezovalne kamnite bloke, ki so po prerezu potekali čez vse tri sloje (vezniška zveza) – glej sliko 1 v prilogi B (v nadaljevanju poglavja 6.5 sklicevanje opuščam).

Georadarske in IRT preiskave smo opravili z isto merilno opremo kot za neporušne preiskave laboratorijskih betonskih preizkušancev, ki sem jih opisala v poglavju 6.4.1. Za IRT smo preizkušance greli približno 30 min z IR grelci na oddaljenosti 10 cm, njihovo ohlajanje pa merili 45 min pri frekvenci zajemanja slik 0,2 Hz. Postopek georadarske meritve ustreza opisu v poglavju 6.4.1, prav tako tudi koraki predhodne obdelave georadarskih in IR podatkov.

Z neporušnimi preiskavami smo preverili možnost zaznavanja teksture in morfologije zidov. Prek simulirane seizmične obremenitve s cikličnim strižnim testom (glej sliki 2 in 3) smo preverili še možnost zaznavanja odstopanja ometa in nastanka razpok. Poleg neobremenjenega zidu smo spremljali dve stanji obremenitve. Prvo stanje ustreza začetnemu odstopanju ometa in pojavu prvih razpok (prvo in drugo mejno stanje ometa iz preglednice 1), drugo stanje pa ustreza močno poškodovanemu oz. odstopanemu ometu (tretje mejno stanje ometa iz preglednice 1).

Za validacijo učinkovitosti zaznavanja odstopanja ometa smo uporabili tako vizualen pregled kot tudi 3D fotogrametrično tehniko.

6.5.2 Rezultati

Vizualizacija morfologije zidov

Morfologijo trislojnih zidov smo jasno zaznali z georadarskih meritev, kot je prikazano na sliki 4. Iz georadarskega profila in grafičnega prikaza prereza je razvidno, da se odboji pojavijo v vsaki drugi vrsti, kjer ni povezovalnih kamnitih blokov. Sklepamo lahko, da je razlika v dielektrični konstanti med malto in kamnom dovolj velika, da lahko zaznamo odbiti signal. Rezultati na sliki 4 še kažejo, da smo z veliko natančnostjo lahko določili debelino zidov.

Vizualizacija teksture zidov

Pri zaznavanju anomalij zelo blizu površja smo z georadarjem omejeni z vertikalno ločljivostjo antene in tudi z reaktivno cono, kjer je možna induktivna sklopitev odbitega valovanja s poljem antene. Kljub temu smo podometno teksturo zidu lahko zaznali z grafičnega prikaza prereza na globini 1,3 cm (slika 5a). Teksturo bistveno slabše zaznamo, če je pri meritvi medsebojni razmik med vzporednimi georadskimi profili 10 cm (slika 5b). Iz slike 5 je še razvidno, da dobimo pri IRT s faznimi slikami veliko boljšo ločljivost, kot je to možno s termogrami (slikami površinskih temperatur).

Zaznavanje odstopanja ometa in širjenja razpok z metodo gručenja

Na sliki 6 so prikazani rezultati georadarske in IRT meritve pri posameznih stanjih obremenitve zidu kot tudi rezultati fotogrametrične preiskave. Tako georadarski kot termografski rezultati kažejo, da se z večanjem strižne sile površina odstopanega ometa veča – pri georadarju to vidimo iz večjih amplitud, pri faznih slikah pa iz večjih faz. Kljub temu pa se natančnost zaznavanja med metodama bistveno razlikuje. Iz primerjave z rezultati fotogrametrične preiskave vidimo, da lahko z IRT zaznamo 2 mm zračno rego že v prvem stanju obremenitve zidu, medtem ko georadar zazna odstopanje v velikosti 8 mm šele v drugem stanju obremenitve.

Razpoke smo zaznali na faznih slikah pri višjih frekvencah, saj so te občutljive na manjše temperaturne kontraste, medtem ko smo odstopanje ometa vselej zaznali pri najnižji frekvenci. Primer zaznane površinske razpoke v drugem stanju obremenitve zidu je prikazan za IR fazno sliko pri višji frekvenci ($2,22 \cdot 10^{-3}$ Hz) na sliki 8. Slika 8 še prikazuje odstopanje ometa, ki smo ga zaznali na georadarskem grafičnem prikazu prereza in IR fazni sliki pri osnovni frekvenci ($3,7 \cdot 10^{-4}$ Hz). Kot je prikazano na sliki 9 smo z IR faznimi slikami pri višjih frekvencah lahko zaznali tudi podometne razpoke.

Zaradi kompleksne strukture samega zidovja anomalij nismo mogli kvantitativno karakterizirati z uporabo pulzno-fazne termografije. V praksi bi za zaznavanje anomalij v večslojnih zidovih tako bilo potrebno združevanje georadarskih in termografskih rezultatov, vendar ne po globini. V našem primeru smo združevanje z gručenjem zato izvedli na nivoju posamezne slikovne točke za

segmentacijo združenih georadarskih in IR slik. Rezultat na sliki 8 pokaže, da lahko z gručenjem (z algoritmom GK) zaznamo tako odstopan omet kot tudi površinsko razpoko. Z uteženim povprečjem razpoke ne moremo zaznati.

6.6 Neporušne preiskave laboratorijskega opečnatega zidu pod vplivom različne vlažnosti

6.6.1 Eksperimentalne metode in materiali

Neporušne tomografske preiskave smo izvedli na laboratorijskem opečnatem zidu dimenzije $139 \times 99 \times 74\,\mathrm{cm}^3$. Preizkušanec vsebuje votline različnih velikosti. Tomografske preiskave smo izvedli za prerez zidu čez največjo votlino dimenzije $27 \times 27 \times 27\,\mathrm{cm}^3$ – glej sliko 1 v prilogi C (v nadaljevanju poglavja 6.6 sklicevanje opuščam). Raziskavo vpliva vlažnosti na zaznavanje votline z georadarjem, ultrazvočno metodo in geoelektrično (kompleksno-uporovno) metodo smo izvedli za dve vlažnosti (za 3 in 8 masnih %). Preizkušanec pri 3 masnih % vlažnosti imenujemo suh, pri 8 masnih % pa vlažen.

Georadarske meritve smo opravili z georadarskim sistemom SIRveyor SIR-20 podjetja GSSI. Uporabili smo ločeni oddajni in sprejemni anteni s središčno frekvenco 1,5 GHz. Točkovne meritve smo z vseh strani preizkušanca zajemali na razmiku 13 cm na suhem zidovju in 5 cm na vlažnem (glej sliki 2 in 3).

Ultrazvočno tomografijo smo opravili z longitudinalnimi piezoelektričnimi senzorji tipa Acsys SO202, ki oddajajo zvočno valovanje s frekvenco 25 kHz. Uporabili smo 40 μs dolg kvadratni pulz s frekvenco ponavljanja 20 Hz. Dober stik senzorja s preizkušancem smo zagotovili z uporabo vazelina. Postopek meritve je bil enak kot pri georadarski tomografiji.

Geoelektrične meritve smo izvedli z dvema merilnima opremama – SIP256c in LGM 4-Point-Light (prva za razliko od druge uporablja višje napetosti in deluje v širšem frekvenčnem območju). Uporabili smo tri geometrijske razporeditve elektrod: dipol-dipol, Wenner in Wenner-Schlumberger (slika 2.2 v poglavju 2). Meritve smo zajemali s pomočjo EKG elektrod na razmiku 5 cm.

6.6.2 Rezultati

Rezultati georadarske in ultrazvočne tomografije

Za potrebe tomografskega računa smo iz vseh točkovnih georadarskih in ultrazvočnih meritev določili čas prvega prispelega signala. Ker je izbira začetnega časa lahko podvržena vplivu različnih napak, smo izvedli kalibracijske meritve valovanja v zraku. Opravili smo tudi kontrolo hitrosti valovanja in recipročnosti posamezne meritve. Hitrost valovanja smo izračunali iz znane razdalje med oddajnikom in sprejemnikom ter izmerjenega časa, s kontrolo recipročnosti pa smo preverili razliko v potovalnem času za nasprotno postavljena pretvornika (slika 4). Iz slike 6 je razvidno, da imajo hitrosti, izračunane na podlagi večjih razdalj, večji raztros vrednosti zaradi večjega števila sipanj in lomov valovanja. Večji raztros izračunanih hitrosti izkazuje tudi vlažni

preizkušanec v primerjavi s suhim. To potrjujejo tudi rezultati kontrole recipročnosti (slika 7), ki tudi izključujejo vpliv večjih sistematičnih napak na meritev. Preglednica 1 kaže, da imajo ultrazvočni rezultati na suhem in vlažnem zidovju večji raztros vrednosti kot rezultati georadarske preiskave. Vidimo tudi, da je ultrazvočna metoda bolj občutljiva na spremembe vlažnosti zidovja kot georadar.

Tomografske slike, ki kažejo porazdelitev hitrosti EM in ultrazvočnega valovanja v obravnavanem prerezu preizkušanca, so prikazane na sliki 8. Rezultati na slikah potrjujejo zgornje ugotovitve, da večje razlike nastopijo v porazdelitvi hitrosti zvočnega valovanja. Slabše delovanje ultrazvočne metode napram georadarju pri zaznavanju votline lahko razumemo kot posledico različnega načina potovanja valovanja (zvočno valovanje praktično ne potuje skozi zračno votlino, medtem ko EMV potuje). Preglednica 2 kaže, da so hitrosti obeh valovanj v vlažnem zidovju manjše od hitrosti v suhem zidovju (povprečna hitrost EMV v suhem zidovju je 0,13 m/ns, v vlažnem 0,10 m/ns, povprečna hitrost zvočnega valovanja v suhem zidovju pa je 3100 m/s, v vlažnem 2800 m/s). Iz slike 8 še vidimo, da ima vlažnost zidovja pomembnejšo vlogo na način zaznavanja votline kot sam inverzni postopek.

Način zaznavanja votline v odvisnosti od vlažnosti zidovja z obema metodama smo kvantitativno ovrednotili z enačbama (7) in (8). Preglednica 2 kaže, da se sposobnost zaznavanja v vlažnem zidovju za georadarsko tomografijo zmanjša za 9 %, medtem ko je ta padec v primeru ultrazvočne tomografije 14 %.

Rezultati geoelektrične tomografije

Meritve specifične upornosti so bile v splošnem precej zašumljene, najverjetneje zaradi slabega stika elektrod s preizkušancem in zaradi majhnih tokov pri meritvi. To se je še posebej pokazalo za merilno opremo SIP256c, zato v članku prikazujemo le rezultate meritev z merilno opremo LGM 4-Point-Light. Na sliki 10 so za merjeni prerez prikazane amplitude specifične upornosti za Wennerjevo razporeditev elektrod, ki se je v preiskavi večjega števila geometrijskih razporeditev elektrod izkazala kot najustreznejša. Faz kompleksne specifične upornosti nismo mogli upoštevati kot merodajen rezultat zaradi majhnega razmerja signala proti šumu. Iz slike 10 je razvidno, da so vrednosti amplitud specifične upornosti suhega zidovja med 400 in 700 Ωm, za vlažno zidovje pa se vrednosti amplitud gibljejo med 12 in 24 Ωm.

Razvidno je, da spodnjega robu votline z geoelektrično tomografijo ne moremo natančno določiti. To je posledica slabše globinske ločljivosti geoelektrične metode glede na georadar in ultrazvočno metodo. Kljub temu lahko votlino zaznamo že pri suhem zidovju (z 20 % zanesljivostjo), na vlažnem zidovju pa se sposobnost zaznavanja enkrat poveča.

6.7 Neporušne preiskave z večsenzorskim robotnim sistemom BetoScan

Večsenzorski robotni sistem BetoScan [160] je bil razvit v okviru projekta BetoScan (www.betoscan.de). Na inštitutu BAM sistem uporabljajo za neporušne preiskave večjih betonskih površin (v garažnih hišah in na mostovih), ki so poškodovane zaradi korozije armature. Glavni namen preiskav je določitev con poškodovanosti z večjim številom senzorjev, kot prikazuje slika 7 v

prilogi A (sklicevanje na prilogo v nadaljevanju poglavja 6.7 opuščam). Metode gručenja smo zato uporabili na nivoju posamezne slikovne točke za segmentacijo združenih slik EM potencialne metode, metode z vrtinčnimi tokovi in dveh mikrovalovnih merilcev vlage.

6.7.1 Eksperimentalne metode in materiali

Analizirali smo rezultate meritev armirane plošče določene garažne hiše v Nemčiji. Površina preiskovanega območja je merila $5 \times 7\,\mathrm{m}^2$. Razmik med sledmi vozila je znašal 20 cm, med posameznimi točkovnimi meritvami pa 1 cm.

Za EM potencialno metodo, ki meri elektrokemijski potencial armature glede na referenčno elektrodo, smo uporabili napravo Canin+ podjetja Proceq v kombinaciji z referenčno elektrodo $Cu/CuSO_4$. Za metodo z vrtinčnimi tokovi smo uporabili napravo Profometer 5+ podjetja Proceq, ki na podlagi elektromagnetne indukcije omogoča tako lokalizacijo armature kot tudi določitev debeline krovnega sloja betona. Za meritev relativne vlažnosti betona smo uporabili dva mikrovalovna merilca podjetja HF-Sensor – Moist RP (globina penetracije je 4 cm) in Moist PP (globina penetracije je 20 cm).

Za validacijo rezultatov metod iz sistema BetoScan smo uporabili rezultate radar-magnetne metode [161]. S to metodo lahko določimo realno in imaginarno komponento dielektrične konstante preiskovanega materiala.

6.7.2 Rezultati

Na sliki 8a območja z vrednostjo elektrokemijskega potenciala pod -300 mV nakazujejo na visoko verjetnost korozije armature v plošči. Glede na to, da sta za pojav korozije armature odgovorna tako karbonatizacija betona (kot posledica majhnega krovnega sloja betona) kot tudi velika koncentracija kloridnih ionov, smo rezultate EM potencialne metode skušali razložiti z rezultati metode z vrtinčnimi tokovi in z rezultati meritve vlažnosti. S prvo metodo dobljene meritve krovnega sloja betona kažejo, da je za pojav korozije na določenih mestih odgovorna karbonatizacija betona (slika 8b), medtem ko je rezultate meritve vlažnosti težje interpretirati (sliki 8c in 8d). Boljšo korelacijo s koncentracijo kloridnih ionov v betonu da meritev z radar-magnetno metodo, in sicer rezultati imaginarne komponente dielektrične konstante (slika 8f).

Razvidno je, da stopnje poškodovanosti armirane plošče zaradi korozije ne moremo oceniti na podlagi ločene interpretacije rezultatov posamezne metode. Za različne kombinacije neporušnih metod smo zato z gručenjem opravili segmentacijo merjenega območja na cone poškodovanosti. Rezultate prikazujemo za algoritem GK s parametrom $\gamma = 0,1$, ki se je že na rezultatih laboratorijskih betonskih preizkušancev izkazal kot najustreznejši. Kot je razvidno iz slike 9, lahko s celotnim večsenzorskim sistemom BetoScan z veliko natančnostjo določimo tri cone poškodovanosti armirane plošče zaradi korozije.

6.8 Uporaba metod gručenja za avtomatsko klasifikacijo spektroskopskih podatkov na betonskih preizkušancih

Spektroskopijo lasersko inducirane plazme (LIBS) na inštitutu BAM uporabljajo za določitev koncentracije in porazdelitve klora, natrija in žvepla v vzorcih z betonskih konstrukcij. Pri tem ima ključno vlogo določitev spektrov, ki pripadajo le cementni matriki. Za ta namen smo preverili uporabo metod gručenja.

6.8.1 Eksperimentalne metode in materiali

LIBS, ki ga uporablja inštitut BAM, je shematično predstavljen na sliki 1 v prilogi D (v nadaljevanju poglavja 6.8 sklicevanje na prilogo opuščam). Za izvor svetlobe služi laser Nd:YAG (Innolas Spitlight 600) v kombinaciji s sistemom leč. Za odstranitev prašnatih delcev in ojačenje signala uporabljajo helij. Zaznavanje svetlobe omogoča spektrometer tipa Shamrock 303i z detektorjem CCD. Premikanje vzorca omogoča translacijska mizica.

Uporabo gručenja za klasifikacijo spektroskopskih podatkov smo preverili na večjem številu vzorcev. V delu podrobneje prikazujemo rezultate z laboratorijskega preizkušanca, na katerem so bili opravljeni testi alkalno-silikatne reakcije v 3,6 % raztopini NaCl pri 40 °C. Globinski prerez preizkušanca je prikazan na sliki 2. Za pripravo preizkušanca smo uporabili agregat iz kremenovega peščenjaka ter cement tipa CEM I. Spektroskopsko meritev smo opravili na površini $94,5 \times 95\,\mathrm{mm}^2$, pri ločljivosti 0,5 oz. 1 mm.

6.8.2 Rezultati

Za gručenje smo obravnavali naslednje spektralne črte: Ca (849,80 nm), O (844,64 nm), Na (818,32 nm), Cl (837,59 nm), C (833,52 nm) in Ti (846,85 nm). Normalizirane intenzitete posamezne spektralne črte prikazujemo na sliki 4. Razvidno je, da je stopnja heterogenosti preizkušanca visoka. Zato smo za referenčno klasifikacijo vzorca na območje agregata in cementne matrike (slika 6) uporabili tako rezultate standardizirane metode klasifikacije, ki uporablja spektralni črti Ca in O, kot tudi natančen vizualni pregled vzorca.

Na podlagi dveh kazalcev (XB in S) [153] smo določili, da je optimalno število razredov za gručenje 5. Rezultati gručenja so predstavljeni na sliki 7. Razvidno je, da algoritem z dodatnim razredom za najbolj zašumljene podatke (NCFCM) pravilno zbere točke, ki imajo visoko intenziteto natrijeve spektralne črte (slika 7d). Iz slike 7 še opazimo koincidenčni problem algoritma PCM s kazenskim členom (slika 7e). Delovanje vseh algoritmov je strnjeno v preglednici 1. Razvidno je, da sta za segmentacijo vzorca najuspešnejša algoritma NCFCM in PFCM.

V praksi se spektroskopska meritev vzorcev izvaja pri ločljivosti 1 oz. 2 mm. Zato smo za to ločljivost preverili klasifikacijo spektroskopskih podatkov za določitev koncentracije natrijevih ionov kot posledica alkalno-silikatne reakcije. Globinski profil intenzitete natrijeve spektralne črte na sliki 8 kaže, da je klasifikacija podatkov z vsemi obravnavanimi metodami mehkega gručenja natančna. Klasifikacija s standardizirano metodo, ki uporablja spektralni črti Ca in O, močno odstopa od referenčne klasifikacije.

Za popolno avtomatizacijo postopka klasifikacije spektroskopskih podatkov z algoritmoma NC-FCM in PFCM predlagamo uporabo kazalca XB. Za PFCM je merodajen njegov globalni minimum, medtem ko je za NCFCM vrednost kazalca potrebno omejiti okoli 1.

6.9 Zaključki in obeti

Glavni namen disertacije je bil razviti ustrezen postopek za združevanje slik, ki bi temeljil na metodah gručenja in bi omogočil učinkovito in zanesljivo obdelavo podatkov večsenzorskih neporušnih preiskav gradbenih konstrukcijskih elementov. V delu sem opisala uporabo gručenja za združevanje podatkov večsenzorskih neporušnih preiskav laboratorijskih betonskih in zidanih preizkušancev. Metode gručenja smo uporabili tudi v dveh aplikativnih ogrodjih združevanja podatkov: za združevanje podatkov večsenzorskega robotnega sistema BetoScan ter za popolnoma avtomatizirano klasifikacijo spektroskopskih podatkov betonskih preizkušancev.

Osrednje področje naloge je bila uporaba metod združevanja podatkov na rezultatih georadarskih in IRT meritev betonskih in zidanih preizkušancev. Namen združevanja podatkov je bil izboljšati zaznavanje različnih anomalij v območju blizu površja. V sklopu preiskav smo izvedli tudi obsežno analizo občutljivosti obeh metod. Na betonskih preizkušancih analiza pokaže, da je občutljivost georadarja do 3–4,5 cm globine manjša, kot je občutljivost IRT. IRT v splošnem izkazuje počasno slabšanje sposobnosti zaznavanja do 7,5 cm, kar je predvsem posledica uporabe fazno-kontrastnih slik. Za obe metodi ugotovimo, da ima ključno vlogo pri materialni karakterizaciji anomalij razlika v dielektrični konstanti oz. toplotni prevodnosti med anomalijo in preiskovanim materialom. Zaradi tega georadar natančneje zazna vodno anomalijo kot zračno, obratno pa velja za IRT.

Uporaba metod gručenja za združevanje podatkov na nivoju značilnic kaže, da najboljše deluje algoritem GK s parametrom $\gamma = 0,1$. S tem algoritmom in parametrom smo hkrati dosegli robustno delovanje metode, obenem pa tudi najbolje zaznali plastične cevi v betonu. Z GK smo cevi lahko zaznali, ker algoritem prepoznava razrede poljubne oblike in ne le sferične kot FCM in PFCM. Slednja algoritma sta v splošnem pokazala zelo podobno delovanje, kar pomeni, da ima pri preiskovanju tipičnih anomalij v betonskih konstrukcijskih elementih šum manjšo vlogo. Primerjava z rezultati simbolnega združevanja potrjuje, da metode gručenja delujejo robustno pri združevanju podatkov v primerih s še posebno omejenim vedenjem o sestavi strukture preizkušanca.

Hkratna uporaba georadarja in IRT je omogočila tudi celostno karakterizacijo strukture ometanih kamnitih zidov. Poleg morfologije in teksture zidov smo lahko zaznali tudi odstopanje ometa. Izkaže se, da lahko IRT zazna odstopanje, ki ustreza prvemu mejnemu stanju ometa (≈ 2 mm rega), medtem ko georadar zazna šele velikost odstopanja za tretje mejno stanje (≈ 8 mm rega). Pri IRT smo s faznimi slikami pri višjih frekvencah lahko zaznali tudi površinske in podometne razpoke, medtem ko smo odstopanje ometa in teksturo zidu zaznali na faznih slikah pri najnižji frekvenci. V primeru preiskovanja zidovja se izkaže, da zaradi njegove heterogene strukture ne moremo uporabiti kvantitativnih tehnik obdelave termografskih podatkov, ki so uporabne na betonu. Zato predlagamo združevanje georadarskih in IR podatkov na nivoju posamezne slikovne

točke, in sicer za segmentacijo slik. Tako lahko uspešno zaznamo odstopan omet in razpoke.

Meritev vpliva vlažnosti zidovja na zaznavanje votline z georadarsko, ultrazvočno in geoelektrično tomografijo pokaže, da je ultrazvočna metoda bolj občutljiva kot georadar na spremembe vlažnosti. Ultrazvočni podatki imajo obenem tudi večji raztros vrednosti kot georadarski podatki. Najbolj zanesljiva neporušna metoda za zaznavanje votline v suhem in vlažnem zidovju je georadar. Za ultrazvočno tomografijo opazimo, da je za uspešno zaznavanje votline potreben daljši čas merjenja in natančna določitev časa prvega prispelega signala. Tudi z geoelektrično tomografijo lahko zaznamo votlino pri obeh vlažnostih zidovja, vendar ima metoda slabšo globinsko ločljivost v primerjavi z georadarjem in ultrazvokom. Dodatne težave povzroča slab stik med elektrodami in preizkušancem.

Metode gručenja smo uspešno uporabili v dveh sistemih za segmentacijo podatkov neporušnih preiskav. Za identifikacijo cementne matrike v betonskih preizkušancih na podlagi spektroskopskih (LIBS) podatkov najboljše delovanje izkazujeta algoritma NCFCM in PFCM. S predlaganim optimizacijskim postopkom dosežemo popolnoma avtomatizirano klasifikacijo podatkov, kar ima ključen pomen za prenos tehnike LIBS v prakso. Na podatkih večsenzorskega robotnega sistema BetoScan metode gručenja omogočijo določitev con poškodovanosti armirane plošče zaradi korozije.

Na podlagi zgornjih ugotovitev lahko zaključimo, da so metode gručenja dovolj robustne, da jih lahko implementiramo v različne večsenzorske sisteme za neporušne preiskave v gradbeništvu. Njihova prednost je, da jih lahko v celoti avtomatiziramo, kar ima ključen pomen pri prenosu neporušnih preiskav v prakso v obliki uporabniku preproste, a vendar zanesljive interpretacije podatkov.

REFERENCES

[1] Büyüköztürk, O. (ed.), Taşdemir, M. A. (ed.), Güneş, O. (ed.), Akkaya, Y. (ed.). 2013. Nondestructive Testing of Materials and Structures, RILEM Bookseries, Vol. 6. Springer Netherlands: 1278 p.

[2] Whiting, D., Todres, A., Nagi, M., Yu, T., Peshkin, D., Darter, M., Holm, J., Andersen, M., Geiker, M. 1993. Synthesis of Current and Projected Concrete Highway Technology. Strategic Highway Research Program. Washington, DC, National Research Council: 286 f.

[3] Rhazi, J. 2001. NDT in civil engineering: the case of concrete bridge decks. e-Journal of Nondestructive Testing & Ultrasonics 6, 5. http://www.ndt.net/article/v06n05/rhazi/rhazi.htm (Accessed 20 December 2013).

[4] Banville, M. H. 2008. Assessment and repair of concrete structures. In: RCI's 23rd Int. Convention & Trade Show, Phoenix, Arizona, Feb 28 – Mar 4, 2008. pp. 1–9. http://www.rci-online.org/interface/2008-07-banville.pdf (Accessed 14 February 2014).

[5] Verma, S. K., Bhadauria, S. S., Akhtar, S. 2013. Review of nondestructive testing methods for condition monitoring of concrete structures. Journal of Construction Engineering 2013: 1–11.

[6] Wiggenhauser, H. 2009. Advanced NDT methods for quality assurance of concrete structures. In: Abraham, O. (ed.), Derobert, X. (ed.). Proc. of the 7th Int. Symp. on NDT in Civil Engineering (NDTCE'09), Nantes, France, Jun 30 – Jul 3, 2009. Nantes, LCPC: pp. 1–12. http://www.ndt.net/article/ndtce2009/papers/1002.pdf (Accessed 19 February 2012).

[7] Schutter, G. D. 2012. Damage to Concrete Structures. Boca Raton, FL, CRC Press: 209 p.

[8] Wiggenhauser, H., Taffe, A. 2012. NDT in civil engineering: research, application, validation and training. In: Manfred, J. (ed.). Proc. of the 18th World Conf. on Nondestructive Testing, Durban, South Africa, Apr 16–20, 2012. SAINT: pp. 1–13. http://www.ndt.net/article/wcndt2012/papers/612_wcndtfinal00611.pdf (Accessed 14 February 2014).

[9] Binda, L., Saisi, A. 2009. Application of NDTs to the diagnosis of historic structures. In: Abraham, O. (ed.), Derobert, X. (ed.). Proc. of the 7th Int. Symp. on NDT in Civil Engineering (NDTCE'09), Nantes, France, Jun 30 – Jul 3, 2009. Nantes, LCPC: pp. 1–28. http://ndt.net/article/ndtce2009/papers/1005.pdf (Accessed 19 February 2012).

[10] Breysse, D. (ed.). 2012. Non-Destructive Assessment of Concrete Structures: Reliability and Limits of Single and Combined Techniques, State-of-the-Art Report of the RILEM Technical Committee 207-INR, RILEM State-of-the-Art Reports, Vol. 1. Springer Netherlands: 374 p.

[11] McCann, D. M., Forde, M. C. 2001. Review of NDT methods in the assessment of concrete and masonry structures. NDT&E Int. 34, 2: 71–84.

[12] Wiggenhauser, H. 2009. Automated NDE of PT concrete structures. In: NDT presentations, ACI, Seville, Spain, Oct 15, 2009. http://www.germann.org/Publications/Sevilla/Automated%20NDE%20of%20PT%20concrete%20structures,%20Wiggenhauser.pdf (Accessed 19 February 2012).

[13] Maierhofer, C., Wöstmann, J. 1998. Investigation of dielectric properties of brick materials as a function of moisture and salt content using a microwave impulse technique at very high frequencies. NDT&E Int. 31, 4: 259–263.

[14] Maierhofer, C., Zacher, G., Kohl, C., Wöstmann, J. 2008. Evaluation of radar and complementary echo methods for NDT of concrete elements. J. Nondestruct. Eval. 27, 1–3: 47–57.

[15] Tsui, F., Matthews, S. L. 1997. Analytical modelling of the dielectric properties of concrete for subsurface radar applications. Constr. Build. Mater. 11, 3: 149–161.

[16] Maierhofer, C., Kind, T. 2003. Application of georadar for the determination of moisture content and distribution of masonry. In: Binda, L. (ed.), de Vekey, R. C. (ed.). Proc of the Int. RILEM Workshop on On Site Control and Non Destructive Evaluation of Masonry Structures and Materials, Mantova, Italy, Nov 12–14, 2003. Bagneux, RILEM: pp. 227–238.

[17] Maierhofer, C., Leipold, S. 2001. Radar investigation of masonry structures. NDT&E Int. 34, 2: 139–147.

[18] Krause, M., Maierhofer, C., Wiggenhauser, H. 1995. Thickness measurement of concrete elements using radar and ultrasonic impulse echo techniques. In: Forde, M. C. (ed.). Proc. of the 6th Int. Conf. on Structural Faults and Repair, London, U.K., Jul 3, 1995, Vol. 1. Edinburgh, Engineering Technics Press: pp. 17–24.

[19] Afshari, A., Frazer, D., Creese, R. 1996. Ultrasonic techniques for the bonding of rebar in concrete structure. In: Hartbower, P. E. (ed.), Stolarski, P. J. (ed.). Structural Materials Technology – An NDT Conference, San Diego, U.S.A., Feb 20–23, 1996. Lancaster, Basel, Technomic Publishing Co., Inc.: pp. 3–8.

[20] Krause, M., Mielentz, F., Milmann, B., Streicher, D., Müller, W. 2003. Ultrasonic imaging of concrete elements: state of the art using 2d synthetic aperture. In: Proc. of the Int. Symp. Non-Destructive Testing in Civil Engineering (NDTCE 2003), Berlin, Germany, Sep 16–19, 2003. Berlin, DGZfP: V51, BB 85-CD.

[21] Hévin, G., Abraham, O., Pedersen, H. A., Campillo, M. 1998. Characterization of surface cracks with rayleigh waves: a numerical model. NDT& E Int. 31, 4: 289–297.

[22] Krause, M., Milmann, B., Mielentz, F., Streicher, D., Redmer, B., Mayer, K., Langenberg, K.-J., Schickert, M. 2008. Ultrasonic imaging methods for investigation of post-tensioned concrete structures: a study of interfaces at artificial grouting faults and its verification. J. Nondestruct. Eval. 27, 1–3: 67–82.

[23] Im, S. B., Hurlebaus, S., Trejo, D. 2010. Inspection of voids in external tendons of post-tensioned bridges. Transport. Res. Rec. 2172: 115–122.

[24] Krause, M., Mayer, K., Friese, M., Milmann, B., Mielentz, F., Ballier, G. 2011. Progress in ultrasonic tendon duct imaging. Eur. J. Environ. Civ. En. 15, 4: 461–485.

[25] Tinkey, Y., Olson, L. D., Wiggenhauser, H. 2005. Impact echo scanning for discontinuity detection and imaging in posttensioned concrete bridges and other structures. Mater. Eval. 63, 1: 64–69.

[26] Ata, N., Mihara, S., Ohtsu, M. 2007. Imaging of ungrouted tendon ducts in prestressed concrete by improved SIBIE. NDT&E Int. 40, 3: 258–264.

[27] Beutel, R., Reinhardt, H. W., Grosse, C. U., Glaubitt, A., Krause, M., Maierhofer, C., Algernon, D., Wiggenhauser, H., Schickert, M. 2008. Comparative performance tests and validation of NDT methods for concrete testing. J. Nondestruct. Eval. 27, 1–3: 59–65.

[28] Sadri, A. 2003. Application of impact-echo technique in diagnoses and repair of stone masonry structures. NDT&E Int. 36, 4: 195–202.

[29] Cantini, L. 2011. Research on the construction roles of ancient buildings: use of appropriate diagnostic non-destructive techniques. Doctoral Dissertation. Milano, (L. Cantini): 323 f.

[30] Uranjek, M. 2011. Propadanje in trajnostna obnova ovoja stavbne dediščine (Degradation and sustainable renovation of heritage buildings envelope). Doktorska disertacija (Doctoral Dissertation). Ljubljana, (M. Uranjek): 261 f.

[31] Maierhofer, C., Röllig, M., Arndt, R. 2009. Non-destructive testing of concrete and masonry structures using active thermography – influence of surface and bulk properties. Mater. Test. 51, 9: 587–592.

[32] Bosiljkov, V., Maierhofer, C., Köpp, C., Wöstmann, J. 2010. Assessment of structure through non-destructive tests (NDT) and minor destructive tests (MDT) investigation: Case study of the church at carthusian monastery at Zice (Slovenia). Int. J. Archit. Herit. 4, 1: 1–15.

[33] Bosiljkov, V., Uranjek, M., Žarnić, R., Bokan-Bosiljkov, V. 2010. An integrated diagnostic approach for the assessment of historic masonry structures. J. Cult. Herit. 11, 3: 239–249.

[34] Arndt, R., Maierhofer, C., Röllig, M., Weritz, F., Wiggenhauser, H. 2004. Structural investigation of concrete and masonry structures behind plaster by means of pulse phase thermography. In: Proc. of the 7th Int. Conf. on Quantitative Infrared Thermography (QIRT), Rhode-St.-Genese, Belgium, Jul 5–8, 2004. pp. 1–6.

[35] Maierhofer, C., Röllig, M. 2009. Active thermography for the characterization of surfaces and interfaces of historic masonry structures. In: Abraham, O. (ed.), Derobert, X. (ed.). Proc. of the 7th Int. Symp. on NDT in Civil Engineering (NDTCE'09), Nantes, France, Jun 30 – Jul 3, 2009. Nantes, LCPC: pp. 1–6.
http://www.ndt.net/article/ndtce2009/papers/17.pdf (Accessed 20 February 2012).

[36] Avdelidis, N. P., Moropoulou, A. 2004. Applications of infrared thermography for the investigation of historic structures. J. Cult. Herit. 5, 1: 119–127.

[37] Avdelidis, N. P., Koui, M., Ibarra-Castanedo, C., Maldague, X. 2007. Thermographic studies of plastered mosaics. Infrared Phys. & Techn. 49, 3: 254–256.

[38] Theodorakeas, P., Ibarra-Castanedo, C., Sfarra, S., Avdelidis, N. P., Koui, M., Maldague, X., Paoletti, D., Ambrosini, D. 2012. NDT inspection of plastered mosaics by means of transient thermography and holographic interferometry. NDT&E Int. 47: 150–156.

[39] Wild, W., Buscher, K., Wiggenhauser, H. 1998. Amplitude sensitive modulation-thermography to measure moisture in building materials. In: Snell, J. (ed.), Wurzbach, R. (ed.). Thermosense XX, Vol. 3361, Proc. of SPIE, Orlando, FL, U.S.A., Apr 13, 1998. SPIE: pp. 156–163.

[40] Maierhofer, C., Krankenhagen, R., Röllig, M., Schlichting, J., Schiller, M., Seidl, T., Mecke, R., Kalisch, U., Hennen, C., Meinhardt, J. 2010. Investigating historic masonry structures at different depths with active thermography. In: Maldague, X. (ed.). Proc. of the 10th Int. Conf. on Quantitative Infrared Thermography (QIRT10), Québec, Canada, Jul 27–30, 2010. Les Éboulements, É. du CAO: pp. 1–7.

[41] Maierhofer, C., Brink, A., Röllig, M., Wiggenhauser, H. 2002. Transient thermography for structural investigation of concrete and composites in the near surface region. Infrared Phys. Techn. 43, 3–5: 271–278.

[42] Maierhofer, C., Wiggenhauser, H., Brink, A., Röllig, M. 2004. Quantitative numerical analysis of transient IR-experiments on buildings. Infrared Phys. Techn. 46, 1–2: 173–180.

[43] Maierhofer, C., Arndt, R., Röllig, M., Rieck, C., Walther, A., Scheel, H., Hillemeier, B. 2006. Application of impulse-thermography for non-destructive assessment of concrete structures. Cement Concrete Comp. 28, 4: 393–401.

[44] Weritz, F., Arndt, R., Röllig, M., Maierhofer, C., Wiggenhauser, H. 2005. Investigation of concrete structures with pulse phase thermography. Mater. Struct. 38, 283: 843–849.

[45] Maierhofer, C., Arndt, R., Röllig, M. 2007. Influence of concrete properties on the detection of voids with impulse-thermography. Infrared Phys. Techn. 49, 3: 213–217.

[46] Shokouhi, P., Zoega, A., Wiggenhauser, H. 2010. Nondestructive investigation of stress-induced damage in concrete. Advances in Civil Engineering 2010: 9.

[47] Saenger, E. H., Kocur, G. K., Jud, R., Torrilhon, M. 2011. Application of time reverse modeling on ultrasonic non-destructive testing of concrete. Appl. Math. Model 35, 2: 807–816.

[48] Akevren, S. 2010. Non-destructive examination of stone masonry historic structures – quantitative IR thermography and ultrasonic testing. M. Sc. Thesis. Ankara, (S. Akevren): 126 f.

[49] Maierhofer, C., Krankenhagen, R., Myrach, P., Meinhardt, J., Kalisch, U., Hennen, C., Mecke, R., Seidl, T., Schiller, M. 2013. Monitoring of cracks in historic concrete structures using optical, thermal and acoustical methods. In: Proc. of Built Heritage 2013, Monitoring Conservation Management, Milan, Italy, Nov 18–20, 2013. Milano, Politechnico di Milano: pp. 1–8.

[50] Tung, S. H., Shih, M. H., Sung, W. P. 2008. Development of digital image correlation method to analyse crack variations of masonry wall. Sadhana 33, 6: 767–779.

[51] Salmanpour, A. H., Mojsilović, N. 2013. Application of digital image correlation for strain measurements of large masonry walls. In: Proc. of the APCOM & ISCM, Singapore, Dec 11–14, 2013. APACM, IACM: pp. 1–7.

[52] Hall, D. L., Llinas, J. 1997. An introduction to multisensor data fusion. In: Proc. of the IEEE, Vol. 85, 1. IEEE: pp. 6–23.

[53] Liu, Z., Forsyth, D. S., Komorowski, J. P., Hanasaki, K., Kirubarajan, T. 2007. Survey: state of the art in NDE data fusion techniques. IEEE T. Instrum. Meas. 56, 6: 2435–2451.

[54] Krause, M., Bärmann, M., Frielinghaus, R., Kretzschmar, F., Kroggel, O., Langenberg, K., Maierhofer, C., Müller, W., Neisecke, J., Schickert, M., Schmitz, V., Wiggenhauser, H., Wollbold, F. 1997. Comparison of pulse-echo methods for testing concrete. NDT&E Int. 30, 4: 195–204.

[55] Pöpel, M., Flohrer, C. 1995. Combination of a covermeter with a radar system – an improvement of radar application in civil engineering. In: Schickert, G. (ed.), Wiggenhauser, H. (ed.). Proc. of the Int. Symp. on Non-Destructive Testing in Civil Engineering (NDT-CE), Berlin, Germany, Sep 26–28, 1995. Berlin, DGZfP: pp. 737–743.

[56] Dérobert, X., Aubagnac, C., Abraham, O. 2002. Comparison of NDT techniques on a post-tensioned beam before its autopsy. NDT&E Int. 35, 8: 541–548.

[57] Naumann, J., Haardt, P. 2003. NDT methods for the inspection of highway structures. In: Proc. of the Int. Symp. Non-Destructive Testing in Civil Engineering (NDTCE 2003), Berlin, Germany, Sep 16–19, 2003. Berlin, DGZfP: BB 85-CD.

[58] Goueygou, M., Abraham, O., Lataste, J. F. 2008. A comparative study of two non-destructive testing methods to assess near-surface mechanical damage in concrete structures. NDT&E Int. 41, 6: 448–456.

[59] Wendrich, A., Trela, C., Krause, M., Maierhofer, C., Effner, U., Wöstmann, J. 2006. Location of voids in masonry structures by using radar and ultrasonic traveltime tomography. In: Proc. of the 9th Eur. NDT Conf. (ECNDT 2006), Berlin, Germany, Sep 25–29, 2006, Vol. 11, 11. Berlin, DGZfP: pp. 1–11 (CD-ROM).

[60] Binda, L., Bosiljkov, V., Saisi, A., Zanzi, L. 2006. Guidelines for the diagnostic investigation of historic buildings. In: Proc. of the 7th Int. Masonry Conf., London, UK, Oct 30 – Nov 1, 2006. London, British Masonry Society: pp. 1–10.

[61] Kruschwitz, S., Niederleithinger, E., Trela, C., Wöstmann, J. 2010. Complex resistivity and radar investigation of building material: first results of field scale measurements. Acta Geophys. 58, 1: 96–113.

[62] Gros, X. E. (ed.). 2001. Application of NDT Data Fusion. Boston, Dordrecht, London, Kluwer Academic Publishers: 277 p.

[63] Georgel, B., Lavayssière, B. 1994. Fusion de données: un nouveau concept en cnd. In: Proc. of the 6th Eur. Conf. on NDT, Nice, France, Oct 24–28, 1994, Vol. 1. pp. 31–35.

[64] Gros, X. E., Strachan, P., Lowden, D. W., Edwards, I. 1994. NDT data fusion. In: Proc. of the 6th Eur. Conf. on NDT, Nice, France, Oct 24–28, 1994, Vol. 1. pp. 355–359.

[65] Gros, X. E., Liu, Z., Tsukada, K., Hanasaki, K. 2000. Experimenting with pixel-level NDT data fusion techniques. IEEE T. Instrum. Meas. 49, 5: 1083–1090.

[66] Dong, C. Y., Yuan, Q., Wang, Q. 2010. A combined wavelet analysis-fuzzy adaptive algorithm for radar/infrared data fusion. Expert. Syst. Appl. 37, 3: 2563–2570.

[67] Balakrishnan, S., Cacciola, M., Udpa, L., Rao, B. P., Jayakumar, T., Raj, B. 2012. Development of image fusion methodology using discrete wavelet transform for eddy current images. NDT&E Int. 51: 51–57.

[68] Zhang, Z. L., Wang, Q., Sun, S. H. 1999. A new fuzzy neural network architecture for multisensor data fusion in non-destructive testing. In: Proc. of IEEE Int. Fuzzy Syst. Conf. (FUZZ-IEEE '99), Seoul, South Korea, Aug 22–25, 1999, Vol. 3. IEEE: pp. 1661–1665.

[69] Gros, X. E., Bousigue, J., Takahashi, K. 1999. NDT data fusion at pixel level. NDT&E Int. 32, 5: 283–292.

[70] Horn, D., Mayo, W. R. 2000. NDE reliability gains from combining eddy-current and ultrasonic testing. NDT&E Int. 33, 6: 351–362.

[71] Kaftandjian, V., Zhu, Y. M., Dupuis, O., Babot, D. 2005. The combined use of the evidence theory and fuzzy logic for improving multimodal nondestructive testing systems. IEEE T. Instrum. Meas. 54, 5: 1968–1977.

[72] Ploix, M.-A., Garnier, V., Breysse, D., Moysan, J. 2011. NDE data fusion to improve the evaluation of concrete structures. NDT&E Int. 44, 5: 442–448.

[73] Liu, Z., Forsyth, D. S., Safizadeh, M.-S., Fahr, A. 2008. A data-fusion scheme for quantitative image analysis by using locally weighted regression and Dempster-Shafer theory. IEEE T. Instrum. Meas. 57, 11: 2554–2560.

[74] Li, G., Huang, P., Chen, P., Hou, D., Zhang, G., Zhou, Z. 2011. Application of multisensor data fusion in defects evaluation based on Dempster-Shafer theory. In: Proc. of the 2011 IEEE Instrumentation and Measurement Technology Conference (I2MTC), Binjiang, China, May 10–12, 2011. IEEE: pp. 1–5.
http://www.ndt.net/article/aspnde2009/papers/15.pdf (Accessed 13 February 2012).

[75] Reza, H. P. R., Rezaie, A. H., Sadeghi, S. H. H., Moradi, M. H., Ahmadi, M. 2007. A density-based fuzzy clustering technique for non-destructive detection of defects in materials. NDT&E Int. 40, 4: 337–346.

[76] Kohl, C., Krause, M., Maierhofer, C., Wöstmann, J. 2005. 2D-and 3D-visualisation of NDT-data using data fusion technique. Mater. Struct. 38, 9: 817–826.

[77] Cui, J., Huston, D. R., Arndt, R., Jalinoos, F. 2010. Data fusion techniques of multiple sensors nondestructive evaluation of a concrete bridge deck. In: Proc. of NDE/NDT for Highway Bridges: Structural Materials Technology (SMT) 2010 Conference, New York City, NY, USA, Aug 16–20, 2010.

[78] Bensaid, A. M., Hall, L. O., Bezdek, J. C., Clarke, L. P., Silbiger, M. L., Arrington, J. A., Murtagh, R. F. 1996. Validity-guided (re)clustering with applications to image segmentation. IEEE T. Fuzzy Syst. 4, 2: 112–123.

[79] Santoro, M., Prevete, R., Cavallo, L., Catanzariti, E. 2006. Mass detection in mammograms using gabor filters and fuzzy clustering. In: Bloch, I. (ed.), Petrosino, A. (ed.), Tettamanzi, A. G. B. (ed.). Fuzzy Logic and Applications, Revised Selected Papers on the 6th Int. Workshop, WILF 2005, Crema, Italy, Sep 15–17, 2005. Berlin Heidelberg, Springer: pp. 334–343.

[80] Paasche, H., Tronicke, J., Holliger, K., Green, A. G., Maurer, H. 2006. Integration of diverse physical-property models: subsurface zonation and petrophysical parameter estimation based on fuzzy c-means cluster analyses. Geophysics 71, 3: 33–44.

[81] Paasche, H., Tronicke, J. 2007. Cooperative inversion of 2d geophysical data sets: a zonal approach based on fuzzy c-means cluster analysis. Geophysics 72, 3: 35–39.

[82] MacQueen, J. B. 1967. Some methods for classification and analysis of multivariate observations. In: Cam, L. M. L. (ed.), Neyman, J. (ed.). Proc. of the 5th Berkeley Symp. on Math. Statist. and Prob., Berkeley, U.S.A., Jun 21 – Jul 18, 1965, Dec 27 –Jan 7, 1966, Vol. 1. Berkeley, University of California Press: pp. 281–297.

[83] Bezdek, J. Z. 1981. Pattern Recognition with Fuzzy Objective Function Algorithms. New York, Plenum Press: 256 p.

[84] Dave, R. N. 1991. Characterization and detection of noise in clustering. Pattern. Recogn. Lett. 12, 11: 657–664.

[85] Gustafson, D., Kessel, W. 1979. Fuzzy clustering with a fuzzy covariance matrix. In: 1978 IEEE Conf. on Decision and Control including the 17th Symp. on Adaptive Processes. IEEE: pp. 761–766.

[86] Timm, H., Borgelt, C., Kruse, R. 2001. Fuzzy cluster analysis with cluster repulsion. In: Proc. of the Eur. Symp. on Intelligent Technologies, Hybrid Systems and their implementation on Smart Adaptive Systems, Tenerife, Spain, Dec 13–14, 2001. EUNITE: pp. 1–7 (CD-ROM).

[87] Pal, N. R., Pal, K., Keller, J. M., Bezdek, J. C. 2005. A possibilistic fuzzy c-means clustering algorithm. IEEE T. Fuzzy Syst. 13, 4: 517–530.

[88] Maierhofer, C., Köpp, C., Binda, L., Zanzi, L., Santiago, J. R., Knupfer, B., Johansson, B., Modena, C., Porto, F., Marchisio, M., Gravina, F., Falci, M., Ruiz, J. C., Tomaževič, M., Bosiljkov, V., Hennen, C. 2006. Project Report EUR 21696 EN – Onsiteformasonry project – On-site investigation techniques for the structural evaluation of historic masonry buildings, Deliverable D7.1–D7.4. Luxembourg, European Comission, Office for Official Publications of the European Communities: 139 f.

[89] Sansalone, M. J., Streett, W. B. 1998. The impact-echo method. NDTnet 3, 2: 1–8. http://www.ndt.net/article/0298/streett/streett.htm (Accessed 20 December 2013).

[90] Huang, M., Jiang, L., Liaw, P. K., Brooks, C. R., Seeley, R., Klarstrom, D. L. 1998. Using acoustic emission in fatigue and fracture materials research. JOM 50, 11. http://www.tms.org/pubs/journals/JOM/9811/Huang/Huang-9811.html (Accessed 18 December 2013).

[91] Ward, S. H. 1990. Resistivity and induced polarization methods. In: Ward, S. H. (ed.). Geotechnical and Environmental Geophysics, Vol. 1. Society of Exploration Geophysicists: pp. 147–190.

[92] Stoppel, M. 2011. Differenzpotentialfeldmessung in der automatisierten Prufung von Stahlbetonbauteilen. Doctoral Dissertation. Berlin, (M. Stoppel): 171 f.

[93] Hülsenbeck & Co. 1926. German Pat. No. 489434.

[94] Neal, A. 2004. Ground-penetrating radar and its use in sedimentology: principles, problems and progress. Earth-Science Reviews 66: 261–330.

[95] Daniels, J. D. 2004. Ground-penetrating radar, 2nd ed. London, The Institution of Electrical Engineers: 726 p.

[96] Jol, H. M. (ed.). 2009. Ground Penetrating Radar: Theory and Applications. Amsterdam, Oxford, Elsevier Science: 544 p.

[97] Powers, M. 1997. Modeling frequency-dependent GPR. The Leading Edge 16, 11: 1657–1662.

[98] Schlumberger, C. 1920. Étude sur la prospection électrique du sous-sol. Paris, Gaultier-Villars et Cie.: 96 p.

[99] Loke, M. H. 2001. Tutorial: 2-D and 3-D electrical imaging surveys.

[100] Marshall, D., Madden, T. 1959. Induced polarization, a study of its causes. Geophysics 24, 4: 790–816.

[101] Kruschwitz, S. 2008. Assessment of the complex resistivity behavior of salt affected building materials. Doctoral Dissertation. Berlin, (S. Kruschwitz): 165 f.

[102] Dey, A., Morrison, H. F. 1979. Resistivity modelling for arbitrary shaped two-dimensional structures. Geophys. Prospect. 27: 106–136.

[103] Nichols, J. T. 1935. Temperature measuring, U.S. Pat. No. 2008793.

[104] Maldague, X. P. V. 2001. Theory and Practice of Infrared Technology for Nondestructive Testing. New York, Chichester, John Wiley & Sons, Inc.: 684 p.

[105] Cielo, P. 1984. Pulsed photothermal evaluation of layered materials. J. Appl. Phys. 56, 1: 230–234.

[106] Almond, D. P., Lau, S. K. 1994. Defect sizing by transient thermography. I. An analytical treatment. J Phys D: Appl Phys 27, 5: 1063–1070.

[107] Busse, G., Wu, D., Karpen, W. 1992. Thermal wave imaging with phase sensitive modulated thermography. J. Appl. Phys. 71, 8: 3962–3965.

[108] Spicer, J. W. M., Kerns, W. D., Aamodt, L. C., Murphy, J. C. 1992. Source patterning in time-resolved infrared radiometry of composite structures. In: Eklund, J. K. (ed.). Thermosense XIV, Vol. 1682, Proc. of SPIE – An Int. Conf. on Thermal Sensing and Imaging Diagnostic Applications, Orlando, FL, U.S.A., Apr 22–24, 1992. SPIE: pp. 248–257.

[109] Ibarra-Castanedo, C., Tarpani, J. R., Maldague, X. P. V. 2013. Nondestructive testing with thermography. Eur. J. Phys. 34: S91–S109.

[110] Halliday, D., Resnick, R., Krane, K. S. 1992. Physics, Vol. 2, 4th ed. John Wiley & Sons, Inc.: 688 p.

[111] Arpaci, V. S. 1966. Conduction Heat Transfer. Addison-Wesley Pub. Co.: 550 p.

[112] Parker, W. J., Jenkins, R. J., Butler, C. P., Abbott, G. L. 1961. Flash method of determining thermal diffusivity, heat capacity, and thermal conductivity. J. Appl. Phys. 32, 9: 1679–1684.

[113] Chen, L., Clarke, D. R. 2009. A numerical solution based parameter estimation method for flash thermal diffusivity measurements. Comp. Mater. Sci. 45, 2: 342–348.

[114] Maldague, X. P., Marinetti, S. 1996. Pulse phase infrared thermography. J. Appl. Phys. 79, 5: 2694–2698.

[115] Cielo, P., Maldague, X., Deom, A. A., Lewak, R. 1987. Thermographic nondestructive evaluation of industrial materials and structures. Mater. Eval. 45, 6: 452–460.

[116] Allport, J., McHugh, J. 1988. Quantitative evaluation of transient video thermography. In: Thompson, D. O. (ed.), Chimenti D. E. (ed.). Review of Progress in Qunatitative Nondestructive Evaluation, Vol. 8A. New York, Plenum Press: pp. 253–262.

[117] Krapez, J.-C., Maldague, X., Cielo, P. 1991. Thermographic nondestructive evaluation: data inversion procedures. Res. Nondestruct. Eval. 3, 2: 101–124.

[118] Balageas, D. L., Deom, A. A., Boscher, D. M. 1987. Characterization and nondestructive testing of carbon-epoxy composites by a pulsed photothermal method. Mater. Eval. 45, 4: 456–465.

[119] Grinzato, E., Vavilov, V., Bison, P. G., Marineti, S., Bressan, C. 1995. Methodology of processing experimental data in transient thermal nondestructive testing (NDT). In: Semanovich, S. A. (ed.). Thermosense XVII, Vol. 2473, Proc. of SPIE, Bellingham, WA, U.S.A., Mar 28, 1995. SPIE: pp. 167–178.

[120] Ibarra-Castanedo, C., Maldague, X. 2004. Pulsed phase thermography reviewed. Quant. Infrared Thermogr. J. 1, 1: 47–70.

[121] Maldague, X., Galmiche, F., Ziadi, A. 2002. Advances in pulsed phase thermography. Infrared Phys. Techn. 43, 3–5: 175–181.

[122] Press, W. H., Teukolsky, S. A., Vetterling, W. T., Flannery, B. P. 2007. Numerical Recipes 3rd ed.: The Art of Scientific Computing. New York, Cambridge University Press: 1256 p.

[123] Arndt, R. 2007. Rechteckimpuls-Thermografie im Frequenzbereich, Adaption der Puls-Phasen-Thermografie für die qualitative und quantitative zerstörungsfreie Prüfung oberflächennaher Strukturen im Bauwesen. Doctoral Dissertation. Berlin, (R. Arndt): 178 f.

[124] Favro, L. D., Han, X. 1998. Thermal wave material characterization and thermal wave imaging, in sensing for materials characterization, processing, and manufacturing. In: Birnbaum, G. (ed.), Auld, B. A. (ed.). Sensing for Materials Characterization, Processing and Manufacturing, Vol. 1. ASNT TONES: pp. 399–415.

[125] Vavilov, V., Marinetti, S. 1999. Thermal methods pulsed phase thermography and fourier-analysis thermal tomograph. Russian Journal of Nondestructive Testing 35, 2: 134–145.

[126] Busse, G., Rosencwaig, A. 1980. Subsurface imaging with photoacoustics. Appl. Phys. Lett. 36, 10: 815–816.

[127] Ibarra-Castanedo, C. 2005. Quantitative subsurface defect evaluation by pulsed phase thermography: depth retrieval with the phase. Doctoral Dissertation. Laval, (C. Ibarra-Castanedo). .

[128] Ibarra-Castanedo, C., Maldague, X. P. V. 2005. Interactive methodology for optimized defect characterization by quantitative pulsed phase thermography. Res. Nondestruct. Eval. 16: 175–193.

[129] Arndt, R., Maierhofer, C., Röllig, M. 2006. Quantitative pulse-phase-thermography for masonry and concrete structures. In: Proc. of the 9th Eur. NDT Conf. (EC-NDT 2006), Berlin, Germany, Sep 25–29, 2006. pp. 1–8.
http://www.ndt.net/article/ecndt2006/doc/P149.pdf (Accessed 16 April 2012).

[130] Arndt, R. W. 2010. Square pulse thermography in frequency domain as adaptation of pulsed phase thermography for qualitative and quantitative applications in cultural heritage and civil engineering. Infrared Phys. Techn. 53, 4: 246–253.

[131] Arndt, R. 2008. Square pulse thermography in frequency domain. In: Vavilov, V. P. (ed.), Burleigh, D. D. (ed.). Thermosense XXX, Vol. 6939, Proc. of SPIE, Orlando, FL, U.S.A., Mar 16, 2008. SPIE: pp. 1–12.
http://proceedings.spiedigitallibrary.org/proceeding.aspx?articleid=834339
(Accessed 13 September 2012).

[132] Kuo, M. K., Lin, T. R., Liu, P. L., Wu, T. T. 1998. Locating the crack tip of a surface-breaking crack, Part I. Line crack. Ultrasonics 36, 7: 803–811.

[133] Cheeke, J. D. N. 2002. Fundamentals and applications of ultrasonic waves. Boca Raton, Florida, CRC Press LLC: 480 p.

[134] Shokouhi, P., Wiggenhauser, H. 2011. Multi-probe ultrasonic testing for detection of delamination in concrete bridge decks. Transportation Research Board (TRB) 91st Annual Meeting, Washington, DC, U.S.A., Jan 22-26, 2012.
http://amonline.trb.org/1sl7d2/1 (Accessed 10 December 2012).

[135] Schickert, M., Krause, M., Müller, W. 2003. Ultrasonic imaging of concrete elements using reconstruction by synthetic aperture focusing technique. J. Mater. Civ. Eng. 15, 3: 235–246.

[136] Maierhofer, C. (ed.), Reinhardt, H. W. (ed.), Dobmann, G. (ed.). 2010. Non-destructive Evaluation of Reinforced Concrete Structures, Vol. 2: Non-destructive Testing Methods. Oxford, Cambridge, New Delhi, Woodhead Publishing: 624 p.

[137] Lago, S., Brignolo, S., Cuccaro, R., Musacchio, C., Albo, P. G., Tarizzo, P. 2014. Application of acoustic methods for a non-destructive evaluation of the elastic properties of several typologies of materials. Appl. Acoust. 75: 10–16.

[138] NDT Education Resource Center. 2001–2012. Piezoelectric Transducers. http://www.ndt-ed.org/EducationResources/CommunityCollege/Ultrasonics/EquipmentTrans/piezotransducers.htm (Accessed 10 January 2014).

[139] Wendrich, A. 2009. Zerstorungsfreie Ortung von Anomalien in historischem Mauerwerk mit Radar und Ultraschall – Moglichkeiten und Grenzen. Doctoral Dissertation. Berlin, (A. Wendrich): 185 f.

[140] Gros, X. E. 1997. NDT Data Fusion. London, Arnold: 205 p.

[141] Bogaert, P., Fasbender, D. 2007. Bayesian data fusion in a spatial prediction context: a general formulation. Stoch. Environ. Res. Risk Assess. 21, 6: 695–709.

[142] Gros, X. E., Strachan, P., Lowden, D. W. 1995. Fusion of multiprobe NDT data for ROV inspection. In: Conf. Proc. OCEANS'95 MTS/IEEE, Challenges of Our Changing Global Environment, San Diego, CA, U.S.A., Oct 9–12, 1995, Vol. 3. IEEE: pp. 2046–2050.

[143] Höppner, F., Klawonn, F., Kruse, R., Runkler, T. 1999. Fuzzy Cluster Analysis: Methods for Classification, Data Analysis and Image Recognition. Chichester, John Wiley & Sons Ltd.: 300 p.

[144] Pedrycz, W. 2005. Clustering and fuzzy clustering. In: Knowledge-Based Clustering: From Data to Information Granules. Hoboken, NJ, U.S.A., John Wiley & Sons, Inc.: pp. 1–27.

[145] Babuška, R. 2009. Fuzzy clustering. In: Fuzzy and Neural Control DISC Course Lectures Notes (November 2009). Delft, Netherlands, Delft University of Technology: pp. 59–75. http://www.dcsc.tudelft.nl/~disc_fnc/transp/fncontrol.pdf (Accessed 12 December 2013).

[146] Kruse, R., Doring, C., Lesot, M. J. 2007. Fundamentals of fuzzy clustering. In: Oliveira, J. V. (ed.), Pedrycz, W. (ed.). Advances in Fuzzy Clustering and its Applications. Chichester, England, John Wiley & Sons Ltd.: pp. 3–30.

[147] Gath, I., Geva, A. B. 1989. Unsupervised optimal fuzzy clustering. IEEE Trans. Pattern Anal. Mach. Intell. 11, 7: 773–780.

[148] Dave, R. N. 1990. Use of the adaptive fuzzy clustering algorithm to detect lines in digital images. In: Casasent, D. P. (ed.). Proc. of SPIE, Intelligent Robots and Computer Vision VIII: Algorithms and Techniques, Vol. 1192. SPIE: pp. 600–611.

[149] Krishnapuram, R., Kim, J. 1999. A note on the Gustafson–Kessel and adaptive fuzzy clustering algorithms. IEEE T. Fuzzy Syst. 7, 4: 453–461.

[150] Babuška, R., van der Veen, P. J., Kaymak, U. 2002. Improved covariance estimation for Gustafson-Kessel clustering. In: Proc. of the 2002 IEEE Int. Conf. on Fuzzy Systems (FUZZ-IEEE'02), Vol. 2, Honolulu, Hawaii, May 12–17, 2002. IEEE: pp. 1081–1085.

[151] Krishnapuram, R., Keller, J. M. 1996. The possibilistic c-means algorithm: insights and recommendations. IEEE Trans. Fuzzy Syst. 4, 3: 385–393.

[152] Pal, N. R., Pal, K., Bezdek, J. C. 1997. A mixed c-means clustering model. In: Proc. of the 6th IEEE Int. Conf. on Fuzzy Systems, Barcelona, Spain, Jul 1–5, 1997, Vol. 1. IEEE: pp. 11-21.

[153] Abonyi, J., Feil, B. 2007. Aggregation and visualization of fuzzy clusters based on fuzzy similarity measures. In: Oliveira, J. V. (ed.), Pedrycz, W. (ed.). Advances in Fuzzy Clustering and its Applications. Chichester, England, John Wiley & Sons Ltd.: pp. 95–121.

[154] Xie, X. L., Beni, G. 1991. A validity measure for fuzzy clustering. IEEE T. Pattern Anal. 13, 8: 841–847.

[155] Balasko, B., Abonyi, J., Feil, B. 2011. Fuzzy Clustering and Data Analysis Toolbox. Veszprem, Hungary, University of Veszprem, Department of Process Engineering: 77 p. `www.fmt.vein.hu/softcomp` (Accessed 22 July 2011).

[156] FLIR A320 Technical Specifications. `http://www.shopflir.com/crm_uploads/flir-a320-specifications.pdf` (Accessed 28 February 2012).

[157] Sandmeier, K. J. 2004. Reflexw, instruction manual for processing of seismic, acoustic or electromagnetic reflection, refraction and transmission data, Ver. 3.5.

[158] Yelf, R., Yelf, D. 2006. Where is true time zero? Electromagnetic Phenomena 7, 1: 158–163.

[159] Altman, D. G., Bland, J. M. 1994. Statistics notes: Diagnostic tests 1: sensitivity and specificity. BMJ 308: 1552.

[160] Stoppel, M., Taffe, A., Wiggenhauser, H., Kurz, J. H., Boller, C. 2011. Automated multi-sensor systems in civil engineering for condition assessment of concrete structures. In: Grantham, M. (ed.). Proc. of the 4th Int. Conf. on Concrete Repair, Dresden, Germany, Sep 26–28, 2011. Boca Raton, FL, CRC Press: pp. 397-403.

[161] Krause, H. J., Rath, E., Sawade, G., Dumat, F. 2007. Radar-Magnet-Betontest: Eine neue Methode zur Bestimmung der Feuchte und des Chloridgehalts von Brückenfahrbahnplatten aus Beton. Beton- und Stahlbetonbau 102, 12: 825–834.

LIST OF PUBLICATIONS

[1] Cotič, P., Niederleithinger, E., Wilsch, G. 2014. Unsupervised clustering of laser-induced breakdown spectroscopy data from concrete. JAAS (Sent for publication).

[2] Cotič, P., Jagličić, Z., Niederleithinger, E., Bosiljkov, V. 2014. Image fusion for improved detection of near-surface defects in NDT-CE using unsupervised clustering methods. J. Nondestruct. Eval. doi:10.1007/s10921-014-0232-1.

[3] Heidari, S., Safaei, E., Wojtczak, A., Cotič, P. 2013. Oxalate-bridged binuclear iron(III) complexes of two pyridine-based aminophenol ligands. Inorg. Chim. Acta. 405: 134–139.

[4] Počuča-Nešić, M., Marinković Stanojević, Z., Branković, Z., Cotič, P., Bernik, S., Sousa Góes, M., Marinković, B., Varela, J., Branković, G. 2013. Mechanochemical synthesis of yttrium manganite. J. Alloy. Compd. 552: 451–456.

[5] Cotič, P., Jagličić, Z., Bosiljkov, V. 2013. Validation of non-destructive characterization of the structure and seismic damage propagation of plaster and texture in multi-leaf stone masonry walls of cultural-artistic value. J. Cult. Herit. doi:http://dx.doi.org/10.1016/j.culher.2013.11.004.

[6] Karimpour, T., Safaei, E., Wojtczak, A., Cotič, P. 2013. Synthesis and characterization of oxalate-bridged binuclear iron(III) complex: $[(N)_2(O)_2Fe(\mu\text{-ox})Fe(N)_2(O)_2]$. J. Mol. Struct. 1038: 230–234.

[7] Cotic, P., Jaglicic, Z., Niederleithinger, E., Effner, U., Kruschwitz, S., Trela, C., Bosiljkov, V. 2013. Effect of moisture on the reliability of void detection in brickwork masonry using radar, ultrasonic and complex resistivity tomography. Mater. Struct. 46, 10: 1723–1735.

[8] Heidari, S., Safaei, E., Wojtczak, A., Cotič, P., Kozakiewicz, A. 2013. Iron(III) complexes of pyridine-based tetradentate aminophenol ligands as structural model complexes for the catechol-bound intermediate of catechol dioxygenases. Polyhedron 55: 109–116.

[9] Cotič, P., Jagličić, Z., Bosiljkov, V., Niederleithinger, E. 2013. GPR and IR thermography for near-surface defect detection in building structures. In: Grum, J. (ed.), Kek, T. (ed.). Proc. of the 12th Int. Conf. of the Slovenian Society for Non-Destructive Testing titled Application of contemporary non-destructive testing in engineering, Portorož, Slovenia, Sep 4–6, 2013. Ljubljana, Slovenian Society for Non-Destructive Testing: pp. 225–232.

[10] Cotič, P., Niederleithinger, E., Bosiljkov, V., Jagličić, Z. 2013. NDT data fusion for the enhancement of defect visualization in concrete. In: Damage assessment of structures X: selected, peer reviewed papers from the 10th Int. Conf. on Damage Assessment of Structures (DAMAS 2013), Dublin, Ireland, Jul 8-10, 2013. Basu, B. (ed.) Key Engineering Materials 569–570: 175–182.

[11] Saberikia, I., Safaei, E., Rafiee, M., Cotič, P., Bruno, G., Rudbari, H. A. 2012. A biologically relevant iron(III) phenoxyl radical complex: A thermodynamic investigation on the structure-radical stability relationship. J. Mol. Struct. 1022: 109–116.

[12] Saberikia, I., Safaei, E., Kowsari, M. H., Lee, Y.-I., Cotic, P., Bruno, G., Rudbari, H. A. 2012. A new iron(III) complex of glycine derivative of amine-chloro substituted phenol ligand: Synthesis, characterization and catechol dioxygenase activity. J. Mol. Struct. 1029: 60–67.

[13] Bosiljkov, V., Cotič, P., Uranjek, M., Kržan, M. 2012. Uncertanties in the assessment of the seismic vulnerability of stone masonry buildings. In: Roman, H. R. (ed.), Parsekian, G.

A. (ed.). Proc. of the 15th Int. Brick and Block Masonry Conference, Florianópolis, Santa Caterina, Brazil, Jun 3–6, 2012. Florianópolis, Federal University of Santa Catarina: pp. 1–10.

[14] Kržan, M., Cotič, P., Bosiljkov, V. 2012. Laboratorijske preiskave troslojnih kamnitih zidov = laboratory experimental tests on three-leaf stone masonry walls. In: Lopatič, J. (ed.), Markelj, V. (ed.), Saje, F. (ed.). Zbornik 34. zborovanja gradbenih konstruktorjev Slovenije, Bled, Hotel Golf, Slovenia, Oct 11–12, 2012. Ljubljana, Slovensko društvo gradbenih konstruktorjev: pp. 203–210.

Appendices

APPENDIX A: ARTICLE 1

Image fusion for improved detection of near-surface defects in NDT-CE using unsupervised clustering methods

P. Cotič, Z. Jagličić, E. Niederleithinger, M. Stoppel & V. Bosiljkov

J Nondestruct Eval (2014)
DOI 10.1007/s10921-014-0232-1

J Nondestruct Eval
DOI 10.1007/s10921-014-0232-1

Image Fusion for Improved Detection of Near-Surface Defects in NDT-CE Using Unsupervised Clustering Methods

Patricia Cotič · Zvonko Jagličić · Ernst Niederleithinger · Markus Stoppel · Vlatko Bosiljkov

Received: 28 August 2013 / Accepted: 24 January 2014

Abstract The capabilities of non-destructive testing (NDT) methods for defect detection in civil engineering are characterized by their different penetration depth, resolution and sensitivity to material properties. Therefore, in many cases multi-sensor NDT has to be performed, producing large data sets that require an efficient data evaluation framework. In this work an image fusion methodology is proposed based on unsupervised clustering methods. Their performance is evaluated on ground penetrating radar and infrared thermography data from laboratory concrete specimens with different simulated near-surface defects. It is shown that clustering could effectively partition the data for further feature level-based data fusion by improving the detectability of defects simulating delamination, voids and localized water. A comparison with supervised symbol level fusion shows that clustering-based fusion outperforms this, especially in situations with very limited knowledge about the material properties and depths of the defects. Additionally, clustering is successfully applied in a case study where a multi-sensor NDT data set was automatically collected by a self-navigating mobile robot system.

Keywords Non-destructive testing · Concrete · Defect detection · Data fusion · Cluster analysis

P. Cotič (✉) · Z. Jagličić
Institute of Mathematics, Physics and Mechanics, Jadranska 19, 1000 Ljubljana, Slovenia
e-mail: patricia.cotic@imfm.si

P. Cotič · Z. Jagličić · V. Bosiljkov
Faculty of Civil and Geodetic Engineering, University of Ljubljana, Jamova 2, 1000 Ljubljana, Slovenia

P. Cotič · E. Niederleithinger · M. Stoppel
BAM Federal Institute for Materials Research and Testing, Division VIII.2, Unter den Eichen 87, 12205 Berlin, Germany

1 Introduction

In civil engineering (CE), several non-destructive testing (NDT) methods such as ground penetrating radar (GPR), ultrasonic, impact echo and infrared (IR) thermography are used to image the internal structure and to detect defects such as delamination, spalling, surface and subsurface cracks, reinforcement corrosion, the presence of small air voids, and moisture distribution [1–5]. However, these methods are characterized by different penetration depths, as well as different sensitivity to the physical properties of the material [6–9]. Therefore, in order to fully characterize the objects under inspection and to increase the accuracy, several NDT techniques should be applied simultaneously. Consequently, often a huge amount of data has to be processed and interpreted efficiently. Currently data processing and interpretation of the results are performed for each NDT technique individually. This is both costly and time consuming and does not provide a reliable and straightforward evaluation of the structural condition. To overcome these constraints, data fusion techniques can be used.

To improve imaging results and defect characterization, image fusion has already been proposed for non-destructive evaluation (NDE). Methods from Bayesian inference, the Dempster–Shafer (D–S) theory of evidence, and wavelet multi-resolution analysis were used on eddy current and IR thermography images from composite and steel structures [10–13]. In NDT-CE applications, image fusion was performed on GPR data acquired at different frequencies and polarizations, and on GPR and ultrasonic data on prestressed concrete bridge beams and test specimens [8,14,15]. However, the applied fusion techniques were restricted to simple arithmetical methods.

The present work deals with clustering-based image fusion of NDT data acquired on concrete with defects in the

Published online: 15 February 2014

near-surface region. For image fusion, clustering methods have already been applied in medical imaging for pattern recognition (e.g. for the detection of cancerous cells from magnetic resonance images [16] and mammograms [17]), as well as on spectroscopic spatial measurement results from concrete for cement identification [18]. Their main advantage is that they can work fully unsupervised. This is of particular interest in implementing NDT in practice in terms of automated application by trained engineers and technicians rather than scientists.

Data fusion should both improve the results where NDT methods respond complementarily and put more weight upon the method with better performance. Therefore, to assess the effectiveness of mining data for the detection of near-surface defects in concrete structures, laboratory concrete specimens with simulated defects were studied by GPR and IR thermography, regarded as complementary methods in the near-surface region. Defects in the form of variations in the material, shape and depth below the surface were taken into account. Some preliminary results on data fusion from this data set have been presented in [19]. However, this paper develops a complete data fusion framework based on a quantitative evaluation with respect to the sensitivity calculation. Based on the outcome of the fusion methodology derived for GPR and IR thermography data on concrete, we further apply clustering methods to a case study where a multi-sensor NDT data set was automatically collected by a self-navigating mobile robot system.

2 Image Fusion with Clustering

Image fusion is applied in many fields, including medical imaging, microscopic imaging, remote sensing, computer vision and robotics. It can be performed at different levels, i.e. at pixel, feature and symbol level. At pixel level, images are fused at each pixel individually without using pre-processing units. Feature level fusion on the other hand tends to fuse features extracted by segmentation in the pre-processing step using clustering, neural networks (NN) and wavelet methods, whereas symbol level fusion is in most cases based on sensor modelling [20]. Regardless of the level used, statistical averaging, Bayesian, D–S, as well as fuzzy logic can be used for the fusion algorithm. One of the main restrictions in using probabilistic methods for symbol level fusion is the correct assignment of the conditional and a priori probabilities as well as mass functions which govern the evaluation. Although many studies have proposed different approaches for its calculation [12,21–23], none of the methods can work fully unsupervised. For feature level fusion on the other hand, wavelet analysis and NN require an appropriate wavelet filter with definition of the decomposition level to be used and good training data set, respectively [13]. In contrast, clustering methods require some sensitivity measures to be set, which, however, do not affect the analysis significantly, but they do not need a priori knowledge of the statistical data distribution. This is especially promising in the field of NDT, where knowledge about sample composition is limited due to the large diversity of specimens.

Clustering refers to the task of grouping a set of data (observations) into subsets (clusters, groups and classes) in such a way that the members of a cluster are as similar as possible, whereas members belonging to different clusters are as dissimilar as possible [24]. For objective-based clustering, starting with a random grouping of observations into clusters, the observations are iteratively moved to the cluster whose centre is the nearest to them until a convergence limit is reached. A common measure of similarity between two observations x_1, x_2 is the Euclidian distance d, which for M variables can be written as

$$d = \left(\sum_{i=1}^{M} (x_{1i} - x_{2i})^2 \right)^{1/2} = \| \mathbf{x}_1 - \mathbf{x}_2 \| \ . \tag{1}$$

In partitioning an unlabelled data set $\mathbf{X} = \{\mathbf{x}_1, \mathbf{x}_2, \ldots, \mathbf{x}_N\}$ into c clusters by iteratively assigning labels u_{ij} to vectors in $\mathbf{X}$ by the partition matrix $\mathbf{U}_{c\times N} = \left[u_{ij}\right]$, the target is to minimize an objective function J, which is the sum of the distances of N observations to their respective cluster centre $\mathbf{v}$:

$$J_m(\mathbf{U}, \mathbf{V}; \mathbf{X}) = \sum_{i=1}^{c} \sum_{j=1}^{N} u_{ij}^m \left\| \mathbf{x}_j - \mathbf{v}_i \right\|^2. \tag{2}$$

With respect to the partition matrix, clustering algorithms can be classified as hard (or crisp), fuzzy probabilistic or fuzzy possibilistic [24]. In contrast to hard clustering where u_{ij} possess values of only 0 or 1($u_{ij} \in \{0, 1\}$), fuzzy probabilistic clustering is defined as soft partitioning, allowing observations to belong to more than one cluster with a calculated probability, i.e. u_{ij} may possess any number between 0 and 1 ($u_{ij} \in [0, 1]$). This is especially promising in the case of NDT data, where u_{ij} could be regarded as the reliability of the NDT system. Moreover, since the hard k-means algorithm [25] was found to be particularly sensitive to initialization [18], hard clustering was not considered in this paper.

The best known fuzzy probabilistic algorithm is the fuzzy c-means (FCM) algorithm [26]. Here u_{ij} describes the membership of observation $\mathbf{x}_j$ in the ith cluster, which can be interpreted as probability (hence "probabilistic clustering"). The "fuzzing" exponent or "fuzzifier" m, introduced in Eq. 2, is a positive real number and is recommended to range from 1.2 to 2 (in our calculation m was fixed to 2, the value most often recommended by other authors). To optimize J, u_{ij} and $\mathbf{v}_i$ have to be updated in each iteration by

$$u_{ij} = \frac{1}{\sum_{k=1}^{c} (d_{ij}/d_{kj})^{2/(m-1)}}, \tag{3}$$

$$\mathbf{v}_i = \frac{\sum_{j=1}^{N} u_{ij}^m \cdot \mathbf{x}_j}{\sum_{j=1}^{N} u_{ij}^m}, \tag{4}$$

with $d_{ij} = \left\| \mathbf{x}_j - \mathbf{v}_i \right\|, 1 \le i \le c, 1 \le j \le N$.

Due to the fact that the Euclidian distance is used, the FCM method is based on the assumption of spherical clusters and is sensitive to outliers and disturbances. To account for the first assumption, the Gustafson-Kessel (GK) algorithm [27], the adaptive fuzzy clustering (AFC) algorithm [28] or the GK algorithm with adaptive cluster volumes (GKA ρ) [29] could be used to detect clusters of different shapes in one data set. All three algorithms employ an adaptive distance norm, which adapts the FCM functional as

$$J_m(\mathbf{U}, \mathbf{V}; \mathbf{X}) = \sum_{i=1}^{c} \sum_{j=1}^{N} u_{ij}^m \left(\mathbf{x}_j - \mathbf{v}_i\right)^{\mathrm{T}} \mathbf{A_i} \left(\mathbf{x}_j - \mathbf{v}_i\right), \tag{5}$$

where $\mathbf{A}_i$ is the norm-inducing matrix of the ith cluster that should be calculated on the basis of the cluster volume ρ_i and the fuzzy covariance matrix $\mathbf{F}$ [30].

Since the AFC and GKA ρ algorithms were found to produce poor partitions if little is known about the initial determination of the cluster volumes, we used the general GK algorithm with cluster volumes fixed to $\rho_i = 1$ [29]. To improve the numerical performance of the GK algorithm (to account for the singularity problems of $\mathbf{F}$), we used the algorithm proposed by Babuška et al. [30], where two additional parameters (β and γ) are introduced. As suggested by the authors, parameter β (the parameter that limits the condition number of $\mathbf{F}$) was fixed to $\beta = 10^{15}$, whereas parameter $\gamma \in [0,1]$ (i.e. the tuning parameter which constraints the clusters to have a more or less equal shape) was varied as discussed in Sect. 3.3. Additionally, we followed Kruse et al. [31] in using the final FCM partition for the initialization of the GK algorithm.

The sensitivity of the FCM algorithm to outliers can be overcome either by using noise clustering [32], where an additional noise cluster is introduced, or by fuzzy possibilistic clustering algorithms (for some variants, refer to [33–36]). Among the latter, the possibilistic-fuzzy c-means (PFCM) algorithm [36] worked particularly well on our NDT data, where the following objective function should be minimized:

$$J_{m,\eta}(\mathbf{U}, \mathbf{T}, \mathbf{V}; \mathbf{X}, \gamma) = \sum_{i=1}^{c} \sum_{j=1}^{N} (a u_{ij}^m + b t_{ij}^{\eta}) \cdot \left\| \mathbf{x}_j - \mathbf{v}_i \right\|^2 + \sum_{i=1}^{c} \gamma_i \sum_{j=1}^{N} (1 - t_{ij})^{\eta}, \tag{6}$$

where $a > 0$, $b > 0$, $m > 1$ and $\eta > 1$ are user-defined parameters and γ_i should be calculated as proposed in [33]. To minimize J, the necessary conditions for memberships u_{ij}, typicalities t_{ij} and cluster centres have to be adapted as well. In our version of the PFCM algorithm we used the final FCM partition for initialization, as well as fixed parameter values $a = 1.4$, $b = 1.8$, $m = 2$ and $\eta = 1.8$, which produced the best partition among several other parameter combinations. The chosen combination of parameters also worked well in our previous studies on spectroscopic spatial clustering [18].

It should be noted that the number of clusters is a user-defined parameter. Although several validity indices have been proposed to automatically define the optimal number of clusters, it was observed that this procedure does not deliver a proper interpretation of the results in our case. As evident throughout our study, the number of clusters should rather be defined according to the suspected severity of the damage and the heterogeneity of the inspected material.

3 Development of an Image Fusion Framework Based on Clustering

For the development of an image fusion framework based on clustering, GPR and IR thermography measurements were carried out on laboratory concrete specimens with artificial defects. The numerous factors that govern the performance of these two methods such as material properties, type, shape and the size of defects were taken into account.

3.1 Specimen Description

All concrete specimens have a size of 50 × 50 × 15 cm^3 and were made from the same concrete. The specimens contain inbuilt anomalies varying in material (polystyrene, air and water) and depth below the surface (Fig. 1). The inbuilt cuboids in specimen S2 have a size of 8 × 8 × 6 cm^3, while the size of S1 cuboids is 8 × 8 cm^2 with varying thickness. Specimen S2 features reinforcement with different densities (horizontal distance between bars 5 or 10 cm), but a uniform concrete cover of 2.5 cm. The polystyrene plates (simulating delamination) in specimen S3 have a thickness of 1 cm (a) and 2 cm (b), and the diameters of the plastic pipes are 1, 1.5 and 2.5 cm (from left to right in Fig. 1, S3). The concrete cover over all the defects in specimen S3 is between 1.5 and 2 cm. Defect specifications for all the specimens are summarized in Table 1.

3.2 Methods

3.2.1 Ground Penetrating Radar

GPR is based on the propagation and reflection of high frequency electromagnetic impulses produced by an antenna

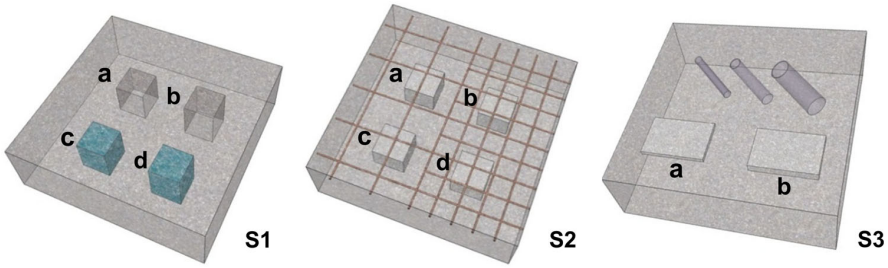

Fig. 1 Sketches of laboratory concrete test specimens with marked inbuilt defects

Table 1 Material and concrete cover of simulated defects for specimens S1–S3

Defect	Defect material	Concrete cover (cm)
S1a	Air	6
S1b	Air	3
S1c	Water	6
S1d	Water	3
S2a,b	Polystyrene	6.6
S2c,d	Polystyrene	4.6
S3a,b	Polystyrene	1.5–2
S3pipes	Plastic	1.5–2

system, where reflections occur at the interfaces between materials with different dielectric properties. In the near-surface region, the analysis and interpretation of GPR data is often complicated by the influence of near-field antenna coupling/induction effects, which according to [37] range to a depth of $1.5 \cdot \lambda$, where λ is the wavelength of the electromagnetic waves. For concrete with a dielectric constant of around 9 and an antenna with a central frequency of 1.6 GHz, the wavelength is around 6.3 cm and the near-field region extends up to a depth of almost 10 cm. Apart from the near-field effects the performance of GPR is also dependent on the resolution. For calculation of the depth resolution (defined as the ability to differentiate two adjacent signals in time), $0.25 \cdot \lambda$ has been proposed [38].

The GPR data used for this study was obtained with equipment from MALÅ Geoscience, using a 1.6 GHz monostatic shielded antenna. A calibrated survey wheel was used and radargrams were collected in both directions with a line spacing of 5 cm and a point distance of 0.5 cm.

3.2.2 Square Pulse Thermography in the Frequency Domain

IR thermography is based on recording the IR radiation from the previously heated surface of the specimen and allows detection of the presence of defects to within a depth of approximately 10 cm [39]. In order to enhance the detectability of thermal images, the use of the pulse phase thermography technique was originally proposed by Maldague and Marinetti [40] and further adapted for the special requirements of NDT-CE by Arndt [41] in terms of square pulse thermography (SPT) in the frequency domain. Here, the specimen is square pulse heated [42] and analysis of the recorded temperature evolution versus time of each pixel is performed in the frequency domain by fast Fourier transformation, deriving amplitude and phase images. Phase images in particular exhibit higher depth penetration, higher resolution and are less sensitive to non-uniform heating than thermal and amplitude images [43]. Arndt [41] additionally proposed a quantitative method where the depth z of a defect can be expressed by the frequency f_{ch} of the maximum phase or amplitude contrast between the defect and the sound area through the following equation

$$z = k_c \cdot \sqrt{\frac{\alpha}{f_{ch}}}, \tag{7}$$

where k_c is a correction factor and α is the thermal diffusivity of the investigated material.

The IR thermography data used for this study was acquired with a FLIR A320 IR camera, having a thermal sensitivity of 50 mK (at 30 °C), a spatial resolution of 1.36 mrad and a focal plane array with a resolution of 320 × 240 pixels and a spectral range of 7.5–13 µm. For heating the specimens, two IR heaters (1.2 kW each) were moved parallel to the surface at a distance of about 45 cm. All thermal images were recorded at a frame rate of 0.2 Hz. The heating and cooling down times were adjusted with regard to the problem.

3.2.3 Image Fusion and Validation

GPR and IR thermography images were combined on a feature level-based data fusion using fuzzy clustering methods for data segmentation and simple weighted averaging to fuse the derived memberships for each pixel according to

$$\overline{x_{US(i,j)}} = \frac{u_{R,i}x_R + u_{T,j}x_T}{u_{R,i} + u_{T,j}}, \tag{8}$$

where x_R and x_T refer to a specific pixel of GPR and IR images and u_R and u_T are the associated membership val-

ues. Index i marks that observation x, which is segmented to cluster i, should be weighted with its corresponding membership to that cluster. Different indices (i, j) particularly refer to independent segmentation of GPR compared to IR thermography. For GPR C-scans were used, whereas for IR thermography phase images at particular frequencies served as input data. Since the concrete test validation specimens contained defects at known depths, the quantitative approach of SPT in the frequency domain with respect to the material properties of concrete and the defects was applied. As a result, the phase contrast images could be regarded as depth slices, enabling a direct correlation with the GPR C-scans. Before fusion, data alignment was performed and a common spatial reference was established. In addition, both data sets were globally normalized; amplitudes for GPR and phase contrasts for IR thermography. In this paper we present the results obtained using the FCM, GK and PFCM clustering methods performed for each depth separately. Noise clustering, though normally extremely powerful in handling noisy data [18], failed in our case as signals of very high amplitude (detected defect) were classified as noise.

Based on ground truth reference, the results from fusion on concrete were assessed both qualitatively and quantitatively. The quality of the resulting images was estimated by visual inspection, whereas quantitative evaluation was based on the known area of the defects. Sensitivity and specificity values [44] were calculated from the number of true positive, true negative, false positive and false negative calls by using

$$sens = \frac{TP}{TP + FN}, \tag{9}$$

$$spec = \frac{TN}{TN + FP}, \tag{10}$$

where positive and negative refer to an identified and a rejected defect, respectively. Thus, a true positive call means that a pixel was correctly identified as a defect. A combined sensitivity measure c_sens was further calculated by

$$c\_sens = \frac{a \cdot sens + b \cdot spec}{a + b}, \tag{11}$$

where weights a and b refer to the specimen's corresponding defect and non-defect area, respectively.

The clustering results were additionally compared with the results obtained after applying supervised symbol level fusion, based on the assignment of weights referring to the probability of defect detection of the measurement system. Based on results from previous experiments on concrete with the same measurement system, a recommendation for weights of both NDT methods was given in accordance with the depth of defects through sensitivity curves [45]. In this study we refer to the sensitivity curve calculated for polystyrene defects since it covers the investigated depth range. For the fusion algorithm, weighted averaging and the D–S rule of combination were used (we preferred the D–S to Bayesian theory approaches, since the D–S does not assign belief or disbelief to the fused image if there is insufficient knowledge). For our data sets, weighted averaging for each pixel was calculated according to

$$\overline{x_w} = \frac{w_R x_R + w_T x_T}{w_R + w_T}, \tag{12}$$

where w_R and w_T are the weights associated with the probability of defect detection of the GPR and IR thermography measurement system and x_R and x_T refer to a specific pixel of GPR and IR images. Following Gros et al. [10] for the application of the D–S [46], we first introduce a frame of discernment Θ as a set of mutually exclusive events a and b, where $\Theta = \{a\text{- GPR is true}, b\text{- thermography is true}\}$. A power set $P(\Theta) = \{\emptyset,\ a,\ b,\ \Theta\}$ is defined and for each element of $P(\Theta)$ masses, associated with the probability of defect detection of the GPR and IR thermography measurement system, are assigned. With the mass assignment, evidential intervals could be determined for GPR and thermography images by applying the D–S rule of combination [46], which can be mathematically expressed as

$$m_{R,T}(z) = m_R \oplus m_T(z) = \frac{\sum\limits_{x \cap y = z} m_R(x) m_T(y)}{1 - \sum\limits_{x \cap y = 0} m_R(x) m_T(y)}, \tag{13}$$

where m_R and m_T are mass functions of GPR and IR thermography, respectively. In our case, $m_{R,T}(a)$ refers to the evidence that the information on the GPR image is correct, and the same is true for $m_{R,T}(b)$ referring to the evidence for the IR image. To obtain a fused image, derived evidences were combined through weighted averaging

$$\overline{x_{DS}} = \frac{m_{R,T}(a)\ x_R + m_{R,T}(b)\ x_T}{m_{R,T}(a) + m_{R,T}(b)}. \tag{14}$$

3.3 Results and Discussion

The results of GPR and IR thermographic inspections are shown for the specimens S1 at the depth of 3 cm (Fig. 2), S2 at the depth of 4.6 cm (Fig. 3) and S3 at the depth of 1.5 cm (Fig. 4) (results obtained at other depths are not taken into account due to the suspected movement of defects during concreting). Red rectangles mark the known position of the defects, which served as a reference to evaluate the effectiveness of image fusion. For a qualitative evaluation, images resulting from both feature (based on the FCM clustering algorithm) and symbol (based on the supervised assignment of weights) level fusion using weighted averaging are shown next to images used as input data. For symbol level fusion,

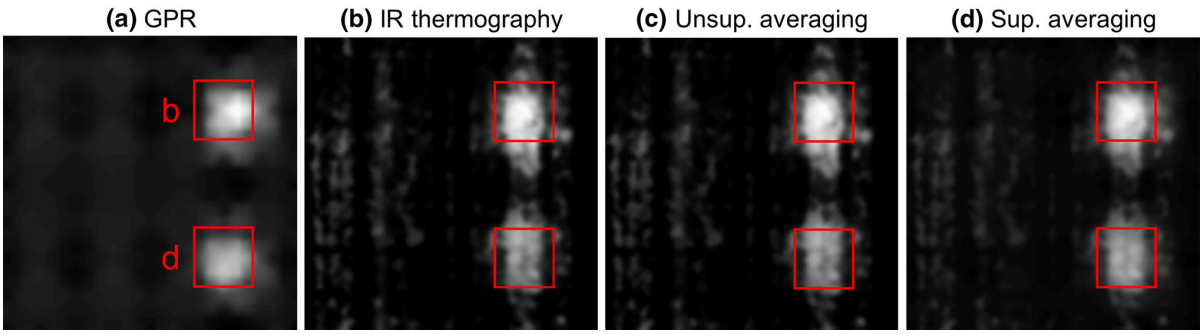

Fig. 2 Results from specimen S1 at the depth of 3 cm with marked defects according to Table 1 [the *upper* defect refers to air (**b**), the *lower* to water (**d**)]: GPR depth slice (**a**), IR phase contrast image at frequency 6.2×10^{-4} Hz (**b**), results from weighted averaging of images (**a**) and (**b**) using unsupervised feature level fusion (**c**) and supervised symbol level fusion (**d**)

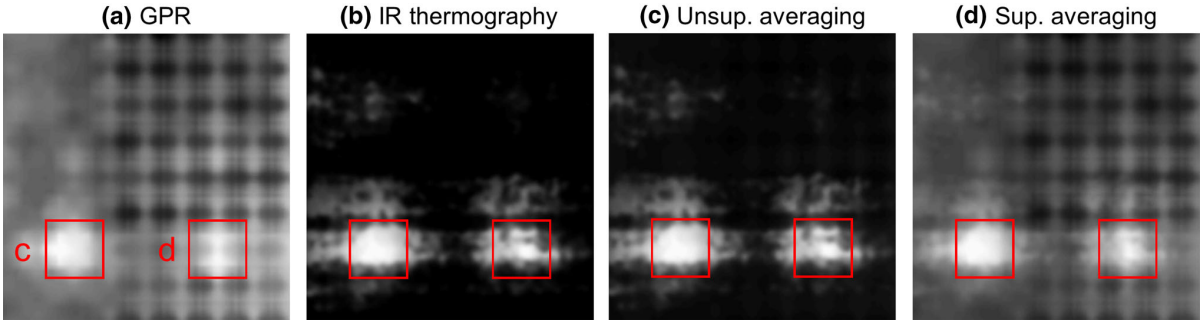

Fig. 3 Results from specimen S2 at the depth of 4.6 cm with marked defects according to Table 1 (the *right* part of the images refers to the part of the specimen with dense reinforcement): GPR depth slice (**a**), IR phase contrast image at frequency 3.0×10^{-4} Hz (**b**), results from weighted averaging of images (**a**) and (**b**) using unsupervised feature level fusion (**c**) and supervised symbol level fusion (**d**)

the weights used for the GPR/IR images were 0.88/0.89 for specimen S1 at the depth of 3 cm, 0.89/0.89 for specimen S2 at the depth of 4.6 cm and 0.75/0.91 for specimen S3 at the depth of 1.5 cm [45]. In Fig. 2 the lower rectangle refers to the water (d) and the upper to the air (b) defect. It can be seen that due to the overlapping performance of the two NDT methods both unsupervised feature level (Fig. 2c) as well as supervised symbol level fusion (Fig. 2d) yielded very similar results. However, in the case of specimen S2, clustering-based image fusion helped particularly in identifying the defect below the more dense reinforcement as well as in eliminating the reinforcement pattern detected by GPR (Fig. 3c). Although it was hoped that clustering would differentiate between the air and water defect when employing higher cluster numbers, this was not the case since GPR could not derive any information about the phase at the depth of 3 cm.

In contrast to specimens S1 and S2, the weights assigned in the case of specimen S3 at the depth of 1.5 cm tended to assign much more knowledge to IR thermography (0.91 for IR thermography compared to 0.75 for GPR). Consequently, the shape of the plastic pipes, that were more accurately detected by IR thermography, could be well visualized when using both supervised averaging and the D–S rule of combination, where a slightly higher contrast refers to D–S (Fig. 4e). However, it can be seen that the fusion with the FCM algorithm yielded an image with even higher contrast, where both plates and pipes could be well resolved (Fig. 4c).

To account for the drawback of the subjective visual evaluation of image fusion we further evaluated the results quantitatively. To perform the sensitivity calculation (in accordance with Eq. 11) in regard to whether a defect was detected or not, images were partitioned into two clusters. To provide an objective comparison of the results and thus to avoid the assignment of a threshold value for the classification, the standard FCM algorithm was employed, where the threshold value is assigned automatically with respect to the condition for minimizing the functional J in Eq. 2 (we preferred the FCM to the hard k-means algorithm to avoid the k-means initialization problems as noted in Sect. 2). To obtain a hard association of the most probable cluster, only the cluster with the highest membership degree was taken into account. Table

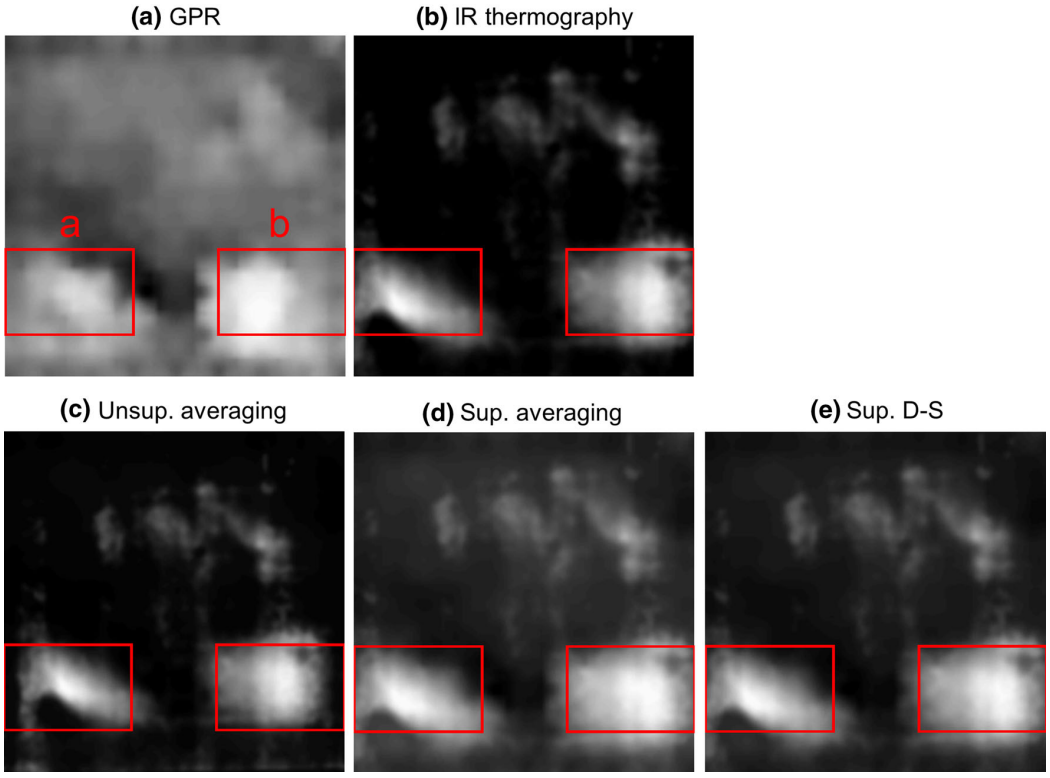

Fig. 4 Results from specimen S3 at the depth of 1.5 cm with marked polystyrene plates according to Table 1: GPR depth slice (**a**), IR phase contrast image at frequency 3.7×10^{-3} Hz (**b**), results from weighted averaging of images (**a**) and (**b**) using unsupervised feature level fusion (**c**) and supervised symbol level fusion (**d**), and results from D–S of images (**a**) and (**b**) using supervised symbol level fusion (**e**)

Table 2 Results (in %) of the combined sensitivity (*c_sens*) for the detection of different defects by GPR and IR thermography, as well as by data fusion using the unsupervised averaging with fuzzy c-means (FCM) algorithm, and the supervised averaging and Dempster–Shafer (D–S)

Defect	GPR	IR thermo.	Unsup. average	Sup. average	Sup. D–S
S1b	89.8	90.1	90.5	90.4	90.3
S1d	92.9	91.9	93.7	93.7	93.7
S2d	54.4	89.0	89.7	76.0	77.2
S3b	74.9	92.3	90.6	89.7	90.8

For the defect specifications refer to Table 1

2 presents the results of *c_sens* when only the GPR or IR image was taken into account in comparison to the results obtained with weighted averaging using the FCM algorithm as well as with weighted averaging and D–S using sensor information. It can be seen that at the depth of 3 cm IR thermography has a slightly higher probability of detecting an air void (defect S1b) than GPR, whereas a water void at the same depth (defect S1d) was better detected by GPR. This is consistent with the expected performance of the two methods, where the dielectric constant and the thermal conductivity govern the behaviour of GPR and IR thermography, respectively. The greater difference in dielectric constant between water and concrete compared to air and concrete (for air, water and concrete the dielectric constants are approximately 1, 81 and 9, respectively) results in a higher amplitude of the reflected radar signal and thus better image contrast. For IR thermography, the opposite relation exists for the difference in the thermal conductivity between water and concrete compared to air and concrete (for air, water and concrete the thermal conductivities are approximately 0.024, 0.58 and 2.1 W/mK, respectively). It can be seen that for both the air and water defect, where the sensitivities of the two NDT methods did not differ greatly, clustering-based fusion with the FCM further improved defect detection. However, in the case of specimen S2, the calculated sensitivity of GPR at the part of the specimen with dense reinforcement is much smaller than the sensitivity of IR thermography (see results for defect S2d). It was thus expected that the fused image would not outperform the IR image. Nevertheless, the results show that the FCM even further improved the detectability of the defect below dense reinforcement. In the case of specimen

S3, quantitative evaluation is presented only for the right (b) polystyrene plate (the left plate seems to have tilted during concreting and the exact position of the plastic pipes could not be assessed due to small movements during concreting). As already observed from visual inspection, the results show that IR thermography detects the plate more accurately. Here, the FCM could not improve localization, but at the same time worsened the sensitivity of IR thermography only to a small extent.

Regarding the outcome from supervised averaging and D–S in Table 2, it is evident that in general both D–S and weighted averaging performed similarly. Moreover, where remarkably higher weights were assigned to the system with better performance, it was suspected that both supervised methods would outperform clustering-based fusion. On the contrary, only negligible improvement was obtained with D–S (see results for defect S3b). On the other hand, where weights were not assigned according to the reliability of the two NDT methods (in the case of dense reinforcement), the performance of both averaging and D–S deteriorated to a considerable extent (see results for defect S2d). This proves that the operation of both methods depends greatly upon the a priori selected weights, which has already been argued in [10]. In contrast, clustering methods work unsupervised and can handle various data sets without knowledge about the data.

To derive an optimal clustering-based data fusion framework, we further compared the performance of different fuzzy clustering algorithms for segmentation of the data. A qualitative comparison of the resulting classification of specimen S3 is given in Fig. 5, where the cluster colour is displayed according to the hard association of the most probable cluster (the cluster with the highest membership degree), whereas the factor of transparency takes into account the membership degree (e.g. $u_{ij} = 1$: opaque, $u_{ij} = 0.5$: 50 % transparency). The results show that the GK algorithm (with parameter $\gamma = 0$) outperforms the FCM for the detection of pipes, whereas for the PFCM no improvement from the FCM can be seen. The good performance of the GK is understandable since the method is able to detect clusters of various shapes, whereas the FCM and PFCM algorithms are restricted to clusters of equal shape. However, it should be noted that clustering methods treat each data point (pixel value) independently. Thus, the shape of clusters should not refer to the geometrical shapes detected from the GPR and IR thermography images, but rather to the geometrical shapes obtained from data plots correlating the GPR and IR thermography data. For specimen S3, correlation plots between GPR and IR thermography data are shown in Fig. 6 using the FCM and GK (for $\gamma = 0$) algorithms. It can be seen that in contrast to the FCM, the GK yields an elongated black cluster (corresponding to the black (non-defect) data points in Fig. 5c) with GPR extending over the whole dimension and limiting IR thermography to the smallest values. This means that the GK is able to classify data points with respect to the more relevant (IR thermography) results while treating GPR data as more noisy. That is in accordance with Fig. 4a, where especially in the region of the plastic pipes, GPR data exhibit poor contrast.

To quantitatively prove the clustering results above, Table 3 summarizes the outcome from sensitivity calculation for all the defects taken into account. The results show that the behaviour of PFCM in general resembles the one of FCM. This suggests that noise does not appreciably restrict the detection of defects in the case of our NDT data. However, this is contrary to the results of an eddy current inspection of stainless steel cladding tubes [13], or spectroscopic measurement results on concrete [18] where noise played an important role. In addition, it can be seen that the GK performs differently with regards to the FCM when parameter γ does not additionally restrict the shape of clusters (for $\gamma = 0$). Although the GK with $\gamma = 0$ could best visualize the plastic pipes, its poor performance stands out particularly in the case of defect S2d, where its localization deteriorated by more than 10 % compared to the FCM. An explanation for this could be derived from the GPR results in Fig. 3a. Due to the detection of reinforcement, the cluster centres are close to each other and the clusters are extremely long in one direction, which has been reported to produce poor models [30]. In contrast, by only slightly restricting the algorithm with $\gamma = 0.1$, the GK performed similarly to the FCM while being at the same time also sensitive to the detection of elongated defects. To summarize, by taking into account both the robust performance of the methods as well as the sensitivity to small variations, the modified GK (restricted by β and γ) can be regarded as the most recommendable clustering algorithm for the investigated NDT data sets.

4 Image Fusion Applied to a Case Study

As already mentioned in Sect. 1, one of the main tasks in deriving a generalized data fusion framework for NDE-CE applications is to promote fast, efficient and reliable evaluation of large data sets. Examples of large area inspection include parking garages and bridge decks suffering from severe corrosion of the reinforcement, which is reflected in cracking, spalling and losses of the concrete cross section. In order to evaluate the extent of degradation adequately, investigation of surfaces of some thousand square metres with a dense grid is necessary. To solve this problem, a self-navigating mobile robot system has been developed within the BetoScan project (www.betoscan.de). The key task of the BetoScan system is to divide the investigated structure into zones with defined damage classes. Therefore, potential maps together with other parameters such as the distribution

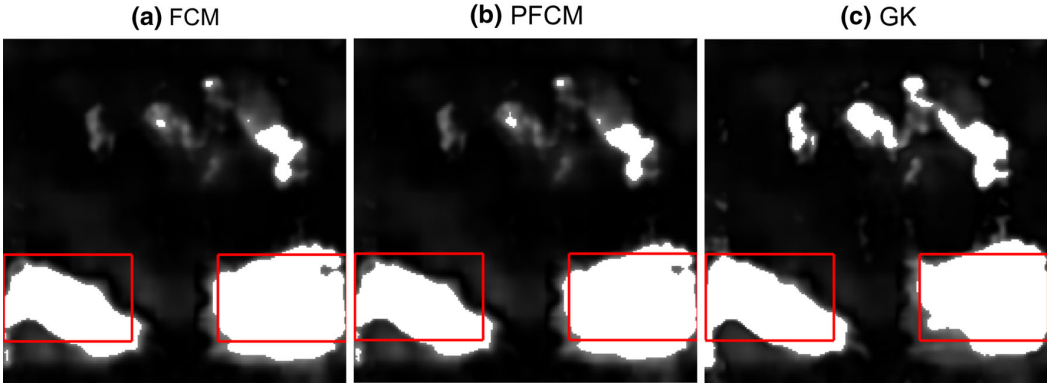

Fig. 5 Results from clustering of images Fig. 4a, b using the fuzzy c-means (FCM) (**a**), possibilistic-fuzzy c-means (PFCM) (**b**) and Gustafson-Kessel (GK) with $\gamma = 0$ (**c**) algorithms. *White* cluster refers to detected defects, *black* to non-defect area with the factor of transparency referring to the membership degree

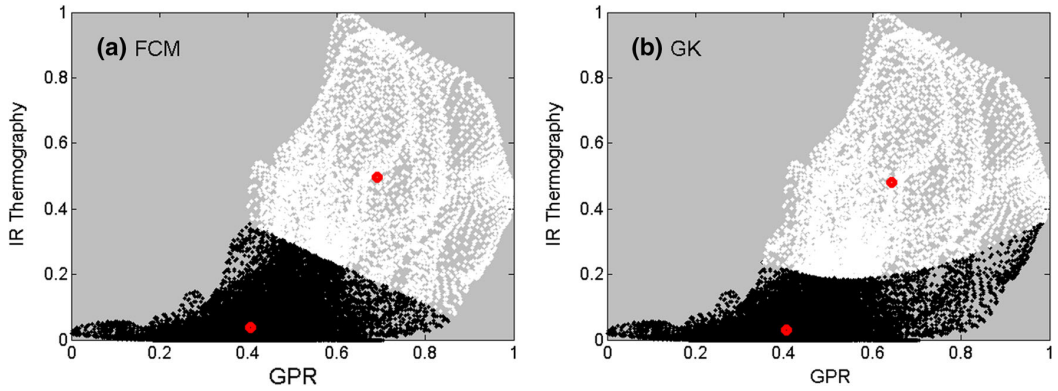

Fig. 6 Correlation plots between GPR and IR thermography normalized data from specimen S3 using the fuzzy c-means (FCM) (**a**) and Gustafson-Kessel (GK for $\gamma = 0$) (**b**) algorithms. *White* and *black* data points refer to the *white* and *black* cluster in Fig. 5, whereas the *red* point marks the corresponding cluster centre

Table 3 Results (in %) of the combined sensitivity (*c_sens*) for the detection of different defects with data fusion using the fuzzy c-means (FCM), possibilistic-fuzzy c-means (PFCM) and Gustafson-Kessel (GK) algorithms

Defect	FCM	PFCM	GK ($\gamma = 0$)	GK ($\gamma = 0.1$)
S1b	90.5	90.5	90.6	90.5
S1d	93.7	93.7	94.4	93.7
S2d	89.7	89.3	80.3	87.0
S3b	90.6	90.6	91.5	90.8

For the defect specifications refer to Table 1

of concrete cover and moisture have to be assessed simultaneously. With the BetoScan system this is achieved by an automated multi-sensor system comprising the following NDT methods (Fig. 7):

- potential mapping (to assess the probability of active corrosion),
- eddy current + GPR (to assess the concrete cover above the reinforcement layer),
- ultrasonic (to assess the thickness of the investigated structure, the presence of voids and cracks),
- microwave (to assess the humidity distribution).

Except for ultrasonic, all the sensors can collect data contactlessly, enabling a driving speed from 0.1 up to 0.5 m/s (depending on the methods used). As well as the methods given above, additional methods and devices with a digital interface may be included in the system. A more detailed description of a current multi-sensor system is given in [47]. Although the BetoScan system has a fully automated data acquisition system, data analysis is currently performed manually by direct comparison of the results. The development of an efficient and reliable data fusion framework is therefore of major interest.

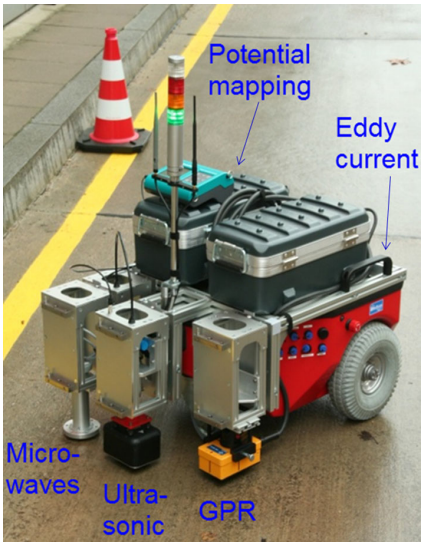

Fig. 7 The BetoScan robotic system with NDT sensors

4.1 Methods

We tested our clustering-based data fusion methodology for data segmentation on a BetoScan data set acquired from the reinforced concrete floor of a parking garage in Germany. The area inspected measured approximately 5 × 7 m^2. The spacing between tracks was around 20 cm, with about 1 cm between data points of each track. Before data fusion, normalization and alignment of the data was performed and a common spatial reference with data interpolation was established.

Potential mapping, eddy current, as well as microwave moisture sensors were used simultaneously. Potential mapping is based on measurement of the electrochemical potentials of the reinforcement on the concrete surface by the use of a reference electrode known as a half-cell and a high-impedance voltmeter. A potential lower than –300 mV indicates a high probability of active corrosion. For the BetoScan system, a Canin+ instrument from Proceq was used in combination with a copper/copper sulphate reference wheel electrode. For eddy current, which is based on electromagnetic pulse induction to detect flaws in conductive materials, a Profometer 5+ from Proceq was used, which combines rebar detection and measurement of concrete cover. To measure the relative moisture distribution of the concrete, the microwave-based devices Moist RP (4 cm penetration) and Moist PP (20 cm penetration) from HF-Sensor were used. The microwave method is based on the fact that with increase in moisture content of the material, microwaves lose more energy due to induced oscillations of the electric field during transmission.

To support the results obtained by the BetoScan system, we additionally took into account the data obtained by a radar-magnetic method—a relatively new technique still in the state of development [48]. Here, the moisture and the salinity of concrete are estimated by the real and imaginary parts of the dielectric constant of the concrete covering the reinforcement. Firstly, the static magnetic field of pre-magnetized rebars is measured. The depth of the rebars is obtained through a knowledge of the magnetic field components orthogonal to the rebar direction. The mathematical approximation was described by Krause et al. in [48]. Secondly, the real (ε_r') and imaginary part (ε_r'') of the dielectric constant are calculated using the travel time t_r and reflection amplitude r_{tot} measured by GPR, as well as the concrete cover previously assessed by the magnetic method.

Measurements with the radar-magnetic method were performed with a system introduced by the same authors, applying the GPR RAMAC system from MALÅ Geoscience with a 1 GHz monostatic antenna and a set of four GMR magnetometers. The acquired data was aligned in accordance with the scanned area by the BetoScan.

4.2 Results and Discussion

From the surface plot of the electrochemical potentials of the concrete floor investigated, critical areas with a high probability of corrosion could be identified by potentials lower than –300 mV (Fig. 8a). The main effects that induce corrosion in concrete structures are carbonation and high chloride concentration [49]. In general, the probability of carbonation increases with decreasing concrete cover above the reinforcement layer. The results show that at some parts of the surface where the concrete cover was even less than 30 mm, the corrosion process was very intensive (compare the right side of Fig. 8a and Fig. 8b). However, it is hard to draw conclusions from the moisture measurements alone. The data acquired by the Moist RP sensor (with a penetration capability of up to 4 cm depth) suggest a variable humidity distribution of the scanned area that cannot be correlated with either the potential or concrete cover results (Fig. 8c). On the other hand, the humidity distribution assessed by the Moist PP sensor suggests a relative humidity of more than 3 vol. % in parts with low concrete cover (Fig. 8d). Therefore, the striking corrosion on the right side of the floor is probably due to both carbonation and a high salinity concentration (by assuming a correlation between moisture and salinity concentration).

To support our assumption, we additionally present results by the radar-magnetic method. As shown from the results of the Moist RP sensor, the real part of the dielectric constant also suggests a variable humidity distribution (Fig. 8e). In contrast, the plot of the imaginary part of the dielectric constant ε_r'' is in good agreement with the results from potential mapping and eddy current (Fig. 8f). Since ε_r'' refers to energy losses of the electromagnetic wave due to free charges in the material, a high value of ε_r'' refers to concrete with higher

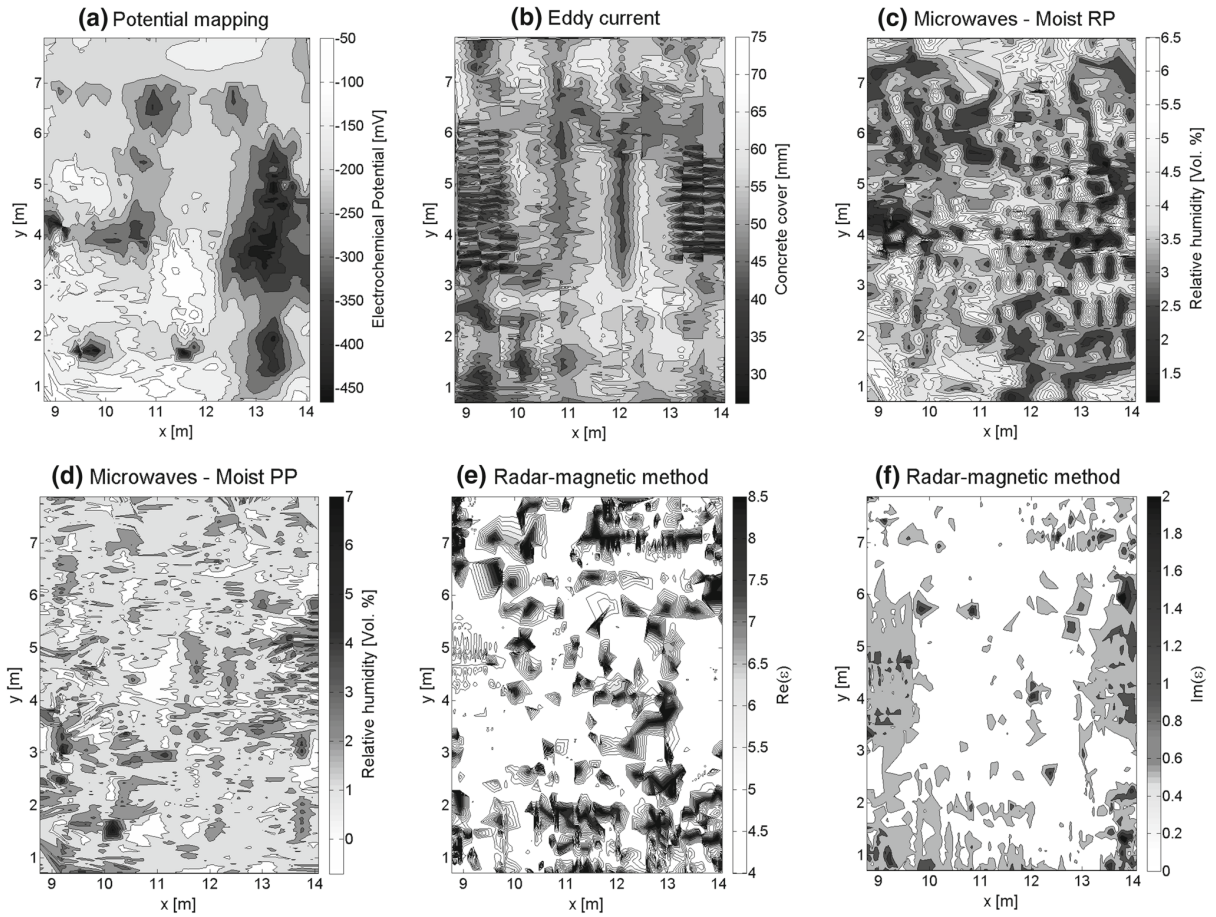

Fig. 8 Results from the BetoScan measurement of a concrete parking deck using potential mapping (**a**), eddy current (**b**), microwaves with a Moist RP sensor (**c**) and microwaves with a Moist PP sensor (**d**). Results from the radar-magnetic measurement with the real (**e**) and imaginary (**f**) part of the dielectric constant (note that due to the chosen *colour bar* in Fig. 8f, the *white* area corresponds to values up till 0.35 of the imaginary part of the dielectric constant)

salinity. This demonstrates the information from salinity concentration to be better correlated to corrosion than moisture.

The BetoScan data, as well as the data from the radar-magnetic measurement, show that estimation of the condition of the structure is not straightforward. Each of the applied NDT methods suffers from limited reliability in identifying certain parameters. The efficiency of using clustering methods to estimate zones with a different degree of degradation is demonstrated in Fig. 9. Only the results obtained using the GK algorithm with $\gamma = 0.1$ are presented when using three clusters. FCM produced an almost similar result for this data set. Regarding the correlation between data, the optimal solution would be to combine potential mapping, eddy current and radar-magnetic measurement data with the imaginary part of the dielectric constant (Fig. 9a) (for the correlation plot for this data set see Fig. 10). However, the resulting partitions show that for the combination of potential mapping, eddy current and microwaves with the Moist PP sensor, zones with a higher probability of damage can also be clearly detected (Fig. 9b). Here, the red cluster could be identified with the zone of severe corrosion, the black cluster with the area of either small concrete cover or high salinity content (or both) where the corrosion process is not yet observable, whereas the white area could be characterized as undamaged (or minimally damaged) concrete as a result of higher concrete cover and good concrete quality. To prove the robustness of the clustering methods, we further evaluated the whole of the BetoScan data. In Fig. 9c it can be seen that although the data acquired by microwave with the Moist RP sensor worsened the final partition, the most important damage zone can still be well recognized.

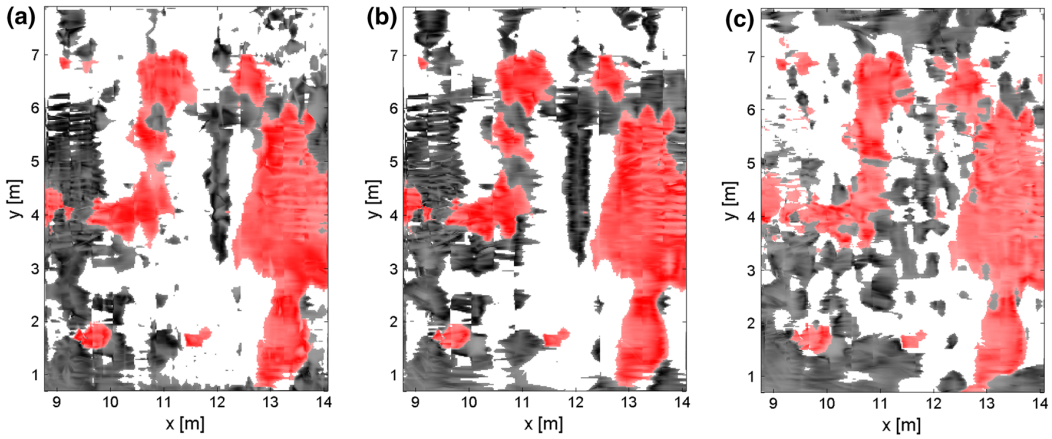

Fig. 9 Results from image fusion using the Gustafson-Kessel (GK) clustering algorithm while taking into account different data sets: potential mapping + eddy current + radar-magnetic method (Imε) (**a**), potential mapping + eddy current + microwaves with sensor Moist PP (**b**) and potential mapping + eddy current + microwaves with sensors Moist PP and Moist RP (**c**). *Red* cluster could be identified with the area of severe corrosion, the *black* one with the area of either small concrete cover or high salinity content (or both) where the corrosion process is not yet observable, whereas the *white* area could be characterized as undamaged (or minimally damaged). The factor of transparency refers to the cluster membership degree

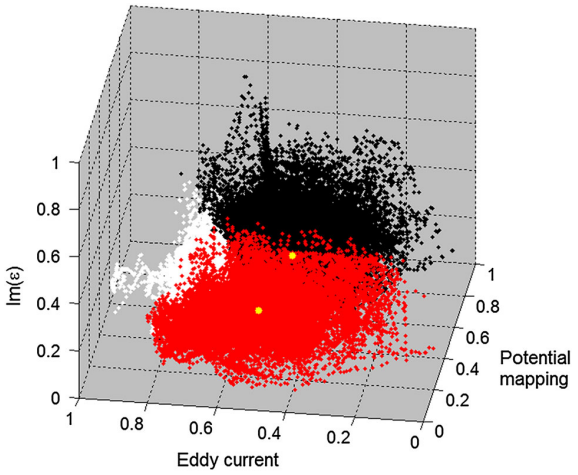

Fig. 10 Correlation plots between potential mapping, eddy current and radar-magnetic method (Imε) normalized data using the Gustafson-Kessel (GK) clustering algorithm. *Cluster colours* refer to the colours in Fig. 9a, whereas the *yellow points* mark the corresponding cluster centre

5 Conclusions

The use of clustering methods for image classification of fused NDT-CE data sets was studied. The clustering's direct classification outcome as well as their use in feature-level fusion were taken into account. The methods proved particularly helpful in detecting near-surface defects simulating delamination, voids and localized water as well as in partitioning a reinforced concrete floor from a parking garage into damage zones, and thus provided both defect localization as well as characterization of the defects.

The use of fuzzy probabilistic clustering (employing the FCM and GK algorithms), as well as fuzzy possibilistic clustering (with the PFCM algorithm), was explored on concrete validation specimens with GPR and IR thermography data. Results from the sensitivity evaluation showed that the PFCM in general performed similarly as the FCM, which suggests that noise has only a minor effect on the resulting partition. On the contrary, the use of the modified version of the GK method helped particularly to detect clusters of arbitrary shape, since the algorithm is not restricted to spherical clusters as are the FCM and PFCM. Elongated clusters were produced when the method took into account the relevance of only one method, such as for the detection of plastic pipes and cracks. For best performance of the GK it is suggested that the parameter γ be set to 0.1.

The efficiency of using clustering for data classification in feature level fusion was evaluated through comparison with supervised symbol level fusion using weighted averaging and D–S. The results showed that in the case where more knowledge was assigned to the NDT system with better performance, only a negligible improvement was obtained with supervised fusion using D–S compared to clustering-based fusion. However, if weights were not assigned according to the reliability of the respective NDT methods, the performance of both averaging and D–S deteriorated to a large extent. The unsupervised clustering methods, on the other hand, showed robust performance.

The use of clustering techniques to combine data from GPR and IR thermography in general increased the reliability of NDT inspection in cases where the methods had a com-

plementary penetration capability and sensitivity to different physical properties. Moreover, in cases where one method greatly dominated over the other, they worsened its performance only to a small extent. This shows clustering methods to be robust in situations with very limited knowledge about the material properties and depths of the defects, which was additionally proven by the BetoScan data set. Here, the use of clustering also enabled characterization of the defects. Moreover, it should be emphasized that for a multi-sensor system such as the BetoScan, image fusion with clustering is of particular importance since it delivers one final image that takes into account the correlation between the various NDT methods. In practice, displaying only one reliable image rather than multiple ones to the end-user is of the utmost importance.

Acknowledgments The first author acknowledges the financial support of the Slovenian Research Agency through grant 1000-10-310156 and the Slovene Human Resources and Scholarship Fund through grant 11012-13/2012. The authors wish to thank Dr. Hans-Joachim Krause and colleagues for the radar-magnetic data set. Contributions and support from Assoc. Prof. Violeta Bokan Bosiljkov, Primož Murn and Dr. Parisa Shokouhi are acknowledged.

References

1. McCann, D.M., Forde, M.C.: Review of NDT methods in the assessment of concrete and masonry structures. NDT E Int. **34**, 71–84 (2001)
2. Beutel, R., Reinhardt, H.W., Grosse, C.U., Glaubitt, A., Krause, M., Maierhofer, C., et al.: Comparative performance tests and validation of NDT methods for concrete testing. J. Nondestruct. Eval. **27**, 59–65 (2008)
3. Shokouhi, P., Wiggenhauser, H.: Multi-probe ultrasonic testing for detection of delamination in concrete bridge decks. TRB Annual Meeting Online (AMOnline). http://amonline.trb.org/1sl7d2/1 (2011). Accessed 5 January 2013
4. Maierhofer, C., Arndt, R., Röllig, M., Rieck, C., Walther, A., Scheel, H., et al.: Application of impulse-thermography for nondestructive assessment of concrete structures. Cem. Concr. Compos. **28**, 393–401 (2006)
5. Cotič, P., Jagličić Z, Bosiljkov, V.: Validation of non-destructive characterization of the structure and seismic damage propagation of plaster and texture in multi-leaf stone masonry walls of cultural-artistic value. J. Cult. Herit. (2013). doi:10.1016/j.culher.2013.11.004
6. Cotic, P., Jaglicic, Z., Niederleithinger, E., Effner, U., Kruschwitz, S., Trela, C., et al.: Effect of moisture on the reliability of void detection in brickwork masonry using radar, ultrasonic and complex resistivity tomography. Mater. Struct. **46**, 1723–1735 (2013). doi:10.1617/s11527-012-0011-3
7. Maierhofer, C., Wöstmann, J.: Investigation of dielectric properties of brick materials as a function of moisture and salt content using a microwave impulse technique at very high frequencies. NDT E Int. **31**(4), 259–263 (1998)
8. Maierhofer, C., Zacher, G., Kohl, C., Wöstmann, J.: Evaluation of radar and complementary echo methods for NDT of concrete elements. J. Nondestruct. Eval. **27**, 47–57 (2008)
9. Wiggenhauser, H.: Advanced NDT methods for quality assurance of concrete structures. In: Proceedings NDTCE'09, Nondestructive testing in civil engineering. LCPC, Paris (2009)
10. Gros, X.E., Bousigue, J., Takahashi, K.: NDT data fusion at pixel level. NDT E Int. **32**, 283–292 (1999)
11. Gros, X.E., Liu, Z., Tsukada, K., Hanasaki, K.: Experimenting with pixel-level NDT data fusion techniques. IEEE T Instrum. Meas. **49**(5), 1083–1090 (2000)
12. Liu, Z., Forsyth, D.S., Safizadeh, M.S., Fahr, A.: A data-fusion scheme for quantitative image analysis by using locally weighted regression and Dempster–Shafer theory. IEEE T Instrum. Meas. **57**(11), 2554–2560 (2008)
13. Balakrishnan, S., Cacciola, M., Udpa, L., Rao, B.P., Jayakumar, T., Raj, B.: Development of image fusion methodology using discrete wavelet transform for eddy current images. NDT E Int. **51**, 51–57 (2012)
14. Kohl, C., Krause, M., Maierhofer, C., Wöstmann, J.: 2D-and 3D-visualisation of NDT-data using data fusion technique. Mater. Struct. **38**, 817–826 (2005)
15. Cui, J., Huston, D.R., Arndt, R., Jalinoos, F.: Data fusion techniques of multiple sensors nondestructive evaluation of a concrete bridge deck. TRB Annual Meeting Online (AMOnline). http://amonline.trb.org/2vdh1b/2vdh1b/1 (2010). Accessed 11 February 2012
16. Bensaid, A.M., Hall, L.O., Bezdek, J.C., Clarke, L.P., Silbiger, M.L., Arrington, J.A., et al.: Validity-guided (re)clustering with applications to image segmentation. IEEE T Fuzzy Syst. **4**(2), 112–123 (1996)
17. Santoro, M., Prevete, R., Cavallo, L., Catanzariti, E.: Mass detection in mammograms using gabor filters and fuzzy clustering. In: Bloch, I., Petrosino, A., Tettamanzi, A.G.B. (eds.) Fuzzy logic and applications. WILF 2005: Proceedings of the 6th international workshop, pp. 334–343. Springer, Berlin (2006)
18. Cotič, P., Niederleithinger, E., Wilsch, G.: Unsupervised clustering of spatially acquired laser-induced breakdown spectroscopy data from concrete. Cem. Concr. Res. (submitted)
19. Cotič, P., Niederleithinger, E., Bosiljkov, V., Jagličić, Z.: NDT data fusion for the enhancement of defect visualization in concrete. Key Eng. Mater. **569–570**, 175–182 (2013)
20. Liu, Z., Forsyth, D.S., Komorowski, J.P., Hanasaki, K., Kirubarajan, T.: Survey: state of the art in NDE data fusion techniques. IEEE T Instrum. Meas. **56**, 2435–2451 (2007)
21. Kaftandjian, V., Zhu, Y.M., Dupuis, O., Babot, D.: The combined use of the evidence theory and fuzzy logic for improving multimodal nondestructive testing systems. IEEE T Instrum. Meas. **54**(5), 1968–1977 (2005)
22. Bogaerta, P., Fasbender, D.: Bayesian data fusion in a spatial prediction context: a general formulation. Stoch Environ. Res. Risk Assess. **21**, 695–709 (2007)
23. Li, G., Huang, P., Chen, P., Hou, D., Zhang, G., Zhou, Z. Application of multi-sensor data fusion in defects evaluation based on Dempster–Shafer theory. IEEE Xplore Digital Library. http://ieeexplore.ieee.org/xpl/articleDetails.jsp?arnumber=5944335 (2011). Accessed 13 February 2012
24. Höppner, F., Klawonn, F., Kruse, R., Runkler, T.: Fuzzy cluster analysis: methods for classification, data analysis and image recognition, 1st edn. Wiley, Chichester (1999)
25. MacQueen, J.B.: Some methods for classification and analysis of multivariate observations. Proceedings of the 5th Berkeley symposium on mathematical statistics and probability, vol 1: Statistics, pp. 281–297. University of California Press, Berkeley (1967)
26. Bezdek, J.Z.: Pattern recognition with fuzzy objective function algorithms. Plenum Press, New York (1981)
27. Gustafson, D., Kessel, W.: Fuzzy clustering with a fuzzy covariance matrix. Proceedings of the 1978 IEEE conference on decision and control including the 17th Symposium on adaptive processes, pp. 761–766. IEEE Control Systems Society, San Diego (1979)

28. Dave, R.N.: Use of the adaptive fuzzy clustering algorithm to detect lines in digital images. In: Casasent, D.P. (ed.) Intelligent robots and computer vision VIII: algorithms and techniques, vol 1192. SPIE, pp. 600–611 (1990)
29. Krishnapuram, R., Kim, J.: A note on the Gustafson-Kessel and adaptive fuzzy clustering algorithms. IEEE T Fuzzy Syst. **7**(4), 453–461 (1999)
30. Babuška, R., van der Veen, P.J., Kaymak, U.: Improved covariance estimation for Gustafson-Kessel clustering. In: Proceedings of the 2002 IEEE international conference on fuzzy systems, vol 2. IEEE, pp. 1081–1085 (2002)
31. Kruse, R., Döring, C., Lesot, M.J.: Fundamentals of fuzzy clustering. In: Oliveira, J.V., Pedrycz, W. (eds.) Advances in fuzzy clustering and its applications, pp. 3–30. Wiley, Chichester (2007)
32. Dave, R.N.: Characterization and detection of noise in clustering. Pattern Recogn. Lett. **12**(11), 657–664 (1991)
33. Krishnapuram, R., Keller, J.M.: The possibilistic c-means algorithm: insights and recommendations. IEEE Trans. Fuzzy Syst. **4**(3), 385–393 (1996)
34. Pal, N.R., Pal, K., Bezdek, J.C.: A mixed c-means clustering model. In: Proceedings of the 6th IEEE international conference on fuzzy systems, vol 1. IEEE, pp. 11–21 (1997)
35. Timm, H., Borgelt, C., Kruse, R.: Fuzzy cluster analysis with cluster repulsion. CiteSeer$^{X}_{\beta}$. http://citeseerx.ist.psu.edu/viewdoc/summary?doi=10.1.1.100.9787 (2001). Accessed 16 November 2012
36. Pal, N.R., Pal, K., Keller, J.M., Bezdek, J.C.: A possibilistic fuzzy c-means clustering algorithm. IEEE T Fuzzy Syst. **13**(4), 517–530 (2005)
37. Daniels, J.D. (ed.): Ground-penetrating radar, 2nd edn. The Institution of Electrical Engineers, London (2004)
38. Jol, H. (ed.): Ground penetrating radar: theory and applications, 1st edn. Elsevier Science, Amsterdam, Oxford (2009)
39. Maierhofer, C., Röllig, M.: Application of active thermography to the detection of safety relevant defects in civil engineering structures. In: Proceedings OPTO 2009 & IRS^2 2009. AMA, pp. 215–220 (2009)
40. Maldague, X.P., Marinetti, S.: Pulse phase infrared thermography. J. Appl. Phys. **79**, 2694–2698 (1996)
41. Arndt, R.: Square pulse thermography in frequency domain. SPIE Digital Library. http://proceedings.spiedigitallibrary.org/proceeding.aspx?articleid=834339 (2008). Accessed 13 September 2012
42. Vavilov, V., Burleigh, D.: Heat transfer. In: Maldague, X., Moore, P.O. (eds.) Nondestructive handbook, infrared and thermal testing, vol. 3, 3rd edn. ASNT Press, Columbus (2001)
43. Weritz, F., Arndt, R., Röllig, M., Maierhofer, C., Wiggenhauser, H.: Investigation of concrete structures with pulse phase thermography. Mater. Struct. **38**, 843–849 (2005)
44. Altman, D.G., Bland, J.M.: Statistics notes: diagnostic tests 1: sensitivity and specificity. BMJ **308**, 1552 (1994)
45. Cotič, P., Jagličić, Z., Bosiljkov, V., Niederleithinger, E.: GPR and IR thermography for near-surface defect detection in building structures. In: Grum, J. (ed.) Proceedings of the 12th international conference of the Slovenian society for non-destructive testing, Application of Contemporary Non-Destructive Testing in Engineering. Slovenian Society for Nondestructive testing, Ljubljana (2013)
46. Shafer, G.: A mathematical theory of evidence. Princeton University Press, Princeton (1976)
47. Stoppel, M., Taffe, A., Wiggenhauser, H., Kurz, J.H., Boller, C.: Automated multi-sensor systems in civil engineering for condition assessment of concrete structures. In: Grantham, M. (ed.) Proceedings of the 4th International Conference on Concrete Repair, pp. 397–403. CRC Press, Boca Raton (2011)
48. Krause, H.J., Rath, E., Sawade, G., Dumat, F.: Radar-Magnet-Betontest: Eine neue Methode zur Bestimmung der Feuchte und des Chloridgehalts von Brückenfahrbahnplatten aus Beton. Beton- und Stahlbetonbau **102**(12), 825–834 (2007)
49. Reichling, K., Raupach, M., Wiggenhauser, H., Stoppel, M., Dobmann, G., Kurz, J.: BETOSCAN: an instrumented mobile robot system for the diagnosis of reinforced concrete floors. Restor. Build. Monum. **15**(4), 277–286 (2009)

APPENDIX B: ARTICLE 2

Validation of non-destructive characterization of the structure and seismic damage propagation of plaster and texture in multi-leaf stone masonry walls of cultural-artistic value

P. Cotič, Z. Jagličić & V. Bosiljkov

J Cult Herit (2013)
DOI http://dx.doi.org/10.1016/j.culher.2013.11.004

Journal of Cultural Heritage xxx (2013) xxx–xxx

Available online at ScienceDirect www.sciencedirect.com

Elsevier Masson France EM|consulte www.em-consulte.com/en

Original article

Validation of non-destructive characterization of the structure and seismic damage propagation of plaster and texture in multi-leaf stone masonry walls of cultural-artistic value

Patricia Cotič[a,b,*], Zvonko Jagličić[a,b,1], Vlatko Bosiljkov[b,2]

[a] Institute of Mathematics, Physics and Mechanics, Jadranska 19, 1000 Ljubljana, Slovenia
[b] Faculty of Civil and Geodetic Engineering, University of Ljubljana, Jamova 2, 1000 Ljubljana, Slovenia

ARTICLE INFO

Article history:
Received 2 July 2013
Accepted 7 November 2013
Available online xxx

Keywords:
Multi-leaf stone masonry
Seismic damage propagation
Non-destructive validation
Ground penetrating radar
Infrared thermography
Data fusion

ABSTRACT

Assessment of multi-leaf stone masonry in earthquake-prone areas is mostly related to the evaluation of its texture, morphology, leaf detachment and structural cracking due to previous seismic activity, as well as disintegration due to material deterioration. For the plastered masonry with heritage or artistic value (paintings, frescoes etc.), both the type of structure and the extent of damage should be characterized with minimal interference to the structure, which could be overcome solely by non-destructive testing (NDT). However, due to the complexity of plastered multi-leaf masonry structure, the performance of well-known NDT methods could be significantly worsened. Therefore, as a prerequisite for applying NDT on multi-leaf stone masonry in practice, a validation process should be carried out. In this study, complementary ground penetrating radar (GPR) and infrared (IR) thermography measurements on plastered laboratory three-leaf stone masonry walls were performed. Apart from assessing the wall texture and morphology with the type of connection between the leaves, detection of gradual plaster delamination and crack propagation while subjecting the walls to an in-plane cyclic shear test was taken into account. The results showed that GPR could successfully visualize header stones passing through the whole depth of the specimen. The masonry texture behind the plaster could be well resolved by both methods, although GPR near-field effects worsened its localisation. For the detection of plaster delamination, IR thermography outperformed GPR by detecting delamination as small as 2 mm as well as structural crack patterns, whereas GPR only detected delamination larger than 8 mm. It was shown that the performance of both methods for defect detection could be further improved by image fusion based on unsupervised clustering methods.

1. Research aims

The aim of this study was to evaluate the complementary performance of ground penetrating radar and infrared thermography in non-destructively assessing the type of structure (texture and morphology with type of connection) and seismic related damage (plaster detachment and crack propagation) of plastered multi-leaf stone masonry. The application of NDT methods to such masonry with artistic or cultural-heritage value is of particular importance in evaluating the structural condition with minimal interference.

2. Introduction

A large proportion of existing stone masonry buildings in European Mediterranean countries, as well as elsewhere, represent cultural heritage assets. Very often, the stone masonry consists of several leaves, of which three-leaf masonry is one of the most characteristics [1]. Here, the outer leaves consist of stones arranged in various masonry bonds (hereinafter referred to as texture), whereas the inner core is a mixture of stone rubble and loose adhesive material. The leaves may be connected with so-called header stones, i.e. connecting stones passing through the whole depth of the specimen [2].

In most cases, this type of building is vulnerable to material deterioration and seismic action, resulting in leaf detachment and cracks which can be further emphasized due to the presence of internal voids. For effective repair of the masonry, an accurate diagnosis of the defects present and visualization of the structural model defining the behaviour of the structure should be carried

* Corresponding author. Institute of Mathematics, Physics and Mechanics, Jadranska 19, 1000 Ljubljana, Slovenia. Tel./fax: +386 1 426 71 78.
E-mail addresses: patricia.cotic@imfm.si (P. Cotič), zvonko.jaglicic@imfm.si (Z. Jagličić), vlatko.bosiljkov@fgg.uni-lj.si (V. Bosiljkov).
[1] Tel.: +386 1 426 71 78; fax: +386 1 426 71 78.
[2] Tel.: +386 1 425 06 81; fax: +386 1 425 06 81.

1296-2074/$ – see front matter © 2013 Elsevier Masson SAS. All rights reserved.
http://dx.doi.org/10.1016/j.culher.2013.11.004

out. For that, the structure's geometry, texture and morphology (the multi-leaf structure and connections between the leaves), as well as the material properties of the masonry and its constituents (stones/bricks and mortar) need to be determined [3].

Taking into account that for cultural heritage buildings with artistic value the structural condition should be assessed with the minimal possible intervention, the application of non-destructive testing (NDT) methods for both structural visualization and defect detection play an essential role. Several NDT methods have been proposed for structural investigation of building elements [4]. Contact methods, such as ground penetrating radar (GPR), ultrasonic, sonic and impact echo are especially promising in imaging the inner structure of buildings at depths of more than 5 to 10 cm, depending on the specific method [5]. On masonry, such methods have been applied for detection of the morphology, localization of voids and metal inclusions, determination of the moisture distribution, detection of severe delamination, as well as to control the effectiveness of repair by injection techniques [6–10]. On the other hand, non-contact active infrared (IR) thermography (hereinafter we omit "active") has been shown to be a powerful technique for imaging the structure very close to the surface, such as for visualization of the masonry texture, surface cracks, moisture distribution and plaster delamination [1,11–13], as well as for the investigation of mosaics [14,15].

All the above methods are characterized by a certain optimal depth resolution (i.e. the ability to detect defects at a certain depth with high probability), penetration capability, as well as sensitivity to the different physical properties of the masonry [16–18]. Moreover, due to the inhomogeneity of the masonry material, several methods have been used complementarily to fully characterize the structure [1,3,19]. Taking into account that the inhomogeneity of a complex structure of multi-leaf stone masonry could further worsen the performance of well-known NDT methods, the methods should be validated as a precondition for their practical application on-site.

Within the framework of the EU research project PERPETUATE (www.perpetuate.eu), the complementary use of GPR and IR thermography was studied for the structural assessment of plastered laboratory three-leaf stone masonry walls. Additionally, the performance of both methods was evaluated for defect detection such as gradual plaster delamination and crack propagation while subjecting the walls to an in-plane cyclic shear test monitored by a three dimensional (3D) digital image correlation (DIC) technique. The well-defined conditions enabled performance of a complete validation process of the efficiency of the methods applied for the detection of seismic related damage, this being of the utmost importance for bringing NDT into practice for on-site investigations.

3. Experimental

3.1. Specimen description

The performance of NDT methods was studied on four plastered laboratory three-leaf masonry walls measuring $100 \times 150 \times 40\,cm^3$. For the two layers of plaster (both coarse and fine), traditional recipes based on lime mortar were used. The external leaves of the masonry were constructed from regular coursed squared ashlar rough tooled limestone, while the internal core was filled with stone rubble and lime mortar. Two of the specimens had header stones in every second row passing through the whole depth of the specimens (Fig. 1a), whereas the other two had no connecting stones (Fig. 1b).

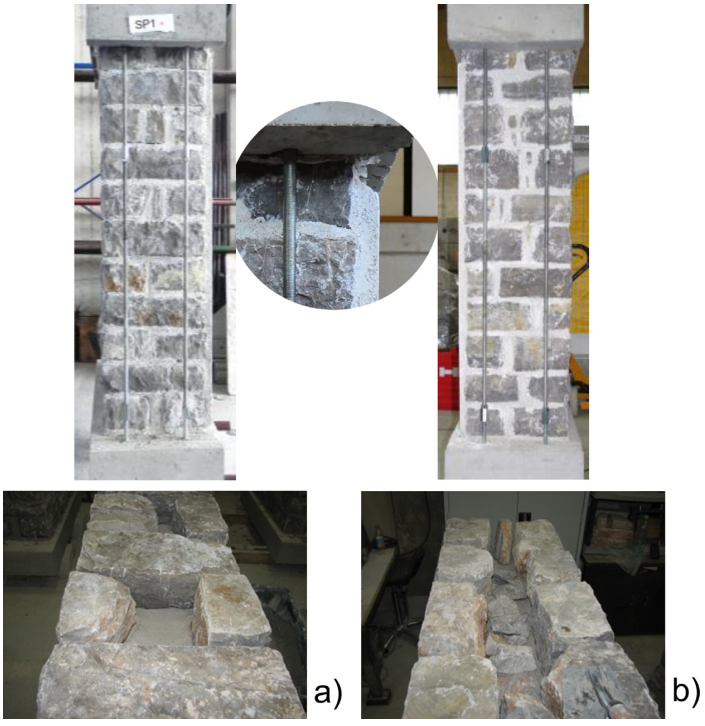

Fig. 1. The morphology of the connected (a) and unconnected (b) walls with two layers of plaster applied.

3.2. Methods

3.2.1. Ground penetrating radar

GPR is based on the propagation and reflection of high frequency electromagnetic impulses produced by an antenna system, where reflections occur at the interfaces between materials with different dielectric properties. In complex specimens, the analysis and interpretation of GPR data is often complicated by the influence of near-field antenna coupling/induction effects, which according to Daniels [20] range up to a depth of 1.5 λ, where λ is the wavelength of the electromagnetic waves. For masonry with a dielectric constant of around 9 and an antenna with a central frequency of 1.6 GHz, the wavelength is around 6.3 cm and the near-field region extends to a depth of almost 10 cm. Apart from the near-field effects, the performance of GPR is also dependent on the resolution. For calculation of the depth resolution (defined as the ability to differentiate two adjacent signals in time), a value of 0.25 λ has been proposed [21].

The GPR data used for this study was obtained with equipment from MALÅ Geoscience, using a 1.6 GHz monostatic shielded antenna. A calibrated survey wheel was used and radargrams were collected in both directions with a line spacing of 5 cm and a point distance of 0.5 cm.

3.2.2. Square pulse thermography in the frequency domain

IR thermography is based on recording IR radiation from the previously heated specimen's surface and allows detection of the presence of defects within a depth of approximately 10 cm [22]. In order to enhance the detectability of thermal images, we applied the pulse phase thermography (PPT) technique originally proposed by Maldague and Marinetti [23], and further adapted for the special requirements of NDT applications in civil engineering by Arndt [24] in terms of square pulse thermography (SPT) in the frequency domain. Here, the specimen is square pulse heated [25] and analysis of the recorded temperature evolution versus time of each pixel is performed in the frequency domain by Fast Fourier Transformation (FFT), deriving the amplitude and phase images. The phase images in particular exhibit higher depth penetration, higher resolution and are less sensitive to non-uniform heating than the thermal and amplitude images [26].

Table 1
Limit states (LS) for the wall structure and plaster subjected to seismic loading with respect to the displacement performance of the structure and the performance of the plaster [2].

LS for the wall structure	
LS of Damage Limitation (DL)	Displacement where the first crack on the structure appears
LS of Significant Damage (SD)	Displacement where the maximum strength of the structure is obtained
LS of Near Collapse (NC)	Maximal displacement of the structure reached
LS for the plaster	
First LS	First detachment of the plaster
Second LS	First visible crack on the plaster
Third LS	Plaster largely detached but still repairable or significantly damaged
Fourth LS	Partial or full collapse of the plaster

The IR thermography data used for the study was acquired with type FLIR A320 IR camera, having a thermal sensitivity of 50 mK (at 30 °C), a spatial resolution of 1.36 mrad and a focal plane array with an IR resolution of 320 × 240 pixels and a spectral range of 7.5–13 μm. For homogeneous heating of the specimens, two IR heaters (1.2 kW each) were moved parallel to the surface at a distance of about 10 cm. The heating time was approximately 30 min, while cooling down was recorded for 45 min at a frame rate of 0.2 Hz at approximately 3 m from the specimen's surface. During heating, the maximal reached temperature of the surface was 45 °C.

3.2.3. Experimental procedure for the detection of plaster delamination and crack propagation

The walls were subjected to an in-plane cyclic shear test, which was originally performed in order to assess the seismic behaviour of the wall structure and plaster. Their state of damage was evaluated through the limit states defined in Table 1 with respect to the displacement performance of the structure and the performance of the plaster, respectively [2]. The shear test set-up and the principle of the test are presented in Fig. 2. However, in our case, the shear test also enabled us to study the application of NDT for assessing gradual plaster delamination, as well as gradual formation of the

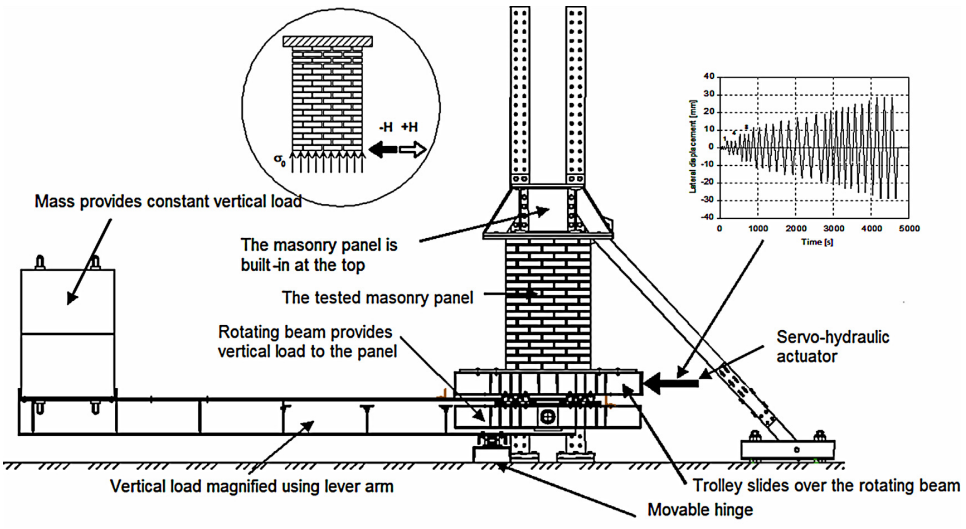

Fig. 2. Shear test set-up and the principle of testing single and both fixed panels.

Fig. 3. GPR and IR thermography test set-up.

crack patterns produced due to the induced shear force through cyclic stepwise loading. NDT measurements were performed at the unloaded (reference) state of the specimen, as well as at two loading steps (hereinafter referred to the 1st and 2nd loading state). The 1st loading state corresponded to the lateral displacement induced where both the first detachment of plaster and the first visible surface cracks appeared (corresponding to the first and second limit state of the plaster according to Table 1). The 2nd loading state was defined by largely detached or significantly damaged plaster, where a complete collapse of the plaster was assumed in the following loading step (corresponding to the third limit state of the plaster according to Table 1). NDT measurements had to be performed while keeping the induced lateral displacement constant, thus preventing their application on more loading steps. For the experimental set-up of the NDT, see Fig. 3.

To assess the wall's deformation shape, a 3D DIC technique which yields a 3D displacement field was applied at each loading step. Following Tung et al. [27], where DIC was used for monitoring crack propagation during the testing of masonry, we used DIC out-of-plane displacements together with visual inspection as a reference estimation of the gradual plaster delamination. The reference served to assess the complementary performance of the applied NDT techniques both qualitatively and quantitatively.

4. Results and discussion

NDT measurements were performed in order to assess the performance of GPR and IR thermography for the visualization of the wall's structure (i.e. the wall's texture and morphology with the type of connection between the leaves), and for the detection of gradual plaster delamination and crack propagation. With respect to the problem investigated, results are referred to the specific wall (W1–W4) and loading state.

4.1. Visualization of masonry morphology

Due to the limited depth resolution of IR thermography, structural visualization of the type of connection was performed only by GPR since the position of the reflections from the inner stones in rows lacking a full connection was expected at a depth of more than 15 cm. The results revealed that the maximum reflections of the radar signal appeared at depths from 16 cm to 20 cm, which was found to be very close to the measured position of the inner stones. Fig. 4 shows the structure detected on a vertical B-scan (b) and on the corresponding depth slice at the depth of 19 cm (c) for wall W3. In the B-scan, reflections appear at every second row of stones lacking a full connection (see full arrows) and can be clearly distinguished from connecting rows with header stones. This suggests that the difference in the dielectric constants of mortar and stone was high enough to be detected at the resolution of the 1.6 GHz antenna. It should be noted that in Fig. 4c, the reflections do not appear at all the expected positions due to the roughness of the stone surface which consequently did not produce a reflection at the same depth. Additionally, Fig. 4b shows that the wall's 40 cm thickness could be clearly detected (see dotted arrow) at the depth of approximately 41 cm, thus with an error being less than the antenna's vertical resolution of around 1.6 cm.

4.2. Visualization of masonry texture

Examination of the stone-mortar texture behind the plaster was performed by GPR and IR thermography. Due to the unevenness of the masonry surface, the plaster thickness varied between 2–3.5 cm. Taking into account both the GPR near-field effects and its vertical resolution, relatively poor localization and resolution was expected for the visualization of the underlying texture using GPR. However, for wall W1 at the depth of 1.3 cm, the amplitudes of the reflected radar signal yielded a clear reconstruction of the texture at a line spacing of 5 cm (Fig. 5a). Since most applications on-site generally restrict the line spacing to 10 cm (for a time efficient measurement), the corresponding reconstruction is presented in Fig. 5b, where the resolution is notably decreased. The IR thermal and phase images are shown in Fig. 5c and d, respectively. The thermal image presented was obtained after 7 min of cooling, whereas the phase image corresponds to the lowest frequency of 3.7×10^{-4} Hz (calculated as $f_{min} = f_s/NFFT$, where f_s is the sampling frequency and $NFFT$ the number of frames). Compared to GPR, IR thermography does not appreciably contribute to the detection of the wall's texture. However, in contrast to the thermal image, the phase image exhibits higher contrast, but on the other hand requires a longer observation time in order to derive information from a certain depth region. Nevertheless, since uniform heating cannot typically be achieved on-site and a varying plaster thickness can be expected (both of which greatly affect the thermal images), the use of IR phase images along with GPR is recommended for the detection of the underlying masonry texture.

4.3. Detection of plaster delamination and crack propagation

The detection of gradual plaster delamination during shear loading was analysed with both NDT methods. For GPR, the amplitudes of the reflected radar signal were taken into account as above. For IR thermography, we refer only to the IR phase images, since the thermal images could neither visualize the delamination limit nor detect cracks. As already mentioned, DIC together with visual inspection served as a reference to evaluate the efficiency of detection for both methods. For wall W1, DIC out-of-plane displacements for the loading states taken into account are shown in Fig. 6. It should be noted that information is derived by DIC from

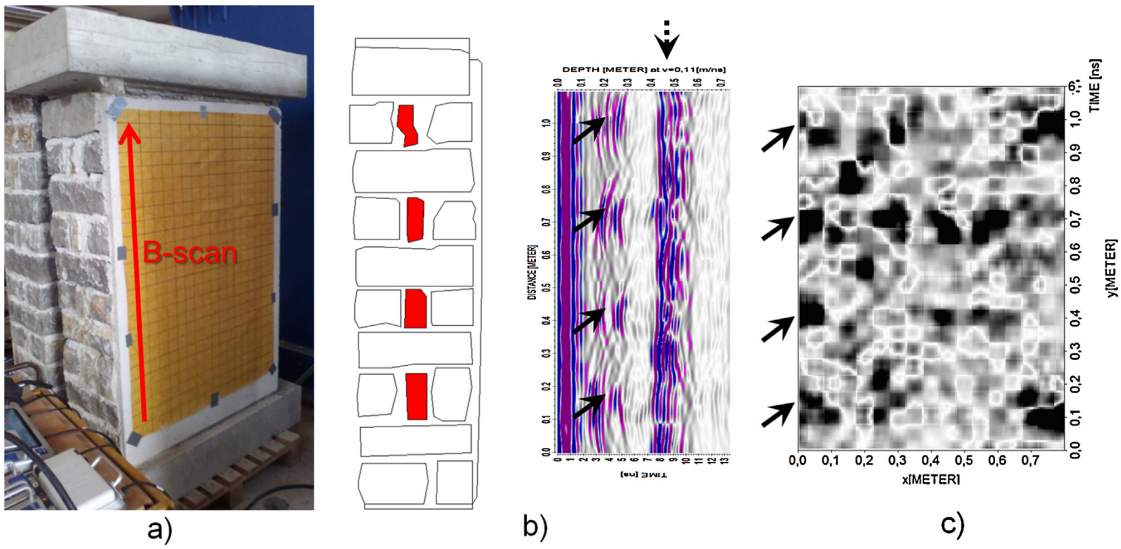

Fig. 4. A photo of specimen W3 with a grid for the GPR measurement and marked B-scan (a); a sketch of the wall morphology and a vertical B-scan (b) and the GPR depth slice at 19 cm (c).

the overall movements of the wall. Thus, both plaster delamination as well as leaf separation should contribute to the resulting out-of-plane displacements. Nevertheless, although the results presented refer to the unconnected wall (outer leaves not connected with header stones), visual leaf separation was not observed at either of the analysed states. Its negligible contribution to the total out-of-plane displacement was also justified by the LVDT data, which showed it to be approximately 0.12 mm at the 2nd loading state. Moreover, the maximum air gap produced by the plaster detached at the top right edge was visually estimated to be around 3.5 mm and more than 12 mm for the 1st and 2nd loading state, respectively. This is in a good agreement with the results in Fig. 6 and therefore proved DIC to be a reliable method for quantitative validation of GPR and IR thermography data.

The results from both NDT methods in Fig. 6 show that the delaminated area detected increases with increasing lateral force. GPR and IR thermography respond to the detected air gap by an increased amplitude of the reflected signal and larger phases (due to higher thermal contrast), respectively. The increased phases can be understood by observing the temperature variation $T(t)$ for a pixel at the non-delaminated (P1) vs. the delaminated (P2) area (see Fig. 6e and Fig. 7). It can be seen that the presence of an air gap slows down the cooling process due to its lower thermal conductivity than that of masonry. For a rough estimate, the temperature variation follows an exponential decay $f(t) = e^{-\alpha \cdot t}$ and the corresponding phase of the Fourier Transform is $\mathrm{ph}(F(\omega)) = \mathrm{atan}(-\omega/\alpha)$. Since pixel P2 has a smaller α than P1, the larger phases refer to P2, i.e. to the delaminated part.

However, the reliability of GPR and IR thermography for delamination detection differs considerably. By comparing the IR phase image at the frequency of 3.7×10^{-4} Hz to the DIC results and visual inspection for the specific wall at the 1st loading state (see Fig. 6d, e), it is evident that an air gap larger than only 2 mm is detected using IR thermography. The latter can also be seen from the results

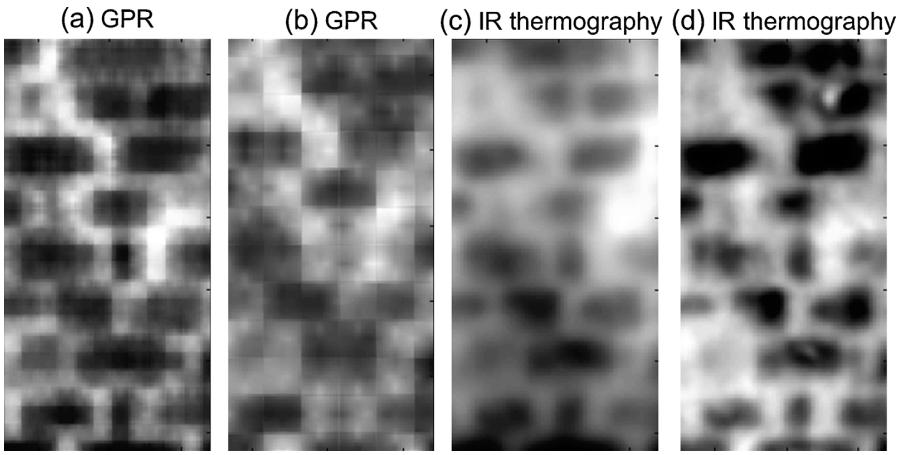

Fig. 5. GPR depth slice at 1.3 cm for 5 cm (a) and 10 cm (b) line spacing; IR thermal image (24.5–29 °C) after 7 min of cooling (c) and IR phase image at the frequency of 3.7×10^{-4} Hz (d) for specimen W1.

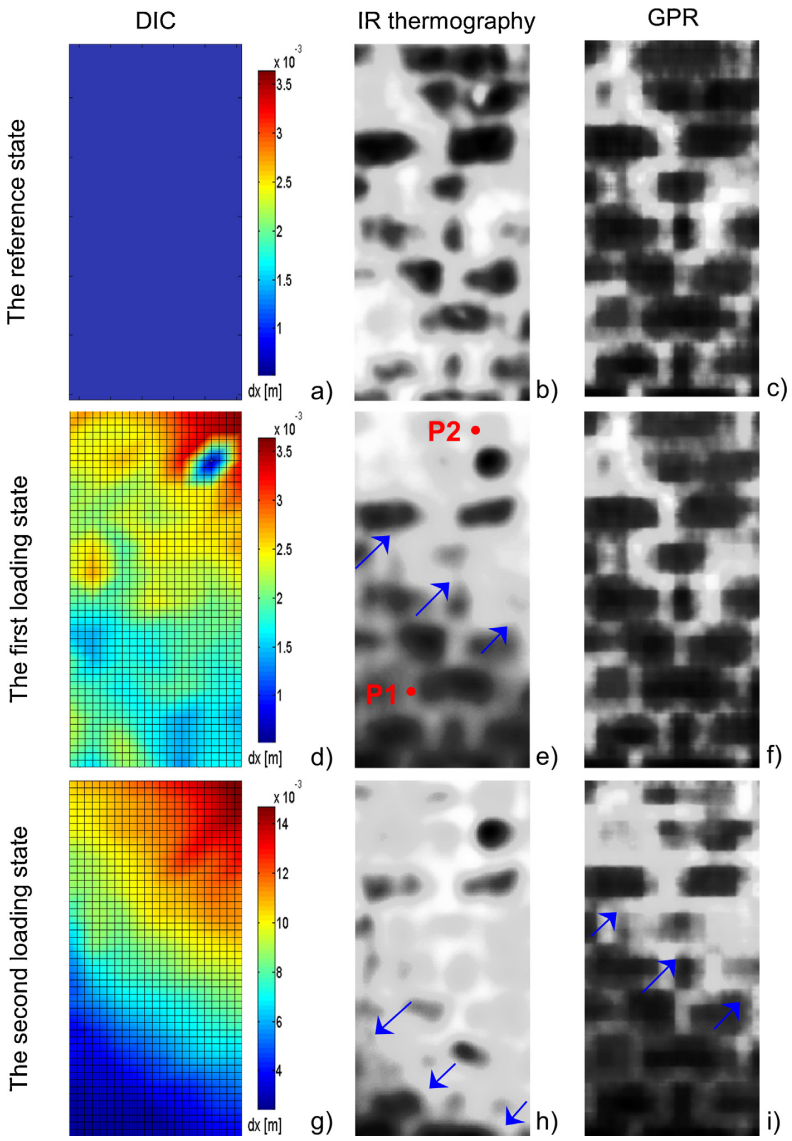

Fig. 6. Detection of plaster delamination by DIC, IR thermography and GPR for specimen W1: DIC out-of-plane displacements (a, d, g), IR phase images at frequency 3.7×10^{-4} Hz (b, e, h) and GPR depth slices at 1.3 cm (c, f, i). Images from the first, second and third rows refer to the reference state, first and second loading states, respectively. The position of the delamination limit is marked with arrows.

in Fig. 6h, obtained at the 2nd loading state, which suggests a delamination over the whole right edge of the specimen. In contrast, at the 1st loading state, GPR yields a very unclear delamination pattern. According to Fig. 6i, at the 2nd loading state, a delamination larger than approximately 8 mm was only detected. Although the results commented here are from only one tested wall, the limits presented for delamination detection were obtained from the overall analysis taking into account the results from all four walls.

Next, the detection of cracks was considered. As expected, this problem could not be handled using GPR [3], whereas IR thermography was found capable of detecting both surface and subsurface crack patterns. The latter was achieved by using IR phase images at higher frequencies, which enable the detection of small thermal contrasts. On the other hand, lower frequencies carry information from the whole depth profile, reflecting the average thermal behaviour of the specimen. Phase images at the lowest frequency (3.7×10^{-4} Hz) were therefore used to visualize the underlying texture and the delamination patterns, whereas higher frequencies were used for the detection of cracks. An example of a detected vertical surface crack at the 2nd loading state of specimen W2 is shown in Fig. 8c for the IR phase image at a frequency of 2.22×10^{-3} Hz. The underlying texture and the delamination patterns are visualized by the corresponding phase image at 3.7×10^{-4} Hz (Fig. 8b), together with the GPR depth slice at the depth of 2 cm (Fig. 8a). In Fig. 9a, the subsurface shear crack pattern at the 2nd loading state of specimen W3 is visualized by the IR phase image at 1.85×10^{-3} Hz before the fall of the plaster. The corresponding photograph of the specimen

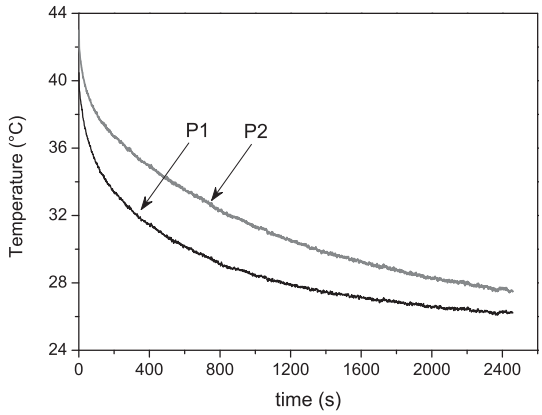

Fig. 7. Temperature variation of pixels P1 and P2 marked in Fig. 6e.

(Fig. 9b) proved that at the time when the IR data was collected, only tiny surface cracks were apparent at the right side of the wall's surface (marked on Fig. 9b). After the plaster fell off, (i.e. following the 2nd loading state), a particular crack pattern could be detected (Fig. 9c). By comparing the latter to the IR phase image (Fig. 9d), it could be suggested that the detected IR pattern on the left side results from the subsurface crack pattern, whereas the IR pattern on the right side most probably results from both the subsurface cracks as well as plaster delamination. However, it should be noted that the method's good performance for the detection of the subsurface cracks resulted from having masonry with joints filled with mortar. In case of partly unfilled joints, a comparison between IR phase images at different frequencies should be carried out.

Although most of the defects could be detected by using IR thermography, estimation of the depth of defects was not possible. Despite the fact that use of quantitative SPT in the frequency domain has been proposed for depth interpretation of laboratory concrete specimens [28], the complexity of the masonry structure, together with the presence of different defects, restricted its use. However, in practice, multi-leaf masonry walls delamination can occur between the plaster layer and the outer leaf, or between different leaves. Cracks together with small air voids may occur anywhere in the masonry structure. Therefore, for correct localization of defects, the fusion of images obtained by GPR and IR thermography (image fusion) should be used to increase the reliability of an NDT inspection on-site.

To improve the imaging results and defect characterization, several algorithms have been proposed for fusion of NDT data. Bayesian inference, the Dempster-Shafer (D-S) theory of evidence, wavelet and multi-resolution analysis have been used on eddy current and IR thermography images from composite and steel structures [29–32]. In NDT applications in civil engineering, image fusion was performed on GPR data acquired at different frequencies and polarizations, and on GPR and ultrasonic data on prestressed concrete

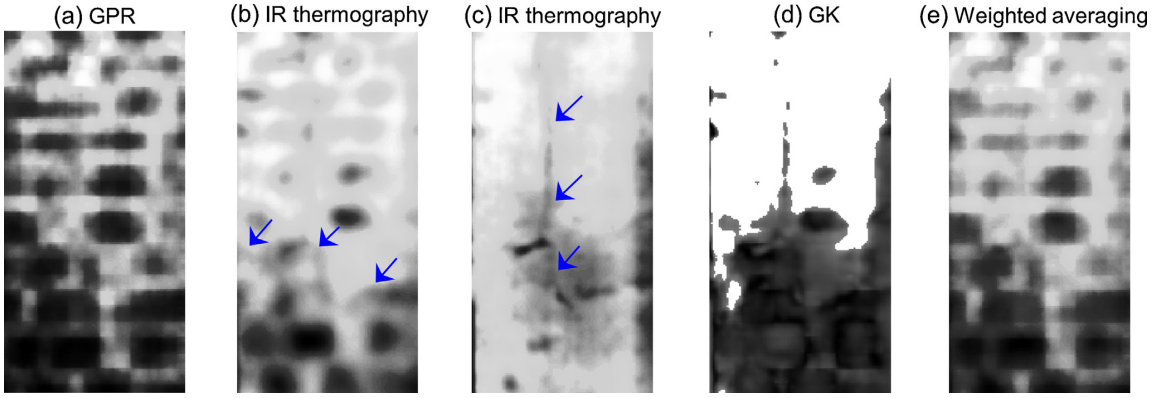

Fig. 8. Detection of plaster delamination and surface cracks by GPR and IR thermography for specimen W2 at the second loading state: GPR depth slice at 2 cm (a), IR phase images at frequencies 3.7×10^{-4} Hz (b) and 2.22×10^{-3} Hz (c), results from image fusion of images (a)–(c) using the Gustafson-Kessel (GK) algorithm (d) and weighted averaging (e). The position of the delamination limit and surface crack is marked with arrows.

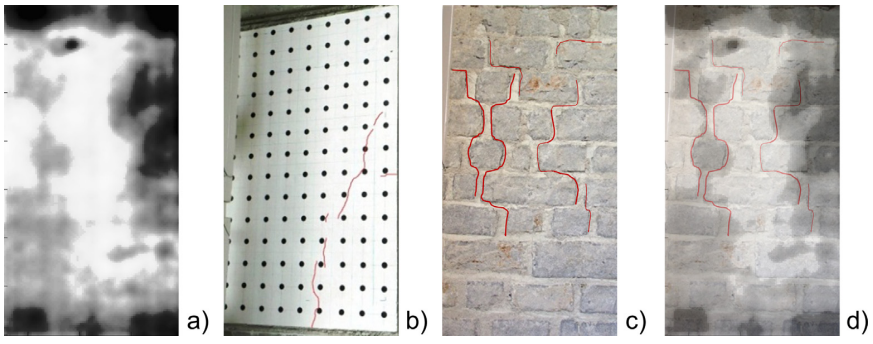

Fig. 9. IR phase image at frequency 1.85×10^{-3} Hz (a) and a corresponding photo of the surface cracks at the second loading state of specimen W3 (b); a photo of the subsurface crack pattern after fall of the plaster (c); overlapped Fig. (a) and (c), (d).

bridge beams and test specimens [33–35]. Here, the applied fusion techniques were restricted to simple arithmetical methods. In our case, GPR and IR thermography images were fused on a pixel-by-pixel basis using clustering methods to derive a partitioned image, where the defects of different patterns could be localized and characterized. As an image fusion technique, we have already applied clustering methods to spectroscopic spatial measurement results on concrete for cement identification [36], as well as to laboratory concrete specimens with simulated defects for defect detection [37]. There, various fuzzy clustering algorithms were assessed and the results showed the Gustafson-Kessel (GK) algorithm [38] to be the most efficient for defect detection. The target of clustering techniques is to group a set of data (observations) into groups (or clusters) by minimizing an objective function [39]. Their main advantage is that they can work fully unsupervised, i.e. they do not need a priori knowledge of the statistical distribution of data.

In the example of the 2nd loading state of wall W2, a vertical surface crack was detected in the IR phase image at a frequency of 2.22×10^{-3} Hz, whereas the underlying texture and delamination pattern were detected by GPR and the IR phase image at 3.7×10^{-4} Hz (Fig. 8). The results suggest that for a supervised fusion algorithm more weight should be given to IR thermography, being more effective in the detection of delamination and crack patterns than GPR. However, an unsupervised clustering algorithm should provide an image where the superior thermal data prevails. Following the outcome of our previous experiments with clustering methods, the GPR and IR thermography data were fused using the GK algorithm, which is able to detect clusters of different shapes in one data set. The results are shown in Fig. 8d. For comparison, the results of image fusion using supervised weighted averaging are presented in Fig. 8e. Here, the weights were roughly estimated from previous experiments on concrete specimens, i.e. 0.85/0.90 for GPR/IR images at the depth of 1.5 cm [40]. It can be seen that both the delamination as well as the crack pattern could be distinguished using the GK algorithm, whereas the vertical crack could not be resolved by averaging. It should be noted that the use of the GK algorithm helped particularly in identifying the vertical crack.

5. Conclusions

The challenge to assess non-destructively the type of structure and seismic damage of plastered multi-leaf stone masonry was tackled through the complementary use of GPR and IR thermography. To validate the methods' performance for assessment of the type of the structure, laboratory three-leaf walls with well-known geometry and structure were investigated. Moreover, the methods' performance in assessing seismic damage of various extents was investigated by subjecting the walls to an in-plane cyclic shear test which produced gradual plaster delamination and crack propagation monitored by a 3D DIC. The DIC out-of-plane displacements proved to be in direct correlation to the plaster delamination and therefore served for quantitative validation of GPR and IR thermography data.

As expected, GPR proved especially powerful in probing the deeper inner structure, where inner stones in rows lacking a full connection produced a strong and accurately positioned reflection of the radar signal and could be therefore clearly distinguished from connecting rows with header stones. Moreover, in spite of the GPR near-field effects, the underlying stone-mortar texture, appearing at the depth of 2–3.5 cm, could be well visualized although its localisation was slightly worsened. IR thermography, on the other hand, did not greatly contribute to the detection of the texture, but outperformed GPR in detecting an air gap produced by the detachment of plaster as small as 2 mm, compared to the minimum 8 mm air gap detected by GPR. By taking into consideration the performance limit states of the plaster as defined in Table 1, it can be concluded that the first limit state could be resolved by IR thermography with high reliability. Moreover, since it yielded the extent of damage from the whole area and not only the visible parts, it could be regarded as a potential method for defining the performance limit state of the plaster. The use of a non-contact method for defining the characteristic limit points of the plaster on masonry walls in cultural heritage structures plays an important role since very often such walls have valuable frescoes, stuccos or mosaics. In contrast, only the extent of damage referred to the third limit state could be detected by 1.6 GHz GPR. Taking into account that applying GPR on a plaster of the third limit state could cause even more damage, GPR could not be regarded as a useful technique for defining the plaster's performance limit state. However, a complementary use of both methods would still be acknowledged where accurate localization of minor delamination is of importance.

IR thermography proved additionally capable of detecting surface and subsurface crack patterns. We showed that phase images of higher frequencies should be used in order to resolve small thermal contrasts resulting from cracking, while phase images at the lowest frequency are better suited for imaging the underlying texture and delamination pattern. However, it should be noted that for masonry with partly unfilled joints, additional post-processing of IR phase images should be performed.

To conclude, the results from this study showed that by complementary use of GPR and IR thermography the structure and extent of damage of laboratory three-leaf walls could be fully assessed. It is believed that the outcome should contribute appreciably in understanding the challenges of both methods for their application to multi-leaf walls in general. However, for further characterisation of variable masonry in practice, we showed that an even more robust performance of both methods could be achieved by image fusion based on clustering methods. Since the methods work unsupervised, they could also be used in situations with very limited knowledge about the masonry and the defects. Moreover, they could shorten the NDT evaluation process and contribute to the decision process regarding the condition of the masonry.

Acknowledgements

Part of the results were obtained through the project PERPETUATE (www.perpetuate.eu), funded by the European Commission in the 7th Framework Programme (FP7/2007-2013), under grant agreement nº 244229. The first author acknowledges the financial support of the Slovenian Research Agency through grant 1000-10-310156. The authors wish to thank the Jožef Stefan International Postgraduate School for the use of their radar system, the company Modri Planet d.o.o. for performing DIC, as well as Damjan Špeglič, Meta Kržan and Franci Čepon for extensive measurement support.

References

[1] L. Binda, A. Saisi, Application of NDTs to the diagnosis of historic structures, in: Proceedings of NDTCE'09 7th International Symposium on Non-Destructive Testing in Civil Engineering, Nantes, June 30–July 3, 2009.
[2] M. Kržan, V. Bosiljkov, Experimental evaluation of the seismic behaviour of multi-leaf stone masonry walls, in: Proceedings of 12th Canadian Masonry Symposium, Vancouver, BC, June 2–5, Masonry Institute of BC, Vancouver, BC, 2013.
[3] L. Binda, V. Bosiljkov, A. Saisi, L. Zanzi, Guidelines for the diagnostic investigation of historic buildings, in: Proceedings of 7th International Masonry Conference, London, October 30–November 1, British Masonry Society, London, 2006.
[4] D.M. McCann, M.C. Forde, Review of NDT methods in the assessment of concrete and masonry structures, NDT E Int. 34 (2001) 71–84.
[5] Ch. Maierhofer, Ch. Köpp, L. Binda, L. Zanzi, J.R. Santiago, B. Knupfer, B. Johansson, C. Modena, F. Porto, M. Marchisio, F. Gravina, M. Falci, J.C. Ruiz, M. Tomazevic, V. Bosiljkov, C.H. Hennen, Project Report EUR 21696 EN – Onsiteformasonry project – On-site investigation techniques for the structural evaluation of historic masonry buildings, European Commission, Office for Official Publications of the European Communities, Brussels, 2006.

[6] D. Ranalli, M. Scozzafava, M. Tallini, Ground penetrating radar investigations for the restoration of historic buildings: the case study of the Collemaggio Basilica (L'Aquila, Italy), J. Cult. Herit. 5 (2004) 91–99.
[7] C.H. Maierhofer, J. Wöstmann, Non-destructive investigation of complex historic masonry structures with impulse radar, in: Proceedings of NDT-CE 2003, International Symposium on Non-Destructive Testing in Civil Engineering, Berlin, September 16–19, DGZfP, Berlin, 2003.
[8] A. Anzani, L. Binda, A. Carpinteri, S. Invernizzi, G. Lacidogna, A multilevel approach for the damage assessment of historic masonry towers, J. Cult. Herit. 11 (2010) 459–470.
[9] A. Sadri, Application of impact-echo technique in diagnoses and repair of stone masonry structures, NDT E Int. 36 (2003) 195–202.
[10] L. Binda, M. Lualdi, A. Saisi, L. Zanzi, Radar investigation as a complementary tool for the diagnosis of historic masonry buildings, Int. J. Mater Struct. Integr. 5 (2011) 1–25.
[11] R. Arndt, Ch. Maierhofer, M. Röllig, F. Weritz, H. Wiggenhauser, Structural investigation of concrete and masonry structures behind plaster by means of pulse phase thermography, in: Proceedings of 7th International Conference on Quantitative Infrared Thermography (QIRT), Rhode-St-Genese, July 5–8, 2004.
[12] N.P. Avdelidis, A. Moropoulou, Applications of infrared thermography for the investigation of historic structures, J. Cult. Herit. 5 (2004) 119–127.
[13] Ch. Maierhofer, M. Röllig, Active thermography for the characterization of surfaces and interfaces of historic masonry structures, in: Proceedings of NDTCE'09, 7th International Symposium on Non-Destructive Testing in Civil Engineering, Nantes, June 30–July 3, 2009.
[14] P. Theodorakeas, C. Ibarra-Castanedo, S. Sfarra, N.P. Avdelidis, M. Koui, X. Maldague, D. Paoletti, D. Ambrosini, NDT inspection of plastered mosaics by means of transient thermography and holographic interferometry, NDT E Int. 47 (2012) 150–156.
[15] N.P. Avdelidis, M. Koui, C. Ibarra-Castanedo, X. Maldague, Thermographic studies of plastered mosaics, Infrared Phys. Techn. 49 (2007) 254–256.
[16] Ch. Maierhofer, S. Leipold, Radar investigation of masonry structures, NDT E Int. 34 (2001) 139–147.
[17] S. Kruschwitz, E. Niederleithinger, C.H. Trela, J. Wöstmann, Complex resistivity and radar investigation of building material: first results of field scale measurements, Acta Geophys. 58 (2010) 96–113.
[18] P. Cotic, Z. Jaglicic, E. Niederleithinger, U. Effner, S. Kruschwitz, C. Trela, V. Bosiljkov, Effect of moisture on the reliability of void detection in brickwork masonry using radar, ultrasonic and complex resistivity tomography, Mater Struct 46 (2013) 1723–1735, http://dx.doi.org/10.1617/s11527-012-0011-3.
[19] L. Binda, L. Zanzi, M. Lualdi, P. Condoleo, Complementarity of non-destructive techniques in the diagnosis of damaged historic structures, in: Proceedings of 10th International Conference on Structural Faults and Repair, London, July 1–3, Engineering Tech Press, London, 2003.
[20] J.D. Daniels (Ed.), Ground-penetrating Radar, second ed., The Institution of Electrical Engineers, London, 2004.
[21] H. Jol (Ed.), Ground Penetrating Radar: Theory and Applications, first ed., Elsevier Science, Amsterdam, Oxford, 2009.
[22] C.H. Maierhofer, M. Röllig, Application of active thermography to the detection of safety relevant defects in civil engineering structures, in: Proceedings of OPTO 2009 & IRS^2 2009, SENSOR+TEST Conference, Nürnberg, May 26–28, 2009.
[23] X.P. Maldague, S. Marinetti, Pulse phase infrared thermography, J. Appl. Phys. 79 (1996) 2694–2698.
[24] R. Arndt, Square pulse thermography in frequency domain, in: V.P. Vavilov, D.D. Burleigh (Eds.), Thermosense XXX, Proceedings of SPIE, Orlando, FL, March 16, Society of Photo Optical, 2008, pp. 69390X–69390X-12.
[25] V. Vavilov, D. Burleigh, Heat Transfer, in: X.P. Maldague, P.O. Moore (Eds.), Nondestructive Handbook, Infrared and Thermal Testing, vol. 3, third ed., ASNT Press, Columbus, Ohio, 2001.
[26] F. Weritz, R. Arndt, M. Röllig, Ch. Maierhofer, H. Wiggenhauser, Investigation of concrete structures with pulse phase thermography, Mater Struct. 38 (2005) 843–849.
[27] S.H. Tung, M.H. Shih, W.P. Sung, Development of digital image correlation method to analyse crack variations of masonry wall, Sadhana 33 (2008) 767–779.
[28] R. Arndt, Ch. Maierhofer, M. Röllig, Quantitative pulse-phase-thermography for masonry and concrete structures, in: Proceedings of 9th European NDT Conference (ECNDT), Berlin, September 25–29, DGZfP, Berlin, 2006.
[29] X.E. Gros, J. Bousigue, K. Takahashi, NDT data fusion at pixel level, NDT E Int. 32 (1999) 283–292.
[30] X.E. Gros, Z. Liu, K. Tsukada, K. Hanasaki, Experimenting with pixel-level NDT data fusion techniques, IEEE T Instrum. Meas. 49 (2000) 1083–1090.
[31] Z. Liu, D.S. Forsyth, M.S. Safizadeh, A. Fahr, A data-fusion scheme for quantitative image analysis by using locally weighted regression and Dempster–Shafer theory, IEEE T Instrum. Meas. 57 (2008) 2554–2560.
[32] S. Balakrishnan, M. Cacciola, L. Udpa, B.P. Rao, T. Jayakumar, B. Raj, Development of image fusion methodology using discrete wavelet transform for eddy current images, NDT E Int. 51 (2012) 51–57.
[33] C. Kohl, M. Krause, Ch. Maierhofer, J. Wöstmann, 2D-and 3D-visualisation of NDT-data using data fusion technique, Mater Struct. 38 (2005) 817–826.
[34] Ch. Maierhofer, G. Zacher, C. Kohl, J. Wöstmann, Evaluation of radar and complementary echo methods for NDT of concrete elements, J, Nondestruct. Eval. 27 (2008) 47–57.
[35] J. Cui, D.R. Huston, R. Arndt, F. Jalinoos, Data fusion techniques of multiple sensors non-destructive evaluation of a concrete bridge deck, in: Proceedings of NDE/NDT for Highway Bridges: Structural Materials Technology (SMT) Conference, New York City, NY, August 16–20, 2010.
[36] P. Cotič, E. Niederleithinger, G. Wilsch, Unsupervised clustering of laser-induced breakdown spectroscopy data from concrete. Cement Concrete Res (submitted for publication).
[37] P. Cotič, Z. Jagličić, E. Niederleithinger, M. Stoppel, V. Bosiljkov, Image fusion for improved detection of near-surface defects in NDT-CE using unsupervised clustering methods. J Nondestruct Eval (submitted for publication).
[38] D. Gustafson, W. Kessel, Fuzzy clustering with a fuzzy covariance matrix, in: Proceedings of the 1978 IEEE Conference on Decision and Control including the 17th Symposium on Adaptive Processes, San Diego, CA, January 10–12, IEEE Control Systems Society, San Diego, CA, 1979, pp. 761–766.
[39] F. Höppner, F. Klawonn, R. Kruse, T. Runkler, Fuzzy Cluster Analysis: Methods for Classification, Data Analysis and Image Recognition, John Wiley & Sons Ltd, Chichester, 1999.
[40] P. Cotič, Z. Jagličić, V. Bosiljkov, E. Niederleithinger, GPR and IR thermography for near-surface defect detection in building structures, in: Proceedings of the 12th International Conference of the Slovenian Society for Non-Destructive Testing, "Application of Contemporary Non-Destructive Testing in Engineering", Ljubljana, September 4–6, 2013.

APPENDIX C: ARTICLE 3

Effect of moisture on the reliability of void detection in brickwork masonry using radar, ultrasonic and complex resistivity tomography

P. Cotič, Z. Jagličić, E. Niederleithinger, U. Effner, S. Kruschwitz, C. Trela & V. Bosiljkov

Mater Stuct (2013) **46**(10):1723–1735
DOI 10.1617/s11527-012-0011-3

Materials and Structures (2013) 46:1723–1735
DOI 10.1617/s11527-012-0011-3

ORIGINAL ARTICLE

Effect of moisture on the reliability of void detection in brickwork masonry using radar, ultrasonic and complex resistivity tomography

Patricia Cotic · Zvonko Jaglicic · Ernst Niederleithinger · Ute Effner · Sabine Kruschwitz · Christiane Trela · Vlatko Bosiljkov

Received: 8 June 2012 / Accepted: 21 December 2012 / Published online: 10 January 2013

Abstract The influence of moisture on the reliability of detection of larger voids in brickwork masonry was investigated using three non-destructive techniques: radar, ultrasonic and complex resistivity (CR). Radar and ultrasonic travel time tomography, as well as CR tomography, were performed over a specific cross section of a specimen containing a large void at a known position to determine the influence of different levels of moisture content in the brickwork on the wave velocities and the CR magnitude. We defined a numerical estimator to quantitatively determine the void detection efficiency from the images obtained when exposing the specimen to moisture. The results showed radar to be the most reliable technique for void detection in both dry and wet masonry, while CR performed much better in detecting larger air voids in wet masonry.

P. Cotic (✉) · Z. Jaglicic
Institute of Mathematics, Physics and Mechanics, Jadranska 19, 1000 Ljubljana, Slovenia
e-mail: patricia.cotic@imfm.si

P. Cotic · Z. Jaglicic · V. Bosiljkov
Faculty of Civil and Geodetic Engineering, University of Ljubljana, Jamova 2, 1000 Ljubljana, Slovenia

E. Niederleithinger · U. Effner · S. Kruschwitz · C. Trela
BAM Federal Institute for Materials Research and Testing, Unter den Eichen 87, 12205 Berlin, Germany

Keywords Radar, ultrasonic and complex resistivity tomography · Masonry · Moisture · Void detection

1 Introduction

For some time, the non-destructive testing (NDT) community has worked on the application of several techniques on brick and stone masonry structures. Contrary to the original application of NDT techniques on homogeneous materials (e.g. steel), its application to masonry needs extensive calibration to ensure deeper understanding of the effect of typical problems in masonry structures. Besides, complementary use of different non-destructive techniques may better resolve the structural inhomogeneity of masonry structures under different conditions, rather than a single method [1, 3, 5].

Typical problems related to masonry structures are the detection of multiple leaf walls, detachment of layers, the presence of layers of different materials, grouting faults, inclusions, larger voids and deterioration due to moisture [1, 18]. While recent studies in infrared thermography show increasing success in detecting near-surface features in masonry [1, 19], radar and sonic techniques exploit the capability of surveying the deeper inner structure [1, 2, 6, 18, 20]. Among the previously stated problems, the presence of larger voids and inclusions especially may indicate lack of connection and decrease in resistance of load

bearing walls and pillars in masonry buildings. For spatial imaging of inclusions and larger voids, tomography should be performed. Although it cannot be regarded as a standard technique for the investigation of masonry structures due to its complexity, tomography may resolve some ambiguities encountered in echo configuration measurements [14].

Beside a carefully conducted tomographic measurement, the inversion procedure (imaging) also plays an important role. Different inversion techniques for acoustic and electromagnetic waves have been developed. In addition to conventional travel time tomography (TT) and amplitude tomography (AT), Camplani et al. [7] as well as Valle et al. [27] explored the benefit of migration tomography (MIG) as well as diffraction tomography (DT). Both have been highlighted as capable of a remarkable improvement in resolution, especially in edge detection. However, in our study, only TT was performed for ultrasonic and radar data, as it proved to be sufficient to resolve larger voids in the central area of the measured specimen. Up to now, TT on masonry has been explored by only a few authors. Kong and By [13] applied both TT and AT to stone pillars using frequency stepped radar, whereas Binda et al. [4] applied acoustic TT among with attenuation tomography in frequency domain to historic masonry pillars to evaluate masonry quality and homogeneity. A complementary survey of stone masonry bridges with radar and sonic TT, as well as conductivity tomography was performed by Colla et al. [8]. Schuller et al. [22] proposed acoustic TT on masonry wall specimens for the identification of damage patterns following in-plane seismic loading and the effectiveness of grouting injection. Flint et al. [10] demonstrated the response of seismic, radar and electrical resistivity tomography to changes in the condition of the masonry, such as the ingress of water. Wendrich et al. [28] applied radar and ultrasonic TT for the detection of voids in brick masonry structures. There, a comparison between inversion results of experimental data versus numerical modelling was presented.

The aim of this study was to present the capabilities of a complementary survey using radar and ultrasonic TT, as well as complex resistivity (CR) tomography, on masonry for the detection of a larger void while subjecting masonry to different humidity conditions. The effect of moisture on the reliability of detection was explored. It is well known that moisture as an additional typical problem in masonry buildings can affect both the mechanical characteristics of masonry, as well as the plaster and rendering and therefore has to be identified in combination with other structural problems. The influence of moisture content on radar and resistivity measurements has been discussed in Kruschwitz et al. [14] and Maierhofer and Colla [17].

Within the scope of this work, firstly physical effects of material properties on the propagation of electromagnetic and acoustic waves and CR properties are briefly presented, followed by a field scale experiment and tomographic results. Analysis of input data for radar TT is discussed as well.

2 Material properties

2.1 Electromagnetic properties

The radar method is based on high frequency electromagnetic wave propagation. The signal is affected by both the dielectric constant and the electrical conductivity of the various materials within the structure. Since the relative magnetic permeability μ_r can be taken as 1 for most building materials, the velocity of radar wave propagation is given by

$$v = \frac{c}{\sqrt{\varepsilon_r}} \tag{1}$$

where c is the speed of light in a vacuum and ε_r the relative permittivity or dielectric constant of the material.

The wave experiences attenuation due to absorption of its electromagnetic energy. The change in the wave amplitude can be expressed by the attenuation coefficient, which is basically a function of the electromagnetic wave frequency and the material conductivity and can be expressed by Jol [12]

$$\alpha = \omega\sqrt{\mu\varepsilon}\left[\frac{1}{2}\left(\sqrt{1+\frac{\sigma^2}{\omega^2\varepsilon^2}}-1\right)\right]^{1/2} \tag{2}$$

where $\omega = 2\pi f$ is the angular frequency and f is the frequency of the electromagnetic wave; μ is the magnetic permeability of the material, defined by $\mu = \mu_r\mu_0$, where μ_0 is the free-space magnetic permeability; ε is the permittivity of the material, defined by $\varepsilon = \varepsilon_r\varepsilon_0$, where ε_0 is the free-space permittivity; and σ is the electrical conductivity of the material.

The higher the frequency and conductivity, the higher is the attenuation, and consequently the lower is the penetration depth. Moisture increases both the dielectric constant and the conductivity of the material and thus reduces the penetration depth. Moreover, due to the increased moisture content the propagation velocity decreases (Eq. 1) and affects the radar resolution. For TT tomography the following expression has been proposed for its calculation [23]

$$\Delta_{\text{tomo}} \approx \sqrt{\frac{vx_0}{f_c}} \tag{3}$$

where x_0 is the half distance between transducers (as anomaly is in the middle) and f_c is the central frequency of the radar antenna signal. As the propagation velocity decreases the radar resolution improves. However, the ray coverage, accuracy of travel time measurement etc. may further limit the resolution.

2.2 Acoustic properties

In solids, both longitudinal p-waves and transversal s-waves are present. For the investigation of masonry, p-waves are of importance as they are the fastest and thus easy to detect and pick in TT. The sound velocity of p-waves is governed by the equation

$$v = \sqrt{\frac{E(1-\mu)}{\rho(1+\mu)(1-2\mu)}} \tag{4}$$

where E is the modulus of elasticity, ρ is the density and μ is the Poisson ratio of the material. In engineering materials, these properties are related to material strength and moisture content [10].

2.3 Complex resistivity properties

The fundamental physical basis for electrical methods is Ohm's Law. By measuring the potential difference U between adjacent electrodes for a fixed electric current I, the apparent or average resistivity ρ_a of the investigated inhomogeneous material can be determined using a configuration factor K, which depends on the electrode and specimen geometry

$$\rho_a = K\frac{U}{I}. \tag{5}$$

Four-electrode array, separating current injection from voltage measurement, is preferred to minimize the influence of contact resistances. Taking into account the polarization phenomenon of porous building materials, the CR magnitude $|\rho|$ as well as the CR phase shift Φ can be measured in response to a stimulus with an alternating current [14]. The CR ρ'' is given by

$$\rho'' = |\rho|e^{i\Phi}. \tag{6}$$

It should be noted that the electrical resistivity of materials is sensitive to their porosity, the morphology of the pore space and the resistivity of the pore fluid [10]. Therefore, the moisture content should be determined with respect to the amount and type of porosity.

3 Experimental procedure

For the investigation of larger voids in masonry buildings, the "Asterix I" brick masonry test specimen [28] was chosen. The specimen height is 1.39 m, length 0.99 m and width 0.74 m and it has inbuilt voids of different dimensions (simulated by omitting bricks in certain layers during construction). Tomographic measurements were performed only at cross section A–A over the largest void of size 0.27 × 0.27 × 0.62 m^3 (see Fig. 1). The specimen was constructed from solid clay bricks with completely filled mortar joints. Thus it enables the investigation of inbuilt anomalies and moisture under ideal conditions.

To study the influence of the moisture level in the masonry on void detection by radar, ultrasonic and CR techniques, two sets of tomographic measurements were performed: first on a relatively dry specimen with an average moisture content of 3 mass% (hereinafter referred to as the "dry specimen"); second on a wet specimen with an average moisture content of 8 mass% (hereinafter referred to as the "wet specimen") over cross section A–A. The humidity level was determined by the classic Darr test by boring and simultaneously obtaining powder every 0.05 m along the depth of the borehole. The average moisture content was determined as the mean value from four boreholes that were made along the longer size of the specimen with larger depth to the void (top edge of cross section A–A in Fig. 1). After performing the first set of measurements on the dry specimen, the specimen was immersed in a steel water bath for 8 days. The water level reached the top of the 3rd layer of bricks. After immersion, all tomographic measurements were repeated. Altogether,

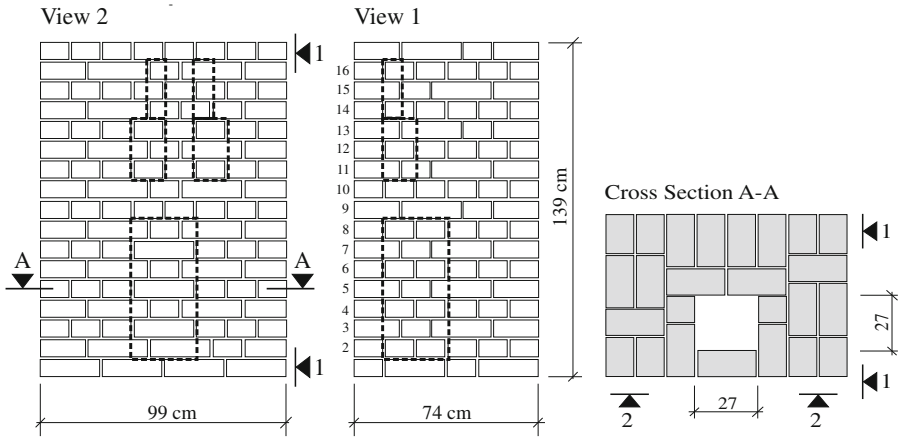

Fig. 1 View 1 and 2 of the "Asterix I" masonry test specimen with the position and the size of voids, and cross section A–A over the largest void

we acquired six sets of NDT data: radar-, ultrasonic- and CR-tomographies of the dry and the wet specimen. It should be mentioned that the radar and ultrasonic tomographic data of the dry state were collected much earlier [28] which results in different number of data collected for the tomography on the dry and wet specimen. Taking into account that the drying and wetting process of the specimen could not be ensured totally homogeneously the Darr test results cannot be extrapolated to assess the moisture distribution over the whole analysed cross section. Therefore, the notations dry and wet should not be linked to the actual moisture content of the specimen but rather to the state before and after immersion.

3.1 Radar equipment

For radar tomographic measurements, the SIRveyor SIR-20 radar system from Geophysical Survey Systems Inc. (GSSI; Salem, USA) was used with bow tie bistatic antennas with a central frequency of 1.5 GHz. The tomographic measurement of the dry specimen was performed in a point measurement mode using a spacing of 13 cm between measurement points, whereas the tomography of the wet specimen was performed in a continuous mode using a calibrated survey wheel and a spacing of 5 cm between measurement points. Altogether, around 500 data was collected on the dry and around 1680 on the wet specimen. Ray paths that were collected by radar tomography on the dry specimen are displayed in Fig. 2. In the radar TT measurements, the transmitter and the receiver antenna, placed on different sides, were moved along the scanned section in a series of possible combinations (Fig. 3). For each transmitter position, the electromagnetic signals were recorded for all moving receiver positions from all four sides.

3.2 Ultrasonic equipment

For ultrasonic tomographic measurements we used Acsys SO202 longitudinal transducers with a frequency of 25 kHz, an arbitrary function generator including an amplifier for signal generation and a preamplifier on the receiver side. Data were recorded by an industry standard analog/digital converter and stored on a PC. For our purposes, a rectangular pulse with a duration of 40 μs and a repetition frequency of 20 Hz was used. Vaseline served as the coupling agent. The ultrasonic measurement for both dry and wet state of the specimen was performed in the same geometry as in radar tomography.

3.3 Complex resistivity equipment

Among electrical methods, the CR method was chosen due to its higher sensitivity compared to normal resistivity methods. Using alternating currents of high frequencies, materials of very low conductivity can be detected. For CR tomography, two devices were used; a multichannel SIP256c device (Radic Research), as well as an LGM 4-Point-Light (Lippmann) device with an ActEle extension (active electrodes for CR tomography) (Fig. 3). Both measure CR magnitude and phase shift across the specimen relative to a shunt resistor with a high input impedance. In comparison with the LGM, the SIP 256c uses a higher applied voltage (up to 230 V) and measurements can be

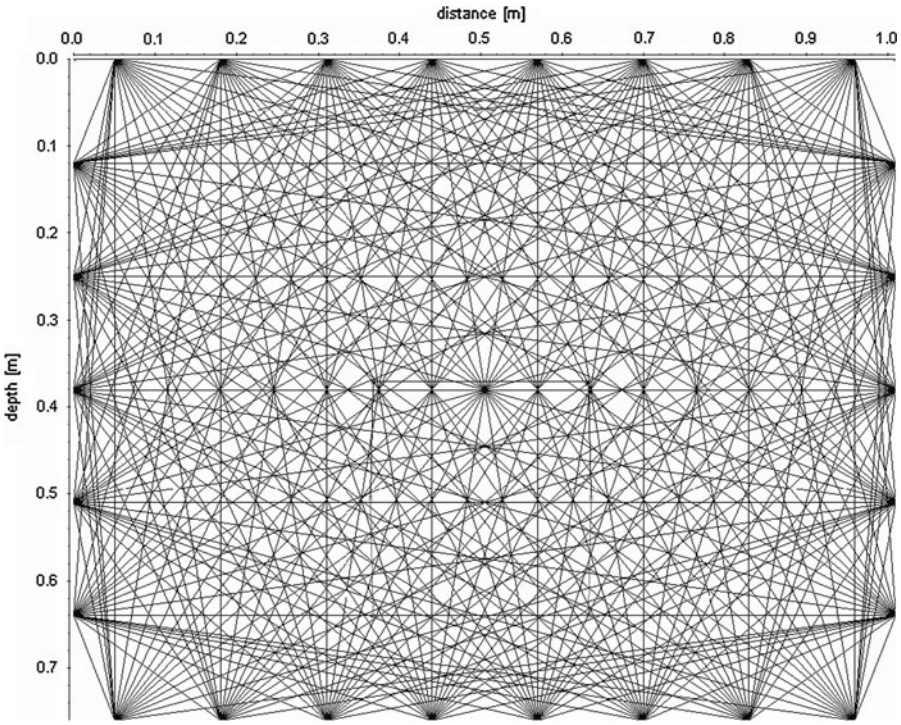

Fig. 2 Ray paths that were collected by radar tomography on the dry specimen

Fig. 3 Radar tomographic measurement over cross section A–A and CR tomographic measurement over several cross sections using the LGM device

acquired over a broader frequency range from 1 mHz to 1 kHz.

The following three electrode configurations were applied: dipole–dipole, Wenner and Schlumberger arrays [15]. For a complete four-sided measurement, 68 electrodes were used with 19 electrodes placed on each longer side and 15 electrodes on each shorter side of the specimen. The measurement was continued until resistivities were determined for all necessary combinations of electrode positions. ECG- (Electrocardiography) electrodes were positioned around the specimen separated by a distance of 0.05 m.

4 Measurement results

4.1 Radar and ultrasonic results

For the tomographic inversion of radar and ultrasonic travel times, initially the first arrival times were picked from the recorded data. For radar waves this was done automatically with the Reflexw commercial software [21]. However, as the ultrasonic data exhibited higher scattering due to noise, an automatic picking algorithm based on the Akaike information criterion (AIC) was used, where the first arrival time was defined by the minimum of the AIC function [16]. For our inversion routine, only transmitted waves needed to be taken into account and distinguished from refracted and reflected waves. In the case of a large incident angle, refracted waves could arrive at the receiver faster than transmitted waves.

It should be noticed that the choice of the first arrival time, which influences the imaging, can be remarkably affected by various sources of distortions, which comprise variable ray coverage, systematically incorrect coordinate position, dislocations of antennas/sensors and the influence of high-frequency uncorrelated noise that decreases the signal to noise ratio [9, 24, 25]. Air calibration measurements and data quality checks of the picked travel times prior to the inversion process may identify possible errors and contribute to more reliable tomographic images [25]. In our study, the latter was taken into account but is not discussed here as it is not the subject of the paper. However, as the first arrival times contain valuable information about the physical effects of material properties on the propagation of electromagnetic and acoustic waves, analysis of the picked travel times can contribute to the interpretation of the tomographic velocity images. Thus, velocity and reciprocity checking of travel times after the removal of outliers is presented. For the velocity check, the velocity of each ray was calculated according to its direct distance and the travel time of the ray. The aim of the reciprocity check was to determine the travel time difference between opposite transmitter and receiver positions, as schematically displayed in Fig. 4. For the velocity check, only rays not passing the void area were used (Fig. 5), whereas for the reciprocity check, the whole data set was investigated.

In Fig. 6 travel time versus ray length dependence is displayed for radar and ultrasonic data on the dry and the wet specimen, whereas in Fig. 7 travel time reciprocity results are displayed. As expected, a linear dependence between the travel times and the ray lengths can be observed from Fig. 6. However, velocities belonging to longer distances are slightly more scattered due to more refractions and scatterings on mortar joints. Nonetheless, this phenomenon is less pronounced than stated in Schuller et al. [22], where acoustic waves produced by an instrumental hammer were used.

Moreover, R-squared values of the fitted lines reveal that both radar and ultrasonic data obtained on the more humid specimen exhibit higher scattering compared to the data acquired on the dry specimen. This is also proved by the normalized reciprocity travel time residuals (normalized on the corresponding measured travel time), on comparing the results of

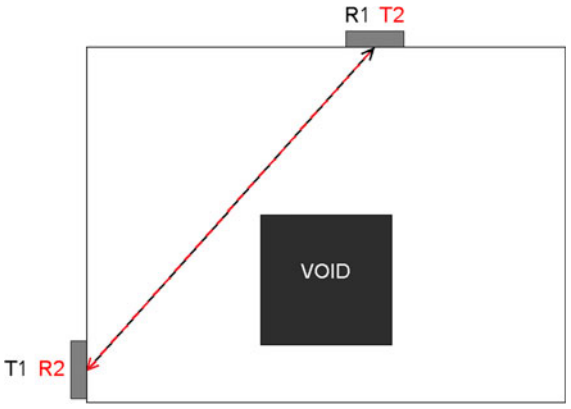

Fig. 4 Representation of the reciprocity check

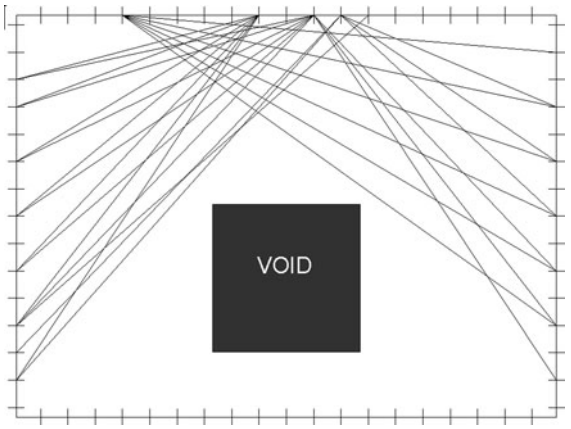

Fig. 5 Part of the region of rays taken into account for the velocity check

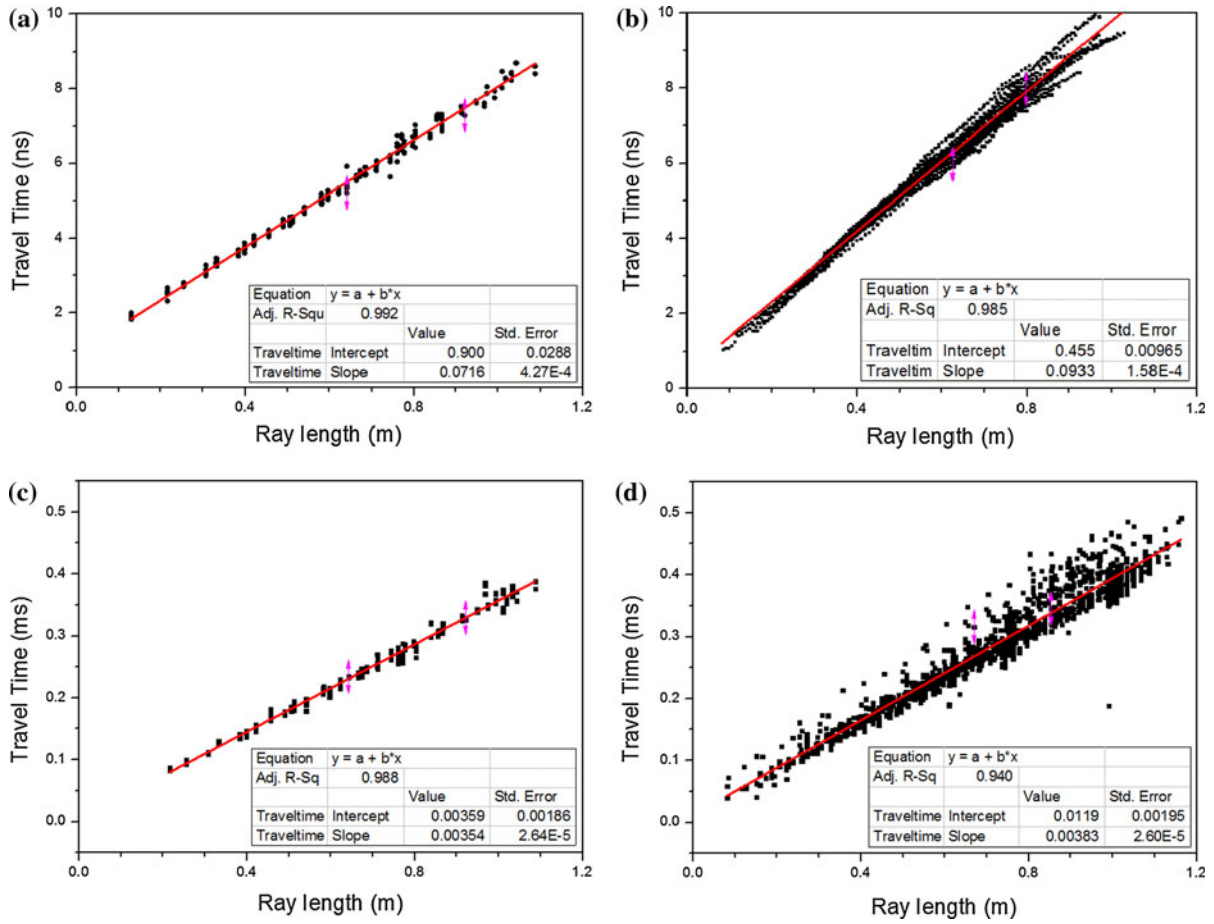

Fig. 6 Velocity check of radar travel times of the dry (**a**) and the wet specimen (**b**), and velocity check of ultrasonic travel times of the dry (**c**) and the wet specimen (**d**)

Fig. 7a–c vs. Fig. 7d–f and Fig. 7g–i vs. Fig. 7j–l. Additionally, the normal distribution of residuals around zero (Fig. 7a, d, g, j) excludes the possibility of apparent systematic errors (only a small deviation from zero can be observed in Fig. 7g). Contrary to results obtained from other studies [25], our results do not exhibit any obvious dependency of normalized travel time residuals on incidence angle either for the radar or the ultrasonic data. In case 7b, e higher residuals can be observed on short distances, which means that the reliability of data collected on short ray lengths is poor. However, as this data contains information from the corners of the specimen, the data should not be discarded before the inversion but rather should the reconstructed velocities at the corners be taken as less reliable. Moreover, for both radar and ultrasonic data the highest normalized residuals were in the majority of the order of 5 % which is at short distances almost the limit of accuracy of both methods. Small antenna dislocation, incorrect transducer positioning, unsmooth surface of the specimen and poor coupling of ultrasonic transducers might all be possible reasons for small systematic travel time residuals.

For a qualitative comparison of the quality of the radar and ultrasonic data, standard deviations (STDV) of normalized reciprocity travel time residuals are displayed in Table 1. As already shown (Figs. 6, 7), the ultrasonic data exhibit higher scattering than the radar data, where according to the STDV up to 16 % higher scattering was obtained on the dry and around 27 % on the wet specimen. Two explanations of this effect are possible. According to the first, the ultrasonic data could be more affected by ambient vibrations at the test

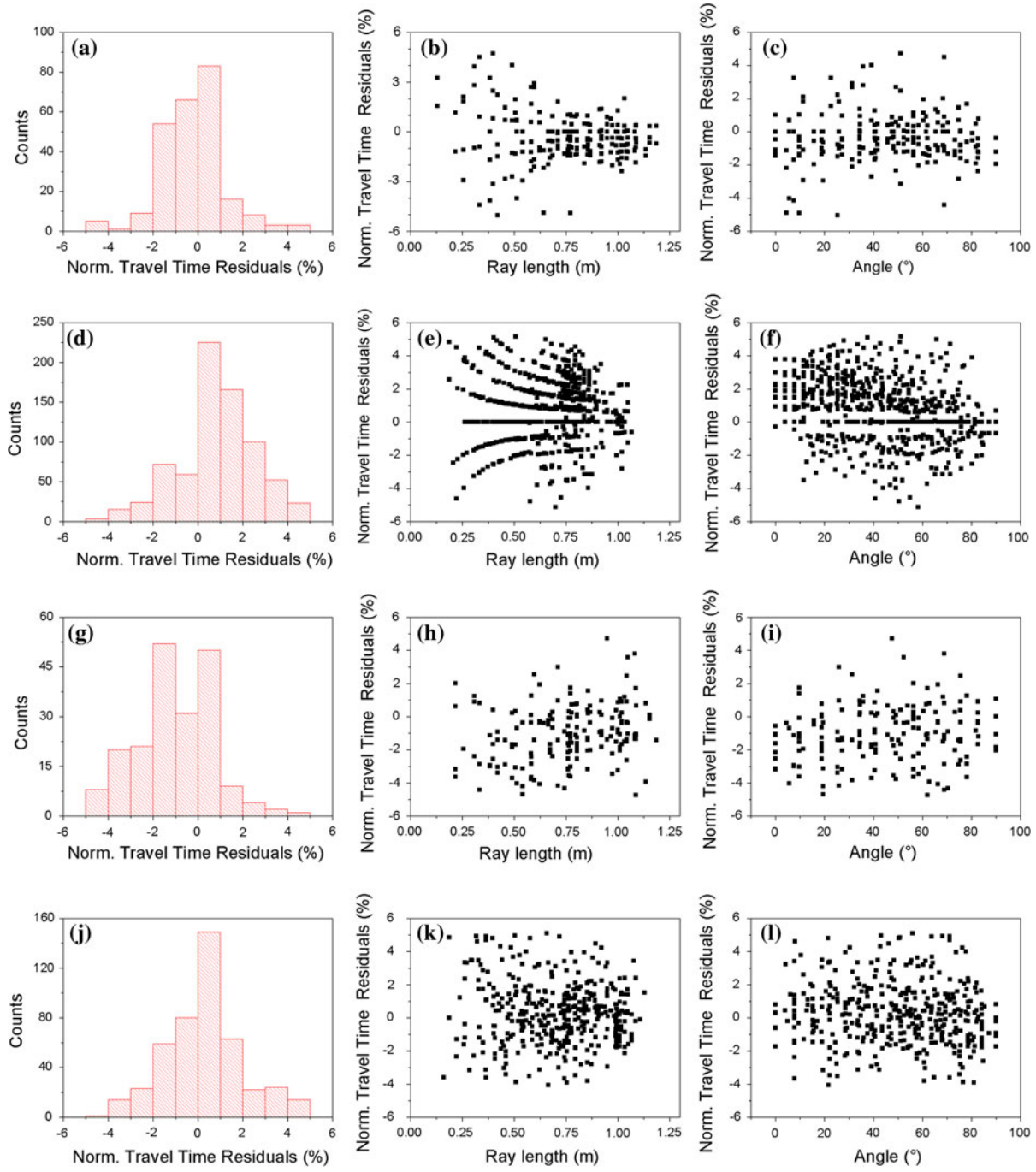

Fig. 7 Reciprocity check of radar travel times of the dry (**a**)–(**c**) and the wet specimen (**d**)–(**f**), and reciprocity check of ultrasonic travel times of the dry (**g**)–(**i**) and the wet specimen (**j**)–(**l**)

site, resulting in a low signal to noise ratio and consequently larger picking errors in comparison to the radar data. The second possibility could be that the high scattering of ultrasonic data is due to stronger variation in acoustic properties of masonry materials compared to the variation in electromagnetic properties. According to Flint et al. [10], this gives rise to larger angles of refraction at various interfaces within masonry (brick

Table 1 Standard deviation of normalized reciprocity travel time residuals for radar and ultrasonic data

	STDV (%)
Radar dry	1.48
Radar wet	1.81
US dry	1.72
US wet	2.30

and mortar joints) and therefore the data appear more scattered. Besides, by comparing the differences in STDV between the wet and the dry specimen for the radar and ultrasonic data, the latter seem to be significantly more sensitive to moisture. One explanation for this could be that moisture produces an even higher variation in acoustic properties of various masonry materials, while leaving the difference in electromagnetic properties relatively unchanged. However, it should be pointed out that also the different data density acquired on the dry and wet specimen could contribute to variations in scattering.

From the recorded travel times, tomographic images of the radar and ultrasonic velocity distribution were obtained for the investigated section (Fig. 8). Presented images were obtained after the removal of outliers detected from the data quality check. For inversion, the commercial software Geo-Tom3D [26] was used. Due to the great difference in the material properties of the investigated section, curved ray inversion was used after a certain number of straight ray iterations. This took into account refractions from internal interfaces and ensured a convergence limit. As expected, higher velocity variations appear at the corners of the specimen due to poor data accuracy at short distances. According to the conclusions from the data quality check, higher variations appear on sound velocity images. Besides, ultrasonic velocity images reveal the inhomogeneous moisture distribution of the analysed cross section, that is especially noticeable from the red coloured area of the wet specimen. It has to be mentioned that the reconstructed velocity values for the void area cannot be assigned to air neither for radar

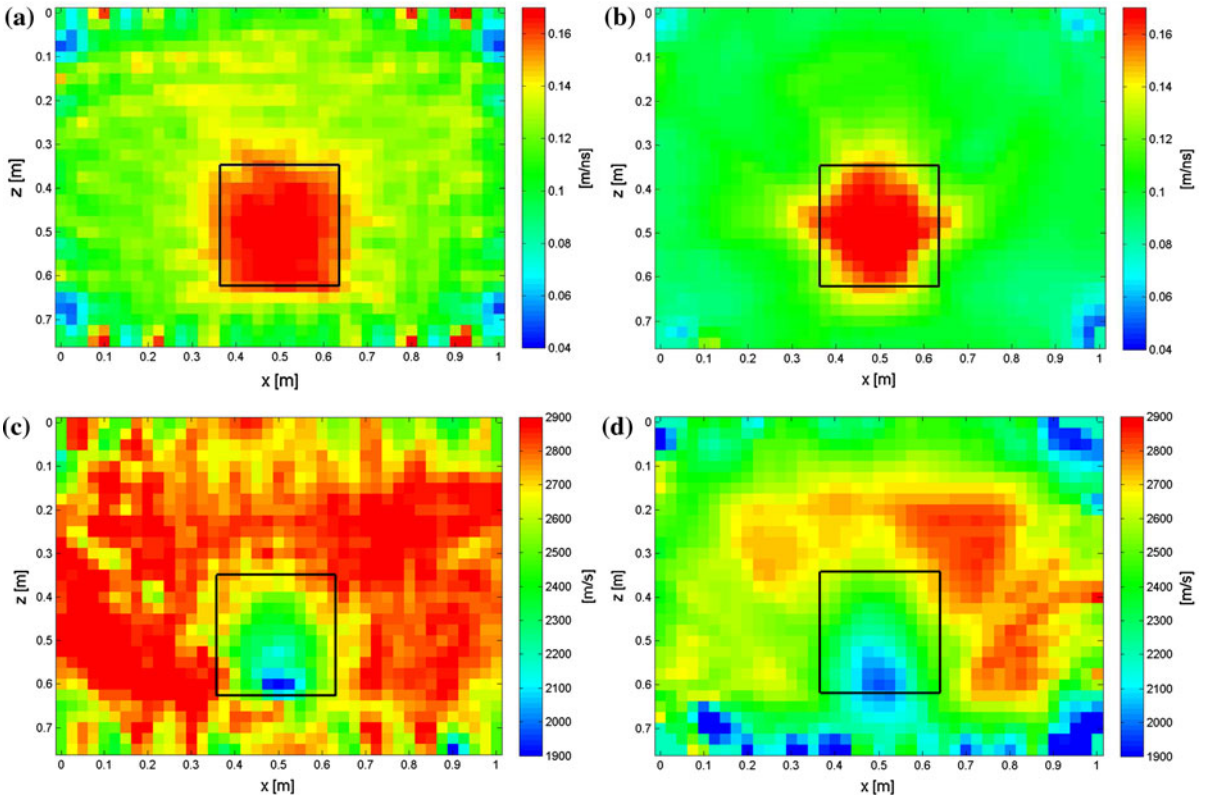

Fig. 8 Velocity images for radar data of the dry (**a**) and the wet specimen (**b**), and ultrasonic data of the dry (**c**) and the wet specimen (**d**) where the rectangle marks the exact position of the void

Table 2 Tomographic results for radar and ultrasonic data of the dry and the wet specimen

	Average surrounding velocity	Void detection efficiency (%)	Level of scattering (%)
Radar dry	0.13 m/ns	89	10
Radar wet	0.10 m/ns	81	11
US dry	3100 m/s	43	4.4
US wet	2800 m/s	37	15

The coefficient of variation (COV) of all average surrounding velocities ranges between 10 and 15 %

nor for ultrasonic results. The main reason for this is the restriction of the inversion process. Unfortunately, this drawback limits the possibility of material characterization of the void but nonetheless, a clear identification of an anomaly can be given. Another weakness of the inversion process is the reconstructed shape of the void, where high material contrast between the surrounding and the void limits the boundary detection. However, according to the tomographic images, the different moisture conditions of the specimen affect the reliability of void detection far more than the inversion process. Note also the much lower resolution at the void area between radar and ultrasonic. The reason for this is the difference in wave propagation between electromagnetic and sound waves, where sound waves by avoiding travelling through the air void result in much poorer ray coverage over the void.

From Table 2 it is evident that the average velocity in the area surrounding the void decreases as a function of moisture increase for both radar and ultrasonic data. For radar a decrement of 25 % in average velocity can be observed with increase in moisture from 3 to 8 mass%, while for ultrasonic only a drop of 10 %. It can be pointed out that moisture remarkably increases the dielectric constant of masonry (already reported by Colla et al. [8]), whereas it has a smaller effect on the elastic properties of masonry. This is, however, contrary to the influence on scattering discussed previously and thus means that on one hand moisture gives rise to a change in acoustic properties of masonry materials, while on the other it has little influence on the average acoustic properties that determine the velocity of propagation of sound waves.

The limits of void detection can hardly be determined effectively by visually examining velocity images (Fig. 8). Therefore, to give a reliable evaluation of the change in efficiency of void detection with the three techniques used, while subjecting masonry to two

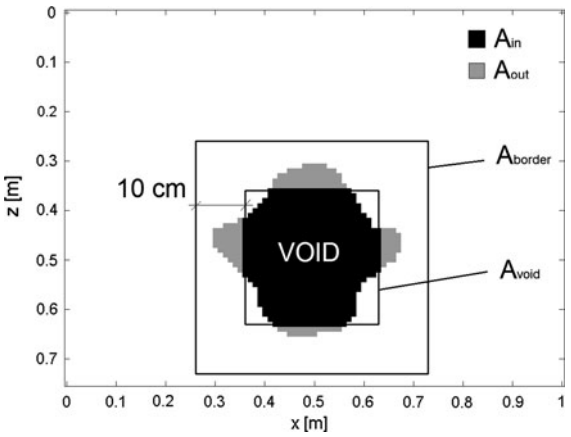

Fig. 9 Parameters for computation of the efficiency of void detection E_{void} and the level of scattering $E_{scatter}$ in the border area outside the void

different moisture levels, an estimator had to be chosen carefully. To assess the efficiency of void detection, we define two estimators: E_{void} and $E_{scatter}$. Besides determining the void detection efficiency directly with E_{void}, the level of scattering (defined by $E_{scatter}$) in a defined border area outside the void should also be taken into account. Firstly, a threshold value was determined for both estimators. This means for radar and ultrasonic tomographic images a velocity threshold value and for CR tomographic images a resistivity threshold value. On trying different values, the mean value between the average velocity/resistivity of the surrounding area and the maximum velocity/resistivity of the void area was found to be the most suitable one. In determining the efficiency of void detection for radar data this means that the void was detected on a particular pixel if the velocity of the pixel was greater than or equal to the threshold value. The two estimators can be given by the following equations:

$$E_{void} = \frac{A_{in}}{A_{void}} \tag{7}$$

$$E_{scatter} = \frac{A_{out}}{A_{border}} \tag{8}$$

where A_{in} is the area belonging to the detected signal in the void area; A_{void} the area of the void; A_{out} the area belonging to the detected signal in the border area; and A_{border} is the area of a 0.10 m border around the void.

Parameters for the computation of the efficiency of void detection, as well as the level of scattering in the border area outside the void, are displayed in Fig. 9. In

an ideal case, E_{void} should equal 1 and $E_{scatter}$ should be 0. According to the efficiency values obtained for void detection (Table 2), a drop of 9 % in radar data can be observed due to the moisture increase, whereas the ultrasonic data decrease by 14 %. This is, however, remarkably lower than the influence of scattering obtained from data quality checks and could therefore be mostly affected by the choice of threshold velocity value. The latter is also dependent on the size of the area detected. Therefore, a quantitative evaluation of the level of scattering outside the void has to be examined carefully in regard to the size of the detected area. However, as expected, both radar and ultrasonic data exhibit higher levels of scattering in wet masonry.

It should be mentioned that the propagation of the electromagnetic signal in wet materials is affected by an increase in depth resolution due to decreased signal velocity, as well as by increased attenuation. In addition, for the ultrasonic signal the attenuation also increases due to stronger scattering. According to our results, we can conclude that the increased attenuation governs the propagation of both electromagnetic and acoustic waves in wet masonry.

4.2 Complex resistivity results

For the inversion routine performed on CR data, a 2-D inversion commercial software program called WallBERT [11], based on FEM (finite element methods), was used. Extensive data analysis using various electrode arrays and varying numbers of electrodes and model elements for the inversion routine revealed that in the majority of cases the Wenner array produced the best tomographic images. This could be explained by the greater depth of penetration and the better signal to noise ratio of the Wenner array in comparison to the dipole–dipole array [15]. Comparing Geotest and SIP256c measurement devices, SIP256c turned out to be more sensitive and consequently produced results with very high errors. As already stated in Kruschwitz et al. [14], all phase data were relatively noisy and could not provide any satisfactory reconstructions. Therefore, only CR magnitudes were investigated.

Moreover, besides the quality of the measured data, the parameter setting of the inversion routine could remarkably affect the quality of the resulting tomographic images. Usually, the best tomographic reconstructions were obtained by using irregular finite elements and a blocky model [15].

The measured CR magnitudes exhibited relatively high error values, probably due to poor electrode coupling and low currents in the measurement equipment. However, in the inversion routine only data with error values lower than 25 % were used. Only the tomographic resistivity images obtained on the dry and the wet specimen using the four-sided Wenner array are discussed. Here (Fig. 10; Table 3) show that CR magnitudes range between 400 and 700 Ωm for the dry specimen, whereas for the wet specimen values are between 12 and 24 Ωm. From the tomographic image of the dry specimen (Fig. 10a) relatively low resistivity magnitude values were obtained in comparison with the values which had been obtained earlier on the same specimen [14]. Even lower resistivities have been detected at the edges. This becomes apparent at the top edge of the dry specimen where resistivity values reach the values as high as the void itself. This clearly shows the problem of poor electrode coupling which greatly affects the reconstructed resistivities at the upper part of the specimen. However, it has only small effect on the reconstructed resistivities of the void area and thus on the estimation of the efficiency value of void detection. On observing both images in Fig. 10, the lower edge of the detected void seems to be slightly shifted downwards. This means that CR has a lower depth resolution than the other two methods, which could be explained by the predominantly surface current flow in the specimen. Another noticeable point is the very low resistivity value of the void in the wet specimen (around 50 Ωm). As already stated for the radar and ultrasonic results, the main reason for this is probably the restriction of the inversion process on the reconstruction of highly contrasting material properties. Despite all the drawbacks of CR, a relatively high efficiency value (20 %) of void detection can be observed even for the dry specimen, while for the wet specimen a tremendous increase of more than 100 % can be noticed from Table 3. Contrary to expectations, the higher level of scattering refers to the wet specimen. The reason for

Table 3 Tomographic results for complex resistivity data of the dry and the wet specimen

	Surrounding complex resistivity magnitude (Ωm)	Void detection efficiency (%)	Level of scattering (%)
Dry	400–700	20	5
Wet	12–24	43	25

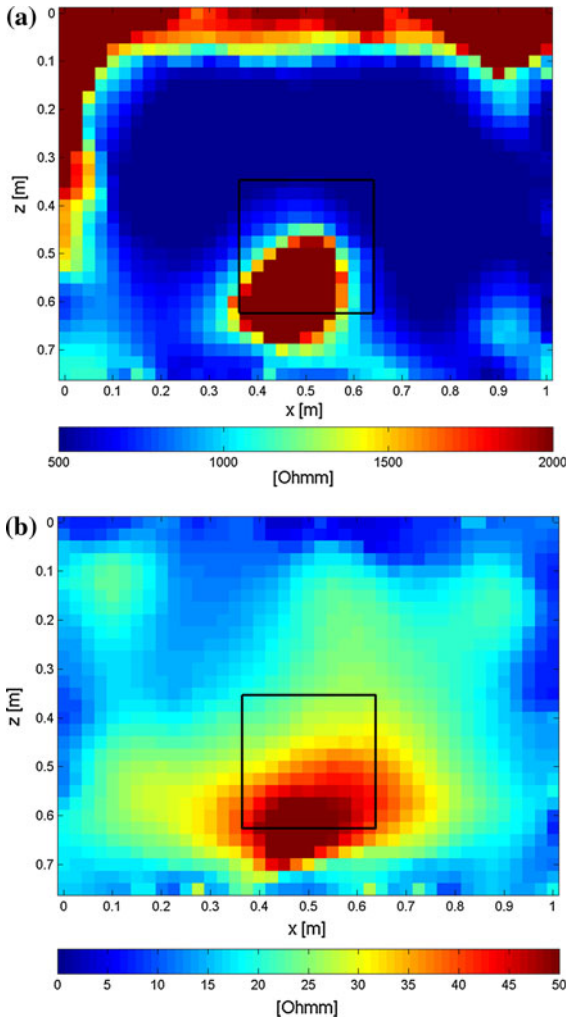

Fig. 10 Complex resistivity tomographic images of the dry (**a**) and the wet specimen (**b**), where the rectangle *marks* the exact position of the void

this is the shift in the detected area which becomes even larger due to increased detectability in wet masonry. Moreover, an inhomogeneous moisture distribution in the wet specimen could also give rise to scattering. Due to the high resistivity variations between the dry and wet state time-lapse resistivity inversion could not contribute to better interpretation of the effect of changing moisture distribution.

5 Conclusion

Three NDT methods were tested for their void detection capability in masonry exposed to different humidity levels. Radar-, ultrasonic- and CR-tomographies were applied to a dry and a wet specimen. Comparing the radar and ultrasonic results, the latter proved to be more scattered and the variations also more sensitive to moisture. This phenomenon could be explained by both the greater effect of ambient vibrations on the ultrasonic data and the stronger difference in the acoustic properties of masonry materials (brick, mortar) compared to the change in the electromagnetic properties.

To achieve a reliable evaluation of the influence of moisture on void detection with the three techniques, two estimators based on a threshold value were defined. The first determines the void detection efficiency directly and the second determines the level of scattering in a defined border area outside the void. Comparing results from the wet versus dry specimen, a decrease in void detection efficiency was observed for radar and ultrasonic data, whereas in CR the efficiency improved remarkably due to the increased conductivity and sensitivity of CR with increased moisture content. The level of scattering was found to be highly sensitive to the threshold value chosen and the depth resolution of the method. However, both proposed estimators proved to be adequately applicable for determining the void efficiency.

All analysed methods proved capable of detecting the large air void though differing significantly in respect to their efficiency. It was shown that radar tomography is by far the most reliable technique for assessing voids in both dry and wet masonry. On the other hand, ultrasonic tomography requires longer measuring times, and a reliable tomographic image can be achieved solely by carefully performed automatic picking. CR tomography turned out to be a reliable technique even at low humidity levels, although it is limited by lower depth resolution than the other two methods and suffers from poor electrode coupling. The latter might also greatly affect the interpretation of the reconstructed resistivities.

Even though the study took into account only one, relatively large sized void and only two moisture levels, these first results already show that each method can be regarded as effective in detection of larger voids under particular masonry conditions, and their complementary use can contribute to better interpretation of more complex inner structures. However, to explore the potential of the analysed methods more precisely, more humidity conditions should be taken into account

and also different tomography configurations that would not restrict the application only to pillars or walls accessible from all four sides as in our study.

Acknowledgments The first author gratefully acknowledges the financial support of the Slovenian Research Agency through grant 1000-10-310156 and the Slovene Human Resources and Scholarship Fund through grant 11012-13/2011. The authors wish to thank Jens Wöstmann and Maria Grohmann for their help during the measurements.

References

1. Binda L, Saisi A (2009) Application of NDTS to the diagnosis of historic structures. In: Proceedings of the 7th international symposium on NDT in civil engineering (NDTCE 2009), p 28
2. Binda L, Lenzi G, Saisi A (1998) NDE of masonry structures: use of radar tests for the characterisation of stone masonries. NDT&E Int 31(6):411–419
3. Binda L, Zanzi L, Lualdi M, Condoleo P (2003) Complementarity of non destructive techniques in the diagnosis of damaged historic structures. In: Proceedings of the international conference on structural faults and repair, p 9
4. Binda L, Saisi A, Zanzi L (2003) Sonic tomography and flatjack tests as complementary investigation procedures for the stone pillars of the temple of S. Nicolo l'Arena (Italy). NDT&E Int 36(4):215–227
5. Binda L, Bosiljkov V, Saisi A, Zanzi L (2006) Guidelines for the diagnostic investigation of historic buildings. In: Proceedings of the 7th international masonry conference: London 2006 (Proceedings of the British Masonry Society, No. 10)
6. Binda L, Lualdi M, Saisi A, Zanzi L (2011) Radar investigation as a complementary tool for the diagnosis of historic masonry buildings. Int J Mater Struct Integr 5(1):1–25
7. Camplani M, Cannas B, Carcangiu S, Concu G, Fanni A, Montisci A, Mulas M (2008) Acoustic tomography for non destructive testing of stone masonry. In: Oea G (ed) ICCSA 2008, part II, LNCS 5073. Springer, Berlin, pp 596–605
8. Colla C, Das P, McCann D, Forde M (1997) Sonic, electromagnetic and impulse radar investigation of stone masonry bridges. NDT&E Int 30(4):249–254
9. Dyer B, Worthington M (1988) Some sources of distortion in tomographic velocity images. Geophys Prospect 36(3):209–222
10. Flint R, Jackson P, McCann D (1999) Geophysical imaging inside masonry structures. NDT&E Int 32(8):469–479
11. Günther T, Rücker C (2008) WallBERT, Version 0.9. Benutzerhandbuch
12. Jol H (ed) (2009) Ground penetrating radar: theory and applications. Elsevier Science, Amsterdam
13. Kong F, By TL (1995) Radar tomography for non-destructive testing. In: Proceedings of the international symposium on NDT in civil engineering (NDT-CE), Berlin, pp 681–688
14. Kruschwitz S, Niederleithinger E, Trela C, Wöstmann J (2010) Complex resistivity and radar investigation of building material: first results of field scale measurements. Acta Geophys 58(1):96–113
15. Loke M (2011) Tutorial: 2-D and 3-D electrical imaging surveys. p 148. http://www.geotomosoft.com. Accessed 7 April 2011
16. Maeda N (1985) A method for reading and checking phase times in auto-processing system of seismic wave data. J Seismol Soc Jpn 38:365–379
17. Maierhofer C, Colla C (2000) Influence of moisture content on the detection of structural features in building construction using impulse radar. In: Alampali S (ed) Structural materials technology IV—an NDT conference. Technomic Publishing Co., Lancaster, pp 343–349
18. Maierhofer C, Leipold S (2001) Radar investigation of masonry structures. NDT&E Int 34(2):139–147
19. Maierhofer C, Roellig M (2009) Active thermography for the characterization of surfaces and interfaces of historic masonry structures. In: Proceedings of the 7th international symposium on NDT in civil engineering (NDTCE 2009), p 6
20. Sadri A (2003) Application of impact-echo technique in diagnoses and repair of stone masonry structures. NDT&E Int 36(4):195–202
21. Sandmeier K (2004) Reflexw, Version 3.5, instruction manual for processing of seismic, acoustic or electromagnetic reflection, refraction and transmission data
22. Schuller M, Berra M, Atkinson R, Binda L (1997) Acoustic tomography for evaluation of unreinforced masonry. Constr Build Mater 11(3):199–204
23. Schuster G (1996) Resolution limits for crosswell migration and traveltime tomography. Geophys J Int 127(2):427–440
24. Tronicke J (2007) The influence of high frequency uncorrelated noise on first-break arrival times and crosshole traveltime tomography. J Environ Eng Geophys 12(2):173–184
25. Tronicke J, Dietrich P, Appel E (2002) Quality improvement of crosshole georadar tomography: pre- and post-inversion data analysis strategies. Eur J Environ Eng Geophys 7:59–73
26. Tweeton D (2001) GEOTOMCG, instruction manual for the three dimensional tomography program
27. Valle S, Zanzi L, Rocca F (1999) Radar tomography for NDT: comparison of techniques. J Appl Geophys 41(2–3): 259–269
28. Wendrich A, Trela C, Krause M, Maierhofer C, Effner U, Wöstmann J (2006) Location of voids in masonry structures by using radar and ultrasonic traveltime tomography. In: Proceedings of the 9th European NDT conference (ECNDT 2006), Berlin, vol 11, p 11

APPENDIX D: ARTICLE 4

Unsupervised clustering of laser-induced breakdown spectroscopy data from concrete

P. Cotič, E. Niederleithinger & G. Wilsch

JAAS (submitted for publication)

ARTICLE TYPE www. rsc.org/xxxxxx | XXXXXXXX

Unsupervised clustering of laser-induced breakdown spectroscopy data from concrete

Patricia Cotič,[*a,b] **Ernst Niederleithinger,**[*a] **and Gerd Wilsch**[a]

Received Xth XXXXXXXXXX 20XX, Accepted Xth XXXXXXXXX 20XX
First published on the web Xth XXXXXXXXXX 200X
DOI: 10.1039/b000000x

Detailed knowledge on the content and distribution of contaminants, such as chlorine, sulphur or sodium is of utmost importance for damage assessment and lifetime prediction of concrete structures. In most cases, only the content of these elements in the cement matrix is relevant. Laser-Induced Breakdown Spectroscopy (LIBS) is able to provide this information as it features a millimetre spatial resolution. However, to associate spectra with the cement matrix only, an automatic method to discriminate the results would be beneficial. To solve issues associated with most conventional separation criteria of LIBS data, which rely on a subjectively estimated threshold value, we evaluated the use of statistical clustering methods. Several algorithms proved to resolve the concrete structure accurately even for large heterogeneity. On the basis of clustering results, smooth depth profiles of sodium content in the cement were obtained. With a parameter optimization procedure, an unsupervised evaluation of LIBS data is proposed.

1 Introduction

Concrete pavements became popular again in the 1990ies, when great stretches of motorway had to be rebuilt and extended after the German reunion. Over several years damage such as cracking or spalling occurred at many points, mainly related to the alkali-silica reaction (ASR) and reinforcement corrosion, induced by de-icing salts in the pore system of the cement matrix. To prevent deterioration in the condition of the concrete, high resolution depth profiles of externally provided sodium and chlorine in the cement part are required to assess the effects of the ASR and corrosion, respectively. An overview of the ASR together with other degradation phenomena is given *e.g.* in Kropp and Hilsberg,[1] Glasser *et al.*[2] and Molkenthin.[3]

Current methods for evaluation of the sodium and chlorine content often lack speed, resolution or relevance. For conventional chemical analysis, cores are taken from structures and larger portions are ground, which needs intensive laboratory work. High resolution alternatives such as X-ray diffractometry do not detect all the important elements or minerals, cover only a small sample volume or require costly sample preparation. Consequently, in practice only few concrete cores are investigated and assumed to be representative for the whole structure.

Laser-induced breakdown spectroscopy (LIBS) is a high speed and high resolution method (up to 100 Hz measurement frequency and 0.5 mm dot pitch for the application presented here). It has been shown to be able to detect all the important elements in concrete, *e.g.* chlorine, sodium and sulphur, which are responsible for particular degradation mechanisms. The method is renowned by its multi-element ability, *i.e.* delivering information from several elements during a single measurement. With a more complex detector (echelle spectrometer), up to 40 spectral lines can be detected simultaneously.[4] Moreover, the method requires only minor sample preparation and can be performed on-site. The current state of the art of LIBS for concrete is described *e.g.* in Molkenthin[3] and Wilsch and Molkenthin.[4]

One of the main aims of spatially acquired LIBS data on concrete is the derivation of accurate depth profiles representing the content of alkali elements in the cement part of concrete at a resolution and efficiency which cannot be met by other chemical methods.[5] For that, proper identification of the measurement points representing cement should be made. However, in most cases its capability is restricted by the heterogeneity of concrete.[6] The amount, type and size of aggregate (mostly locally available gravel or crushed rock, with a size from the sub-millimetre to the centimetre range) influence the acquired spectra. In most cases it is impossible to predict whether a single laser shot hits cement, aggregate or some kind of mixture even when the concrete surface is scanned with a resolution of at least 1 mm. Therefore, criteria based on the content of one or several elements (*e.g.* hydrogen, oxygen, calcium) have to be used on hundreds of spectra to identify those which contain (almost) only information from the ce-

[a] *BAM Federal Institute for Materials Research and Testing, Div. 8.2: Non-Destructive Damage Analysis, Unter den Eichen 87, 12205 Berlin, Germany. Tel.: (+386) 1 4267178; E-mail: Ernst.Niederleithinger@bam.de*
[b] *Institute of Mathematics, Physics and Mechanics, Jadranska 19, 1000 Ljubljana, Slovenia. Tel.: (+386) 1 4267178; E-mail: patricia.cotic@imfm.si*

ment matrix. Three separation criteria are currently used: the oxygen/calcium ratio, the position in ternary diagrams (silica, iron+aluminium, calcium+magnesia) and the hydrogen content (hydrogen being absent in most aggregate minerals). All these criteria contain a subjectively estimated threshold value and cannot be used in automatic evaluation schemes.[6]

Objective statistical clustering or grouping criteria, which can be used without detailed initial knowledge of the sample and human supervision, have been applied to LIBS data before. Methods from multivariate statistics such as principal component analysis (PCA), artificial neural networks or hierarchical and other clustering algorithms have been used to identify groups or outliers in large numbers of samples.[7–12] To our knowledge they have never been applied to the LIBS spatial data of a particular sample, *i.e.* to spectra coming from different positions on the same sample.

In our study, clustering methods were applied for pattern recognition (here: cement identification) of spatial LIBS data on concrete samples subjected to ASR. Clustering methods were chosen since they can work fully unsupervised, which means they do not need any prior knowledge about the statistical distribution of data as conventional statistical methods do. Moreover, they do not require a good training data set as most other objective statistical grouping criteria. This is especially promising for LIBS data, where knowledge about the sample composition is usually limited.

2 Material and methods

2.1 LIBS acquisition system

The data presented here was acquired by the LIBS system used at BAM for the investigation of building materials (Fig. 1). A Nd:YAG-Laser (INNOLAS Spitlight 600, $\lambda = 1064$ nm, $f = 10$ Hz, pulse width $= 7$ ns, energy $= 800$ mJ, irradiance $= 8 \times 1011$ W/cm^2) was focused on the sample surface producing plasma, which vaporized a few μg of the material from the surface. To obtain a small spot size, a beam expander in combination with a lens ($f = 50$ mm) was used. The spot size on the sample surface was in the order of 0.3 mm^2. The volume around the laser plasma was flooded by helium to remove dust and in particular to enhance the chlorine signals in the spectra. Upon cooling of the plasma, the light of wavelengths characteristic of the chemical elements in the plasma (and thus in the specimen) was emitted. This light was guided by an optical fibre to the spectrometer (Shamrock 303i, Czerny-Turner, $f = 303$ mm, aperture = F/4, resolution of 0.1 nm with 1200 l/mm@800nm grating). For light detection, a charge-coupled device (CCD) camera (ANDOR IDUS 420A BR-DD, 1024×256 pixels, 16 bit) with a quantum efficiency of 90 % up to 900 nm was used. The exposure time of the CCD was set to 50 ms to grab the whole plasma radiation of a single pulse. A time resolved measurement was not possible with that type of CCD. For each point, the sum of three successive plasma events was recorded. To map a particular area of the sample, a translation stage was used to move the sample in the plane perpendicular to the laser beam. The system was fully automated and controlled by LabView-based software.

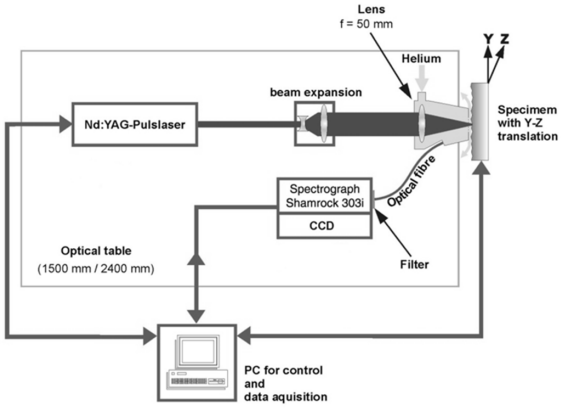

Fig. 1 Experimental configuration of the LIBS system

2.2 Specimen

We investigated one laboratory concrete test specimen, subjected to an ASR performance test, where one side of the specimen was immersed in a 3.6 % NaCl solution under cyclic climate storage at 40 °C. The sample was split in the cross section by dry sawing in order to avoid effects of drilling and to obtain an even surface. A photograph of the concrete core investigated is shown in Fig. 2 (the top edge of the specimen

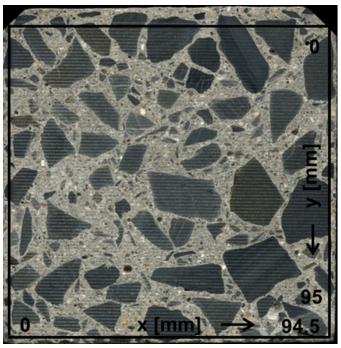

Fig. 2 Concrete specimen with coordinate system. Black lines mark the investigated part, grey lines on aggregate are a result of the LIBS measurement. The top edge of the specimen was subjected to alkalis with penetration in the y-direction

was subjected to alkalis with penetration in the y-direction). The sample is apparently undamaged and contains greywacke aggregates of different colour and size (ranging from the submillimetre size to 5 cm). The cement type CEM I was utilized with a water/cement ratio of 0.45. An area of $94.5 \times 95\,\mathrm{mm}^2$ of the sample was investigated using the LIBS setup described above with a spatial resolution of 0.5 mm by 1 mm, producing 190×96 spectra. The resolution was high enough to map most of the aggregates. The data acquisition time for a complete scan of the sample was 90 min.

2.3 Clustering methods

Clustering or cluster analysis refers to the task of grouping a set of data (observations) into subsets (clusters, groups or classes) in such a way that the members of a cluster are as similar as possible, whereas members belonging to different clusters are as dissimilar as possible.[13] The term similarity refers to differences in observational properties. A common measure of similarity between two observations x_1, x_2 is the Euclidian distance d, which can be for M variables written as

$$d^2(\mathbf{x_1},\mathbf{x_2}) = \sum_{i=1}^{M} (x_{1i} - x_{2i})^2 = \|\mathbf{x_1} - \mathbf{x_2}\|^2. \tag{1}$$

Starting with a random grouping of an unlabelled data set with N observations $\mathbf{X} = \{\mathbf{x_1}, \mathbf{x_2}, \ldots, \mathbf{x_N}\}$ into c clusters, the observations are moved in each step to the cluster whose centre is the nearest to them until a convergence limit is reached. To partition the data set by iteratively assigning labels u_{ij} to vectors in $\mathbf{X}$ by partition matrix $\mathbf{U} = [u_{ij}]_{c\times N}$, many clustering models have been proposed. The target of all of them is to minimize an objective function J, which is the sum of the distances of N observations from their respective cluster centre $\mathbf{v}$:

$$J_m(\mathbf{U},\mathbf{V};\mathbf{X}) = \sum_{i=1}^{c}\sum_{j=1}^{N} u_{ij}^m \|\mathbf{x_j} - \mathbf{v_i}\|^2. \tag{2}$$

As the result may be dependent on the initial random partition, clustering should be repeated several times. The minimum number of clusters is 2 and all have to be non-empty.

With respect to the partition matrix, clustering algorithms can be classified as hard (or crisp), fuzzy probabilistic or fuzzy possibilistic. For hard and fuzzy probabilistic algorithms, the memberships u_{ij} of each observation have to sum to 1 over all clusters, whereas possibilistic clustering drops this constraint. Moreover, for hard clustering (in this study we refer to the k-means algorithm[14]), u_{ij} possess values of only 0 or 1 ($u_{ij} \in \{0,1\}$). On the other hand, fuzzy clustering is defined as soft partitioning, allowing observations to belong to more than one cluster with a calculated probability, *i.e.* u_{ij} may possess any number between 0 and 1 ($u_{ij} \in [0,1]$). This concept is promising for our application, since the observations (LIBS spectra) may contain information from more than one component of the concrete.

2.3.1 Fuzzy probabilistic clustering. The best known fuzzy probabilistic algorithm is the fuzzy c-means (FCM) algorithm of Bezdek.[15] It can be seen as the fuzzy extension of the k-means algorithm, where u_{ij} describes the membership of observation $\mathbf{x_j}$ in the i-th cluster in terms of probability (thus probabilistic clustering). The fuzzing exponent or fuzzifier m, introduced in (2), is a positive real number and is recommended to range from 1.2 to 2 (in our calculation m was fixed to 2, being the value most recommended by other authors). To optimize J, u_{ij} and $\mathbf{v_i}$ should be updated in each iteration by

$$u_{ij} = \frac{1}{\sum_{k=1}^{c} (d_{ij}/d_{kj})^{2/(m-1)}}, \tag{3a}$$

$$\mathbf{v_i} = \frac{\sum_{j=1}^{N} u_{ij}^m \cdot \mathbf{x_j}}{\sum_{j=1}^{N} u_{ij}^m}, \tag{3b}$$

with $d_{ij} = \|\mathbf{x_j} - \mathbf{v_i}\|, \quad 1 \le i \le c, \quad 1 \le j \le N$.

Due to the fact that the Euclidian distance is used, the FCM method is based on the assumption of spherical clusters and is sensitive to outliers and disturbances. To account for the first, the Gustafson-Kessel (GK) algorithm[16] can be used, which uses individually adapted distance functions determined by the covariance matrices of each cluster to account for their different shape (*e.g.* ellipsoidal) and size. However, the GK algorithm cannot be used in a fully automatic mode as some preliminary information about the cluster size needs to be given. Kruse *et al.*[17] recommended using the final FCM partition for the initialization of GK partitioning. This was also used in our version of the algorithm.

The sensitivity to outliers can be overcome by using noise clustering,[18] where an additional noise cluster is introduced. For the noise centre $\mathbf{v_c}$, the distance of observation $\mathbf{x_j}$ to $\mathbf{v_c}$ is $d_{cj} = \delta$ for each observation. Therefore, the distances in (2) and (3a) should be replaced according to

$$d_{ij} = \|\mathbf{x_j} - \mathbf{v_i}\| \quad \text{for} \quad 1 \le j \le N, 1 \le i \le c-1, \tag{4a}$$

$$d_{ij} = \delta \quad \text{for} \quad 1 \le j \le N, i = c,$$

$$\delta^2 = \lambda \cdot \frac{\sum_{i=1}^{c-1}\sum_{j=1}^{N} d_{ij}^2}{N(c-1)}. \tag{4b}$$

For the calculation of δ, parameter λ was estimated by using the standard deviation of the inter-point distances.[18] However, to achieve the best partition, we further multiplied this parameter by factor L, using 1 as the default value (the values taken

into account for this parameter will be discussed within the results). Similarly as for FCM, noise clustering is applicable to the GK or the k-means algorithms.

2.3.2 Fuzzy possibilistic clustering. Apart from noise clustering described above, fuzzy possibilistic clustering algorithms are able to deal with noisy data. Since they drop the constraint that the memberships of each observation have to sum to 1 over all clusters, memberships should rather be interpreted as the typicality of a data point to a specific cluster. The original possibilistic c-means (PCM) algorithm by Krishnapuram and Keller[19] helps to identify outliers, but at the same time is also sensitive to initialization and very often generates coincident clusters. Therefore, we referred to two modifications of the PCM.

Following Pal *et al.*[20,21] we used a mixed c-means approach called the possibilistic-fuzzy c-means (PFCM) algorithm. The model is based on generating both membership and typicality values, where the objective function should be minimized according to

$$J_{m,\eta}(\mathbf{U},\mathbf{T},\mathbf{V};\mathbf{X},\gamma)=\sum_{i=1}^{c}\sum_{j=1}^{N}\left(a u_{ij}^{m}+b t_{ij}^{\eta}\right)\cdot d_{ij}^{2}+\sum_{i=1}^{c}\gamma_i\sum_{j=1}^{N}(1-t_{ij})^{\eta}, \tag{5}$$

where $a>0$, $b>0$, $m>1$ and $\eta>1$ are user-defined parameters and γ_i should be calculated by[19]

$$\gamma_i = K\cdot\frac{\sum_{j=1}^{N}u_{ij}^{m}\cdot d_{ij}^{2}}{\sum_{j=1}^{N}u_{ij}^{m}},\quad K>0. \tag{6}$$

To minimize $J_{m,\eta}$, the necessary conditions for memberships u_{ij}, typicalities t_{ij} and cluster centres are

$$u_{ij}=\frac{1}{\sum_{k=1}^{c}\left(d_{ij}/d_{kj}\right)^{2/(m-1)}}, \tag{7a}$$

$$t_{ij}=\frac{1}{1+\left(\frac{b}{\gamma_i}\cdot d_{ij}^{2}\right)^{1/(\eta-1)}}, \tag{7b}$$

$$\mathbf{v_i}=\frac{\sum_{j=1}^{N}\left(a u_{ij}^{m}+b t_{ij}^{\eta}\right)\cdot\mathbf{x_j}}{\sum_{j=1}^{N}\left(a u_{ij}^{m}+b t_{ij}^{\eta}\right)}. \tag{7c}$$

In our algorithm we used the final FCM partition for initialization as for the GK. The default parameter values were set to $a=1$, $b=1$, $m=2$ and $\eta=2$. While optimizing these parameters, m remained fixed to its default value since this was the most suitable choice made by the authors of the FCM.

Besides using the mixed c-means approach, we employed a PCM variant using a repulsion term proposed by Timm *et al.*[22] The objective function of PCM with repulsion is given by the following equation

$$J_m(\mathbf{T},\mathbf{V};\mathbf{X},\gamma,\omega)=\sum_{i=1}^{c}\sum_{j=1}^{N}t_{ij}^{m}\cdot d_{ij}^{2}+\sum_{i=1}^{c}\gamma_i\sum_{j=1}^{N}(1-t_{ij})^{m}+\omega\cdot\sum_{i=1}^{c}\sum_{k=1,k\neq i}^{c}\left(1/d^{2}(\mathbf{v_i},\mathbf{v_k})\right), \tag{8}$$

where ω is a user-defined parameter. Here, the necessary conditions are given by

$$t_{ij}=\frac{1}{1+\left(\frac{1}{\gamma_i}\cdot d_{ij}^{2}\right)^{1/(m-1)}}, \tag{9a}$$

$$\mathbf{v_i}=\frac{\sum_{j=1}^{N}t_{ij}\cdot\mathbf{x_j}-\omega\cdot\sum_{k=1,k\neq i}^{c}\left(\mathbf{v_k}/d^{2}(\mathbf{v_i},\mathbf{v_k})\right)}{\sum_{j=1}^{N}t_{ij}-\omega\cdot\sum_{k=1,k\neq i}^{c}\left(1/d^{2}(\mathbf{v_i},\mathbf{v_k})\right)}. \tag{9b}$$

As for the PFCM, the final FCM partition was used for initialization.

2.3.3 Selection of the number of clusters. All clustering algorithms described above require the number of clusters c to be determined in advance. The selection of the optimal cluster number, which yields the best partition is a user-defined parameter. However, to perform partitioning without subjective judgement, one can use validity measures to assess the suitability of a partition for a different c, taking into account both compactness and separation between clusters.[15] Compactness should be thought of as a measure of data scattering within a cluster and therefore the optimum c should minimize the compactness, but maximize the separation between clusters.[23] Several quality validity indices have been introduced (see *e.g.* Abonyi and Feil[24]). In our case, we used three of them that account for both compactness and separation of clusters, as well as fuzziness:

1. The **partition index *SC(c)***, describing the ratio of the sum of compactness and separation of the clusters, where normalization is done by the fuzzy cardinality of each cluster N_i:[23]

$$SC(c)=\sum_{i=1}^{c}\frac{\sum_{j=1}^{N}u_{ij}^{m}\|\mathbf{x_j}-\mathbf{v_i}\|^{2}}{N_i\sum_{k=1}^{c}\|\mathbf{v_i}-\mathbf{v_k}\|^{2}}. \tag{10}$$

2. The **separation index *S(c)***, which uses the same nominator as *SC*, but the minimal separation between clusters as the denominator:[23]

$$S(c) = \frac{\sum_{i=1}^{c}\sum_{j=1}^{N} u_{ij}^{m}\|\mathbf{x_j} - \mathbf{v_i}\|^2}{N \cdot \min_{i,k,i\neq k}\|\mathbf{v_i} - \mathbf{v_k}\|^2}. \quad (11)$$

3. **Xie and Beni's index *XB(c)***, which uses the same nominator as the *SC* and *S* indices, but the minimal distance of data points to cluster centres as the denominator:[25]

$$XB(c) = \frac{\sum_{i=1}^{c}\sum_{j=1}^{N} u_{ij}^{m}\|\mathbf{x_j} - \mathbf{v_i}\|^2}{N \cdot \min_{i,j}\|\mathbf{x_j} - \mathbf{v_i}\|^2}. \quad (12)$$

As fuzzy cardinality normalization of the *SC* index makes it insensitive to cluster size, the *S* and *XB* indices were taken into account when searching for the optimal number of clusters, whereas the *SC* index was used to estimate the quality of different partitions for a specific number of clusters. A good partition should minimize all three validity indices.

3 Results and discussion

3.1 LIBS data

Selected spectral lines of Ca (849.80 nm), O (844.64 nm), Na (818.32 nm), Cl (837.59 nm), C (833.52 nm) and Ti (846.85 nm) were used for the investigation of the sample. A comparison between two typical spectra measured on a coarse aggregate (with an area large enough that any effect of material other than the aggregate itself can be excluded) and the part with a high fraction of cement is shown in Fig. 3. The spectrum assigned mainly to the cement part of the specimen shows a very high intensity of the Ca spectral line, whereas the same line is much lower in the case of the coarse aggregate. In addition, the spectrum measured on the cement part has a higher intensity of the Cl and Na spectral lines due to the ingress of the NaCl solution (note that the Cl spectral line is very weak). Although the two spectra prove that a clear distinction between the aggregate and cement part is possible, most often the ablated material is a mixture of both aggregate and cementious material, and thus more sophisticated separation criteria have to be applied.

The intensities of all spectral lines taken into account are presented for the whole investigated area of the sample in Fig. 4. The intensities were normalized according to the global minimum of the background. The figures show that heterogeneity of the concrete sample is large. There is a large proportion of millimetre- or submilimetre-sized aggregates differing in their element content. From Fig. 5, which represents

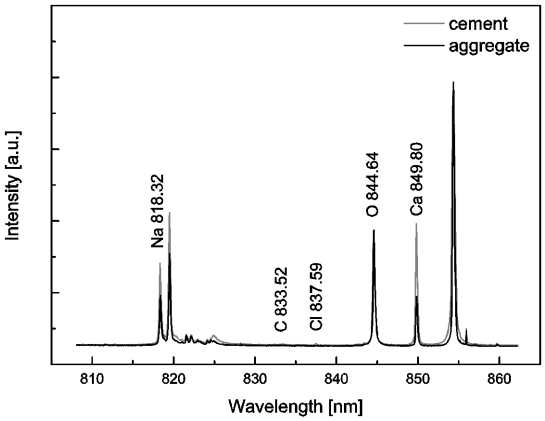

Fig. 3 A comparison between two typical spectra measured on coarse aggregate and the part with high fraction of cement for the range from 808 nm to 862 nm with the identification of the spectral lines

an enlarged part of the investigated sample, it can be seen that the cement part cannot be properly identified using Ca or O spectral intensities alone. Fig. 4 and 5 further show that even larger aggregates which appear to be relatively homogeneous in Fig. 2, differ in their element content (see *e.g.* the Ca spectral line in Fig. 4a). In addition, some aggregates contain a very significant content of Na (Fig. 4c), which would influence conventional chemical analysis. Therefore, for the evaluation of clustering results, the reference for cement identification was determined by a careful evaluation of the surface using the criterion based on the O/Ca ratio explained in the Introduction, as well as by image analysis. The O/Ca criterion was assumed to be significant enough for the resolution used. The reference displayed in Fig. 6 refers to the subjectively estimated optimal threshold value of the O/Ca ratio.

3.2 Clustering results

The spatial intensities of all spectral lines shown in Fig. 4 were used as input data for classification with clustering methods. As a prerequisite for any clustering technique, the optimal number of clusters was determined using the *XB* and *S* indices. The k-means, FCM and GK algorithms were applied with cluster numbers between 2 and 10 and fifteen runs were used to avoid the influence of initialization (the parameter-dependent algorithms were not applied to limit the computational effort). From the *XB* index, which proved more reliable than the *S* index, the optimal number of clusters was chosen to be five, as all methods taken into account exhibited a local minimum at this position.

The resulting partitions of all the clustering methods dis-

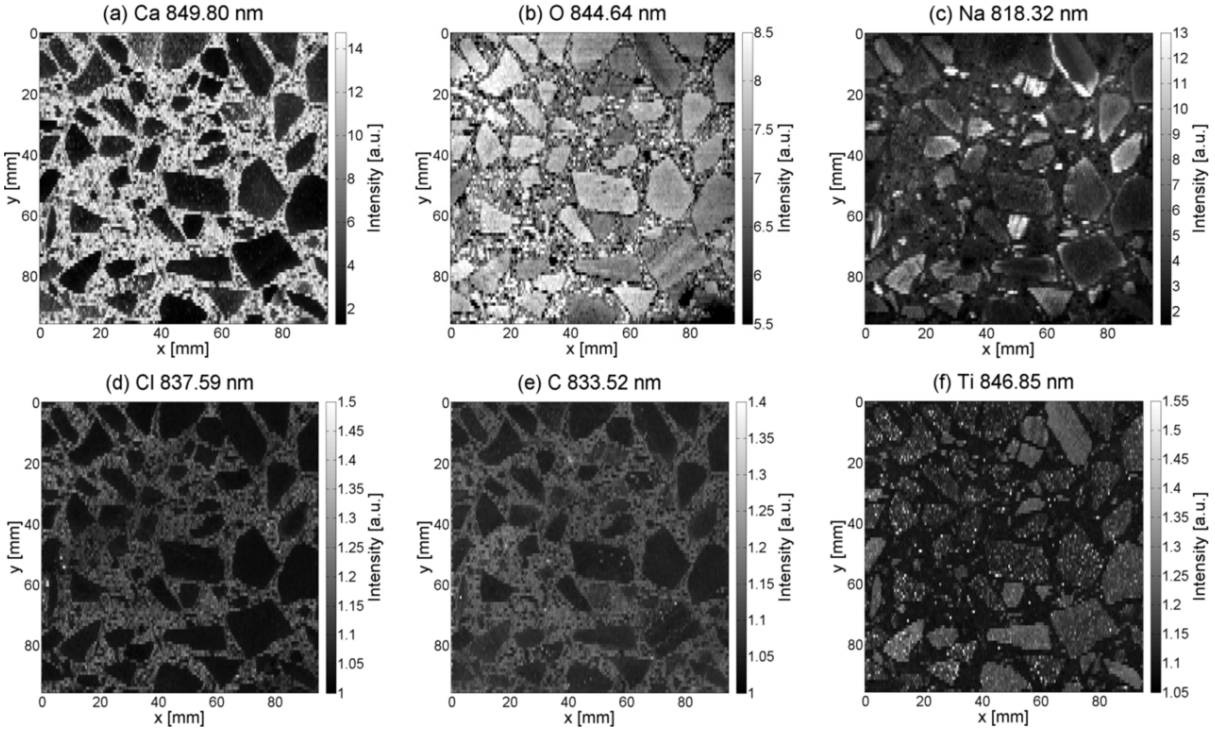

Fig. 4 LIBS normalized spatial intensities for (a) Ca 849.80 nm, (b) O 844.64 nm, (c) Na 818.32 nm, (d) Cl 837.59 nm, (e) C 833.52 nm and (f) Ti 846.85 nm spectral lines

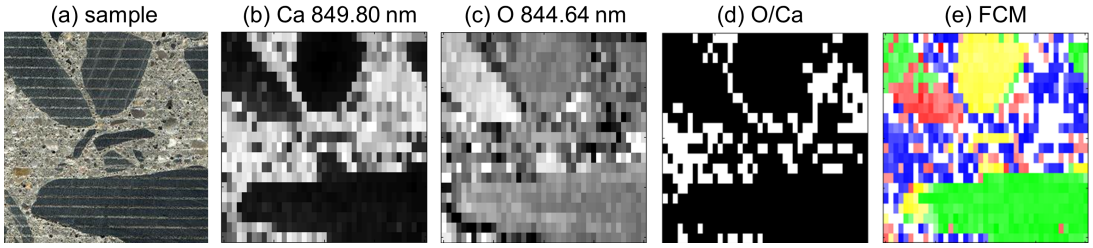

Fig. 5 (a) The sample photo of an area of $20 \times 20\,\mathrm{mm}^2$; LIBS normalized spatial intensities for (b) Ca 849.80 nm and (c) O 844.64 nm spectral lines; classification result using (d) O/Ca conventional criterion and (e) the fuzzy c-means (FCM) algorithm for 5 clusters

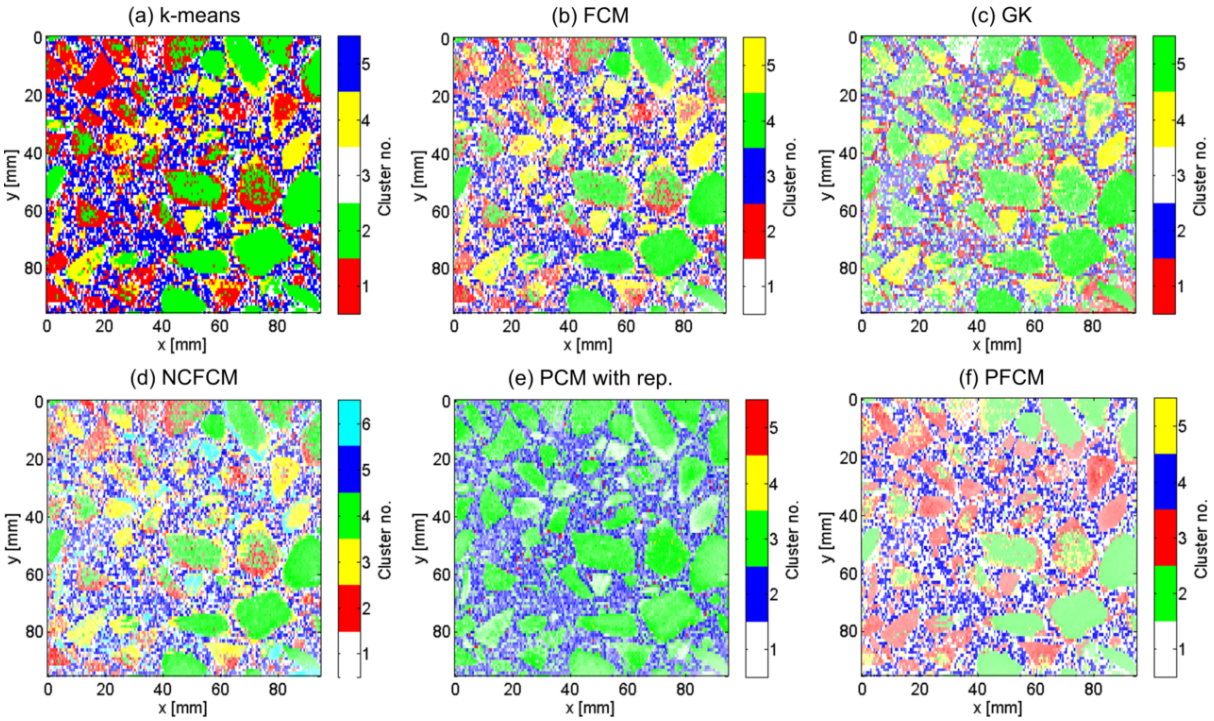

Fig. 7 Clustering partitions for (a) k-means, (b) fuzzy c-means (FCM), (c) Gustafson-Kessel GK, (d) noise clustering FCM (NCFCM), (e) probabilistic c-means (PCM) with repulsion and (f) possibilistic FCM (PFCM) for 5 clusters. For the values of parameters used, refer to Table 1

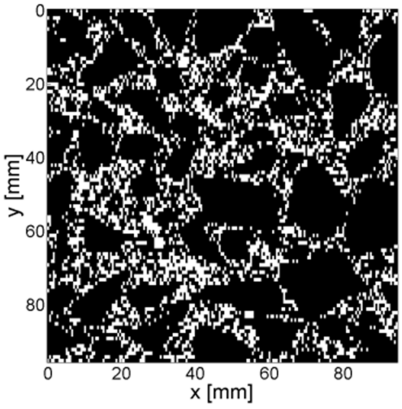

Fig. 6 Result of cement identification (white) by conventional O/Ca criterion and image analysis (used as a reference for the clustering results)

cussed are visualized in Fig. 7 for five clusters. For fuzzy partitions, the cluster colour is displayed according to the hard association of the most probable cluster (the cluster with the highest membership degree), whereas the factor of transparency takes into account the membership degree (*e.g.* $u_{ij} = 1$: opaque, $u_{ij} = 0.5 : 50\%$ transparency). Also the mixed PFCM partition is displayed with respect to the memberships. It can be seen that the algorithms performed differently and assigned both aggregates and the cement part to different clusters. It should be noted that the cluster labels cannot be directly compared between different algorithms, since they depend on random initialization. For the noise clustering partition (here noise clustering FCM NCFCM) it can be seen that cluster 6 collects noisy data, which fits data points with very high spectral intensities for Na (compare Fig. 7d to Fig. 4c). Further, the coincident problem of the PCM with repulsion stands out, where only three clusters are present (Fig. 7e). It has to be stressed that for the NCFCM, PCM with repulsion and PFCM algorithms, the partitions presented refer to the optimal user-defined parameter combination. An explanation of the choice of optimal parameters is given below.

For all partitions, the cluster identified as cement is represented by the blue colour. In the case of the FCM algorithm, it can be seen that the detected cement area resembles the white area from the reference image closely (Fig. 5). However, to quantitatively evaluate the efficiency of all clustering methods for cement identification, we used an objective measure based on the number of false negatives (FN) and false positives (FP) in relation to the reference image in Fig. 6. Here, FN quantifies the number of cement cells identified as aggregate by clustering, whereas FP quantifies the number of aggregate cells identified as cement by clustering. The values of FN and FP are expressed as the percentage of the total number of cement cells (where a cell represents an LIBS measurement point on the concrete surface). For fuzzy partitions, both values were evaluated according to the hard association of the most probable cluster. For the mixed PFCM, where both memberships and typicalities are involved, only memberships were taken into account for the calculation of FN and FP values since they are directly related to memberships from other algorithms and thus enable quantitative comparison.

Table 1 summarizes the results for FN and FP (as the mean value of fifteen runs) for the clustering partitions displayed in Fig. 7. In the interpretation of results, more weight was put on the FP value since it directly reflects the overestimated cement content, being of utmost importance for further calculation of Na content in the cement matrix. The results for FP show that the GK performs worse than the FCM. No improvement could be achieved even by varying the number of clusters. The GK generally delivered good partitions for LIBS data on other concrete samples. The reason for this result with the specimen investigated could be the relatively heterogeneous cement matrix with respect to the aggregates. The hard k-means algorithm proved to be very susceptible to initialization and therefore could not provide stable and reliable results. Among the noise cluster variants, we only present the results for the NCFCM algorithm as the conventional FCM performed best among the k-means and GK algorithms. Here, the user-defined parameter $L = 1$ proved to be the optimal one and reduced the FP value by 40 % in comparison to the FCM. However, the lowest value for FP, *i.e.* 2.77 %, was achieved by using the PFCM algorithm with the parameters set to $a = 1.4$, $b = 1.8$, $m = 2$ and $\eta = 1.7$. It should be noted, however, that low FP values for the PFCM (5.55 %) could already be achieved with the default parameters $a = 1$, $b = 1$, $m = 2$, $\eta = 2$. Therefore, a slightly higher weight on the typicality values (with $b > 1$ and $\eta < 2$) only further improved our results, which is in accordance with the predictions made by the authors of the method.[21] In contrast to noise clustering and the PFCM, which already delivered good results for the default parameters, the PCM with repulsion was found to be a highly parameter-dependent algorithm. Moreover, as already observed (Fig. 7e) it still suffered from producing coincident clusters as the original PCM algorithm and was therefore not included in further studies as well as the k-means due to its initialization problems.

Table 1 Results of false negatives (FN) and false positives (FP) for different clustering methods with 5 clusters

Clustering method	FN (%)	FP (%
k-means	0.05	27.90
fuzzy c-means (FCM)	0.49	12.90
Gustafson-Kessel (GK)	14.50	24.60
noise clustering FCM (NCFCM, $L = 1$)	2.59	7.81
probabilistic c-means (PCM) with rep. ($\omega = 5$)	0.62	35.40
possibilistic FCM (PFCM, $a = 1.4$, $b = 1.8$, $m = 2$, $\eta = 1.7$)	6.02	2.77

3.3 Application of clustering results to the evaluation of sodium content

Reliable, detailed depth profiles of Na in the cement part of samples subjected to ASR or other degradation phenomena is the main outcome from an LIBS investigation. The basis for efficient evaluation is an appropriate cement identification, which has been demonstrated in the previous section. For the sample discussed here, a dens grid (0.5 mm by 1 mm) was used in order to map most of the aggregates in the concrete and thus to provide a credible reference based on the O/Ca criterion for a quantitative evaluation of clustering partitions. In practice, however, the concrete cores taken from structures would be measured with a resolution of 1 mm by 2 mm for a time efficient investigation. In the case of very heterogeneous concrete, the reduced resolution may greatly affect the classification outcome from the O/Ca criterion. To demonstrate this, we present depth profiles of the sodium content in the cement part.

The depth profiles of Na were obtained by averaging the spectral intensity along the horizontal axis (x-direction), taking into account only the cement data, identified by the classification method (different clustering algorithms and the O/Ca criterion) for a spatial resolution of 1 mm by 2 mm. However, as a reference profile, the original resolution of 0.5 mm by 1 mm and the classification shown in Fig. 6 were used. From Fig. 8 it can be seen that the reduced resolution affects the O/Ca criterion to a large extent, which consequently yields a very poor estimate of the Na content. Clustering methods on the other hand derive smoother profiles, closer to the reference. However, small variations between different methods can be observed, which corresponds to the conclusions drawn from the sensitivity evaluation of the methods. In particular, the GK algorithm exhibits some deviations, but in general has still a similar profile to the reference one, whereas the differ-

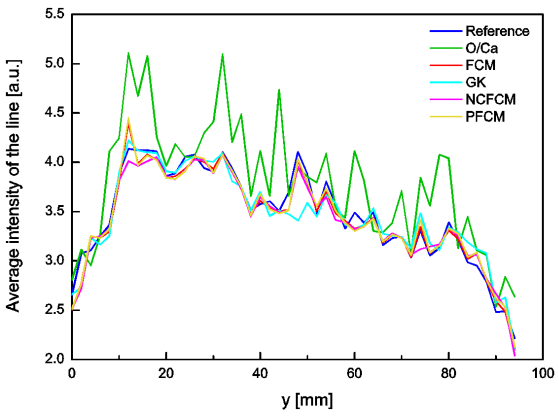

Fig. 8 Depth profiles of Na in the cement matrix of the sample determined using results from various clustering techniques and the conventional O/Ca criterion, compared to the reference. For the values of parameters used, refer to Table 1. The top of the sample is left (y = 0)

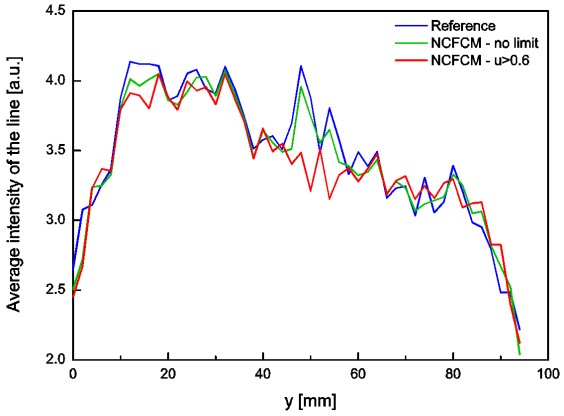

Fig. 9 Depth profiles of Na in the cement matrix for noise clustering FCM (NCFCM) before and after limiting the membership degree to higher than 0.6, compared to the reference. For the parameter L, $L = 1$ was used. The top of the sample is left (y = 0)

ence between the other fuzzy algorithms is not as apparent as in the sensitivity evaluation. All methods show a Na content which is in general higher near the surface exposed to NaCl solution and gradually decreases with depth. This is probably due to de-icing salts. However, very close to the surface exposed to alkalis (0–10 mm) the content is lower due to washout by precipitation. This effect is commonly recognised, but not detectable by standard chemical analysis due to the low spatial resolution of the technique.

The depth profiles displayed in Fig. 8 do not restrict the incorporation of data points according to their degree of membership to the cement cluster. By assuming that this could have an effect on the results, we additionally took into account only cells with a membership degree higher than 0.6. Interestingly, the new results did not bring any improvement, but rather produced a strong deviation of the depth profiles from the reference profile (see Fig. 9 for NCFCM). Small improvements could therefore probably only be achieved by suitably adapting the limit with respect to the cluster number used.

3.4 Automation of the clustering algorithm

A careful sensitivity evaluation showed that both the NCFCM and PFCM algorithms yielded remarkably better partition than the other clustering algorithms analysed. Moreover, contrary to the PCM with repulsion algorithm, both exhibited relatively robust performance and could therefore be suggested for spatial fuzzy clustering of LIBS data from heterogeneous concrete samples.

However, to fully automate the clustering algorithm in order to account for the diversity of concrete specimens, the problem of parameter optimization should be solved. One possibility could be to use a cluster validity function evaluation algorithm. An example of this has been given in Wachs *et al.*[26] where the authors performed parameter optimization of the PCM with repulsion by the use of the XB index. Bensaid *et al.*[23] suggested using the SC index for comparing the effectiveness of various clustering methods at the same number of clusters. We followed both methods. For the PFCM, the SC and XB indices were extended to take into account both membership and typicality as proposed in Zhang *et al.*[27] The outcome was validated by the sensitivity calculation.

The noise clustering parameter L was varied over the range 0.1:0.1:8, whereas the PFCM parameters a, b and η were varied over the ranges $a = 1 : 0.2 : 2$, $b = 1 : 0.2 : 2$ and $\eta = 1 : 0.2 : 2$, with m fixed to 2. In comparison to the SC index, the XB resulted in clear local minima which were in agreement with the sensitivity values of FN and FP. We therefore refer our results only to the XB index. Fig. 10 shows the values obtained for the XB index and FN and FP while varying parameter L in the region up to 2.5. The first local minima of XB appear at $L = 0.3$, $L = 1.0, \ldots$. According to the lowest FP value, $L = 0.3$ should be taken as the optimal parameter. However, Fig. 11 reveals that for $L = 0.3$, the Na profile would deviate greatly from the reference profile. This appeared to be due to the fact that for $L = 0.3$ too many data points were classified as noise, corrupting the behaviour of the algorithm. Due to the high noise level many cement cells were recognized as noise (Fig. 12), which consequently resulted in high FN values. Thus, we suggest that the cluster validity function evaluation algorithm should be restricted to minima of XB close to

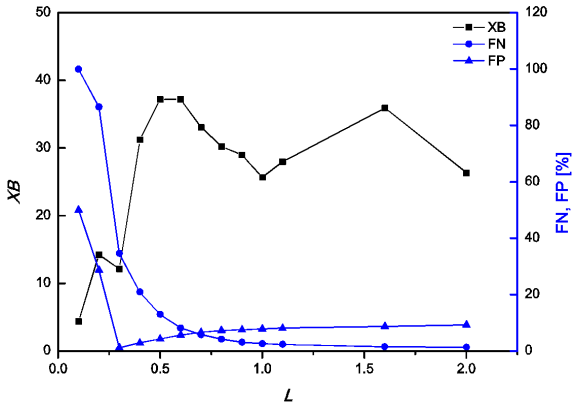

Fig. 10 Results of XB index, false negatives (FN) and false positives (FP) for the optimization of parameter L of noise clustering FCM (NCFCM)

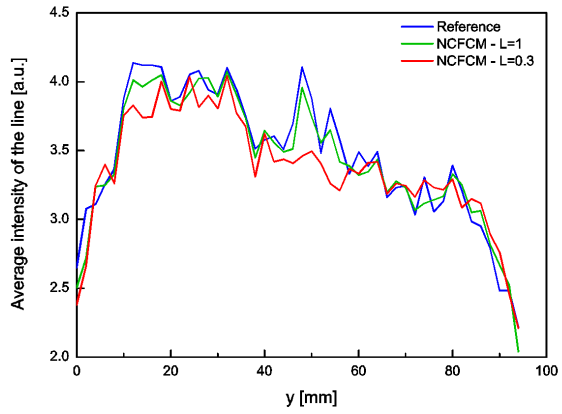

Fig. 11 Depth profiles of Na in the cement matrix for noise clustering FCM (NCFCM) with the value of parameter $L = 0.3$ and $L = 1$, compared to the reference. The top of the sample is left (y = 0)

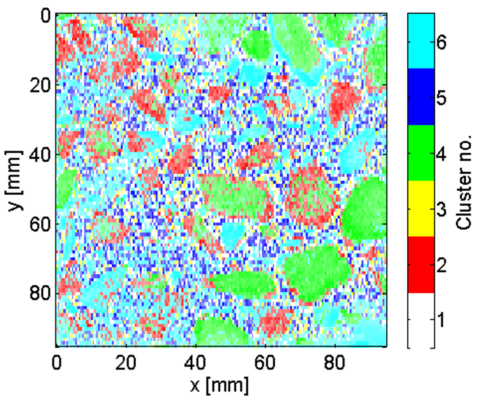

Fig. 12 Clustering partition for noise clustering FCM (NCFM) with the value of parameter $L = 0.3$

the default value.

For the PFCM, Table 2 summarizes the results for the XB index and FN and FP for three combinations of parameters that yielded the lowest XB values. Similarly as for the NCFCM, the parameter combination $a = 1.4$, $b = 1.8$, $m = 2$ and $\eta = 1.7$ with the lowest XB value did not give the lowest FP. However, Fig. 13 reveals that all three parameter combi-

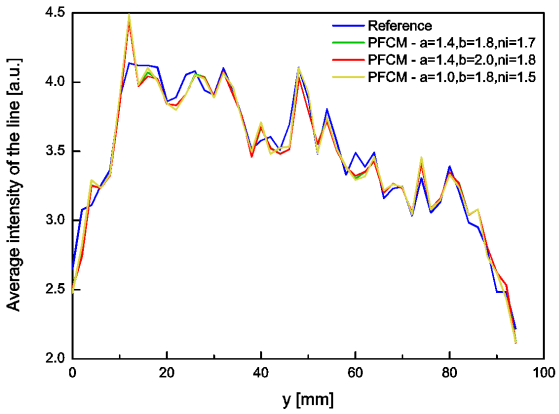

Fig. 13 Depth profiles of Na in the cement matrix for possibilistic FCM (PFCM) with the combination of parameter values set to $a = 1.4$, $b = 1.8$, $m = 2$, $\eta = 1.7$; $a = 1.4$, $b = 2.0$, $m = 2$, $\eta = 1.8$ and $a = 1.0$, $b = 1.8$, $m = 2$, $\eta = 1.5$, compared to the reference. The top of the sample is left (y = 0).

nations would produce very similar depth profiles of the Na content. This suggests that the XB index is a robust validity measure and could be used for the parameter optimization algorithm.

Table 2 Results of the XB index, false negatives (FN) and false positives (FP) for possibilistic-fuzzy c-means (PFCM) with different combinations of parameters.

Parameter combination	XB	FN (%)	FP (%)
$a = 1.4$, $b = 1.8$, $m = 2$, $\eta = 1.7$	64.1	6.02	2.77
$a = 1.4$, $b = 2.0$, $m = 2$, $\eta = 1.8$	71.6	5.24	3.45
$a = 1.0$, $b = 1.8$, $m = 2$, $\eta = 1.5$	78.1	11.0	1.09

4 Conclusions

The use of clustering methods for cement identification of spatial LIBS data from heterogeneous concrete samples subjected to ASR was studied. The use of hard vs. fuzzy clustering, as well as fuzzy probabilistic, noise and fuzzy possibilistic clustering was explored. The separation of LIBS spectra dominated by cement or aggregate content by different clustering algorithms worked well in our application example. The sensitivity evaluation based on the calculation of false negatives and false positives showed that the noise clustering and the mixed possibilistic-fuzzy c-means algorithm in particular provided the optimal partitions. This was justified by the sodium depth profiles, which gave an almost ideal fit to the reference profile and outperformed the standard classification based on the O/Ca criterion to a large extent.

To account for the problem of parameter optimization of noise and PFCM algorithms, we proposed a scheme based on the XB index. For the PFCM, the global minimum of XB was found to characterize the optimal parameter combination, whereas for noise clustering, the search for the optimal value of parameter L should be restricted to local minima in the region close to its default value. Although our results proved the PFCM to be the most reliable clustering algorithm, noise clustering could be seen as the optimal one when also taking into account the computational effort for parameter optimization. For the PFCM, the computational time for optimization of the three parameters greatly increases with respect to the time needed for the optimization of one parameter for noise clustering.

It has to be stressed that although results were presented from only one concrete test specimen subjected to ASR, we also analysed several other laboratory and in-situ concrete cores (also subject to other degradation mechanisms). Overall, noise and possibilistic clustering performed best and can therefore be regarded as capable of dealing with multi-aggregate concrete specimens and noisy LIBS spectra. Contrary to the classification based on the subjectively estimated threshold value of the O/Ca ratio, our proposed parameter optimization model enables the algorithms to work fully unsupervised. Therefore, the improved use of LIBS, being itself reliable and fast, will play an important role in the implementation of the in situ mobile system, which is currently under construction and will bring LIBS into a productive environment.

Acknowledgements

This study was based on preliminary work carried out in our group by Julien Grandemenge. The sample discussed in this text was provided by our colleagues in Division 7.1 of BAM. The first author gratefully acknowledges the financial support of the Slovenian Research Agency through grant 1000-10-310156 and the Slovene Human Resources and Scholarships Fund through grant 11012-13/2012.

References

1 *Performance Criteria for Concrete Durability, RILEM Report No. 12*, ed. J. Kropp and H. K. Hilsdorf, E & FN Spon, London, 1995.
2 F. P. Glasser, J. Marchand and E. Samson, *Cem. Concr. Res*, 2008, **38**, 226–246.
3 A. Molkenthin, Ph.D. Thesis, BAM, Berlin, 2009.
4 G. Wilsch and A. Molkenthin, *Non-Destructive Evaluation of Reinforced Concrete Structures*, Woodhead Publishing Limited, Cambridge, 2007.
5 F. Weritz, A. Taffe, D. Schaurich and G. Wilsch, *Constr. Build. Mater.*, 2009, **23**, 275–283.
6 F. Weritz, D. Schaurich, A. Taffe and G. Wilsch, *Anal. Bioanal. Chem.*, 2006, **385**, 248–255.
7 C. Bohling, D. Scheel, K. Hohmann, W. Schade, M. Reuter and G. Holl, *Appl. Opt.*, 2006, **45**, 3817–3825.
8 N. Labbé, I. M. Swamidoss, N. André, M. Z. Martin, T. M. Young and T. G. Rials, *Appl. Opt.*, 2008, **47**, G158–G165.
9 S. M. Clegg, E. Sklute, M. D. Dyar, J. E. Barefield and R. C. Wiens, *Spectrochim. Acta B*, 2009, **64**, 79–88.
10 A. Koujelev, M. Sabsabi, V. Motto-Ros, S. Laville and S. Lui, *Planet. Space. Sci.*, 2010, **58**, 682–690.
11 S.-L. Lui and A. Koujelev, *J. Anal. At. Spectrom.*, 2011, **26**, 2419–2427.
12 G. Vítková, K. Novotný, L. Prokeš, A. Hrdlička, J. Kaiser, J. Novotný, R. Malina and D. Prochazka, *Spectrochim. Acta B*, 2012, **73**, 1–6.
13 F. Hoeppner, F. Klawonn, R. Kruse and T. Runkler, *Fuzzy Cluster Analysis: Methods for Classification, Data Analysis and Image Recognition*, John Wiley & Sons Ltd., Chichester, 1999.
14 J. B. MacQueen, Proc. of the 5th Berkeley Symp. on Math. Statist. and Prob., Berkeley, U.S.A., Jun 21 – Jul 18, 1965, Dec 27 –Jan 7, 1966, pp. 281–297.
15 J. Z. Bezdek, *Pattern Recognition with Fuzzy Objective Function Algorithms*, Plenum Press, New York, 1981.
16 D. Gustafson and W. Kessel, 1978 IEEE Conf. on Decision and Control including the 17th Symp. on Adaptive Processes, San Diego, CA, Jan 10–12, 1979, pp. 761–766.
17 R. Kruse, C. Doering and M. J. Lesot, *Advances in Fuzzy Clustering and its Applications*, John Wiley & Sons Ltd., Chichester, England, 2007, pp. 3–30.
18 R. N. Dave, *Pattern. Recogn. Lett.*, 1991, **12, 11**, 657–664.
19 R. Krishnapuram and J. M. Keller, *IEEE Trans. Fuzzy Syst.*, 1996, **4, 3**, 385–393.
20 N. R. Pal, K. Pal and J. C. Bezdek, Proc. of the 6th IEEE Int. Conf. on Fuzzy Systems, Barcelona, Spain, Jul 1–5, 1997, pp. 11–21.
21 N. R. Pal, K. Pal, J. M. Keller and J. C. Bezdek, *IEEE T. Fuzzy Syst.*, 2005, **13, 4**, 517–530.

22 H. Timm, C. Borgelt and R. Kruse, Proc. of the Eur. Symp. on Intelligent Technologies, Hybrid Systems and their implementation on Smart Adaptive Systems, Tenerife, Spain, Dec 13–14, 2001, pp. 1–7.
23 A. M. Bensaid, L. O. Hall, J. C. Bezdek, L. P. Clarke, M. L. Silbiger, J. A. Arrington and R. F. Murtagh, *IEEE T. Fuzzy Syst.*, 1996, **4, 2**, 112–123.
24 J. Abonyi and B. Feil, *Advances in Fuzzy Clustering and its Applications*, John Wiley & Sons Ltd., Chichester, England, 2007, pp. 95–121.
25 X. L. Xie and G. Beni, *IEEE T. Pattern Anal.*, 1991, **13, 8**, 841–847.
26 J. Wachs, O. Shapira and H. Stern, *Applied Soft Computing Technologies: The Challenge of Complexity*, Springer Verlag, Berlin, 2006, pp. 77–87.
27 C. Zhang, Y. Zhou and T. Martin, Proc. of IPMU08, Torremolinos, Málaga, Jun 22–27, 2008, pp. 877–882.